INVESTIGATIONS OF CRUSTAL STRUCTURE AND ACTIVE TECTONIC PROCESSES IN THE COAST RANGES, CENTRAL CALIFORNIA

A DISSERTATION

SUBMITTED TO THE DEPARTMENT OF GEOPHYSICS

AND THE COMMITTEE ON GRADUATE STUDIES

OF STANFORD UNIVERSITY

IN PARTIAL FULFILLMENT OF THE REQUIREMENTS

FOR THE DEGREE OF

DOCTOR OF PHILOSOPHY

By

Donna Mae Eberhart-Phillips

January 1989

Abstract

Inversion of 7,696 P and 1,511 S arrivals from earthquakes and 696 P first arrivals from shots for the Coalinga region produced a three-dimensional velocity model with 1- to 2-km gridspacing at hypocentral depths. The shape and location of velocity features correspond well to mapped surface geology and observed gravity, and the inversion can discern details of folds where resolution is good. Inferred uplift amounts are similar to those implied by geologic data. Gravity computed from 3-D velocities, converted to density, matches observed gravity quite well. A shallow low-velocity zone (LVZ) along the fold axis may indicate high pore pressure caused by lateral compressive strain. An empirical relationship, from laboratory measurements, describes how increased pore pressure lowers velocity. A series of deeper LVZ's may represent heterogeneity resulting from deformation along multiple thrust faults.

Interpretation of hypocenters and fault-plane solutions for the 1983 Coalinga earthquakes together with the 3-D velocity model shows that the character of the seismicity varies along the anticline with the amount of previous deformation. The faulting structure beneath the fold consists primarily of southwest-dipping thrusts uplifting blocks of higher-velocity material. Where the previous uplift was largest, the shallow seismicity shows secondary faulting on either side of the fold. Where there was little previous deformation, only diffuse seismicity occurs and the velocity structure does not show evidence of uplifted blocks. The mainshock rupture terminated where the fold trend was no longer uniform, and its upward extent ended at a

lithologic boundary. Thus, the extent of rupture area is limited by the area of uniform structural orientation and by changes in material properties.

Influence of the San Andreas fault (SAF) on crustal strain in adjacent areas is studied through analysis of a 140-km wide trilateration network. The strain orientation near the SAF is consistent with right-lateral shear, with maximum shear 0.38 $\pm$ 0.01 μrad/yr at N63°W. Away from the SAF the strain orientations on both sides are consistent with fault-normal compression, with maximum shear 0.19 $\pm$ 0.01 μrad/yr at N44°W. A vertical SAF below the surface trace fits the data much better than either a dipping fault or a fault located to the south.

Table of Contents

Chapter 1.
Introduction

In this thesis I present an analysis of detailed three-dimensional crustal structure along the eastern margin of the California Coast Ranges and an analysis of active crustal deformation across the San Andreas fault in the northern Transverse Ranges. Additionally, research is described that was carried out to further develop the method of inversion of local earthquake and shot arrival-times to obtain three-dimensional velocity structure. Finally, statistical methods were applied to extract physical property information from laboratory velocity measurements of core samples. In Chapter 2, the crustal structure on the margin of the Coast Ranges, in the vicinity of Coalinga, California, is investigated with three-dimensional P- and S-velocity models obtained through inversion of local earthquake arrival-times and shot data provided by two refraction surveys conducted by the U. S. Geological Survey. In Chapter 3, the active processes that characterize the tectonic history of young folds in the Coast Ranges are studied through combined interpretation of the velocity structure and of hypocenters and focal mechanisms that were recomputed with the 3D model. In Chapter 4, the relationship between the San Andreas transform plate boundary and the near-by active compressional deformation in the northern Transverse Ranges is addressed by analysis of crustal strain calculated from a 140-km wide trilateration network that traverses the San Andreas Fault. In Chapter 5, an empirical relationship between seismic velocity and rock parameters is developed, through statistical

analysis, from a large set of laboratory measurements, in order to enable the estimation of rock parameters and effective pressure from observed velocities.

Tectonic structure and processes are usually interpreted through a combined process of (a) mapping surface geology and analyzing 2D seismic reflection lines to come up with a concept of the tectonic environment, and (b) doing forward modelling of seismic refraction lines and observed gravity to find a specific crustal structure that adequately fits the geophysical data. The type of fault rupture associated with an earthquake is usually inferred from the fault plane solution and the overall regional structure, without detailed knowledge of the local structure near the hypocenter. Large earthquakes are assumed to occur preferentially on pre-existing faults, but identifying those faults, particularly when they are not expressed at the surface, can be difficult. Aftershocks are assumed to occur on the main fault surface or in other parts of the surrounding volume that had large stress changes due to the mainshock. Aftershock locations are often not accurate enough to discern whether the seismicity off the main fault occurs randomly in space, or whether it occurs on secondary pre-existing faults.

The earthquake data itself, through velocity inversion, can be used directly to find the crustal structure. An added benefit of using earthquake data to solve for the structure is that you determine structure in the area that is most seismically active. The earthquake data also reveal the spatial distribution of active faulting and the types of fault rupture presently occurring throughout the volume. Hence the velocity solution and seismicity can be analyzed together to understand the active tectonic processes. The 3D inversion method has previously been used to study regions of strike-slip faulting and to locate magma in active volcanic areas. This is the first time it has been used to study an area dominated by folding and blind thrusts. This

research also extends the inversion method to S-velocity as well as P-velocity. And, because the study area has seismic refraction and reflection lines and gravity observations, we are able to compare the method to other types of geophysical investigations. Thus, this study is unique in doing a comprehensive analysis of an excellent broad data set. The power of the inversion method to obtain new insights into tectonic processes within a crustal volume is shown through careful examination of various velocity solutions and detailed analysis of the velocity variations and earthquake data. Noteworthy findings illuminate the relationship between fold structures and seismic deformation.

I have applied this methodology to study the anatomy of the volume of the crust that produced the May 2, 1983 magnitude 6.7 earthquake, that occurred beneath the Coalinga Anticline in central California, about 30 km east of the San Andreas Fault. Its focal mechanism indicated reverse dip-slip movement and, at the time of its occurrence, it was unexpected to have such a large magnitude event located relatively near the San Andreas Fault but with deformation apparently entirely unlike the right-lateral strike-slip movement typical of the San Andreas plate boundary zone. Thus the Coalinga earthquake raised questions about the structure and active tectonic processes of the region: what is the characteristic style of deformation, how is the mainshock rupture related to surface deformation, and what is the three-dimensional relationship between faults and geologic structures beneath the Coalinga Anticline. Numerous aftershocks followed the Coalinga earthquake, providing an excellent data set that can be used to address some of these questions in a variety of ways. The aftershock data have been used to calculate a three-dimensional P- and S-wave velocity model which shows the structure of the local folds from the surface to hypocentral depths. The 3D model was used to

compute hypocenters and fault-plane solutions which, together with the velocity structure, accurately reveal the active tectonic processes at Coalinga.

Figure 1 illustrates the effectiveness of the method of 3D inversion of travel-time data. Figure 1a shows a contoured velocity cross-section of a 1D velocity model. Figure 1b shows a contoured cross-section of the solution of the 3D velocity inversion. For comparison, Figure 1c shows an interpreted geologic cross-section based on surface geology, well data and a seismic reflection section. The key point is that, using only a 1D initial model and local travel times and without any prior assumptions of the structure, the inversion gives a picture of the 3D structure consistent with independent geologic and geophysical data. The geologic cross-section shows how similar the 3D inversion solution is to the geologic interpretation, with Coalinga Anticline and Pleasant Valley observed on the margin of the San Joaquin Valley. In addition to structure, of course, the 3D velocity inversion yields velocity data that is important for the interpretation of the type of rock.

Thus, the Coalinga results show that the inversion method is an extremely useful technique. The inversion gave a 82 % decrease is data variance and fit the first arrival data significantly better than other 2D models obtained by forward modeling of refraction lines. Evaluation of various initial models showed that it is best to use a simple initial model. Then the results are easier to interpret since the velocity variations are due to the data and not due to complexities in the initial model. The resolution matrix can also be used to evaluate where the results are most accurate and how velocity variations may be smeared. Beyond the computed variance and resolution, the Coalinga 3D velocity structure, computed from a simple 1D initial model, matches the mapped geologic structure and, after conversion to density, can predict the observed gravity field.

The mapped geologic structure shows that Coalinga is a young fold, with about 2-km of uplift, on the edge of the larger Diablo Range. This is borne out by the computed 3D velocity model. Details of the local anticlines and synclines are seen which would be more difficult to interpret with two-dimensional reflection and refraction surveys. Deeper velocity variations are also interesting, in particular the 3D model shows a series of three discontinuous low-velocity zones at hypocentral depths.

The primary feature of deformation below the Coalinga Anticline is upward movement of blocks of higher-velocity material along southwest-dipping listric thrusts. Correspondingly, relatively low-velocity material is being pushed down on the northeastern side of the anticline. At shallower depths, above the main thrust, both aseismic folding and secondary faulting take place. In the sedimentary strata within the core of the anticline a low-velocity zone is indicative of high pore pressure created by the long-term compressional strain.

To interpret velocity variations, seismologists must compare laboratory measurements to volumes of unknown rock of dimension 1 to 3 km. I address this problem by combining the laboratory measured velocities of a wide range of sandstones at various pressures to develop an empirical relationship between seismic velocity, rock parameters and effective pressure. The empirical relationship shows in general how sandstone velocity responds to changes in porosity, clay content or effective pressure. Thus it gives a means to use a large amount of laboratory data to interpret velocities observed in-situ. For instance, the variation in pore pressure within a given sedimentary layer can be estimated from the variation in velocity within that layer. Additionally the concept of developing an empirical relationship to describe a

large suite of rocks may prove useful in the future to characterize other rock types.

There are some aspects of the seismic activity at Coalinga that may be useful in understanding the seismic process in other areas of folds. The character of the seismicity varies along the length of the anticline depending on the amount of previous deformation. Where there was a great amount of previous uplift, the main thrust was well defined. And secondary faulting occurred on both sides of the anticline, on one side the aftershocks were located where there was greatest flexure of the sedimentary rock and on the other side several relatively large secondary earthquakes formed a fault zone with surface rupture. Where there was less prior deformation and the mapped structure showed only gentle folding, there was diffuse seismicity with no indication of well-defined fault zones. An important aspect of the Coalinga mainshock is that the extent of the rupture area is limited by the area of uniform structural orientation and by changes in material properties. The mainshock rupture terminated where the fold trend was no longer uniform but had competing north and west-trending features. The upward mainshock rupture ended at the approximate boundary between the Franciscan and Great Valley Sequence rocks. Above that depth the main southwest-dipping thrust appears to splay into a steeper segment and a near-horizontal segment.

The relation between active compressional deformation and the San Andreas Fault can be studied with geodetic data. It turned out that the most appropriate networks were located south of Coalinga where the San Andreas cuts across the actively uplifting Transverse Ranges. There the Los Padres and Tehachapi networks form 140-km wide transect across the plate boundary at the Big Bend of the San Andreas Fault. By analyzing trilateration data, we find important differences in the crustal strain field along and off the San Andreas

Fault. Additionally, by inverting the geodetic data for slip on specified fault segments, we understand some of the key features of slip at depth near the plate boundary and put some constraints on regional tectonic models.

The deformation along the San Andreas fault is consistent with right-lateral strike-slip movement either below a fairly deep locking depth or over a wide shear zone. Away from the fault, the strain is remarkably similar on both sides of the fault and shows compression normal to the fault. Inversion of the data for fault slip shows that the Garlock fault is actively slipping and that significant shear strain is also occurring south of the San Andreas, possibly on the Big Pine fault. The data are best fit if the active trace of the San Andreas is a vertical fault below its surface trace - not a dipping fault as suggested by use of retrodeformable cross-sections. Computation of the residual displacement between plate motion and San Andreas slip shows that the westerly trend of the Transverse Ranges and of deep high-velocity anomalies is consistent with the orientation of the San Andreas that is expressed in its surface trace.

Thus this thesis reveals crustal structure and active tectonic processes in the Coalinga Anticline on the Coast Ranges / Great Valley margin. It provides insights that can be used to study earthquakes and deformation beneath other folds. It gives a useful description of the relationship between P- and S-velocity and rock parameters in sandstone. And it shows what aspects of the San Andreas Fault and areas away from the fault, on either side, are evidenced by crustal strain.

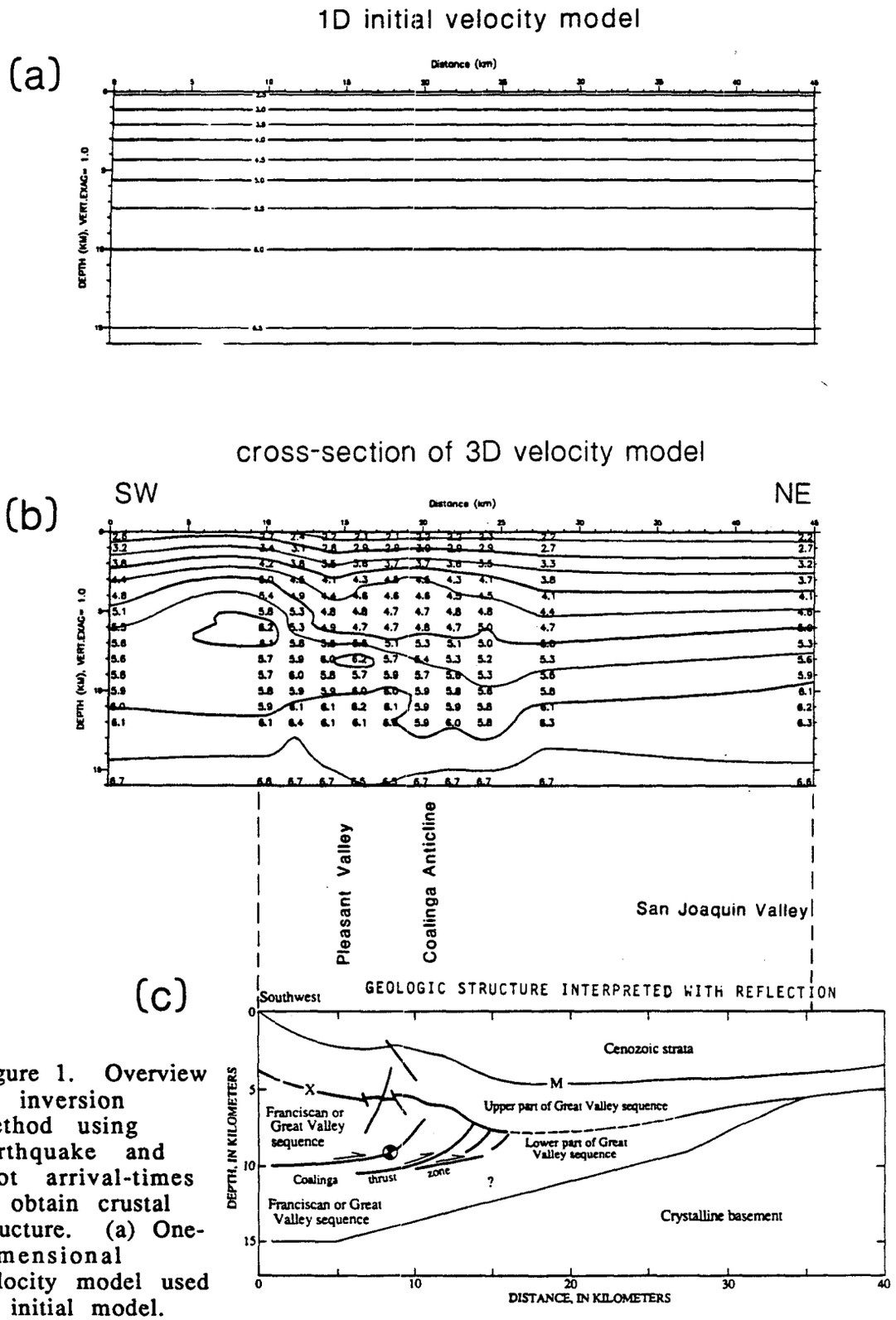

Figure 1. Overview of inversion method using earthquake and shot arrival-times to obtain crustal structure. (a) One-dimensional velocity model used as initial model. (b) Contoured cross-section of the solution of the three-dimensional velocity inversion. This is consistent with the (c) interpreted geologic cross-section, from Wentworth and Zoback (1989), based on surface geology, well data and a seismic reflection section.

Chapter 2.
Three-Dimensional P- and S-Velocity Structure in the Coalinga Region, California

ABSTRACT

The inversion of 7,696 P and 1,511 S arrivals from earthquakes and 696 P first arrivals from shots for the Coalinga region produced a three-dimensional velocity model, that accounts for an 82 % reduction in data variance. The addition of pseudo-bending to the ray-tracing routine makes the ray paths more accurate, particularly for long ray paths and near large velocity gradients. In order to get the most detail where there is the densest ray path coverage a series of three inversions was done, focusing in on the hypocentral area, where gridspacing was 1 to 2 km. A simple starting model gave the best results. Both a simple 1D initial model and a complex initial model derived from the refraction interpretation were tried. An important advantage of using a simple initial model is that the solution features are those required by the data and are not due to peculiarities of the initial model. Where there is low resolution, the inversion will produce only small velocity perturbations. The S-velocity solution has different resolution than the P-velocity solution because it uses a different set of stations, and it has lower resolution because it uses fewer arrival times. While the general patterns of velocity variation are similar for both V_p and V_s, the V_s solution tends to have more smearing of velocity features and can have somewhat different locations of velocity features.

The overall shape and location of velocity features correspond well to

the mapped surface geology. The 3D inversion is able to discern details of folds where the resolution is good, and where resolution is lower minor features may be observed with less accurate shapes. The amounts of uplift inferred for the Diablo Range and the local folds are similar to those implied by geologic data. Rock units can be inferred based on the velocities. Thus Franciscan and GVS rock form the core of the anticline with the Cenozoic strata folding gently above and the gabbroic basement dipping down beneath. The 3D velocity solution compares well to the seismic reflection record. The shape of the sedimentary section agrees well with the reflections from the Cenozoic strata. Compared to the refraction model, the 3D solution has similar velocities and similar locations of velocity features, but is more detailed in the hypocentral zone where it uses more data. The gravity computed from the 3D velocities, converted to density, matches the observed gravity quite well.

The 3D velocity solution has several other interesting features. There is a linear high-velocity body, about 25-km long, from 6- to 8-km depth, that may represent an ophiolite fragment, mafic intrusive or high-grade metamorphic rock. A shallow low-velocity zone extends for 20 km along the fold axis at about 6-km depth, and correlates with LVZ's observed in both the refraction and reflection data. It may indicate high pore pressure caused by lateral compressive strain, in conjunction with barriers provided by shale horizons within the GVS. Deeper LVZ's occur within the Franciscan, and are characterized by horizontal or southwest-dipping zones of varied thickness, 4- to 8-km wide and 5- to 10-km long. These LVZ may represent randomly-distributed heterogeneity within the complex Franciscan melange, or may result from deformation along multiple thrust faults.

INTRODUCTION

The objective of this study is to determine and interpret the three-dimensional (3D) crustal structure in the region of the Coalinga earthquakes. This region is of interest because the tectonic processes at Coalinga may be representative of the entire margin of the Great Valley along the Coast Ranges (Figure 1). The Coalinga Anticline is one of several young active folds on the southeastern edge of the Diablo Range, a dramatically uplifted area with 9 km of relief between it and the adjoining San Joaquin Valley. Coalinga is underlain by seismically active faults which produced a M 6.7 earthquake on May 2, 1983 with numerous well-recorded aftershocks. Nearby refraction and reflection lines also have been recorded. This data set provides a unique opportunity for 3D velocity inversion. Thus an added objective is to improve the application of the 3D inversion method, to evaluate its usefulness, and to compare the results to other methods.

There are few places away from the major strike-slips faults that California has numerous earthquake sources. Because the Coalinga earthquakes occur at varied locations and depths they contain much information about spatial variations in velocity. They have both P and S arrivals so that S velocity can be included in the analysis. In contrast refraction and reflection methods use surface sources and the analysis has usually been limited to P velocity. A previous study of one-dimensional velocity and station corrections showed that the station corrections were correlated with the mapped surface geology. Thus a 3D velocity study is warranted to better describe the lateral heterogeneity attributable to geologic structure. There are also smaller features that the earthquake data may be able to address. For instance, high pore pressures have been found in wells above the anticline. With the earthquake data we can investigate high pore

pressure at depths below the wells.

An inversion of the arrival time data is the best way to study the 3D velocity structure. There are numerous earthquakes and many stations at varied azimuths. An inversion, in contrast to forward modelling, can systematically make use of a large amount of data, and obtain a solution that best fits that data. Refraction first arrivals can also be included. To have adequate resolution the inversion needs ray paths that are distributed uniformly in space and depth. Thus Coalinga is ideal for 3D velocity inversion.

The 3D velocity solution may provide important insight into this region. The structure here is obviously not 1D. But it is also not simply 2D as has been interpreted with forward modelling of data from two refraction lines. There is great structural relief of the Diablo Range and there are plunging local folds of varied orientation. The velocity can show how the shape of the folds varies in all directions. The shape and extent of different rock units can be inferred from the 3D velocity. And the inversion solution can indicate where there are velocity anomalies at hypocentral depths and how such anomalies are related to the shallower fold structure.

METHOD

Local earthquake arrival-time data were used in an iterative damped least-squares inversion for hypocenters and three-dimensional velocity structure, as developed by Thurber (1983). The travel-time residual, r_{ij}, for event i and station j is related to changes in hypocentral (ot, x, y, z) and velocity (V) parameters.

$$r_{ij} = \Delta ot_i + \frac{\partial t_{ij}}{\partial x_i}\Delta x_i + \frac{\partial t_{ij}}{\partial y_i}\Delta y_i + \frac{\partial t_{ij}}{\partial z_i}\Delta z_i + \sum_{n=1}^{N}\frac{\partial t_{ij}}{\partial V_n}\Delta V_n$$

The velocity of the medium is parameterized by assigning velocity values at the intersections (gridpoints) of a three-dimensional (3D) grid. The grid spacing is nonuniform so that gridpoints are closer together where there is the most data. Variational estimates are used for the hypocentral partial derivatives. The velocity and the velocity partial derivatives for a point along a ray path are computed by linearly interpolating between the surrounding eight gridpoints. Parameter separation operates on the matrix of hypocentral and velocity partial derivatives so that the hypocentral calculation is separated from the velocity calculation, thereby reducing the size of the problem and increasing the amount of data that can by used. The normal equations are solved with damped least squares and the resolution and covariance matrices are computed. The damping value is selected empirically to greatly reduce the data variance with a moderate increase in the solution variance (Eberhart-Phillips, 1986). As shown in Figure 2, by running single iteration inversions with a wide range of damping values, an appropriate damping value can easily be found. Additional features in the implementation for this study are improved ray-tracing, inversion for both P and S velocity, and the option of fixing the velocity at specified gridpoints.

An initial ray path is obtained using Thurber's (1983) ART algorithm, where the path with the least travel time is selected from a suite of circular arcs connecting the source and receiver. Then an iterative pseudo-bending approach is applied to the ray path to better approximate the true ray path. Thus the selected ray path is no longer constrained to be planar or arcuate. At each point along the ray path, the velocity gradient and the current estimate of the ray vector are used to define an improved ray path. Following Um and Thurber (1987), the ray path is perturbed so that the path curvature is closer to anti-parallel to the component of the local velocity gradient normal to the path. Once the entire ray path has been perturbed, additional pseudo-bending steps are carried out until a specified maximum number of iterations is reached or the reduction in travel time, Δt, is below a specified cutoff value. The advantage of adjusting an initial ray path rather than doing the three-point scheme of Um and Thurber (1987) is that, within the hypocenter-velocity inversion program, each source-receiver path has to be calculated many times, often after small changes in hypocenter or velocity model, and information from the previous ray path calculation can be used. When the change in hypocenter is less than 5% of the path length the previous pseudo-bending path is the new initial path. Otherwise the nine arcuate paths that are closest to the previous path are searched to select the ART path and then pseudo-bending is applied.

After testing a variety of raypaths a Δt of 0.004 s was selected; and the maximum number of iterations was set to eight for raypaths less than 20 km, and to 18 for longer raypaths since the circular path is fairly accurate at short distances. However convergence to a minimum travel-time path is usually rapid. For the Coalinga data, the average number of pseudo-bending iterations was only 3.2, and only 261 of 8155 (3.2 %) ray paths used the maximum number

of iterations. As shown in Figure 3, the reduction in travel time with pseudo-bending tends to be less than 0.05 s for distances less than 20 km and from 0.05 to 0.20 s for longer distances. The ray paths that have the largest changes tend to either be long or to pass through the areas of largest velocity variation. A small error is shown by the two points, both from station PHB, that have travel-time differences of about -0.025, indicating that the PB path is slower. Figure 4 compares the arcuate and pseudo-bending (PB) ray paths for two events at Coalinga using a detailed 3D velocity model. In the mapviews (Figures 4a, b), we see that most of the PB changes are rather small. Both the arcuate and PB paths tend to curve toward locations of high velocity, however the PB is able to adjust for small-scale variations in velocity. This is well seen in cross-sections across the anticline (Figure 4c,d), which can be compared to velocity cross-sections (Figure 14d,f). For paths that are approximately parallel to the velocity gradient, the PB path is little different from the arcuate path. In fact, to station PHB in the east where the velocity varies smoothly, the smooth arcuate path is better than the PB path which has its curvature calculated at a number of discrete points. The PB adjustment is important for long raypaths which might tend to look more like "flat-bottomed" refracted raypaths than circular arcs. Figure 4e,f shows ray paths for a Coalinga refraction shot along the anticline. This also can be compared to the velocity cross-section (Figure 15a).

In tests, the addition of pseudo-bending took approximately 40% more CPU time. Testing was done using the northern California data of Eberhart-Phillips (1986). The velocity pattern of the inversion solution is almost the same as without the pseudo-bending, except at places where the resolution is very low. Where there is low resolution, changes in a few raypaths near that gridpoint can have a large effect on the corresponding velocity partial

derivatives. The average velocity difference was -0.03 km/s with a standard deviation of 0.15 km/s. Thus the pseudo-bending tended to give slightly lower velocities which is reasonable for shorter raypaths. For the solution that used the pseudo-bending, the rms residual was only 0.001 s less and the data variance was only 1.5 % lower, although the psuedo-bending travel-time differences shown in Figure 3 tend to be about 0.02 s. So the inversion with less accurate ray paths was able to fit the data nearly as well by using slightly different velocity perturbations.

For hypocenter location, addition of PB reduced the rms residuals and changed the hypocenters by about 0.2 km generally and in a few cases by 0.7 km. In summary, our tests showed that the PB adjustments do produce more accurate raypaths and, while these paths are not dramatically different than the ART paths, they do have some effect on the inversion results, particularly on the values of velocity. The overall pattern of velocity variation is very similar though, so that, if CPU time were a major constraint and only relatively short raypaths were included, one might consider using ART alone. In the rest of this study of Coalinga, PB will be used. Path lengths up to 80 km will be included, with decreasing weight from 20 to 80 km, whereas in the previous study (Eberhart-Phillips, 1986), with ART alone, only path lengths less than 45 km were included.

S-velocity was added to the inversion program by using the same grid as for P-velocity and simply having additional array space for the S-velocity values. Then an S arrival time is used exactly the same as a P arrival time, except that in each routine, when a velocity value is needed, a "pointer-value" tells to pick from the S-velocity section of the array. A test data set was created with S travel times twice those of the corresponding P travel times so that the S velocity should be everywhere half of the P velocity. This data was run as P

only, S only, and P and S together. The inversion results were correct once a separate damping value was assigned to the V_s gridpoints. This is necessary when we consider the damped-least-squares solution,

$$\Delta m = \left\{ M^T M + \theta^2 I \right\}^{-1} M^T r$$

where M is a matrix of medium partial derivatives. For similar P and S raypaths, i, and the same gridpoint, k,

$$\frac{\partial t_i}{\partial V_{s_k}} = \frac{V_p}{V_s} \frac{\partial t_i}{\partial V_{p_k}}$$

Thus the S damping, θ_s^2, will be

$$\theta_s^2 = \left(\frac{V_p}{V_s} \right)^2 \theta_p^2$$

Note, however, that this is for S data distributed exactly the same as P data. In actual data sets, there are usually many fewer S arrival times than P arrival times, a factor indicating a smaller θ_s, and their spatial distribution is not as good since not all stations are 3-component, a factor indicating a larger θ_s.

For the Coalinga data, P and S damping values were chosen separately using the empirical approach of Eberhart-Phillips (1986) where the optimal damping is the one that allows a great reduction in the data variance with a moderate increase in the solution variance. Single iteration inversions for P only and S only, with hypocenters fixed, were done with a wide range of damping values. In Figure 2, their data variance and θ are plotted versus their solution variance. The line indicates the selected value. As long as a wide enough range of damping values are tested, it is easy to select an appropriate damping value from this type of plot. Note that, after the solution of the medium parameters, in each iteration, the hypocentral calculations are

carried out using singular value decomposition with a cutoff value to avoid small eigenvalues.

When using earthquake travel times as data, the ray paths will not be uniformly distributed horizontally or vertically since the aftershocks tend to occur in limited regions and are recorded at only a given set of seismograph locations. The most detailed velocity structure can be obtained in the aftershock region, where there is the greatest variety of raypaths. Hence the inversion scheme has been altered so that the velocity can be fixed at specified gridpoints. Then only the non-fixed gridpoints are included in the inversion, so that velocity can be defined on a large number of gridpoints while the size of the inversion matrices corresponds only to the number of non-fixed gridpoints. In this version, velocity can be defined on up to 3000 points, but only 600 gridpoints can be inverted for. A larger-scale inversion can be done for the entire area covered by the stations. Then that solution can be interpolated onto a finer grid as an initial model for an inversion for the area with the densest ray path coverage. Alternatively the fixed gridpoint solution can be used to constrain the solution by fixing shallow velocities to those estimated in seismic refraction or reflection models.

DATA

The May 1983 M 6.7 Coalinga earthquake produced an extremely numerous aftershock sequence with a wide spatial distribution, making an ideal data set for 3D inversion since a large set of varied raypaths is necessary to obtain a good solution. The following year, the region of activity was extended to the south by the Avenal sequence (Eaton, 1985a). Figure 5 shows the array of stations used. The USGS permanent network (CALNET), generally centered along the San Andreas fault provided 54 stations, 15 of which were 3-component. The USGS also deployed 22 additional temporary 5-Day 3-component recording stations in the aftershock regions for two months following the earthquakes. Refraction arrays added another 390 stations. All arrival times, of P or S onset, were timed by hand. Fifty events were taken from Eaton's (1985b) study of the larger aftershocks. Eighteen aftershocks were used that were recorded on the refraction array (McGregor-Scott and Walter, 1985), as well as the nine refraction shots (Colburn and Walter, 1984). One-hundred forty-one other events were chosen that were spatially well-distributed, recorded on most of the 5-Day stations, and of a small enough magnitude (approximately M = 2) that S arrivals could be easily picked with reasonable certainty. It is important to use horizontal components to pick S to avoid mistakenly picking a converted phase. At stations in the San Joaquin Valley, the only prominent secondary arrival on the vertical component is actually an S to P converted phase from the bottom of the sedimentary basin.

Figure 6 illustrates the spatial distribution of the events used in the inversion. There are 209 aftershocks, 18 of which were recorded on the refraction array, and 9 refraction shots, indicated by stars. The earthquakes contribute 7690 P observations and 1511 S observations, and the shots contribute 696 P observations. Thus there are only about 20 percent as many

S data as P data, and the S data are not as well distributed since only the 3-component microearthquake stations are used.

RESULTS

Varying Initial Models

There are two possible approaches to setting up the inversion. One is to start with a velocity model based on previous geologic interpretations and then see how well the travel-time data fit that model and how that model is perturbed as the inversion attempts to fit the observations. Another way is to start with a simple 1D model and let the inversion solution add in only whatever complexity is warranted by the travel-time data. With the first method, the solution will probably look reasonable, but it will be biased by preconceived notions, and it will be difficult to assess what features are actually required by the data. With the second method, the inversion solution will solely reflect the data set used and the solution will have to be studied to obtain a geologic interpretation. Since the earthquake ray paths are not distributed uniformly there will be places where the model has very low resolution. There the damped least squares inversion will not perturb the initial model, and the solution there may not look realistic, but will not have unbelievable perturbations eitner. The second method is generally more satisfying since it is difficult to definitively justify a particular geologic interpretation. Thus, simple 1D initial velocity models are typically used in 3D inversions. In this study, both approaches have been used as well as a combination of the two approaches where interpreted velocities are assigned at those places with lower resolution.

Grid spacing is another factor to consider in setting up a 3D inversion. Since the resolution varies throughout the region, there are some areas where only relatively large gridspacing is warranted, while in the aftershock zone

itself closely spaced velocity gridpoints can be resolved. In a preliminary inversion a grid was selected that had denser gridpoints in the central region. However, this was not really satisfactory for either the central high resolution region or the peripheral low resolution region. So, instead a series of three solutions was done, the first covering the entire area with gridpoints spaced 14 to 29 km horizontally and 4 km vertically, the second a 18 by 59 km area with gridpoints spaced 3 to 9 km, and the third covering only the hypocentral zone from 6 to 12 km depth with gridpoints spaced 2 to 3 km horizontally and 1 km vertically (Figure 5). In each case the results of the previous-scale inversion were interpolated for the initial velocity model.

The initial 1D velocity model and initial hypocenters were from Eberhart-Phillips and Reasenberg (1989), who inverted earthquake arrival-time data for 1D velocity and station corrections. The initial S-velocity was then calculated by using V_p/V_s of 1.78. Because of the smaller amount of S arrivals, only P-velocity was inverted for in the small-scale inversion. For the small-scale inversions a variety of initial models from other sources were also used. In order to use Walter's (1989) detailed interpretations of the two 2D refraction lines, they had to be converted to a 3D grid. To do this in a systematic way, the refraction velocities were interpolated along a structural map of the Kreyenhagen stratigraphic horizon (Zigler et al., 1986). The Kreyenhagen was assigned a velocity of 3.3 km/s and the two refraction lines were projected along structure and transverse to structure. Outside of the area defined by the refraction lines, the medium-scale inversion solution was used.

The various runs are described in Table 1. The best model is E, which was obtained by doing three successively finer scale inversions from an initial 1D velocity model. A large reduction in data variance, from the 1D model, 64 %, was achieved in the large-scale inversion. The total reduction in

data variance, including the medium and small-scale runs is 82 %. The velocity model variance (averaged per point) increases for V_p from 0.061 km^2/s^2 for the large-scale to 0.096 km^2/s^2 for the small-scale. Thus primary velocity features are seen in the large- and medium-scale inversions, but an additional small-scale inversion, in the area with the densest data, shows small-scale velocity variations as well as providing more detail on the location of velocity features.

The velocity model variance for V_s is much lower than V_p, even when it is multiplied by $(V_p/V_s)^2$. This is because there is less well-distributed S data and the inversion will produce only negligible velocity changes where there is low resolution. For example, in the large-scale inversion, the velocity was only changed at 63 S gridpoints compared to 120 P gridpoints. Run C is a medium-scale test run where only 3-component stations were included. In that case the V_p model variance is similar to the V_s model variance multiplied by $(V_p/V_s)^2$.

Note that model E, which we will use for interpretation, is a small-scale inversion with a smoother initial model in the central non-fixed area. The initial model is the medium-scale solution except in the central area, where it is the large-scale solution. The E solution is very similar to the D solution, but the detailed shape and location of some velocity features are different because they are less constrained by the initial model.

Two small-scale runs in Table 1 were done with initial models from interpreted refraction lines. In one the refraction velocities were used everywhere except the central non-fixed area (F). In the other, refraction velocities were only used in the upper 5 km (G), since that is where the refraction data has the best resolution, and is above the detailed small-scale inversion grid, 6 to 12 km. In both solutions the data variance is very high,

higher even than the simple large-scale solution and about 3 times higher than the small-scale solution. The velocity model variances are about twice that of the small-scale solution. Thus, for the first P-arrival data, the refraction models seem overly complex and do not fit the data as well as the simpler inversion models.

Another way, than using the refraction model, to account for additional detail at shallow depths is to include station corrections. In run H, the velocities were fixed to E, our best model, and station corrections were included in the inversion. This reduced the data variance 30 % from the E solution. The station corrections will be used for hypocenter relocations.

Residuals

Figure 7a shows a histogram of travel-time residuals for model E. Most (66 %) are less than $\pm$ 0.10 s. There are slightly more (2 %) positive residuals than negative residuals. Figure 7b shows the residuals plotted versus source-receiver distance, with circles indicating earthquakes and x's indicating shots. Most of the large residuals are at distances larger than 50 km. The fit is poorer because there are fewer long ray paths to provide good resolution and the raytracer is less accurate at large distances. Travel-times from large distances with high residuals received very low weight in the inversion solution, as shown by the weighting scheme in Figure 7b. While there are no earthquake data for hypocentral distances less than 5 km, the short-distance shot data all show positive residuals. This indicates that there is some near-surface material that is slower than our model predicts. The inversion solved for velocity at 0 and 3 km depth, with a gradient between.

The only arrivals that consistently have high residuals are those at refraction stations on the southern end of the north-south refraction line (Figure 5). This is a low-resolution area on the periphery of the inversion

grid so that the 3D solution velocities were not changed much from the 1D initial model; the high residuals indicate that the velocity at the southern corner of the grid should be lower than predicted by our model.

Resolution

Before we evaluate the velocity solution, we must consider the resolution. Figures 8 and 9 show plots of the velocity solution. Figure 8 shows mapviews for 0-, 3-, 6-, 9- and 12-km depth, along with a basemap and a map of the earthquakes used in the inversion. Numbers indicate the computed velocities at each gridpoint; contours were drawn using an automated contouring program. Note that the small-scale solution is shown where applicable, for V_p from 6- to 12-km depth. In the cross-sections in Figure 9, the medium-scale solution is shown so that the S velocities can readily be compared to the P velocities. There is a vertical exaggeration of 1.5 in the cross-sections. To illustrate the spatial variation in resolution with varying density of data, Table 2 lists the diagonal resolution elements of model B for V_p and V_s for a given depth level, z=6 km, and for a given cross-section, y=47 km.

As expected, for z=6 km, the resolution is highest where most of the aftershocks are, from y=30 to y=63. The locations of the lowest resolution (< 0.05) gridpoints are of particular interest for interpreting the solution, because there the velocity perturbations will be small and the solution will not vary much from the initial model. There is low resolution along the southern and northern edges. The northern edge has fewer stations and earthquakes than the central area; there are no stations directly north, but there are many northwest along the San Andreas Fault (Figure 5). The Kettleman Hills sequence was located near the southern edge, but it had fewer earthquakes and fewer temporary stations than the Coalinga sequence. For the cross-section (Table 2b, Figure 9c,d), the lowest resolutions are at the surface and the

deepest level (z=16 km). The surface grid has scattered low resolution where there are no stations close to a gridpoint. The deep grid has low resolution below hypocentral depths except where there are far stations, with downgoing ray paths, to the west and along the east-west refraction line.

The resolution for V_s is quite different than for V_p. There is less S data and the S arrivals cannot be timed as accurately as the P arrivals. The major difference in resolution patterns, though, is caused not by simply having a smaller number of data, but rather by having a different set of stations for the S data. Since only 3-component stations are used for V_s, the S data includes fewer stations to the west, from the permanent network along the San Andreas fault, and no refraction stations. Hence the western edge of the V_s solution has much lower resolution than the V_p solution. Also the deeper gridpoints have poorer resolution since the S data has fewer long ray paths.

Therefore we must be careful in comparing the V_p and V_s solutions. Because of the different resolution patterns, we cannot just map V_p/V_s. Consider the resolution matrix in more detail for some individual gridpoints, x=20,24, z=6,9, on the y=47 cross-sections (Figures 9c and 9d). There is particularly high V_p observed (x=20, z=6), but not a high V_s. Figure 10 shows portions of the rows of the resolution matrix corresponding to this gridpoint and adjoining gridpoints. The elements of each row that correspond to this cross-section are plotted and contoured. For V_p note that the diagonal resolutions are relatively high and that there is little smearing of the resolution from surrounding gridpoints. Thus we conclude that the computed velocities at these gridpoints are reasonable, meaning that the velocity values are distinctly determined and correspond to the correct locations. So the low velocity at z=9 cannot be dismissed as a point where there is low resolution and the high velocity at z=6 cannot be due to higher velocity from basement depths

being smeared up to shallow depth. We must interpret it as a distinct high velocity feature. In contrast, for V_s there is virtually no resolution at the point of high P velocity. So there the S solution is probably just stuck at the initial 1D model, and there could be an undetected high S velocity. For the V_s gridpoint x=20, z=9, there is low resolution and it is influenced by the adjoining gridpoint. For the V_s x=24 gridpoints, there are good diagonal resolution values, but there is vertical smearing, particularly for z=6.

The presence of the high-velocity body (HVB) in the V_p solutions shows the importance that a few stations can have on 3D velocity resolution. As illustrated in Figure 4c,d, only the closer western stations actually have ray paths that sample the HVB. Ray paths to stations farther west pass deeper than the HVB. Thus, of all the stations (Figure 5), only the three vertical-component stations between Coalinga and the San Andreas Fault, PSM, PCR and PCA, showed the HVB. This highlights the importance of the aftershock array for velocity studies. A supplemental array deployed for locating aftershocks can have key weaknesses when it is later used to study velocity. If even one three-component instrument had been put between Coalinga and the San Andreas Fault, it would have greatly improved the V_s resolution.

While the P and S velocity models are similar, we cannot put much importance on different shapes and locations of specific velocity features in the P and S solutions. Consider the y=39 cross-sections (Figure 9a,b). There is a low velocity zone (LVZ) in V_p at 6 km depth. The V_s section has a vertical region of low velocity, which looks unusual because it is not expected from the geologic structure. It looks like a basin underneath the anticline axis. However it probably represents a similar LVZ at z=6-km depth, which has just been smeared toward the surface. Similarly low velocities on the east at 9-km depth are also more spread out in the V_s sections.

To evaluate the V_p and V_s differences more clearly, we ran a test run, C, that included only those stations that had S arrivals. There is still more P data than S data, however the more limited ray path distribution, from using fewer stations, effects the P-velocity solution. The V_p model is less detailed and the V_p model variance is only 60 % of that of the all-station solution. The solution has a correspondingly smaller reduction in data variance. The V_s model is approximately the same, as expected, since it is only coupled to the P solution through the hypocenters. As shown in Figure 11, there is only a hint of the western high-velocity body in the V_p y=39 section. The V_p LVZ is no longer a velocity reversal, but is spatially spread out like in the V_s model. Therefore we conclude that differences in locations of velocity features between P and S solutions are due primarily to different ray path distributions.

Since the P and S resolutions are different, we unfortunately cannot discuss the V_p/V_s ratio in detail. Figure 12 shows a cross-section (corresponding to Figure 9c,d) with V_p/V_s shown at gridpoints that have adequate P and S resolution. These values of V_p/V_s are not precise since there is uncertainty in both the V_p and V_s values. For example, with 0.1 km/s uncertainty in velocity, V_p of 5.8 km/s and V_s of 3.1 km/s could represent V_p/V_s ranging from 1.70 to 1.87. Thus if we were primarily interested in V_p/V_s, V_p/V_s should be solved for instead of V_s. Then there would be less uncertainty in V_p/V_s and damping of model perturbations would be applied to V_p/V_s, making V_p/V_s smoother without unnecessary oscillations.

V_p/V_s tends to be higher in the sedimentary section, where it ranges from 1.6 to 2.3, than in the deeper higher-velocity rock, where it ranges from 1.6 to 1.9. In Figure 12, the low V_p/V_s value at the surface is partly due to resolution; the vertical smearing in V_s means V_s is less able to resolve near-surface lower velocities. There is relatively high V_p/V_s at 3-km depth in the

folded sedimentary rock which could be indicative of high pore pressure, since increased pore pressure causes increased V_p/V_s ratio (Chapter 5). At greater depths, 6 to 9 km, the higher velocity material tends to have lower V_p/V_s.

Velocity Solution

As seen in the mapviews (Figure 8), the shape and location of velocity features generally correspond to the location of the anticline known from the map of surface geology (Figure 8a). In order to best illustrate the 3-dimensional shape of the anticline, Figure 13 shows views of level surfaces for 3 different velocities. For reference, the geologic map is plotted at top. The contours show depths of the specified velocity at all points in the 3D model. The uplift of the Coalinga Anticline is observed, superimposed on the larger uplifted Diablo Range.

In the upper plot (Figure 13b), for velocity of 2.5 km/s, the folding is smooth and there is not a great variation in depth. However there is an observable high corresponding to the Coalinga Anticline which plunges to the southeast. To the south we also see the Kettleman Hills Anticline as a distinct feature, with a different fold axis and smaller amount of uplift. In the middle plot (Figure 13c), for velocity of 4 km/s, the surface has some small-scale features but still shows the distinct Coalinga and Kettleman Hills Anticlines. There is a sharp low corresponding to Pleasant Valley, while there is a more gradual low for the San Joaquin Valley. The lower plot (Figure 13d), for velocity of 6.5 km/s, gives us an idea of the basement surface. The contoured depths range from 11 to 18 km. The surface is shallowest beneath the San Joaquin Valley, farthest from the folds, and tends to dip down towards the southwest. The V_s solution (compared to the V_p solution in Figure 9) is also

similar to the known geologic structure, but is smoother than the P velocity model because of the lower resolution.

For more detailed interpretation of the velocity model, Figure 14 shows a series of cross-sections, normal to the fold axis, through the best small-scale velocity solution. The depths range from 0 to 16 km and there is 1.5 vertical exaggeration. The numbers show the velocity solution at the gridpoints in each cross-section. The gridspacing is densest in the hypocentral region. Contours were drawn using an automated contouring program, so in places they may be more complicated than hand-drawn contours would be. Similarly to the perspective view, we see the uplift of the anticline and the basement dipping down beneath the anticline. Other noteworthy features are a high-velocity body at 6- to 8-km depth on the western edge of the Coalinga area, some particularly low velocities on the eastern edge of the Coalinga Anticline, a low-velocity zone at 6-km depth within the sedimentary rock, and three discontinuous low-velocity zones between 8 and 12 km depth.

The high-velocity body is a relatively linear feature extending for approximately 25 km along the southwestern edge of the fine grid, x=20. It ranges in depth from 6 to 8 km, and has calculated velocities of 6.0 to 6.5 km/s. The largest velocity variation and spatial size are observed on the y=42 section (Figure 14b), at the northwestern end of Pleasant Valley and Coalinga Anticline. It apparently does not extend farther northwest (Figure 8). The peripheral gridpoints have low resolution, but the y=30 grid has reasonable resolution (Table 2a) and still shows no hint of a high-velocity body at 6 km depth.

In contrast, on the other side of the anticline, along the x=38 grid, there are low velocities of 5.2 to 5.3 km/s observed at 9 km depth (Figures 14a to e). This is not a velocity reversal, but rather a thicker section of 5.0 to 5.5 km/s

material than is observed elsewhere. On the eastern side, that velocity material is 4 km thick, compared to less than 1 km thick on the western side. On the northwesternmost sections, y=39, 42, the relatively low-velocity area has even lower velocities, producing a sharp bend in the velocity contours (Figures 8i; 14a,b).

In the core of the Coalinga Anticline, there is a LVZ which is a velocity reversal. It extends approximately 20 km along the fold axis, at 6-km depth (Figures 8g; 9a,c; 14a to e). It does not appear to extend to the southwest to the Kettleman Hills Anticline. The calculated velocities represent a 2 to 8 % decrease in velocity. However, since the velocities at shallower depths were only calculated with medium-scale gridspacing of 3 km vertically, this could represent a thinner LVZ with a larger velocity decrease. The location of a thinner LVZ would still have to be somewhere between the 3- and 6-km depth gridpoints of the medium-scale solution.

At hypocentral depths within the Coalinga Anticline, from 7- to 12-km depth, there is a series of three discontinuous low velocity zones (Figure 14). The most prominent extends, on y=39 to y=54 (Figure 14a to f), from 8- to 10-km depth, dipping from the center of the fold to the southwest. It is not a large velocity variation, but because it extends over a large area, it cannot be discounted. Below and east of this LVZ, there is a smaller LVZ at 12 km depth, observed particularly on y=48 and y=51 (Figure 14d,e). On the southwest, below the high-velocity body, there is third small LVZ observed on most sections.

While, in several of the cross-sections (y=45 to 51, Figure 14c to e), these low velocity zones look like planar features, they are not simple continuous planes throughout the velocity solution. Consider longitudinal sections along the southwestern side of the fold, x=22 (Figure 15a), and along the center of the fold, x=28 (Figure 15b). The LVZ's tend to be continuous for 5 to 10 km lengths.

They are longest at the northwest end of the grid and shortest at the southeast end. The prominent LVZ from 8 to 10 km depth, is also the most continuous LVZ in length. In fact it could be extended throughout the Coalinga Anticline if we included places with relatively low velocity, in addition to places with velocity reversals. The LVZ below and to the east is the least continuous (Figure 15b); it is separated into two zones by an area of relatively high velocity (6.3 km/s) at y=45.

The shape of the LVZ's also varies along the length of the folds, so that they are more like curving zones of varied thickness, than true planes. This does not rule out that they could represent planar features. As discussed above for the Vs solution, some small differences in depth, thickness and amplitude of velocity features could be due to differences in resolution throughout the grid.

There is an unusually low velocity, 5.2 km/s, at 11 km depth at the southern end of the solution area, y=63, x=20 (Figure 14i). Unlike the high velocity body discussed above, this gridpoint has very poor resolution. Its diagonal resolution element is only 0.05 and is not even the largest resolution matrix element corresponding to this gridpoint. The velocity at this point is most strongly influenced by the gridpoint directly below at 12 km depth, the deepest grid in the small-scale solution. Because of deeper rays going to stations to the south, that corner of the 12 km depth grid has very high resolution. Hence we cannot have much, if any, confidence in the low value of velocity at this point. Since this is a low resolution gridpoint on the far corner of the solution grid, it could be largely influenced by low velocities, to the south and below 12 km, outside of the solution area.

Velocity Solution with Refraction Initial Model

Two small-scale inversions were done with initial models interpolated from Walter's (1989) detailed interpretations of two 2D refraction lines. We first tried using the refraction model for all depths as the initial model, in run F. Figure 16 shows the resulting velocity solution for two cross-sections. When compared to the solution E with a simpler initial model (Figure 14b,e), we see that the overall velocity patterns are similar, but F is much more complicated. The previously noted features, including the high-velocity body on the southwest, relatively low velocities on the northeast, and low-velocity zones within the core of the anticline, are all observed in the solution with the complex initial model. The actual values of velocity and shape of velocity patterns vary between solutions E and F. For instance the high-velocity body and the area below 9 km depth tend to have higher values of velocity by 0.1 to 0.4 km/s in F, and the low velocity region within the fold at 6 km depth tends to extend deeper in F.

There is one major discrepancy between the refraction initial-model solution and the simpler initial-model solution. There is a narrow region of high velocities at all depths at x=34 (Figure 16b) in F. This is not even hinted at in other solution (Figure 14e). The refraction initial-model had low velocities at 8 to 11 km depths on the southeast, and perhaps this had a large effect on the solution.

It might be more reasonable to only use the refraction model for the upper sedimentary section where the refraction data are better defined and the Kreyenhagen map, used to guide interpolation, is more applicable. Thus we tried a second type of refraction initial-model, where the refraction interpretation was used only in the 0 to 5-km depth fixed-velocity region, and

the initial model of E was used below that. Cross-sections for this solution, G, are shown in Figure 17.

The patterns of velocity are nearly identical to the other refraction initial-model solution. The actual velocity values vary somewhat, but not necessarily uniformly in amplitude. In particular, the vertical area of high velocity at x=34 is just as well defined as in F. Therefore it is not attributable to the adjoining low velocities at depth in the F model. It must be caused by the shallower part of the refraction interpretation. In general that part of the refraction interpretation is similar to the 3D inversion model (E). Hence, it is difficult to even suggest what detail of the refraction model most contributes to this high-velocity feature.

The use of a complex initial model appears to result in an overly-complex solution. The velocity-solution variance with the refraction initial models is about twice that with a simpler initial model (Table 1). If the data variance was the same for two solutions, we would favor the simpler solution. The complicated solution would only be justified if it were accompanied by a large additional reduction in data variance. However, the data variance for the refraction initial-model solutions is very high, about three times higher than the solution with a simpler initial model.

We conclude that it is better to use a simple initial model instead of trying to incorporate other information in the initial model. Another important advantage of using a simple initial model is that the solution features are those required by the data and are not due to the peculiarities of the initial model. Since the data distribution is never uniform or perfect, the 3D inversion solution will not present a perfect image of the crust. However the resolution matrix allows us to evaluate the calculated velocity variations so that we know which velocity features are important.

Another important point is that, even before the 3D inversion solution is computed, the data variance with the purely 1D velocity model is slightly less than the data variance with the velocity model interpolated from the 2D refraction lines. The refraction model, obtained by considering amplitude information as well as many later arrivals, can emphasize locating velocity discontinuities rather than matching first arrival times. Thus for locating earthquakes, a 1D velocity model can be more appropriate than a complicated 2D refraction velocity model.

Hypocenters

An inversion for velocity structure using local earthquake data also includes hypocenters in the solution. A previous study in northern California (Eberhart-Phillips, 1986) showed that, while the 3D method may provide more accurate hypocenters, the hypocenters obtained with a 1D velocity model with station corrections are usually very similar to the 3D locations.

Figure 18a compares the hypocenters (x's) from our 3D inversion model E with the initial hypocenters (diamonds) from a 1D velocity model with stations corrections. Most hypocenters are similar, moving less than 0.5 km horizontally and about 1 km vertically. The largest changes, up to 3 km horizontally and 7 km vertically, tend to be for events on the edge of the aftershock zone. This is because the simple inversion for 1D velocity and station corrections will result in a location model that best fits the majority of the ray-path data, which means events in the center of the aftershock zone. The more physically realistic 3D model takes into account the different velocity variations along different ray paths to the same station. Thus the 3D model should particularly improve locations away from the center of the aftershock region.

The 3D hypocenters have 0.03 ± 0.05 s lower rms residuals than the 1D hypocenters. The 3D hypocenters tend to be shallower, by 1.1 ± 1.6 km, but horizontally they did not change in a systematic way from the initial 1D hypocenters. Cross-sections (Figures 18c,d) compare the hypocenters for the center of the aftershock zone; events within 10 km of the cross-section are projected onto it. The basic patterns of seismicity are similar but the 1D set contains more scattered hypocenters that make the details of the seismicity pattern less distinct. The 3D hypocenters will be evaluated further in Chapter 3, where a large set of aftershocks are relocated.

Since we have few shallow aftershocks, the uppermost part of our velocity model has 3-km vertical spacing. Hence the model does not provide much detail on near-surface heterogeneity. Station corrections calculated for the 3D model would help account for the near-surface. In run H, station corrections and hypocenters were inverted for, but the velocity model was fixed to E. The hypocenters with station corrections had 0.02 ± 0.02 s lower rms residuals, and tended to move about 0.4 km northeast (Figure 18b). There were no large changes in location; only three events moved as much as 1 km. The events that had larger than average changes in location also tended to have larger reductions in rms residual, indicating that the hypocenters obtained with station corrections are probably more accurate. It is interesting to compare the cross-sections (Figures 18d,e). The patterns are very similar, but the H cross-section (Figure 18e) looks as if it were rotated. It looks almost exactly like the E section (Figure 18d) with its northeast end pushed up about 1 km. This is because the station corrections for the relatively low-velocity San Joaquin Valley sediments tend to be positive, averaging 0.03 s, resulting in shorter ray paths toward the northeast, while stations corrections along the San Andreas fault tend to be negative, averaging -0.14 s, resulting in longer

ray paths toward the southwest. These station corrections are all fairly small, which indicates that the 3D velocity model is able to describe most of the velocity heterogeneity. In contrast the station corrections for the 1D velocity model ranged from -0.51 s to +0.59 s, with typical values of ± 0.30 s.

DISCUSSION

Geologic Structure

It is particularly interesting to apply 3D velocity inversion to an area characterized by folding and uplift. We know that a 1D velocity model is inappropriate in such a region. We want to consider how well the 3D model can describe this type of geologic structure. Rather than using layers or blocks, the velocity is defined on a 3D grid and linearly interpolated between gridpoints. This means, on the one hand, that the amount of uplift of a given rock unit is not described as clearly as when it is defined by a specific velocity discontinuity and that the shape cannot be more detailed than the gridspacing. But, on the other hand, the shape of the fold structure is free to vary in all directions throughout the three-dimensional area.

The California Coast Ranges extend along the western part of the state from Oregon to the Western Transverse Ranges in southern California. The San Andreas Fault cuts across the Coast Ranges, so that in the north it lies to the west and in the south it lies to the east of these mountains (Figure 1). At the southeastern end of the eastern portion of the Coast Ranges, Coalinga is part of an area of young folds located relatively near the San Andreas. One of the most dramatically uplifted sections of the Coast Ranges is the Diablo Range, extending for about 200 km northwest of Coalinga. There approximately 5 to 8 km of uplift has accumulated (Zigler, et al., 1986). The uplift first began in the mid-Miocene, and the principal uplift occurred during the late Pliocene-Quaternary (Page, 1981). In contrast, Coalinga Anticline has been uplifted

about only 2 km since late Pliocene-Quaternary initiation about 2 my ago (Stein and King, 1984).

In order to estimate the amount of uplift from the 3D model, let us consider the 4.0 km/s surface (Figure 13c). Away from the folds, to the east, this has a depth of 4 km. At the northwest corner of the grid, the end of the Diablo Range, it is at the surface, so the estimated uplift there is 4 km. Along the Coalinga Anticline the estimated uplift varies from 2.2 km at the northwest to 1.3 km at the southeast as the anticline plunges to the southeast. Kettleman Hills, at the southeast end of the grid, has an estimated uplift of 1 km, and plunges to the northwest. The trend of Kettleman Hills in the 3D model (Figure 13) is more westerly than Coalinga Anticline, in accord with geologic mapping.

The width of the local folds in the 3D model (Figure 14) is fairly constant at about 12 km. Between the two local folds, at y=63 (Figure 14i), there is very little expression of folding in the 3D model. On a longitudinal section near the fold axes, x=28 (Figure 15b), we can also see the two folds plunging toward this topographic low point.

Adjoining the Coalinga Anticline on the west, is the Pleasant Valley Syncline. At the surface (Figure 13a) this feature is widest near the town of Coalinga and narrows toward Kettleman Hills. The 3D model shows the syncline all along the length of the folds, and it is most apparent at the wider part of Pleasant Valley from y=42 to y=51 (Figure 14b to e), near the central part of Coalinga Anticline.

The San Joaquin Valley is the major structural element east of the Coast Ranges. It is deepest at its southeastern end and has an asymmetric shape, with sedimentary beds dipping fairly steeply on the west side while there is only a gradual slope on the east side. On the geologic map (Jennings, 1977) the

axis of the syncline is only 5 to 10 km from the west side of the roughly 80-km wide valley. The Cenozoic strata have a thickness of 4.5 km on the west side of the valley near Coalinga (Bartow, 1989). In the 3D model the valley is also deepest southwest of Coalinga. There the 4.0 km/s surface, which can be considered to illustrate the shape of the valley, has a depth of 4.5 km (Figure 13c). The details of the shape seem to vary with the local folds. For instance, the 4.0 km/s surface again flexes downward next to the northwestern end of the folds, where the uplift has been the greatest.

The details of the fold structure inferred from the 3D velocity solution can be compared to the map of the Kreyenhagen surface compiled from wells by Zigler et al. (1986). They likewise show the major fold patterns of the Diablo Range and San Joaquin Valley with locally the Coalinga Anticline and Kettleman Hills North Dome. They also map several smaller folds. Northeast of the Joaquin Ridge Anticline, they map another smaller fold, Turk Anticline, with about 0.25 km of relief. This is expressed in the 3D solution (Figure 13c) and the small area, at y=39, that has a somewhat deeper velocity contour, may also be associated with such an anticlinal feature. Between the Coalinga Anticline and the Diablo Range, they map a tightly folded syncline, White Creek Syncline. This shows up quite well in the 3D solution. And within the Pleasant Valley, they map another smaller anticline, Jacalitos Hills. This too is shown, on the west side of Pleasant Valley, in the 3D solution. They consider that Pleasant Valley continues to deepen to the southeast. In contrast, the 3D solution has the deepest part of the basin near the northern tip of Kettleman Hills, however it also has low resolution farther southeast. Thus it appears that the 3D inversion is able to discern details of folds where the resolution is good, and where resolution is lower minor features may be observed with less accurate shapes.

Rock Types

Bartow (1989) has described the stratigraphy of the Coalinga region. The Cenozoic sediments were deposited during various stages of marine transgression and uplift. Thus their composition varies. There are deep-marine mudstones, nearshore and deltaic sandstones, widespread shale units such as the Kreyenhagen, and, since the late Miocene, alluvial fan deposits and fluvial siltstones. They have fairly low densities of 2.2 to 2.6 g/cm^3 (Thompson and Talwani, 1964), and Wentworth and Zoback (1989) have calculated velocities for these layers of 2.1 to 4.0 km/s.

Below these strata lies the Mesozoic Great Valley Sequence (GVS). It is composed of sediments derived from the Sierran magmatic arc and deposited in submarine fan environments. It is predominantly arkosic sandstone and siltstone with some shale and conglomerate. We can estimate a range of GVS velocities with the relationship developed in chapter 5. For estimated clay content of 0.25 to 0.50, estimated porosity of 0.02 to 0.10, and depth of 0 to 6 km, Vp ranges from 3.9 to 5.1 km/s. In a refraction study along the axis of the Great Valley, Colburn and Mooney (1986) have an upper layer of 1.7 to 4.0 km/s rock that may correspond to Cenozoic rocks and sediments, overlying a 4.0 to 4.5 km/s layer that may correspond to GVS rock.

The Franciscan assemblage is the dominant rock unit throughout the Coast Ranges. Although coeval with the GVS, it typically lies structurally below the GVS. The Franciscan is a subduction complex composed of trench and oceanic sediments. As described by Page (1981) and Cowan (1974), the Franciscan is a melange with blocks of resistant rock. The melange matrix is pervasively sheared fine-grained mudstone or siltstone. The blocks are typically metagraywacke, but schist, greenstone, chert, serpentinite and conglomerate are also found. The blocks are usually elongate with length 2 to

3 times width. Their dimension ranges from several centimeters to a few meters. There are also large size, 5 to 20-km long, coherent units of metasandstone or metagraywacke that possess fairly continuous bedding and have variable degrees of folding. Within the Diablo Range Franciscan there are some mafic intrusives such as the Ortigalita Peak sill. For Diablo Range graywacke and melange, measured velocities of dry samples range from 5.7 to 5.9 km/s, and for more metamorphosed jadeite metagraywacke, measured velocities range from 6.1 to 6.3 km/s (Stewart and Peselnick, 1977). Velocities observed in-situ tend to range from 5.7 to 6.2 km/s (Walter and Mooney, 1982). In-situ velocities could be higher because they are fully saturated, or they could be lower because of cracks sampled by the longer wavelength seismic energy.

In the Diablo Range, northwest of Coalinga, the basement consists of a single gabbroic layer from 16-km depth to the Moho (Walter and Mooney, 1982). East of Coalinga, the basement beneath the Great Valley consists of a similar gabbroic layer, but it is underlain by a 7.2 km/s layer, representing mafic oceanic crust or mafic igneous rock that was underplated to the original Great Valley crust (Colburn and Mooney, 1986; Holbrook and Mooney, 1987).

We can try to distinguish different materials by their characteristic velocity. However such classification is not necessarily definitive, both because many rocks have similar velocities and because it is very interpretive to draw in specific units. The 3D model does not have assigned layer boundaries, but has velocity on a 3D grid of points.

To estimate the various rock units from the 3D solution, consider a central cross-section, y=48 (Figure 14d). The 4.0 km/s contour could represent the boundary between the Cenozoic sedimentary rock and the GVS. The material between the v=4.0 and v=5.0 km/s contours could represent the GVS.

The material from 5.5 to 6.2 km/s could represent Franciscan assemblage. The deeper 6.7 km/s material could be considered gabbroic basement. Thus the GVS forms the core of the anticline above 6-km depth and the Cenozoic strata fold gently above it. The Franciscan section is thickest on the west side of the anticline and deepest beneath the fold axis. On the east side of the fold, from 7 to 9-km depth, additional low-porosity GVS rock could be indicated by the 5.0 to 5.3 km/s material since it would have increased velocity with pressure. Little can be said about the basement since the deepest grid has low resolution; but it appears to dip to the southwest beneath the fold.

High-velocity body

One of the most intriguing features of the 3D model is a high-velocity body (HVB) from 6- to 8-km depth located along the southwest side of Pleasant Valley (Figures 8g,14). Its calculated velocities range from 6.0 to 6.5 km/s. It is roughly 25-km long and trends northwest-southeast. It is located on the edge of the small-scale grid so its width is difficult to estimate precisely. However in the larger-scale inversion, it is not observed at the next set of gridpoints located 13 km to the southwest (x=7). So it is probably between 2 and 10 km wide. (Note that details of the HVB shape in Figure 14 are due to the automated contouring program used.)

This HVB may represent an ophiolite fragment, mafic intrusive or high-grade metamorphic rock. Elsewhere in California, similar bodies have been observed or interpreted. From a 2D seismic refraction survey along the axis of the Great Valley, Holbrook and Mooney (1987) interpret a 70-km long HVB, 7.0 km/s at 12-km depth, and postulate that it represents a long string-like slice of ophiolite. Ophiolites are frequently found separating the Great Valley Sequence and the Franciscan assemblage. In the Diablo Range, Page

(1981) notes several ophiolite localities and also infers some ophiolite fragments within the Franciscan. The individual ophiolite exposures have lengths of 1 to 10 km, but the ophiolite extends intermittently for about 30 km. Mafic intrusives are also found such as the Ortigalita Peak gabbroic sill, a 300-m thick 8-km long body, 80-km northwest of Coalinga. Large coherent units of metagraywacke, 2- to 25-km long, occur within the Franciscan. These would typically not have unusually-high velocities, but one highly metamorphosed sample with jadeite, lawsonite and glaucophane had a laboratory-measured dry velocity of 6.3 km/s.

Because of its depth and small size relative to the major geologic structures, this HVB has little influence on the gravity. In order to compare the velocity to gravity, it has been converted to density using the relationship of Gardner et al. (1974) for sedimentary rocks, velocity less than 5.5 km/s, and the relationship of Hill (1978) for rocks with velocity greater than 5.5 km/s. Then, using the 3D grid of density, the gravitational attraction of any layer is computed using the algorithm of Parker (1972), as implemented by R. W. Simpson (written communication 1988). Besides enabling comparison to the observed gravity, this method provides a means to effectively integrate the 3D velocity structure over a specified depth range. The results are shown in Figure 19 for the same area that is shown in the velocity plots in Figure 8. Because the observed gravity has a high frequency character due to near-surface density variations, both the observed and computed gravity plots in Figure 19 have been upward continued 2 km. The observed gravity (Figure 19a) is similar to the computed gravity (Figure 19b) in both amplitude and location of features. Note that there are considerably fewer gravity stations north of 36° 15'; in particular the low at the northwest edge is defined by only two stations. The gravity contributions from depths 0 to 5 km, 6 to 7 km, and 8

to 13 km are shown in Figures 19 c, e and d, respectively. Compared to the overall gravity (Figure 19b), the velocity variations in the 0 to 5-km depth range appear to have the greatest influence on the gravity. The more westerly SJV axis and shallowing of basement to the east, seen in the 8 to 13-km depth range, contribute to the location of the valley low in the overall gravity. The contribution of the HVB in the 6 to 7-km depth range is about at the noise level in the observed gravity.

Comparison to refraction models

In Figure 20 the 3D inversion model is compared to the 2D seismic refraction model of Walter (1989). The 3D model is interpolated along the east-west refraction line. Overall the results are quite similar. The main differences result from the contrasting methods used. The 3D model is an inversion solution of first arrivals from an initial 1D gradient model and the refraction model is from forward modeling of many arrivals. The latter uses specific rock units and emphasizes velocity discontinuities that produce refractions. In places that have little or no ray path coverage, such as the eastern area in Figure 20, both methods result in simple models. But the simple refraction model will have a few layers with sharp discontinuities while the simple inversion model will have a smooth velocity gradient.

The values of velocity are very similar, particularly when recalling that the upper 6 km of the 3D solution was obtained with 3-km gridspacing. The 3D solution will not look as detailed as the refraction model which has numerous thin layers. Since neither method can give a unique indisputable result, it is heartening to have such agreement between the final models.

The shape and location of features are also fairly similar. The LVZ that Walter (1989) notices under the Anticline at 4 to 5-km depth is also found in the 3D solution, although it appears as more of a broad region of low velocity

rather than a thin zone of sharp velocity reduction. In both models the higher velocity basement material dips to the west beneath the fold. The hypocentral area in the core of the anticline has similar velocities in the two models, but the 3D inversion, using many ray paths in this area, has a more detailed model with several small LVZ's. The largest difference in the results is in the area directly east of the fold and 6 to 12-km depth. There the refraction model has a very large volume of 5.1 km/s material. The 3D inversion model also has lower velocity material there, however all the velocity contours are pushed down as if by folding; and the overall inversion velocity of the area is higher than in the refraction model, about 5.5 instead of 5.1 km/s.

Comparison to reflection line

About 8-km south of the east-west refraction line a 45-km long east-west seismic reflection line was shot. It has been analyzed by Wentworth and Zoback (1989). Their simplified line drawing is shown in Figure 21 together with a cross-section, interpolated along the reflection line, through the 3D inversion model.

Well-layered reflections define the sedimentary section. Their calculated interval velocities compare fairly well with the inversion velocities, although they tend to be lower than both the inversion and refraction velocities. The shape of the sedimentary section in the 3D model is in excellent agreement with the reflection line. The deepest point is at about 25-km distance, the anticline at about 12 km, Pleasant Valley at about 6 km, and the strata shallow toward the western end (0 km) of the line.

While there are some scattered patches of continuous reflections, the reflection line below the sedimentary section has few strong reflections and has none that are continuous for more than about 7-km distance. The reflections present appear as scattered patches of reflections, generally in the

area below and west of the fold. Wentworth and Zoback (1989) interpret numerous thrust faults in this region. Intriguingly, this is also the area where the 3D inversion shows complicated velocity variations with several LVZ's. The only problematic area in Figure 21 is at the western end where the 3D inversion indicates a high-velocity body at 6-km depth. While there are no reflections at that point, there are some deeper reflections at about 9-km depth, and hence Wentworth and Zoback (1989) interpret the entire area as layered GVS rock.

Upper LVZ

The shallow LVZ found in the 3D inversion model at 6-km depth correlates with LVZ's observed, within the sedimentary section, in both the reflection and refraction data. Within a given rock unit, an increase in pore pressure (P_p) from hydrostatic to near-lithostatic will cause a large reduction in seismic velocity, as discussed in Chapter 5. Since overpressures have been observed in drillholes in sedimentary rocks, and this shallow LVZ occurs in continuous stratigraphic units, it is likely to be due to high pore pressure. Yerkes et al. (1989) have analyzed the fluid pressure, from drilling mud density, in 324 wells in the southwest San Joaquin Valley, many near Coalinga. They find relatively high fluid pressures in portions of the uplifted Tertiary and Great Valley Sequence rocks below 1.5 km. In some wells, at depths of 4 to 5 km, they find zones with pressures 80 to 90 % of lithostatic that correlate with low velocity in sonic logs.

Velocity reductions are most obvious when occurring as velocity reversals in vertical profiles. However other patterns of velocity reduction can also be important. In the reflection section, with the aid of continuous strongly-reflective horizons to identify stratigraphic layers, horizontal velocity reductions can be attributed to high pore pressure. This is discussed

in Chapter 5, where it is shown that at the anticline axis the Santa Margarita strata may have near-lithostatic fluid pressure. Note that this velocity reduction has the effect of pushing down the velocity contours in the 3D sections so that the fold axis appears less prominent than in the other interpretations (Figures 20,21).

We can also use the empirical relationship to estimate the effective pressure (P_e), and hence the P_p, from the LVZ.

$$\Delta V_p = 0.446\,\Delta\left(P_e - 1.0e^{-16.7P_e}\right)$$

While we have less knowledge of the continuity of rock type than with the reflection record, and velocity variations may be partly due to lithologic variations, the estimated Pe can give us a rough idea of the overpressures that may exist in the core of the anticline. From the refraction data, Walter (1989) computes a ΔV_p at 5-km depth of 0.2 to 0.5 km/s, representing P_e of 0.23 to 0.02 kbar, and P_p of 83 to 97 % of lithostatic. The 3D inversion (Figures 8,9), from 3 to 6-km depth, shows ΔV_p of 0.29 to 0.43 km/s, representing P_e of 0.16 to 0.11 kbar and P_p of 90 to 93 % of lithostatic. Overpressure can also be indicated where there is little or no increase in velocity with depth since velocity should increase with the P_e gradient. Where the 3D solution has a velocity increase of only 0.04 km/s from 3 to 6-km depth, a 44 % increase in P_p to 73 % of lithostatic could be represented.

This LVZ is located, from 4 to 6-km depth, within the anticline. It extends approximately 20 km along the fold axis and is 6 to 8-km wide. There are two things necessary in order for it to be a zone of high pore pressure. One is a source of excess fluid and the other is a barrier to prevent equilibration of fluid pressure. This is a region of active compression with a lateral compressive strain rate estimated at 36 μstrain/yr by Atwater et al. (1989). This compressive strain can cause a reduction in pore volume,

particularly in sedimentary rock. Walder (1984) estimates that, at 4-km depth, this tectonic strain (about 10^{-14} s^{-1}) would be capable of producing near-lithostatic P_p in only 14,000 yr. The LVZ is in the mid to upper part of the GVS in Walter's (1989) interpretation. There are low-permeability shale layers within the GVS, such as the Moreno shale, that could act as effective barriers to fluid movement. Hence it is reasonable for an overpressured zone to exist within the Coalinga anticline and to be evidenced by an LVZ.

Deeper LVZ's

The 3D inversion model also shows a series of three discontinuous LVZ's between 8 and 12-km depth (Figure 14). These could be explained by high P_p as well or by heterogeneity of material or a combination thereof. These LVZ occur within the Franciscan assemblage, which is a complicated rock unit, not continuous layered strata. This is also the hypocentral zone where earthquakes have disrupted the material and numerous thrust faults have been inferred (Wentworth and Zoback, 1989). Thus it is not as simple to assert overpressure here as in the upper sedimentary rock. In addition, while the shape of the upper LVZ nicely corresponds to the shape of the fold, these LVZ tend to be horizontal or southwest-dipping zones of varied thickness, about 4- to 8-km wide and 5- to 10-km long, occurring along the length of the Coalinga Anticline.

If these LVZ are due to heterogeneity of material, that could be caused by a randomly-distributed heterogeneity within the Franciscan unit, or result from deformation along multiple thrust faults. The original subduction zone environment of the Franciscan allowed for incorporation of a wide variety of materials, and the deformation experienced prior to initiation of currently-active local folding created a complicated melange. Geologic mapping shows dimensionally variable blocks of resistant rock type within the melange

(Cowan, 1974). These range from schist and greenstone blocks several meters in diameter to metagraywacke blocks from 10-cm to 20-km long. The measured velocities of the melange and the metagraywacke are very similar (Stewart and Peselnick, 1977).

Other subsurface velocity studies have generally interpreted the Franciscan with spatially uniform velocity. For example, in the Diablo Range, Walter and Mooney (1982) consider the Franciscan to extend from about 3- to 16-km depth with velocity of about 5.5 to 6.0 km/s, increasing with depth. Similarly Blümling et al. (1985) interpret the Franciscan as an 8-km thick layer from 5- to 13-km depth with velocity increasing from 5.7 to 6.3 km/s. These refraction studies did not see any other travel-time branches that could represent strong velocity reversals within the Franciscan. However, in the Coalinga area, particularly in the line that is sub-parallel to the fold axis, Walter (1989) notes evidence of alternating high and low velocity within the Franciscan. There he models the Franciscan as three layers: a 5.5 to 6.0 km/s upper layer, a 5.8 to 6.0 km/s lower layer, and a higher-velocity discontinuous middle layer, 6.0 to 6.15 km/s. This velocity variation is conceptually similar to that found in the 3D inversion solution, which is more detailed since it includes earthquake sources throughout the Franciscan. Thus it seems that the Franciscan rock in the Coalinga area may indeed have a larger degree of velocity variation than it does in such other places as the Diablo Range directly to the northwest.

In that case heterogeneity resulting from multiple thrust faults may be the favored explanation for these LVZ's at hypocentral depths. Fault zones themselves may have a different composition and could be represented by low-velocity. Velocity studies frequently, but not always, reveal low-velocity zones associated with faults. Low velocity has been noted along the San Andreas or

other vertical strike-slip faults by Healy and Peake (1975), Feng and McEvilly (1983), Mooney and Luetgert (1982), Blümling et al. (1985), Thurber (1983) and Eberhart-Phillips (1986). However Mooney and Colburn (1985), Taylor and Scheimer (1982) and Fuis et al. (1984) did not observe low velocity associated with some major faults. Continual deformation along a fault zone could result in velocity reduction through fracturing, formation of fault gouge and increased pore pressure. Moos and Zoback (1983) correlated macroscopic fractures with velocity reductions of 12 to 35 %. Wang (1984) related measured fault gouge velocities to lowered velocity along the fault zone to 10-km depth. Parry and Bruhn (1986) calculated that fluid pressure varied from 52 % to nearly lithostatic on the Wasatch fault to 10-km depth. However for a thrust fault it is perhaps simplest to consider that such faults can easily create low-velocity zones by pushing up deeper high-velocity material over low-velocity material.

The shape of the observed LVZ's is similar to the southwest-dipping thrust faults that are inferred from earthquake focal mechanisms and interpreted from geodetic (Stein, 1986) and reflection data (Wentworth and Zoback, 1989). In Figure 21, to evaluate the feasibility of the velocity variations corresponding to fault zones, lines are drawn through each low-velocity zone in the velocity solution. The agreement is good with the lower plot, which shows the thrust faults interpreted by Wentworth and Zoback (1989) from the reflection line, and may indicate blocks of higher-velocity material moving up along thrust faults.

If these LVZ's are related to faults, then they should be comparable to modelled faults for the Coalinga mainshock. Stein (1986) from geodetic modelling, proposes a listric fault dipping southwest from 7.5- to 9.1-km depth, with 7- by 8-km area, from x=24 to 31 and y=42 to 50. This may correspond to

the middle most prominent LVZ. The LVZ is similar to the geodetic fault-model from y=45 to y=54 (Figure 14c to f), particularly at y=48 and y=51. It tends to continue further downdip to the southwest than the geodetic fault, and it does not extend as continuously as the proposed rupture surface. However LVZ's do occur all along the length of Coalinga Anticline and it is possible that either the LVZ's may be more continuous than they appear in the 3D solution or the fault surface is not as simple as in the geodetic model. Choy (1989) was unable to model the mainshock seismograms with a single event and instead had to use two noncolocated events with 6 and 5-km rupture radius.

Stein and King (1984) note that there has been about 2 km of uplift at Coalinga Anticline over the last 2 my. If the LVZ represent thrust faults, then we could estimate their throw by considering how far each high-velocity piece has moved up over each low-velocity piece. Thus the middle LVZ at about 10-km depth could represent a fault with about 2-km throw, and the smaller, deeper LVZ to the northeast could represent a fault with about 1-km throw. These estimates are similar to the cumulative uplift of the fold.

CONCLUSIONS

The inversion of 7,696 P and 1,511 S arrivals from earthquakes and 696 P first arrivals from shots for the Coalinga region produced a three-dimensional velocity model, with 1 to 2-km gridspacing in the hypocentral area, that accounts for an 82 % reduction in data variance. The velocity model shows the 3D geologic fold structure, and indicates a high-velocity body and low-velocity zones at hypocentral depths. The addition of pseudo-bending to the ray-tracing routine makes the ray paths more accurate, particularly for long ray paths and near large velocity gradients. In order to get the most detail where there is the densest ray path coverage a series of three inversions was done, focusing in on the hypocentral area. Outside of the solution area the velocities are fixed to those of the previous larger-scale inversion.

A simple starting model gave the best results. Both a simple 1D initial model and a complex initial model derived from the refraction interpretation were tried. An important advantage of using a simple initial model is that the solution features are those required by the data and are not due to peculiarities of the initial model. Where there is low resolution, the inversion will produce only small velocity perturbations. The velocity-solution variance with the refraction initial model is about twice that with the simpler initial model. The solution with the refraction initial model also did not fit the data as well; its data variance is about three times higher than with the simpler initial model. Thus the use of a complex initial model appears to result in an overly-complex solution, and it is difficult to understand what details of the initial model cause the large velocity variations.

The S-velocity solution has different resolution than the P-velocity solution because it uses a different set of stations, and it has lower resolution because it uses fewer arrival times. While the general patterns of velocity

variation are similar for both V_p and V_s, the V_s solution tends to have more smearing of velocity features and can have somewhat different locations of velocity features. For instance an LVZ that is indicated by a velocity reversal in V_p may be indicated a more spread-out area of reduced velocity in V_s. The resolution matrices can be used to interpret the velocity variations. Unfortunately, because of the differences in resolution of V_p and V_s in this data set, V_p/V_s cannot be analyzed in much detail.

The hypocenters obtained from the inversion solution have 0.03 ± 0.05 s lower rms residuals than hypocenters from a local 1D velocity model with station corrections. The basic patterns of seismicity are similar but the 1D set contains more scattered hypocenters that make the details of the seismicity pattern less distinct.

The overall shape and location of velocity features correspond well to the mapped surface geology. The 3D inversion is able to discern details of folds where the resolution is good, and where resolution is lower minor features may be observed with less accurate shapes. Coalinga Anticline and Kettleman Hills are seen as distinct features. The shapes of San Joaquin Valley and Pleasant Valley follow those interpreted from well data, including smaller secondary anticlines within these valleys. The amounts of uplift inferred for the Diablo Range and the local folds are similar to those implied by geologic data. Rock units can be inferred based on the velocities. Thus Franciscan and GVS rock form the core of the anticline with the Cenozoic strata folding gently above and the gabbroic basement dipping down beneath.

The 3D velocity solution compares well to the seismic reflection record. The reflection velocities are similar but tend to be somewhat lower. The shape of the sedimentary section is in excellent agreement with the reflections from the Cenozoic strata, although the fold axis appears less prominent in the 3D

solution since the high fluid pressure there has the effect of pushing down the velocity contours. In comparison to the refraction model, the 3D solution has similar velocities and similar shapes and locations of velocity features. The refraction interpretation is more detailed at shallower depths and the 3D solution is more detailed in the hypocentral zone where it uses more data. The gravity computed from the 3D velocities, converted to density, matches the observed gravity quite well.

The 3D velocity solution has several interesting features besides the overall geologic structure. On the western edge of the Coalinga area, there is a high-velocity body. There is a low-velocity zone at 6-km depth within the sedimentary rock. And there are three discontinuous low-velocity zones observed between 7- and 12-km depth beneath the anticline.

The high-velocity body is a linear feature, about 25-km long, southwest of Pleasant Valley from 6- to 8-km depth. It has computed P-velocities of 6.0 to 6.5 km/s. It may represent an ophiolite fragment, mafic intrusive or high-grade metamorphic rock.

The shallower LVZ extends for 20 km along the fold axis at about 6-km depth, and correlates with LVZ's observed in both the refraction and reflection data. It may indicate high pore pressure caused by lateral compressive strain, in conjunction with barriers provided by shale horizons within the GVS.

The deeper LVZ's occur within the Franciscan, and are characterized by horizontal or southwest-dipping zones of varied thickness, 4- to 8-km wide and 5- to 10-km long. The velocities are within the range considered appropriate for the Franciscan assemblage. These LVZ may represent randomly-distributed heterogeneity within the complex Franciscan melange, or may result from deformation along multiple thrust faults.

Note that a thrust fault could create an LVZ simply by pushing up

deeper higher-velocity material over shallower lower-velocity material. The pattern of LVZ's with the hypocentral zone is in agreement with thrusts inferred from the reflection line. If these features did represent thrusts, the middle LVZ could indicate about 2 km of throw and the LVZ that is deeper and slightly northeast could indicate about 1 km of throw. These estimates are similar to the cumulative uplift of the fold.

REFERENCES

Atwater, B. F., D. A. Trumm, J. C. Tinsley, III, R. S. Stein, A. B. Tucker, D. J. Donahue, A. J. T. Jull, and L. A. Payen, Alluvial plains and earthquake recurrence at the Coalinga Anticline, in The Coalinga, California, Earthquake of May 2, 1983, U. S. Geol. Surv. Prof. Pap., edited by M. Rymer and W. Ellsworth, 1989.

Bartow, J. A., Cenozoic stratigraphy and geologic history of the Coalinga region, central California, in The Coalinga, California, Earthquake of May 2, 1983, U. S. Geol. Surv. Prof. Pap., edited by M. Rymer and W. Ellsworth, 1989.

Blümling, P., W. D. Mooney, and W. H. K. Lee, Crustal structure of the southern Calaveras Fault zone, central California, from seismic refraction investigations, Bull. Seismol. Soc. Am., 75, 193-210, 1985.

Choy, G. L., Source parameters of the Coalinga, California earthquake of May 2, 1983 inferred from broadband body waves, in The Coalinga, California, Earthquake of May 2, 1983, U. S. Geol. Surv. Prof. Pap., edited by M. Rymer and W. Ellsworth, 1989.

Colburn, R. H., and W. D. Mooney, Two-dimensional velocity structure along the synclinal axis of the Great Valley, California, Bull. Seismol. Soc. Am., 76, 1305-1322, 1986.

Colburn, R. H., and A. W. Walter, Data report for two seismic-refraction profiles crossing the epicentral region of the 1983 Coalinga, California earthquakes, U. S. Geol. Surv. Open-File Rep. 84-643, 1984.

Cowan, D. S., Deformation and metamorphism of the Franciscan subduction zone complex northwest of Pacheco Pass, California, Geol. Soc. Am. Bull., 85, 1623-1634, 1974.

Eaton, J. P., The North Kettleman Hills earthquake sequence of August 4, 1985 and its first week of aftershocks - a preliminary report, U. S. Geol. Surv., Meno Park, 1985.

Eaton, J. P., The May 2, 1983 Coalinga earthquake and its aftershocks: A detailed study of the hypocenter distribution and of the focal mechanisms of the

larger aftershocks, in Mechanics of the May 2, 1983 Coalinga Earthquake, U. S. Geol. Surv. Open-File Rept. 85-44, edited by M. Rymer and W. Ellsworth, pp. 132-201, 1985.

Eberhart-Phillips, D., and P. A. Reasenberg, Complex faulting structure inferred from local seismic observations of M $\geq$ 1.0 aftershocks, May 2 - June 30, 1983, in The Coalinga, California, Earthquake of May 2, 1983, U. S. Geol. Surv. Prof. Pap., edited by M. Rymer and W. Ellsworth, 1989.

Eberhart-Phillips, D., Three-dimensional velocity structure in Northern California Coast Ranges from inversion of local earthquake arrival times, Bull. Seismol. Soc. Am., 76, 1025-1052, 1986.

Feng, R., and T. V. McEvilly, Interpretation of seismic reflection profiling data for the structure of the San Andreas fault zone, Bull. Seismol. Soc. Am., 73, 1701-1720, 1983.

Fuis, G. S., W. D. Mooney, J. H. Healy, G. A. McMechan, and W. J. Lutter, A seismic refraction survey of the Imperial Valley Region, California, J. Geophys. Res., 89, 1165-1189, 1984.

Healy, J. H., and L. G. Peake, Seismic velocity structure along a section of the San Andreas fault near Bear Valley, Califoria, Bull. Seismol. Soc. Am., 65, 1177-1197, 1975.

Hill, D. P., Seismic evidence for the structure and Cenzoic tectonics of the Pacific Coast States, in Cenozoic Tectonics and Regional Geophysics of the Western Cordillera, edited by R. B. Smith and G. P. Eaton, Geol. Soc. Am. Mem. 152, pp 145-174, 1978.

Holbrook, W. S., and W. D. Mooney, The crustal structure of the axis of the Great Valley, California, from seismic refraction measurements, Tectonophysics, 140, 49-63, 1987.

Jennings, C. W., Geologic map of California, Calif. Geol. Map Series Map No. 2, scale 1:750,000, Calif. Div. Mines and Geol., Sacramento, 1977.

Macgregor-Scott, N., and A. W. Walter, Data report for two earthquake-source refraction profiles crossing the epicentral region of the 1983 Coalinga, California earthquakes, U. S. Geol. Surv. Open-File Rep. 85-435, 1985.

Mooney, W. D., and R. H. Colburn, A seismic refraction profile across the San Andreas, Sargent, and Calaveras Faults, West-Central California, Bull. Seismol. Soc. Am., 75, 175-191, 1985.

Mooney, W. D., and J. H. Luetgert, A seismic refraction study of the Santa Clara Valley and Southern Santa Cruz Mountains, West-Central California, Bull. Seismol. Soc. Am., 72, 901-909, 1982.

Moos, D., and M. D. Zoback, In-situ studies of velocity in fractured crystallinge rocks, J. Geophys. Res., 88, 2345-2358, 1983.

Page, B. M., The Southern Coast Ranges, in The Geotectonic Development of California, Rubey Vol. I, edited by W. G. Ernst, pp. 329-417, Prentice-Hall, Englewood Cliffs, NJ., 1981.

Parker, R. L., The rapid calculation of potential anomalies, Geophys. J. R. Astron. Soc., 31, 447-455, 1972.

Parry, W. T., and R. L. Bruhn, Pore fluid and seismogenic characteristics of fault rock at depth on the Wasatch Fault, Utah, J. Geophys. Res., 91, 730-744, 1986.

Snyder, D. G., C. W. Roberts, R. W. Saltus, and R. F. Sikora, A magnetic tape containing the principal facts of 64,026 gravity stations in the state of California, U. S. Geol. Surv. NTIS PB-82-16827, 1982

Stein, R. S., Evidence for surface folding and subsurface fault slip from geodetic elevation changes associated with the 1983 Coalinga earthquake, in Mechanics of the May 2, 1983 Coalinga Earthquake, U. S. Geol. Surv. Open-File Rept. 85-44, edited by M. Rymer and W. Ellsworth, pp. 225-253, 1985.

Stein, R. S., Postseismic growth of the Coalinga Fold (abstract), EOS Trans. AGU, 67, 1223, 1986.

Stein, R. S., and G. C. P. King, Seismic potential revealed by surface folding: 1983 Coalinga, California, earthquake, Science, 224, 869-872, 1984.

Stewart, R., and L. Peselnick, Velocity of compressional waves in dry Franciscan rocks to 8 kilobars and 300°, J. Geophys. Res., 82, 2027-2039, 1977.

Taylor, S. R., and J. F. Scheimer, P-velocity models and earthquake locations in the Livermore Valley region, California, Bull. Seismol. Soc. Am., 72, 1255-1275, 1982.

Thompson, G. A., and M. Talwani, Crustal structure from Pacific basin to central Nevada, J. Geophys. Res., 69, 4813-4837, 1964.

Thurber, C. H., Earthquake locations and three-dimensional crustal structure in the Coyote Lake area, central California, J. Geophys. Res., 88, 8226-8236, 1983.

Um, J., and C. Thurber, A fast algorithm for two-point seismic ray tracing, Bull. Seismol. Soc. Am., 77, 972-986, 1987.

Walder, J. S., Coupling between fluid flow and deformation in porous crustal rocks, Ph.D. thesis, Stanford Univ., Stanford, Calif., 1984.

Walter, A. W., Velocity structure near Coalinga, California, in The Coalinga, California, Earthquake of May 2, 1983, U. S. Geol. Surv. Prof. Pap., edited by M. Rymer and W. Ellsworth, 1989.

Walter, A. W., and W. D. Mooney, Crustral structure of the Diablo and Gabilan Ranges, central California: a reinterpretation of existing data, Bull. Seismol. Soc. Am., 72, 1567-1590, 1982.

Wang, C-Y., On the constitution of the San Andreas fault zone in central California, J. Geophys. Res., 89, 5858-5866, 1984.

Wentworth, C. M., and M. D. Zoback, Structure of the Coalinga area and thrust origin of the May 2, 1983 earthquake, in The Coalinga, California, Earthquake of May 2, 1983, U. S. Geol. Surv. Prof. Pap., edited by M. Rymer and W. Ellsworth, 1989.

Yerkes, R. F., P. Levine, and C. M. Wentworth, Abnormally high fluid pressures and the Coalinga earthquakes, in The Coalinga, California, Earthquake of May 2, 1983, U. S. Geol. Surv. Prof. Pap., edited by M. Rymer and W. Ellsworth, 1989.

Zigler, J. L., C. M. Wentworth, and J. A. Bartow, Structure contour map of the tops of the Kreyenhagen Formation and Cretaceous strata in the Coalinga area, Fresno and Kings counties, California, U. S. Geol. Surv. Map MF-1843, 1986.

Table 1

Run	Description	P,S	Fixed gridpts	Data Variance			Velocity Model Variance		No. Gridpts Solved For		Variance of ΔV, this Run	
				Final	% Reduction this Run	% Reduction from 1D	P	S	P	S	P	S
A	Large-scale grid, 1D initial velocity	P,S	none	0.0332	64.0	64.0	0.0614	0.0096	120	63	0.1004	0.0267
B	Medium-scale grid, initial velocity from run A	P,S	x<20,x>38 y<21,y>80	0.0184	44.7	80.1	0.0910	0.0196	255	208	0.0660	0.0153
C	Setup as for run B, only use S stations	P,S	x<20,x>38 y<21,y>80	0.0203	50.8 different data		0.0541	0.0194	234	208	0.0547	0.0137
D	Small-scale grid, initial velocity from run B	P	z=0 to 5,z=16 x<20,x>34 y<39,y>63	0.0147	10.4	79.4 (P)	0.0961		495		0.0343	
E	Small-scale grid, initial velocity from run B where fixed, run A for nonfixed	P	z=0 to 5,z=16 x<20,x>34 y<39,y>63	0.0147	17.4	79.4 (P)	0.0955		494		0.0695	
F	Small-scale grid, fixed velocities from refraction model, run A for nonfixed	P	z=0 to 5,z=16 x<20,x>34 y<39,y>63	0.0484	37.1	32.2 (P)	0.1989		495		0.1269	
G	Small-scale grid, for z=0 to 5 km, velocities from refraction, model, rest like run E	P	z=0 to 5,z=16 x<20,x>34 y<39,y>63	0.0422	37.1	40.8 (P)	0.1770		499		0.1300	
H	Invert for station corrections, all velocities from run E	P	all gridpts	0.0100	29.8	86.0 (P)						

Table 2a

Diagonal Resolution Elements for z=6 Level, Run B						
x / y	20	24	27	30	34	38
			P-Velocity			
21	0.10	0.00	0.04	0.01	0.00	0.00
30	0.39	0.07	0.17	0.10	0.13	0.08
39	0.40	0.36	0.16	0.21	0.19	0.25
47	0.33	0.30	0.27	0.27	0.26	0.25
55	0.32	0.19	0.13	0.13	0.20	0.49
63	0.23	0.12	0.06	0.08	0.18	0.32
71	0.18	0.11	0.04	0.05	0.06	0.16
80	0.26	0.03	0.01	0.05	0.02	0.00
			S-Velocity			
21	0.03	0.01	0.02	0.03	0.01	0.00
30	0.25	0.02	0.06	0.20	0.36	0.09
39	0.01	0.07	0.28	0.29	0.51	0.41
47	0.01	0.24	0.42	0.51	0.37	0.30
55	0.00	0.12	0.26	0.30	0.20	0.11
63	0.01	0.11	0.13	0.19	0.29	0.09
71	0.10	0.06	0.10	0.11	0.13	0.05
80	0.00	0.00	0.01	0.01	0.00	0.01

Table 2b

Diagonal Resolution Elements for y=47 Cross-Section, Run B						
x / z	20	24	27	30	34	38
			P-Velocity			
0	0.05	0.14	0.36	0.48	0.12	0.01
3	0.27	0.30	0.50	0.57	0.31	0.08
6	0.33	0.30	0.27	0.27	0.26	0.25
9	0.25	0.17	0.21	0.27	0.15	0.30
12	0.21	0.08	0.07	0.10	0.11	0.24
16	0.18	0.03	0.01	0.02	0.05	0.02
			S-Velocity			
0	0.00	0.06	0.03	0.25	0.03	0.00
3	0.00	0.29	0.14	0.54	0.30	0.10
6	0.01	0.24	0.42	0.51	0.37	0.30
9	0.06	0.23	0.47	0.44	0.27	0.47
12	0.11	0.12	0.06	0.27	0.19	0.53
16	0.07	0.01	0.01	0.02	0.08	0.04

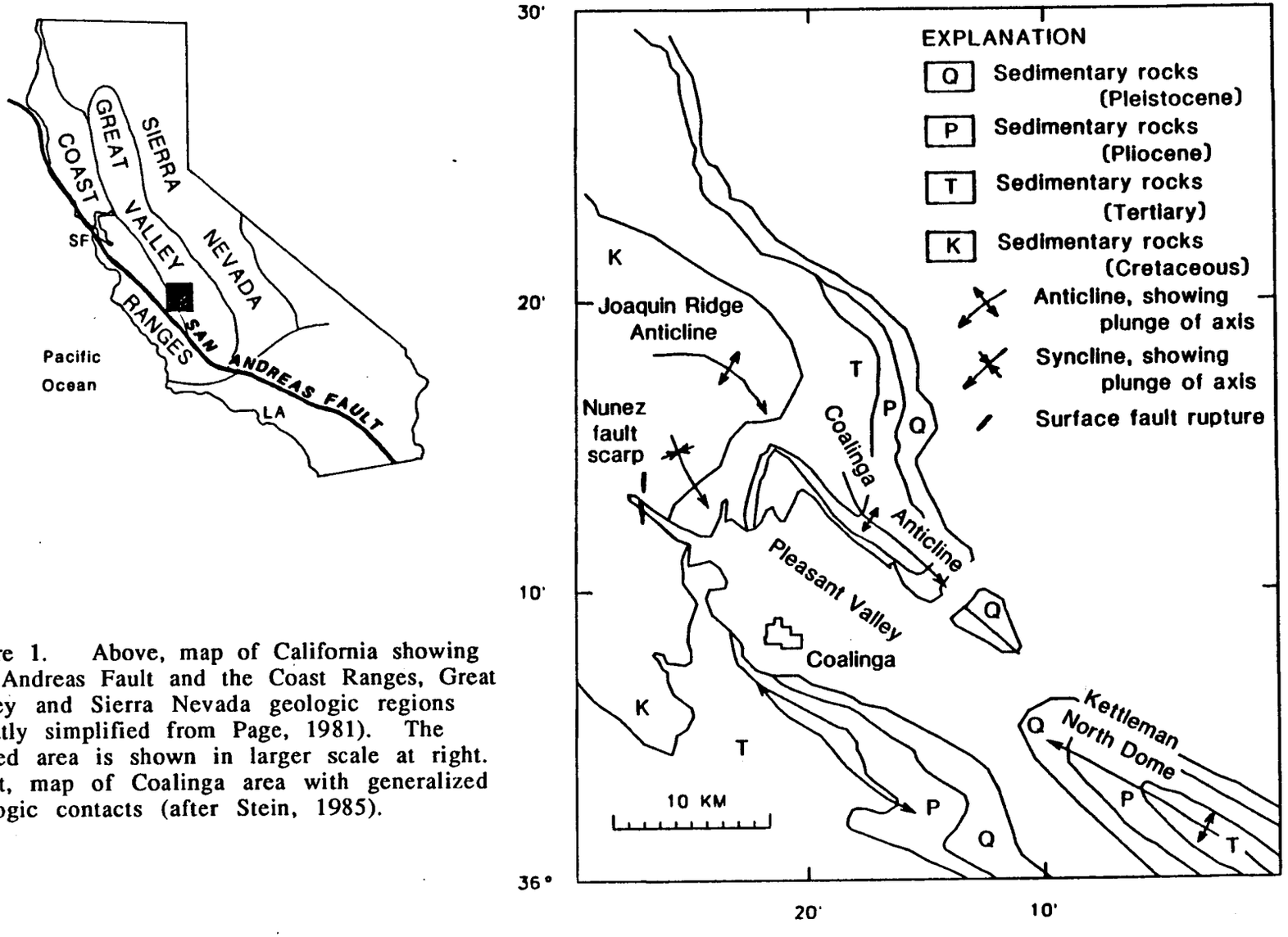

Figure 1. Above, map of California showing San Andreas Fault and the Coast Ranges, Great Valley and Sierra Nevada geologic regions (greatly simplified from Page, 1981). The shaded area is shown in larger scale at right. Right, map of Coalinga area with generalized geologic contacts (after Stein, 1985).

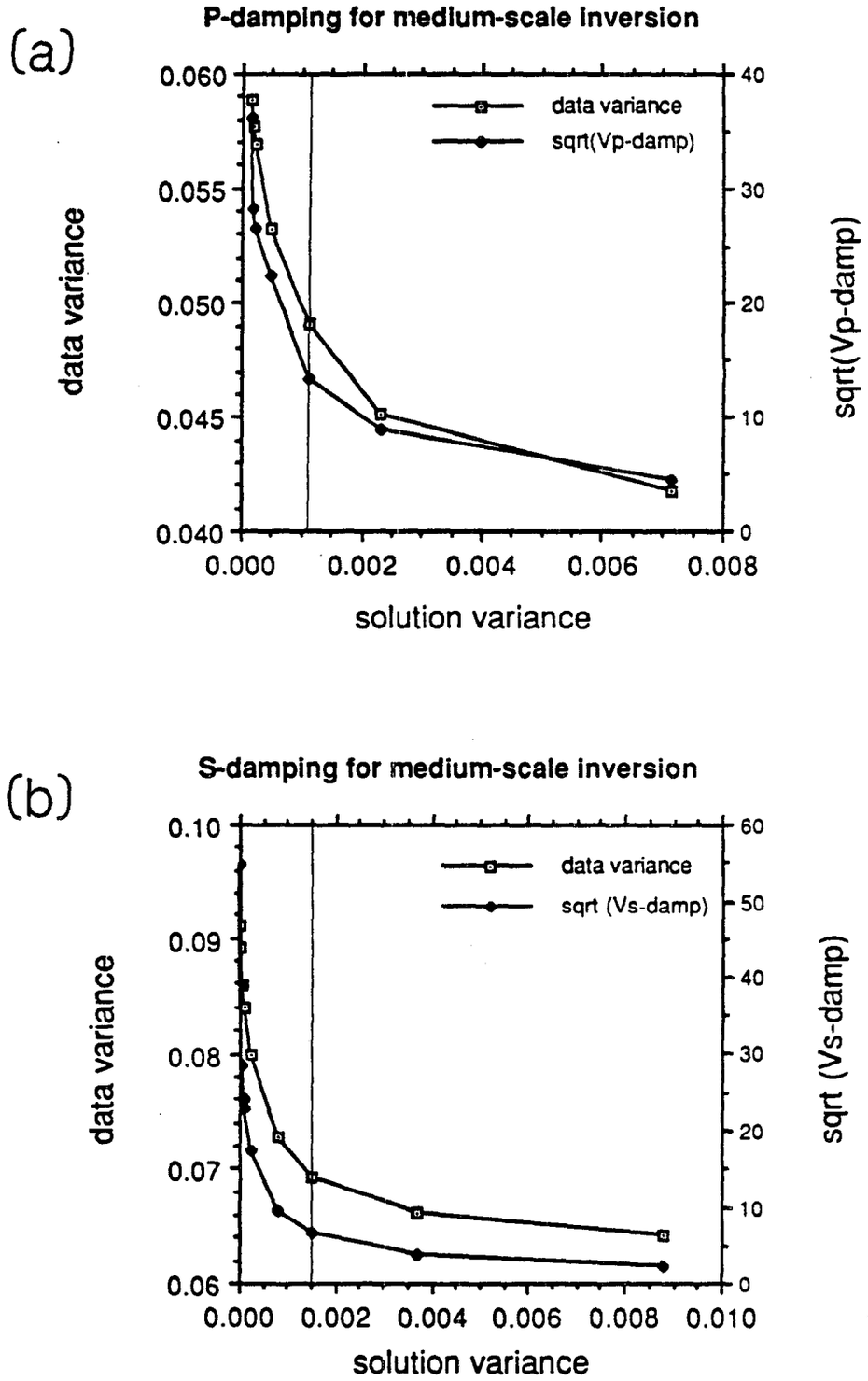

Figure 2. Trade-off curves for selecting optimal damping value for (a) Vp and (b) Vs. The data variance (open squares) and and solution variance are computed after one iteration for the indicated damping (solid squares). The lines indicate selected values, which reduce most of the data variance without causing large increase in the data variance.

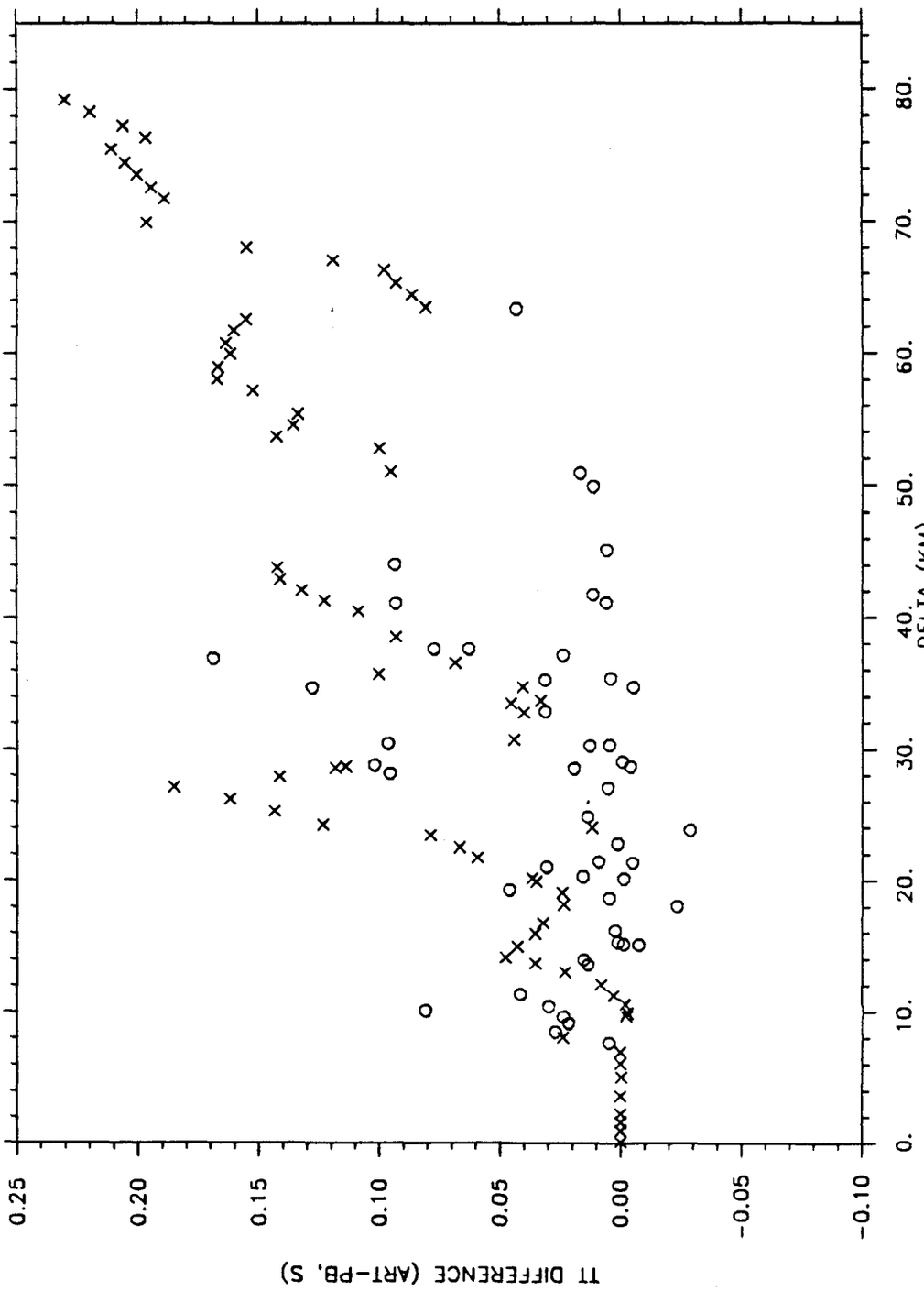

Figure 3. Comparison of arcuate path (ART) and ART with psuedo-bending (PB). ART travel time minus PB travel time plotted versus distance from source to receiver, for the two earthquakes (circles) and refraction shot (X's) shown in Figure 4.

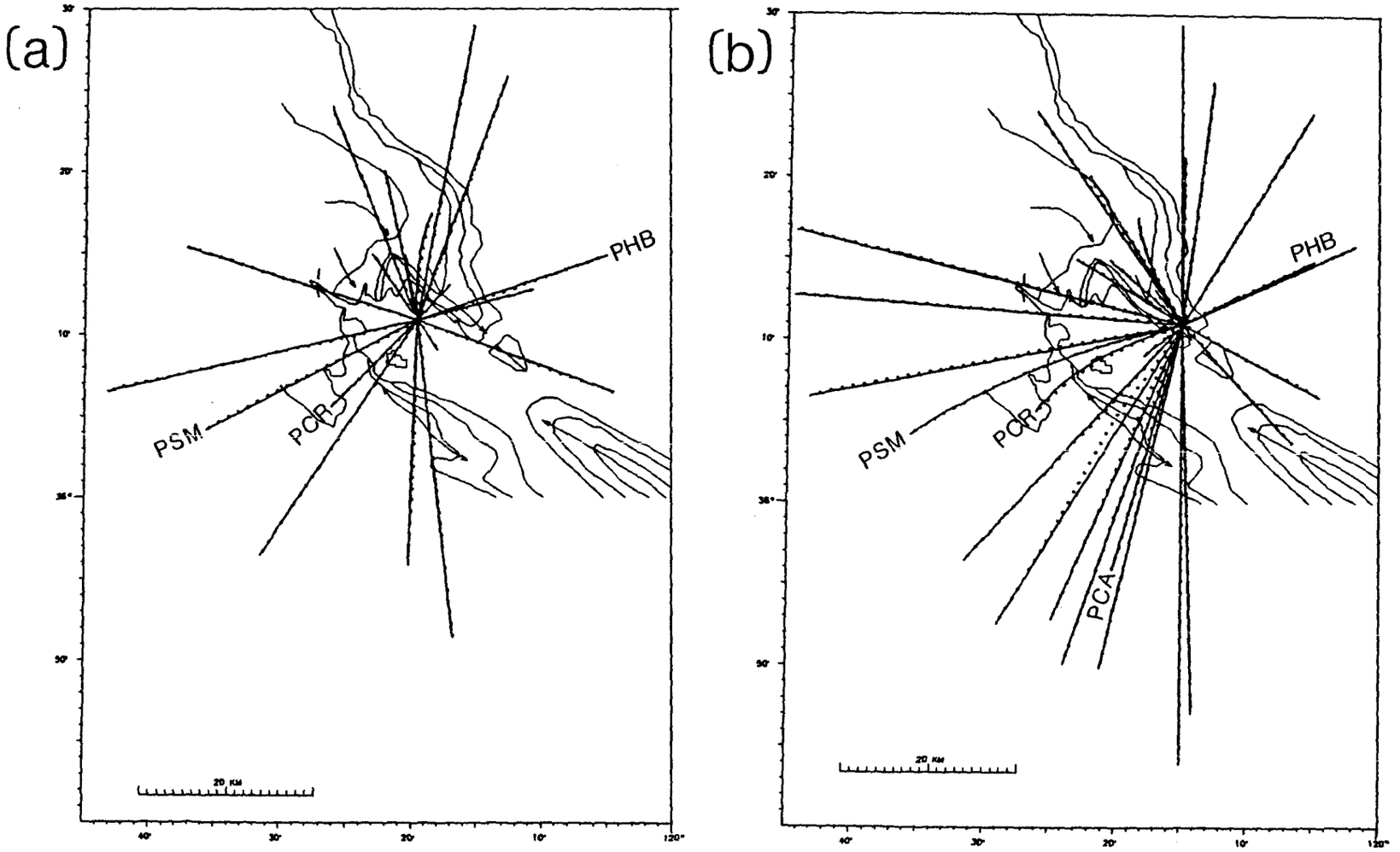

Figure 4. Comparison of 3D ray paths: solid lines = ART (arcuate path), dashed lines = PB (ART plus psuedo-bending). (a) and (b) Map views of earthquake ray paths using velocity model E (Table 1), geologic contacts of Figure 2 are shown for reference, stations PHB, PSM, PCR and PCA are indicated.

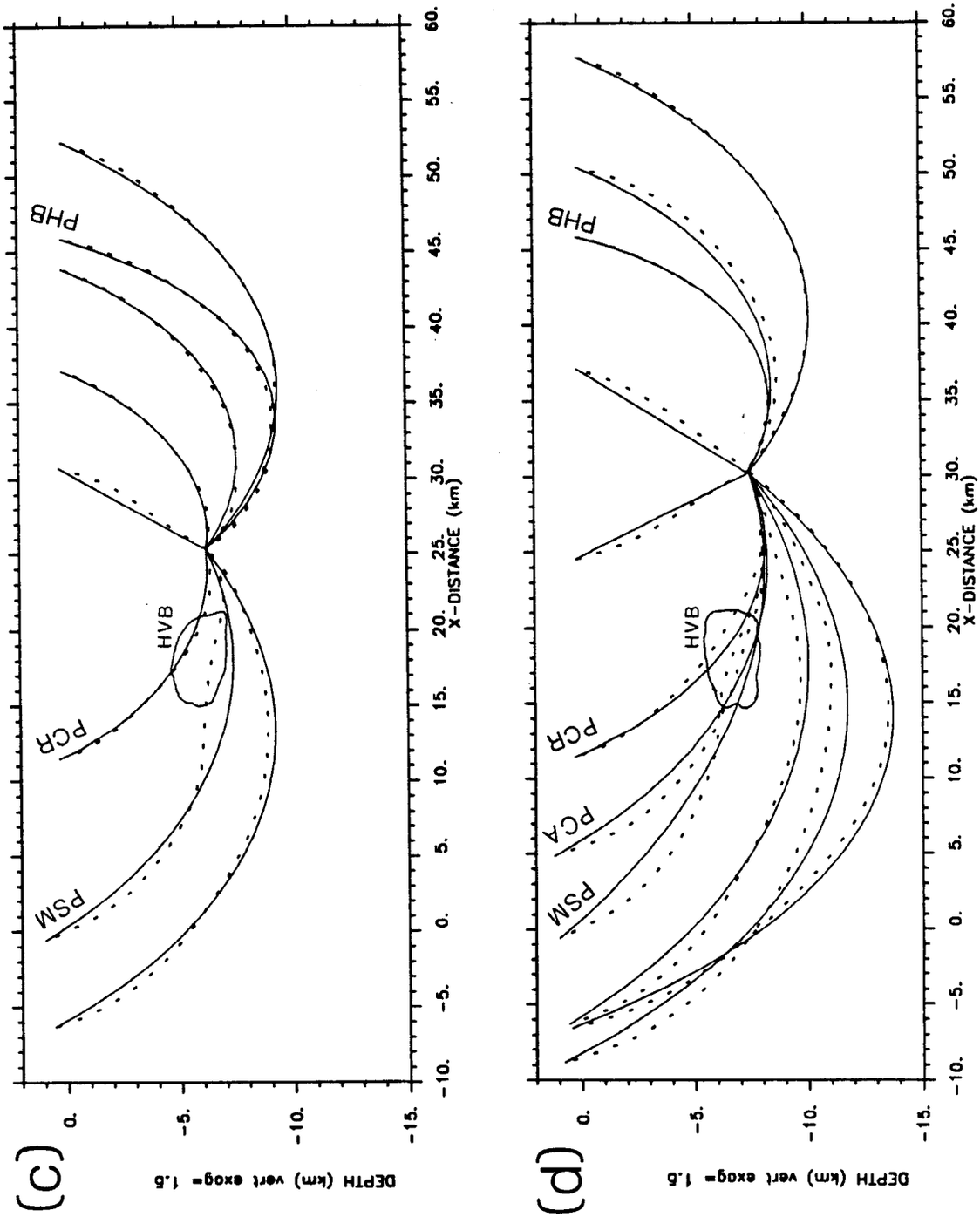

Figure 4 continued. (c) and (d) SW to NE cross-sections for earthquakes (a) and (b), respectively; can be compared to velocity cross-sections (Figures 14d and 14f, respectively). Only ray paths with azimuths within 30° of cross-section are shown. The location of the high-velocity body (HVB) is indicated by the 6.0 km/s contour from Figure 14.

Figure 4 continued. (e) Map view of ray paths for refraction shot. (f) NW to SE cross-section for shot (e). Compare to velocity cross-section Figure 15a.

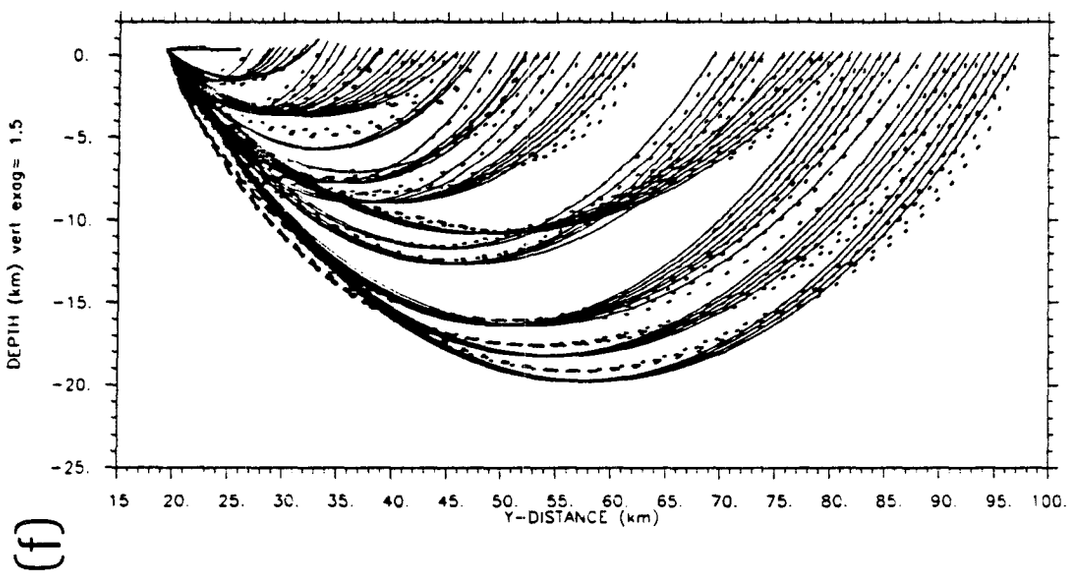

(f)

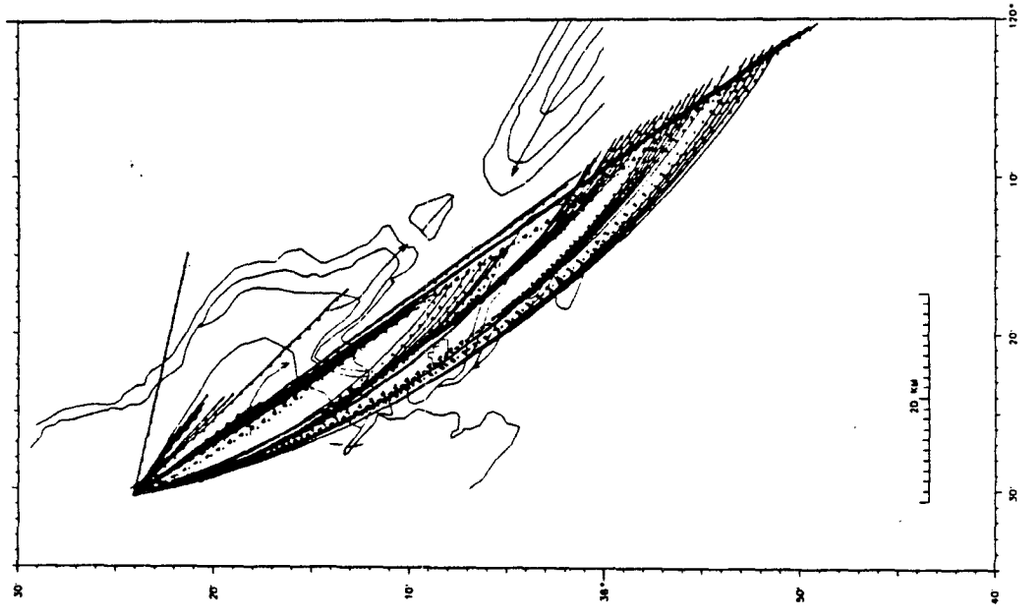

(e)

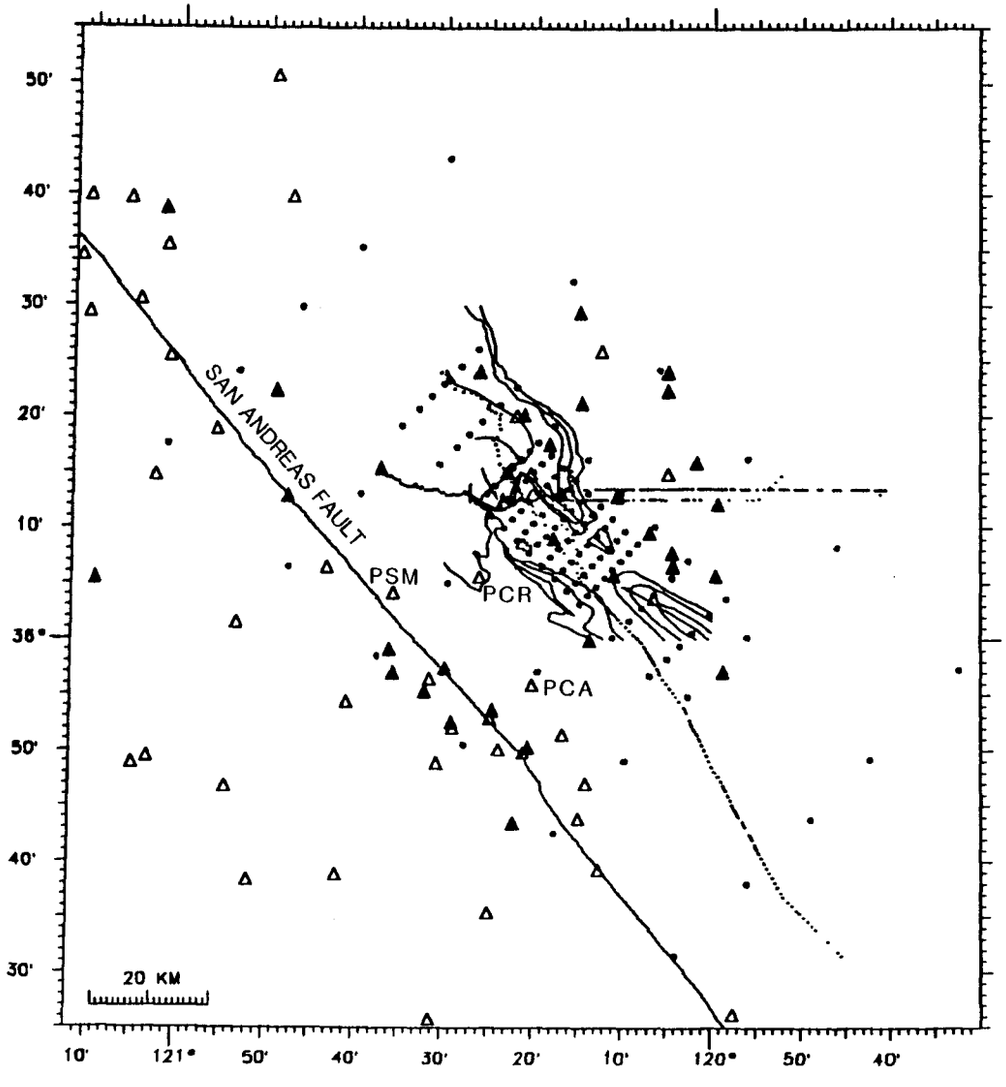

△ Station
▲ 3-Component Station
Refraction Array
• Velocity Gridpoint

Figure 5. Map of stations, along with geologic basemap from Figure 1 and gridpoints for velocity inversion.

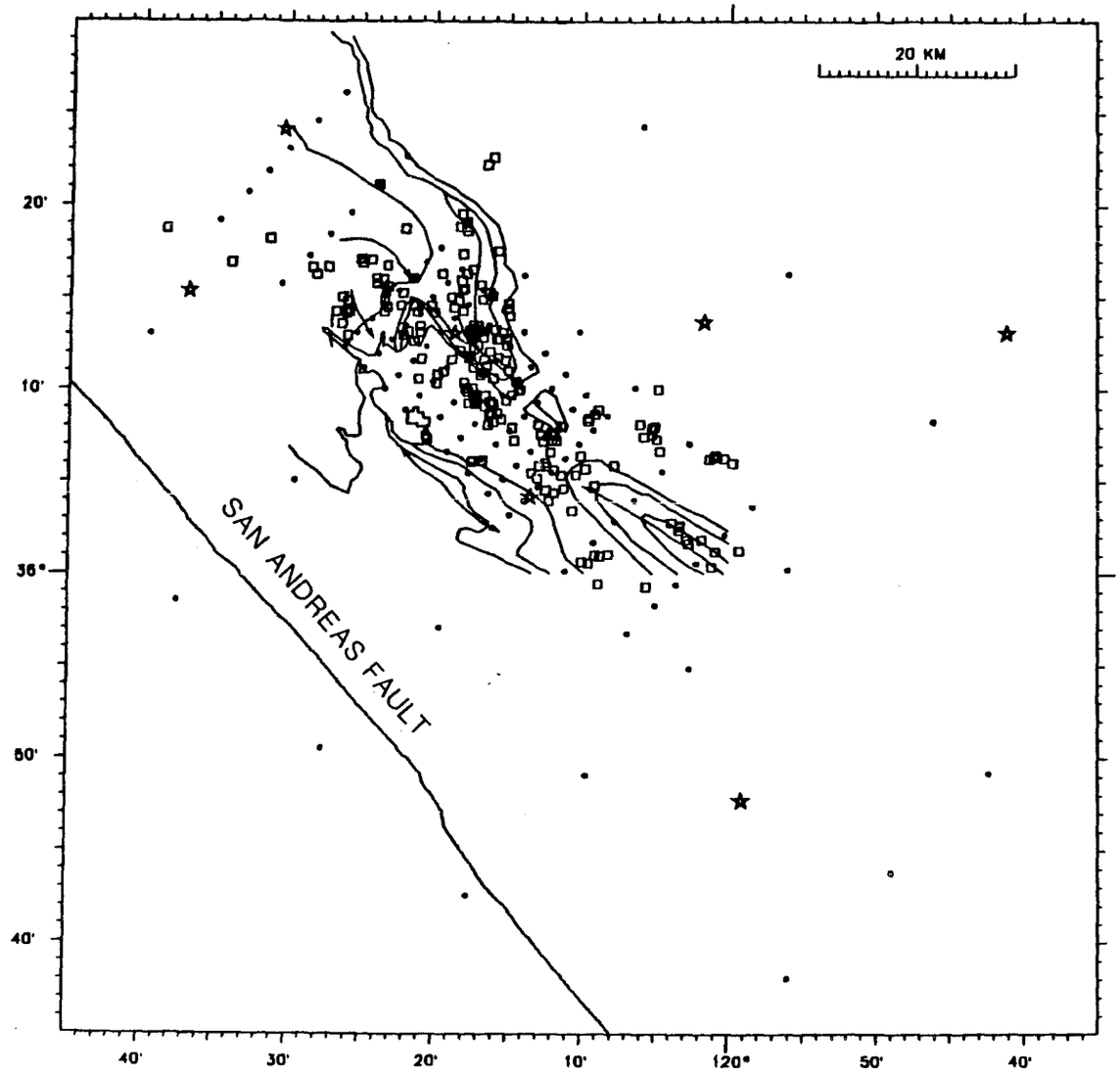

- Earthquake
- ★ Refraction Shot
- • Velocity Gridpoint

Figure 6. Map of earthquakes (squares) and refraction shots (stars) used for velocity inversion, with geologic basemap from Figure 1 and velocity gridpoints.

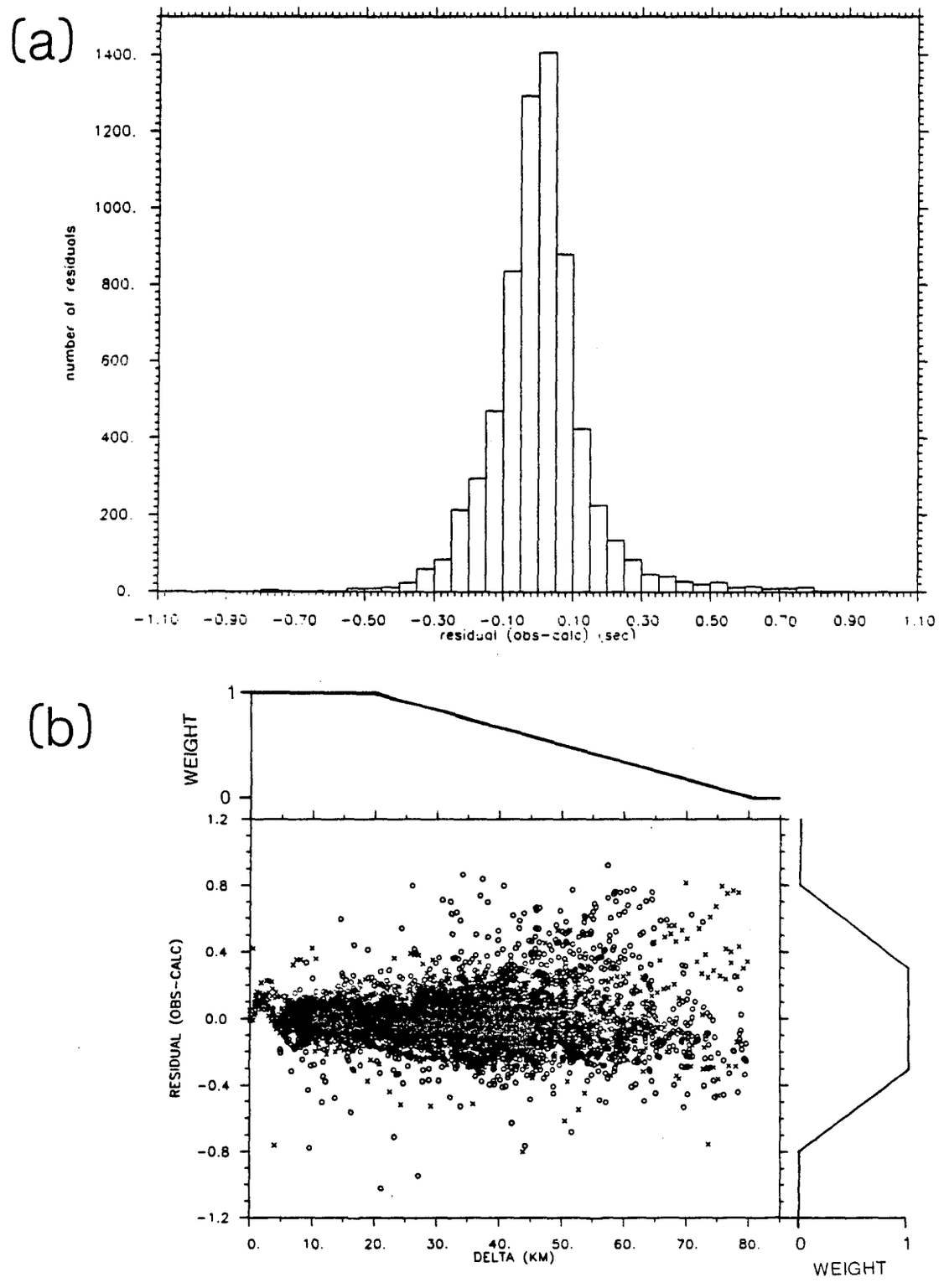

Figure 7. Travel-time residuals for run E (Table 1), observed minus calculated. (a) Histogram. (b) Residuals from earthquakes (circles) and shots (X's) plotted versus source-receiver distance. Also shown is the weighting used, where data from long distances or with high residuals are downweighted.

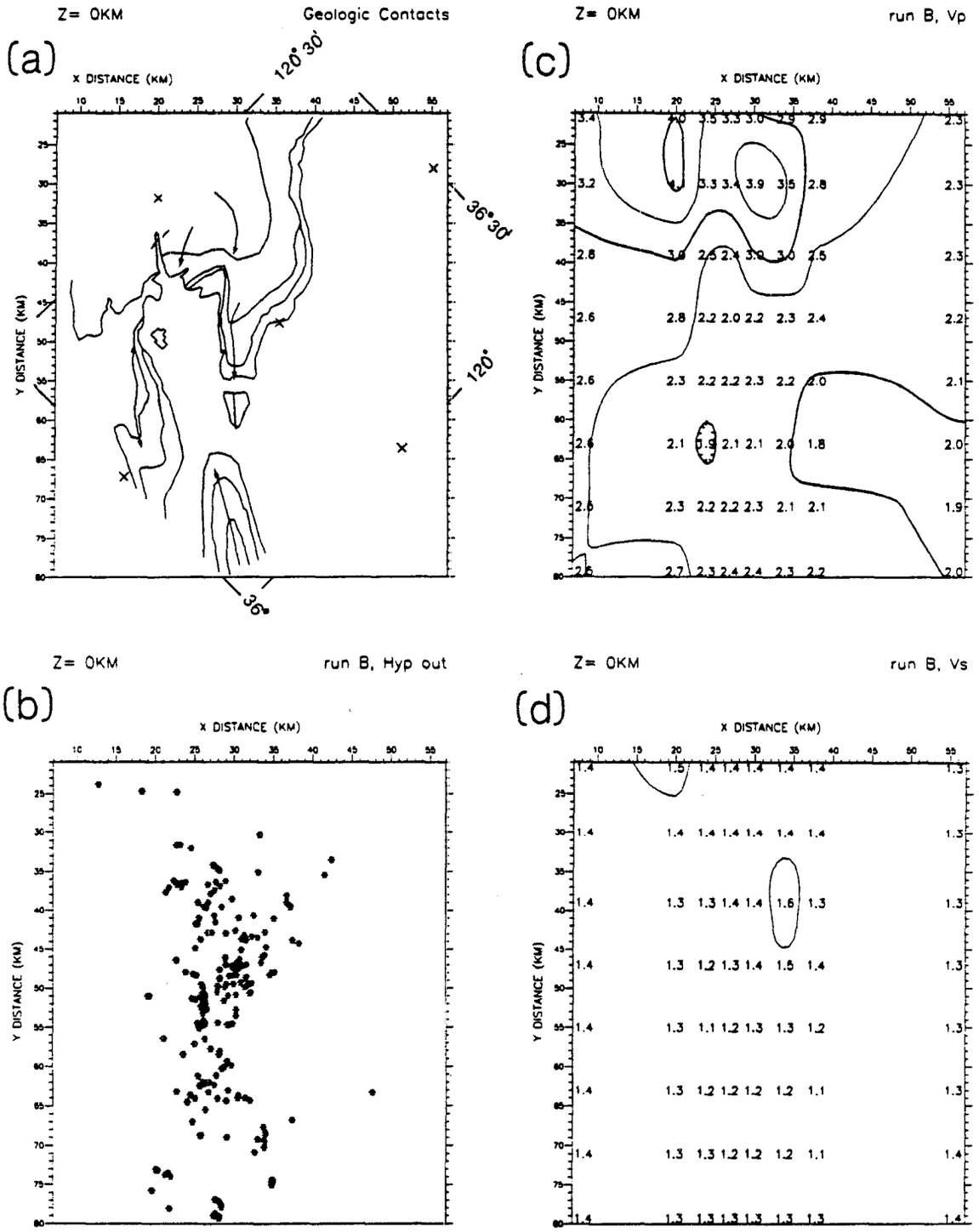

Figure 8. Map views of medium-scale velocity solution, run B (Table 1), with small-scale Vp solution, run E, in the central area from z=6 to 9 km. For reference (a) shows the geologic basemap and (b) shows the earthquakes used in the inversion. Other plots show, for specified depths of the velocity grid, the Vp solution above and Vs solution below. Contour intervals are 0.5 km/s for Vp and 0.25 km/s for Vs. (c) and (d) z=0 km, (e) and (f) z=3 km, (g) and (h) z=6 km, (i) and (j) z=9 km, (k) and (l) z=12 km.

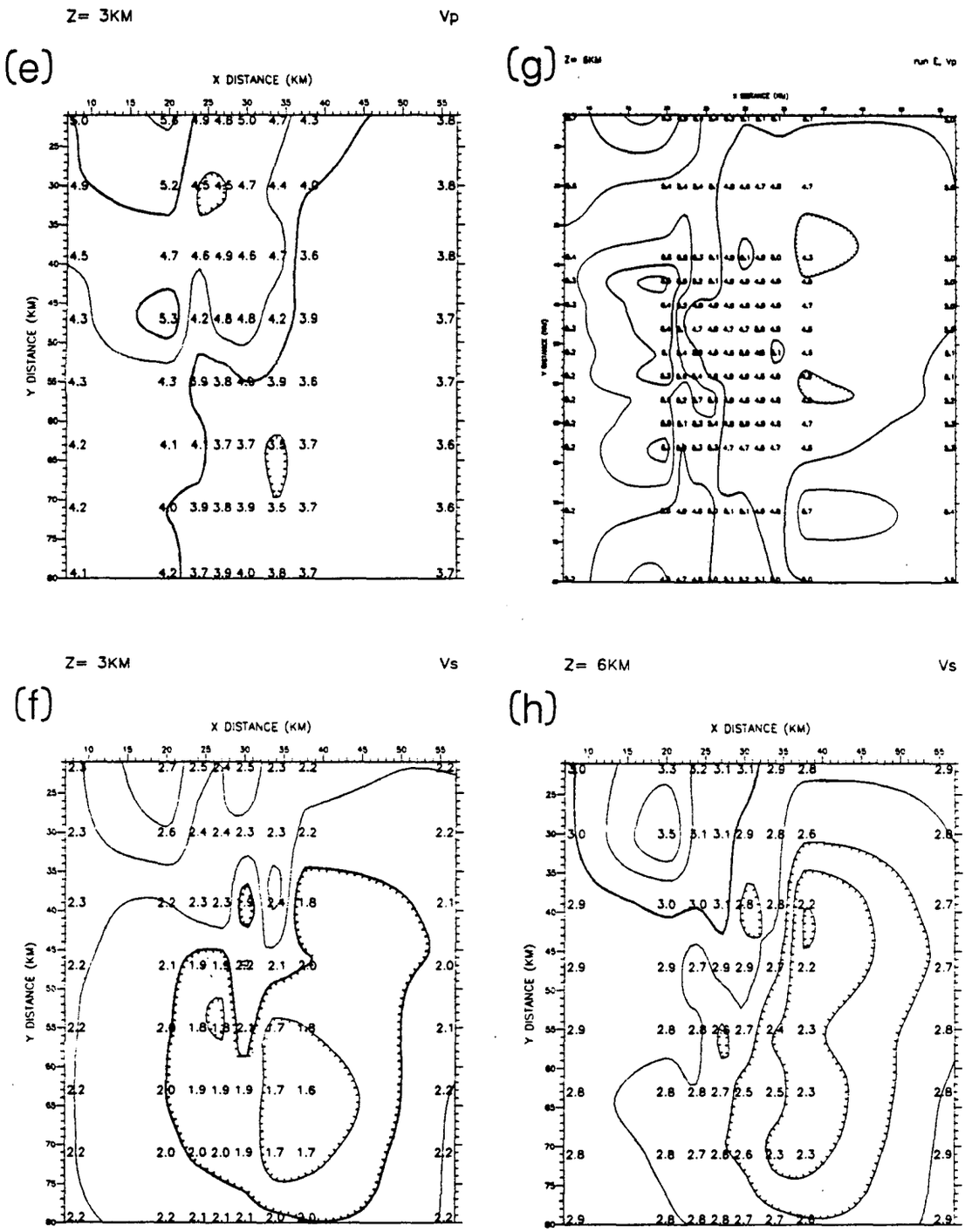

Figure 8 continued.

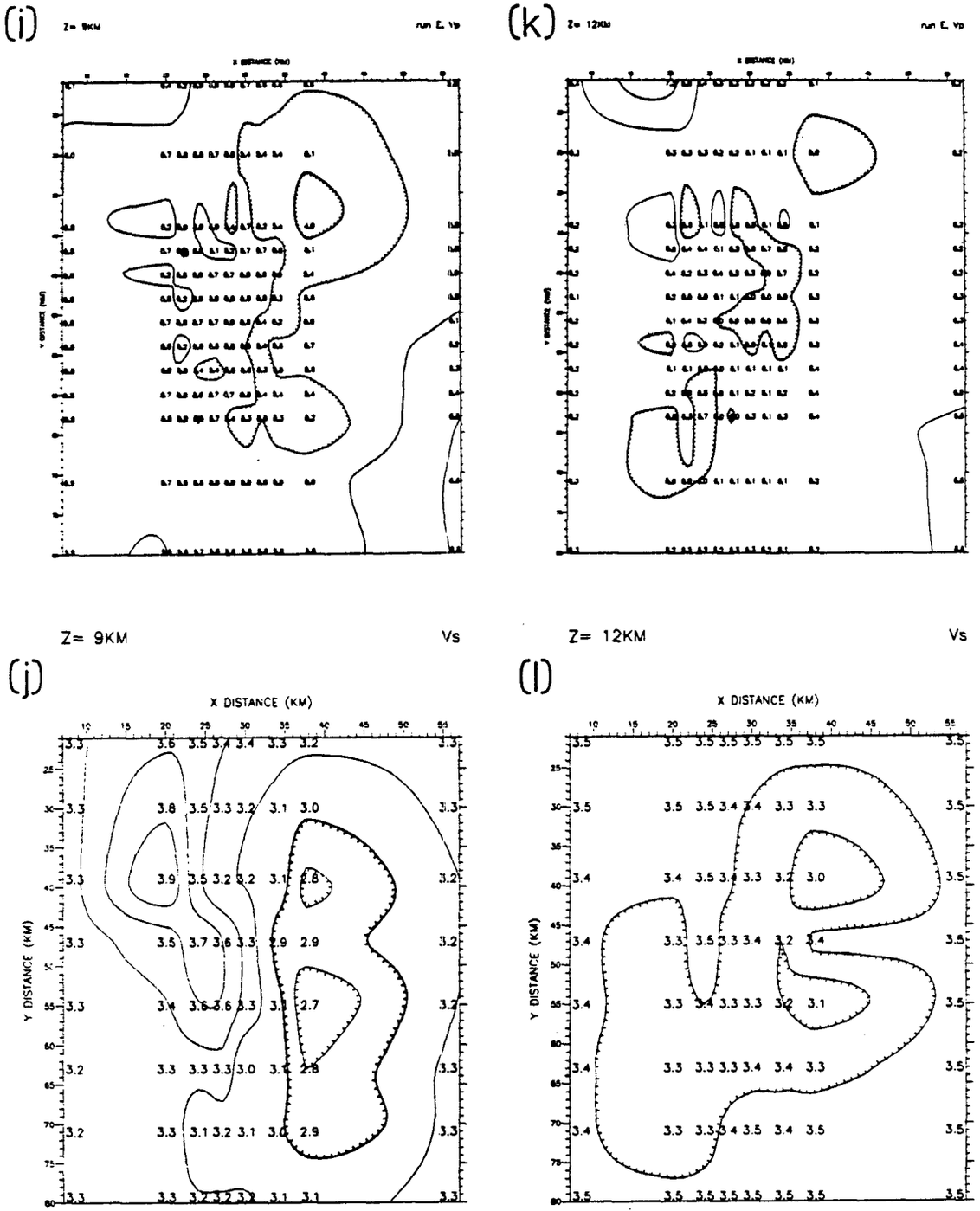

Figure 8 continued.

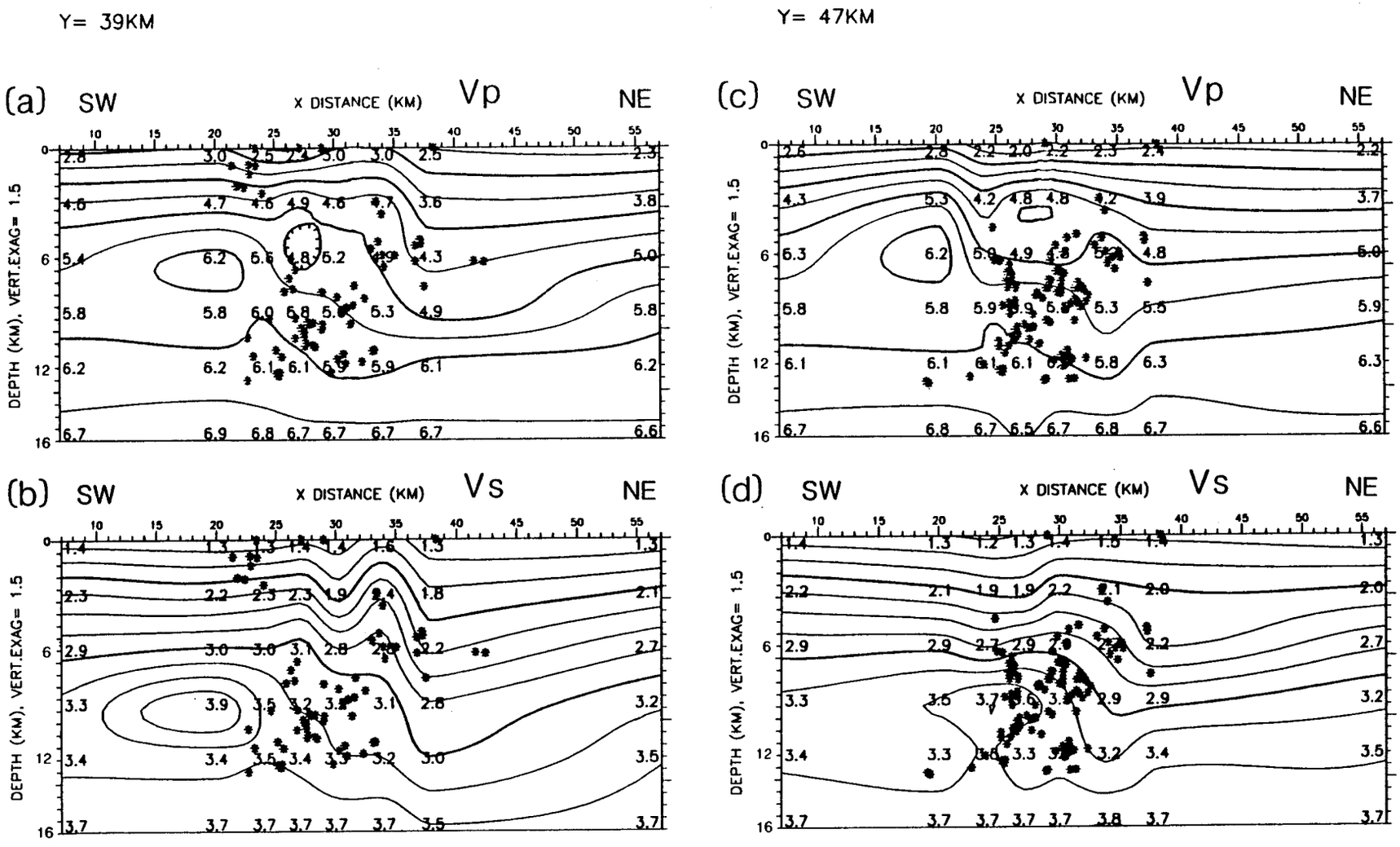

Figure 9. Cross-sections across anticline of medium-scale velocity solution B with Vp above and Vs below. Contour intervals are 0.5 km/s for Vp and 0.25 km/s for Vs. Vertical exaggeration is 1.5 and hypocenters within 1 gridpoint are plotted. x and y coordinates like in Figure 8. (a) and (b) y=39, (c) and (d) y=47, (e) and (f) y=55, (g) and (h) y=63.

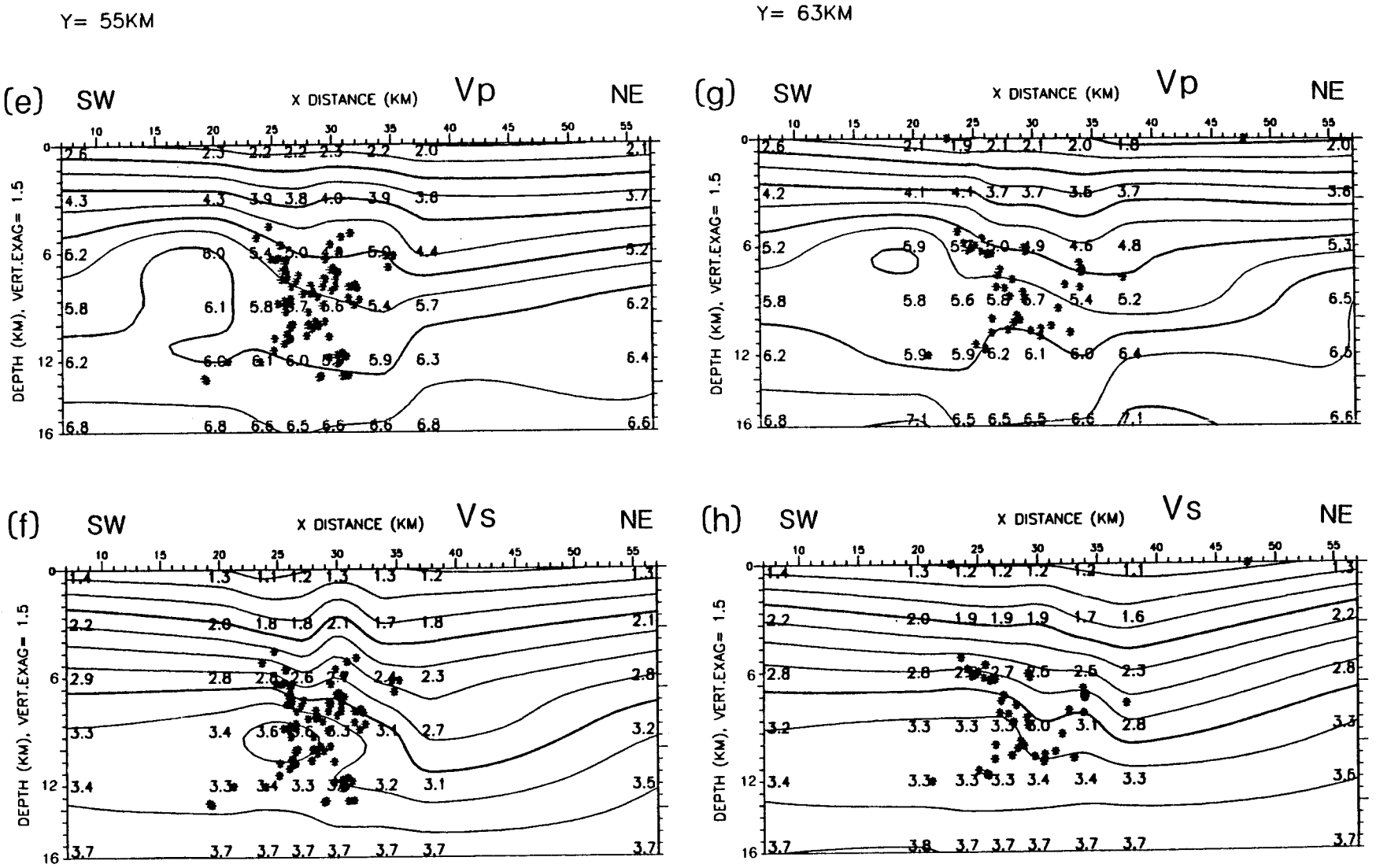

Figure 9 continued.

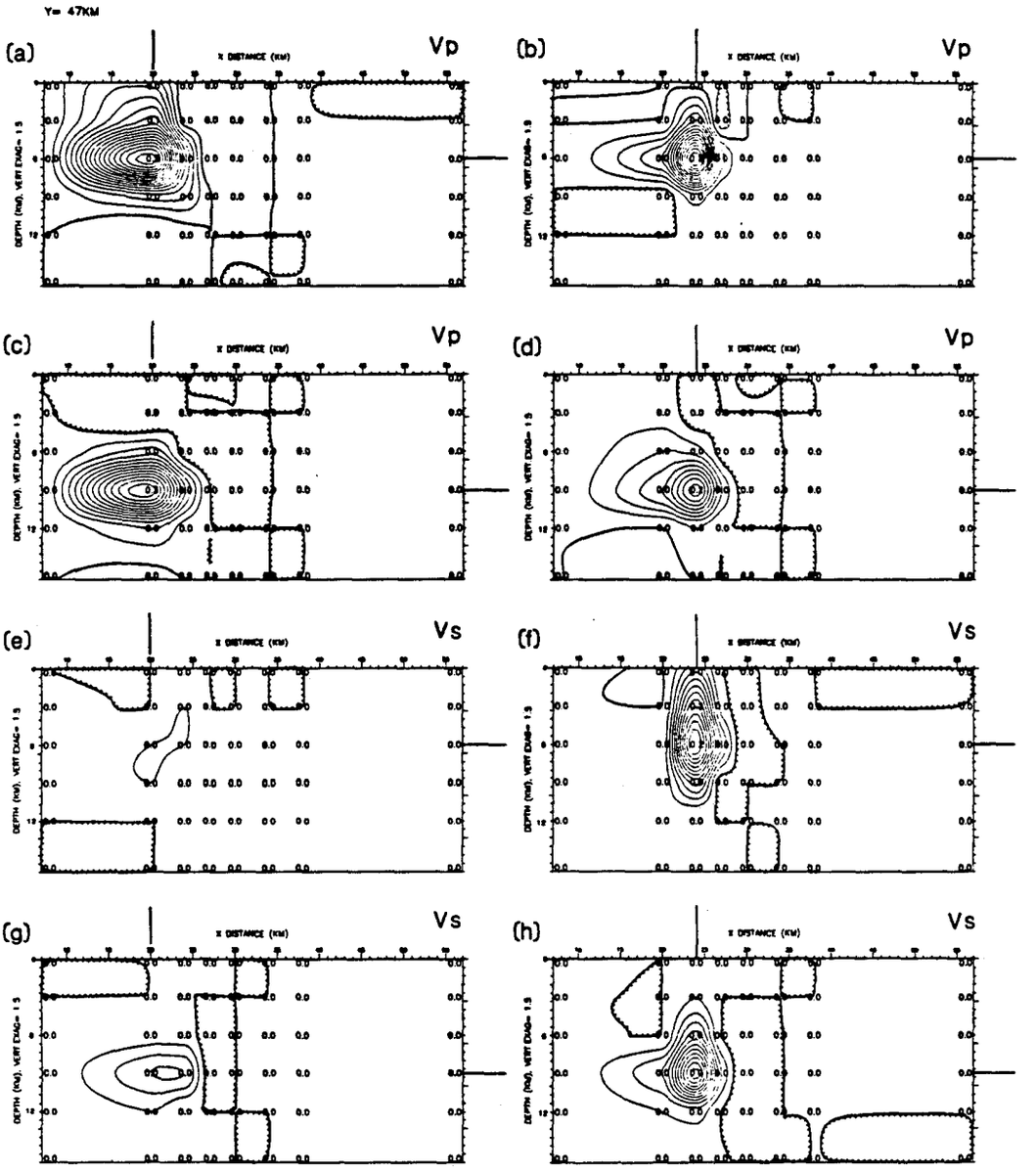

Figure 10. Plots of portions of the resolution matrix for run B. (a) For the resolution row that corresponds to the Vp target point at x=20, y=47, z=6 (indicated by heavy lines at the top and right of the plot, which point to the diagonal element); those elements that correspond to gridpoints in the y=47 cross-section are plotted and contoured. (b) Vp, x=24, y=47, z=6; (c) Vp, x=20, y=47, z=9; (d) Vp, x=24, y=47, z=9; (e) Vs, x=20, y=47, z=6; (f) Vs, x=24, y=47, z=6; (g) Vs, x=20, y=47, z=9; (h) Vs, x=24, y=47, z=9.

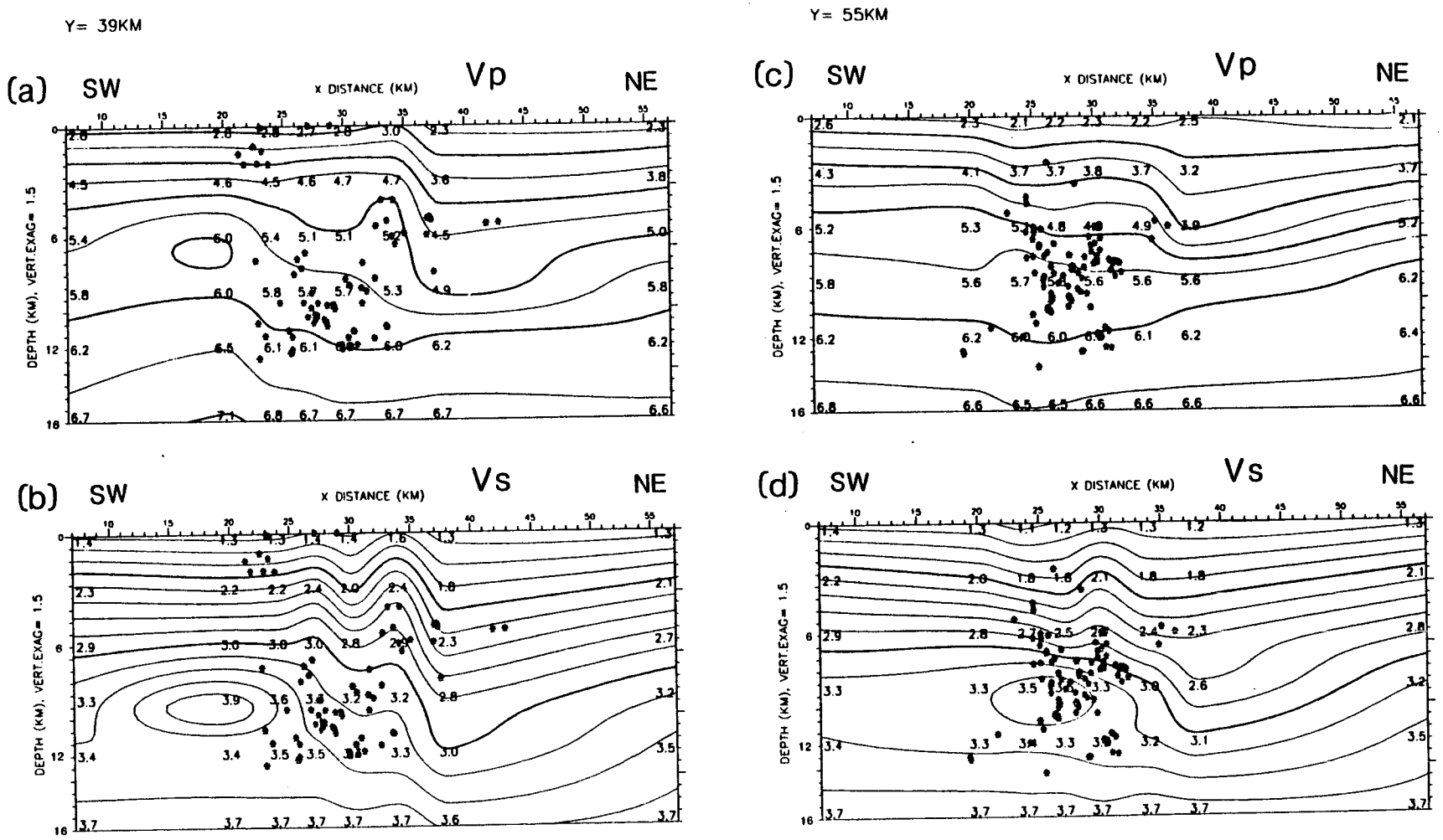

Figure 11. Cross-sections of velocity solution, run C, which only uses S stations. (a) and (b) y=39, (c) and (d) y=55.

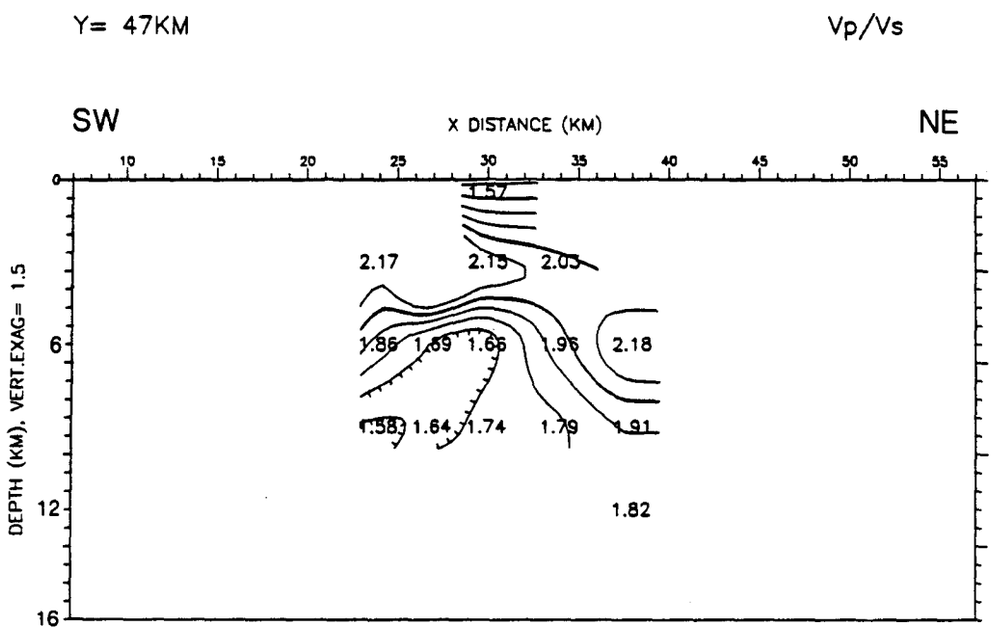

Figure 12. Plot of Vp/Vs ratio for cross-section y=47 (compare to Figure 9c,d). Only those gridpoints are shown that have adequate resolution, diagonal element greater than 0.15 for both Vp and Vs. Contour interval is 0.1.

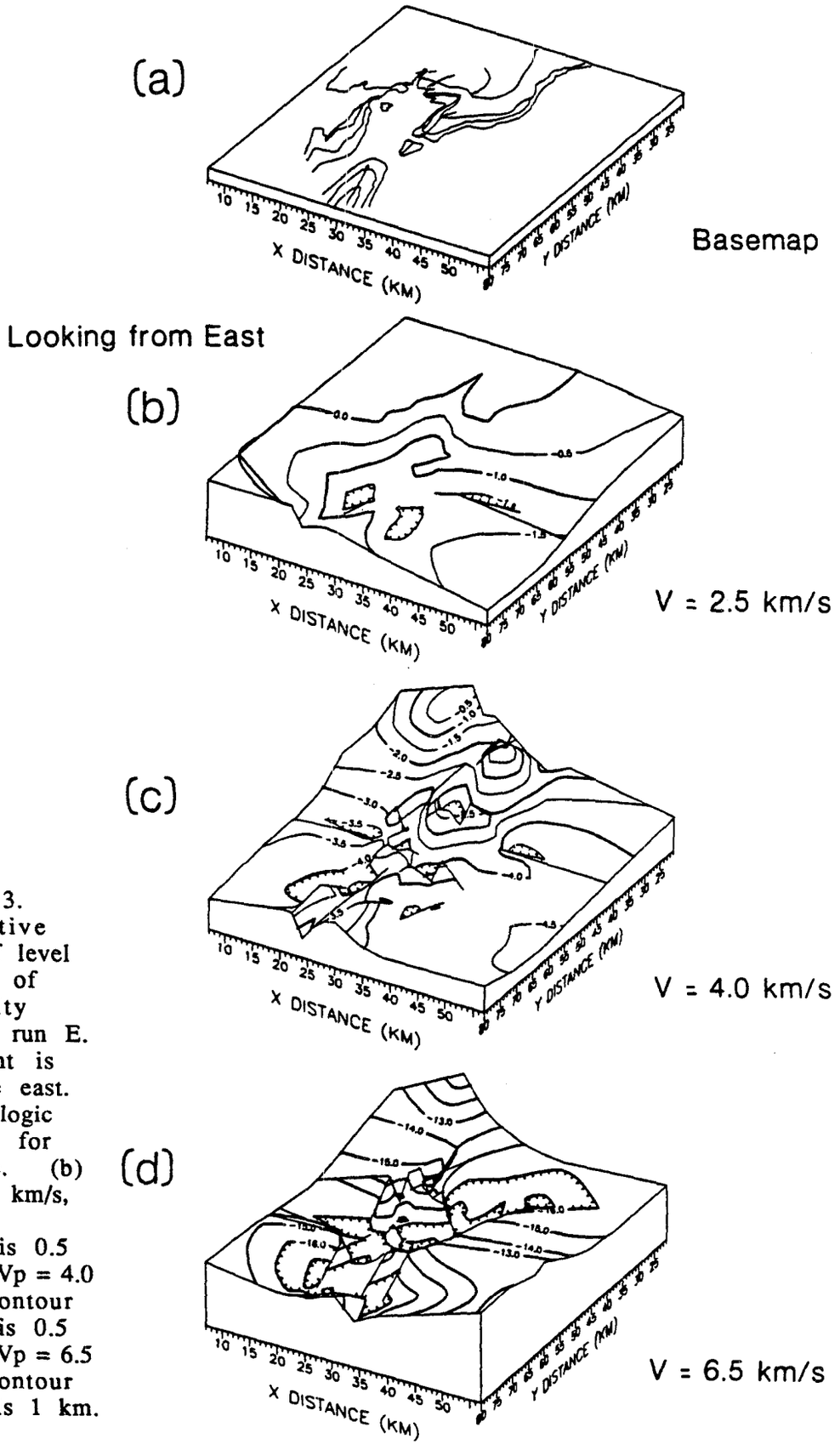

Figure 13. Perspective views of level surfaces of P-velocity solution, run E. Viewpoint is from the east. (a) Geologic basemap for reference. (b) Vp = 2.5 km/s, contour interval is 0.5 km. (c) Vp = 4.0 km/s, contour interval is 0.5 km. (d) Vp = 6.5 km/s, contour interval is 1 km.

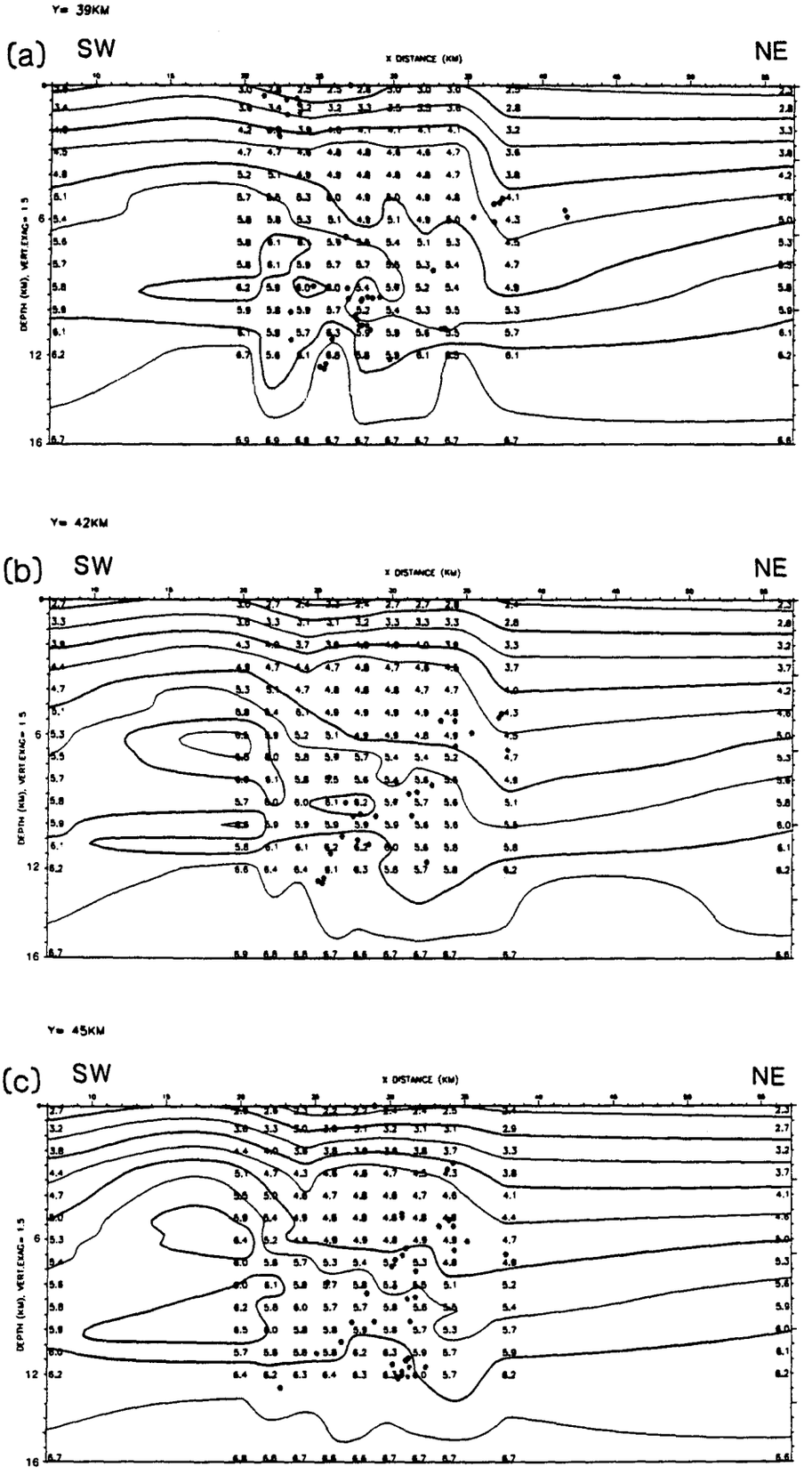

Figure 14. Cross-sections across anticline from SW to NE of small-scale velocity solution, run E (Table 1). Contour interval is 0.5 km/s, vertical exaggeration is 1.5 and hypocenters within 1 gridpoint are plotted on each section. Note that horizontal x and y coordinates correspond to those in Figure 13. (a) y=39, (b) y=42, (c) y=45, (d) y=48, (e) y=51, (f) y=54, (g) y=57, (h) y=60, (i) y=63.

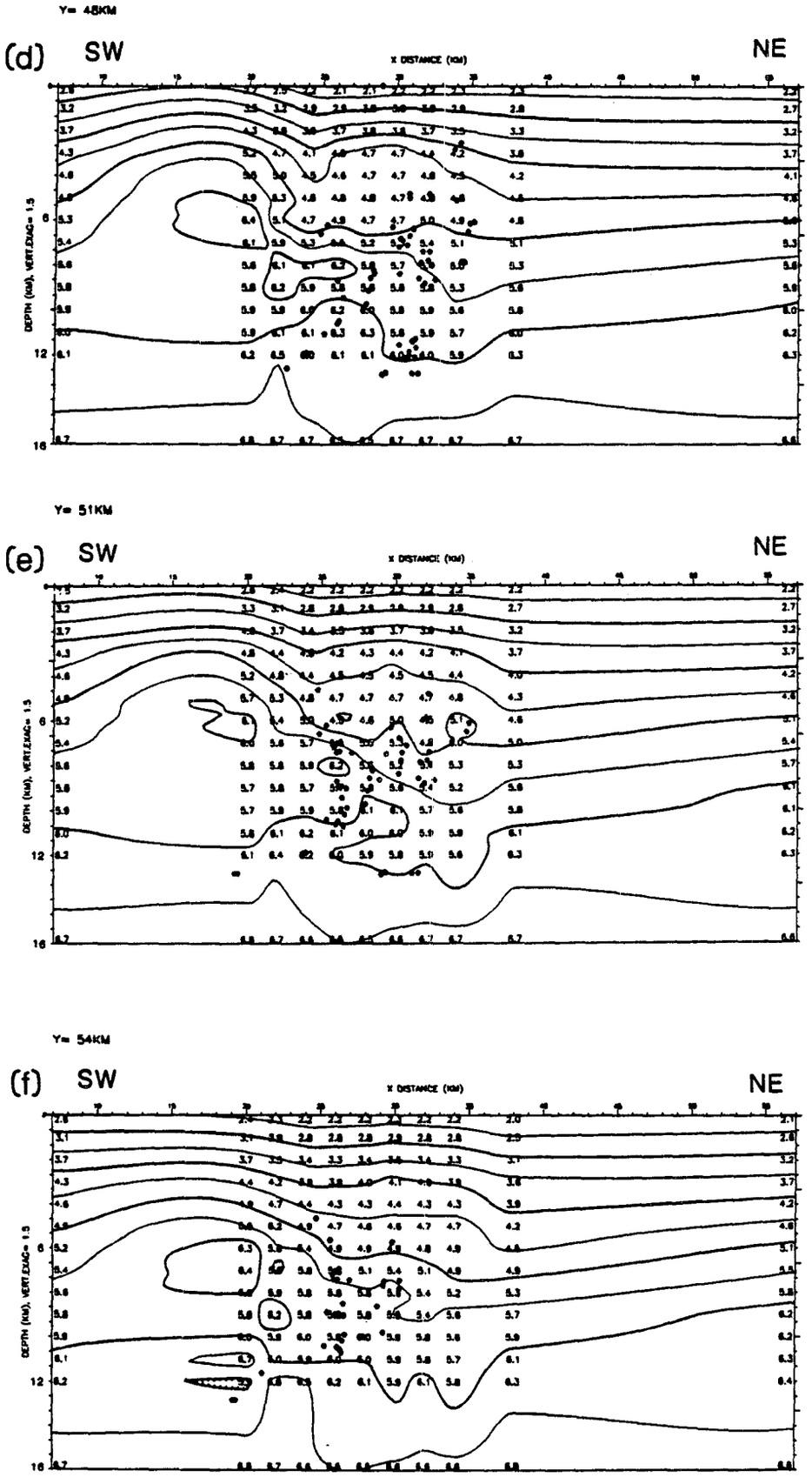

Figure 14 continued.

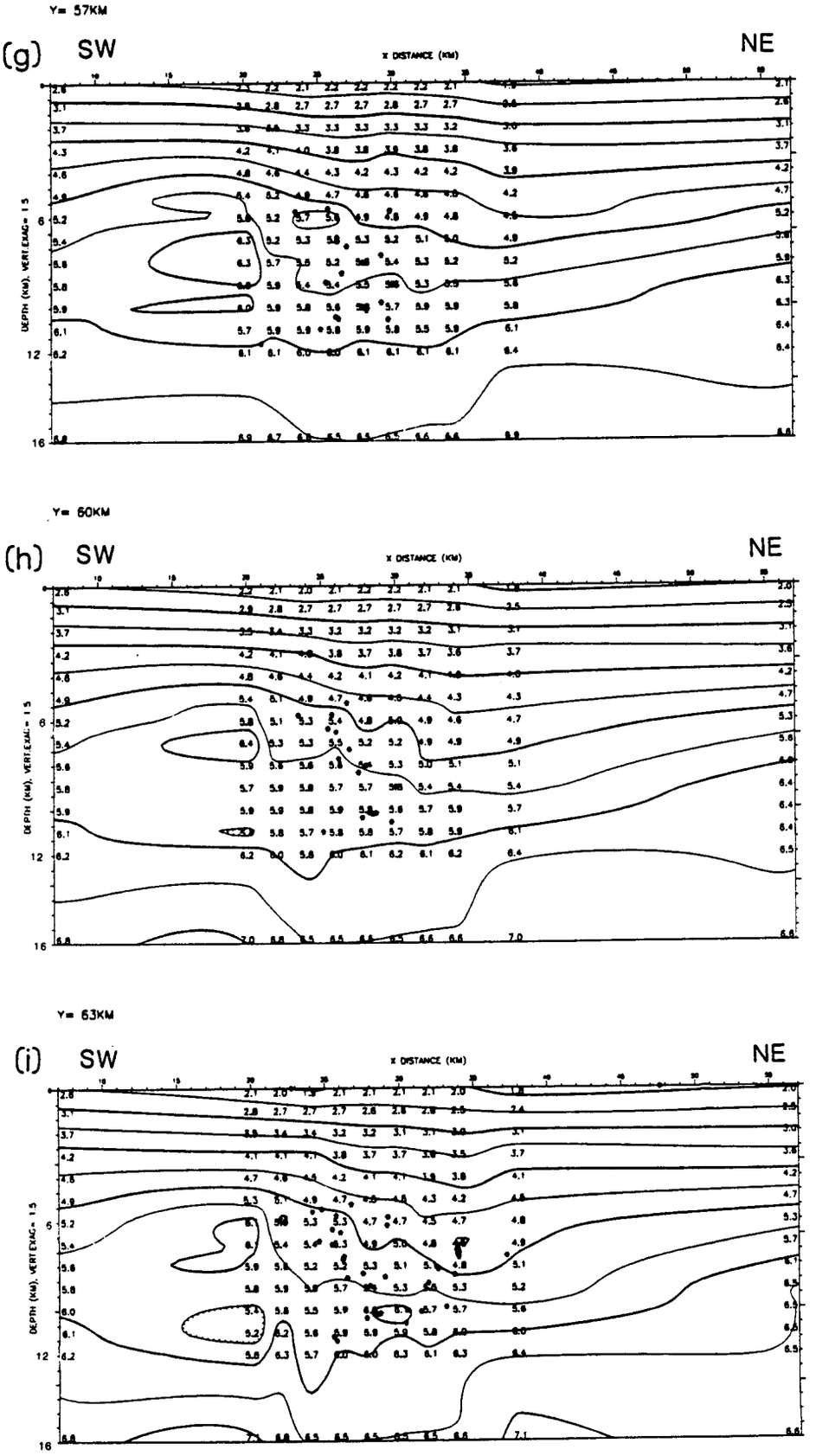

Figure 14 continued.

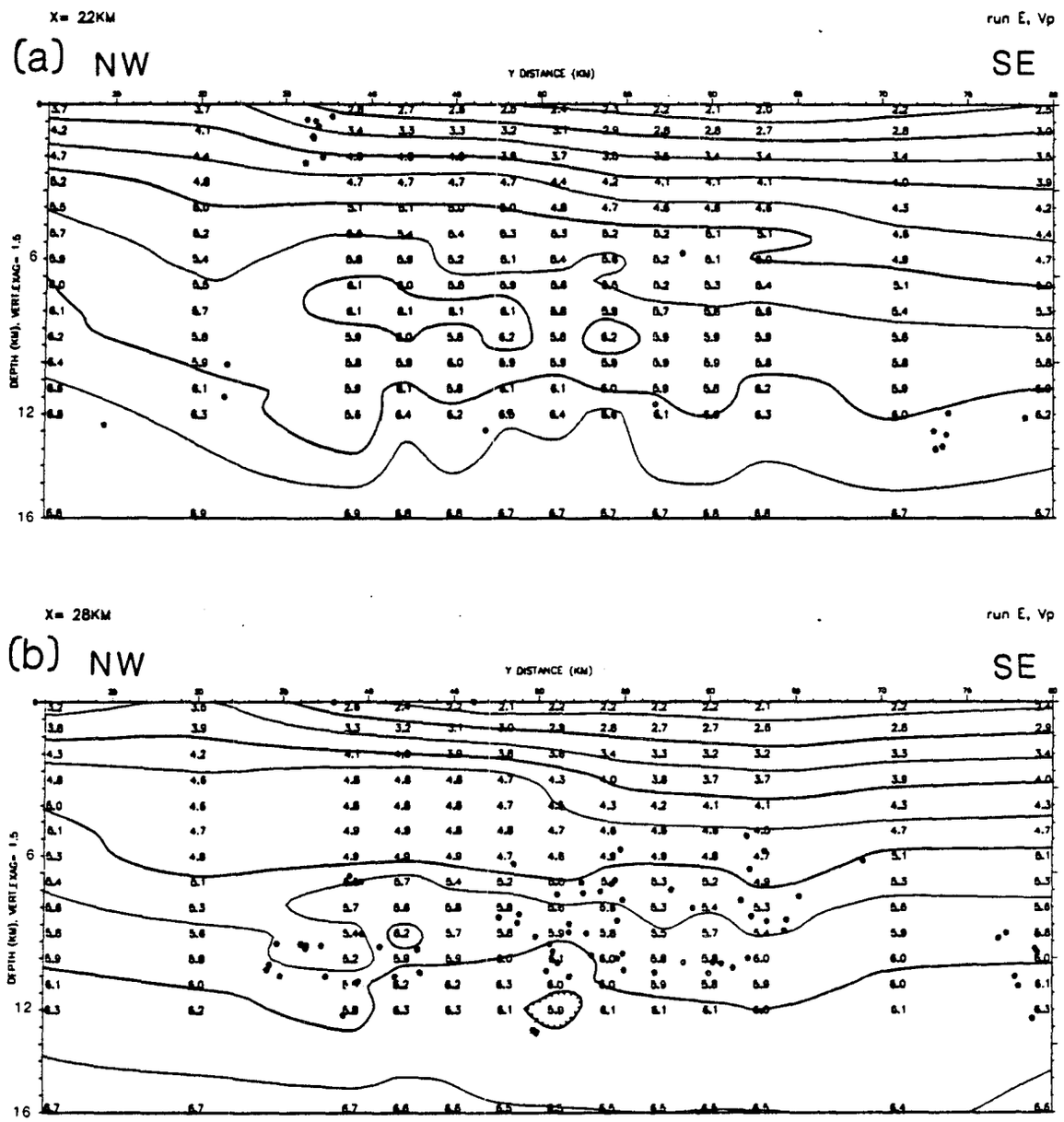

Figure 15. Cross-sections along anticline from NW to SE of small-scale velocity solution, run E (Table 1). Contour interval is 0.5 km/s, vertical exaggeration is 1.5 and hypocenters within 1 gridpoint are plotted on each section. Note that horizontal x and y coordinates correspond to those in Figures 13, 14. (a) x=22, (b) x=28.

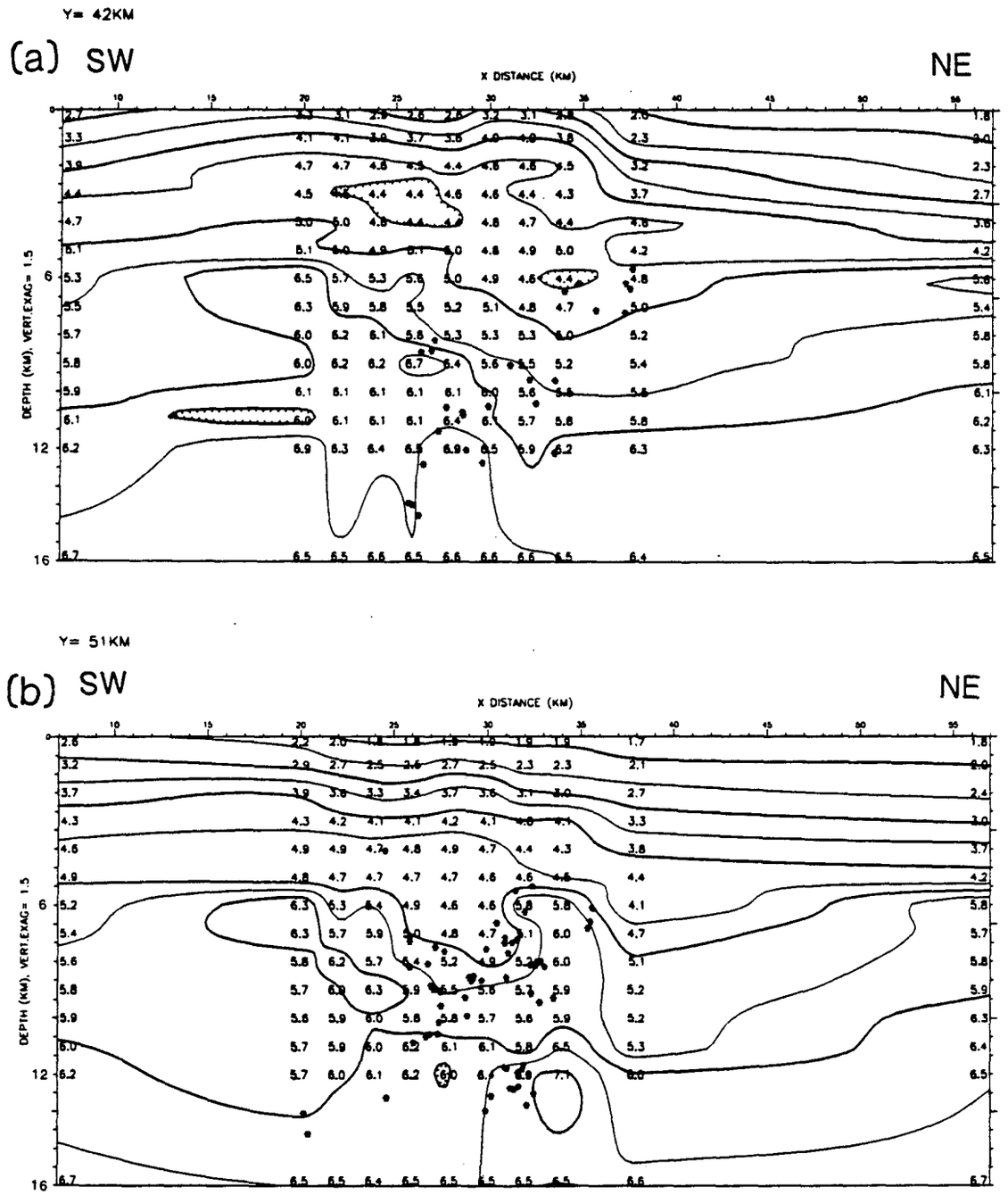

Figure 16. Cross-sections of velocity solution, run F, which uses refraction model velocities. (a) y=42, (b) y=51.

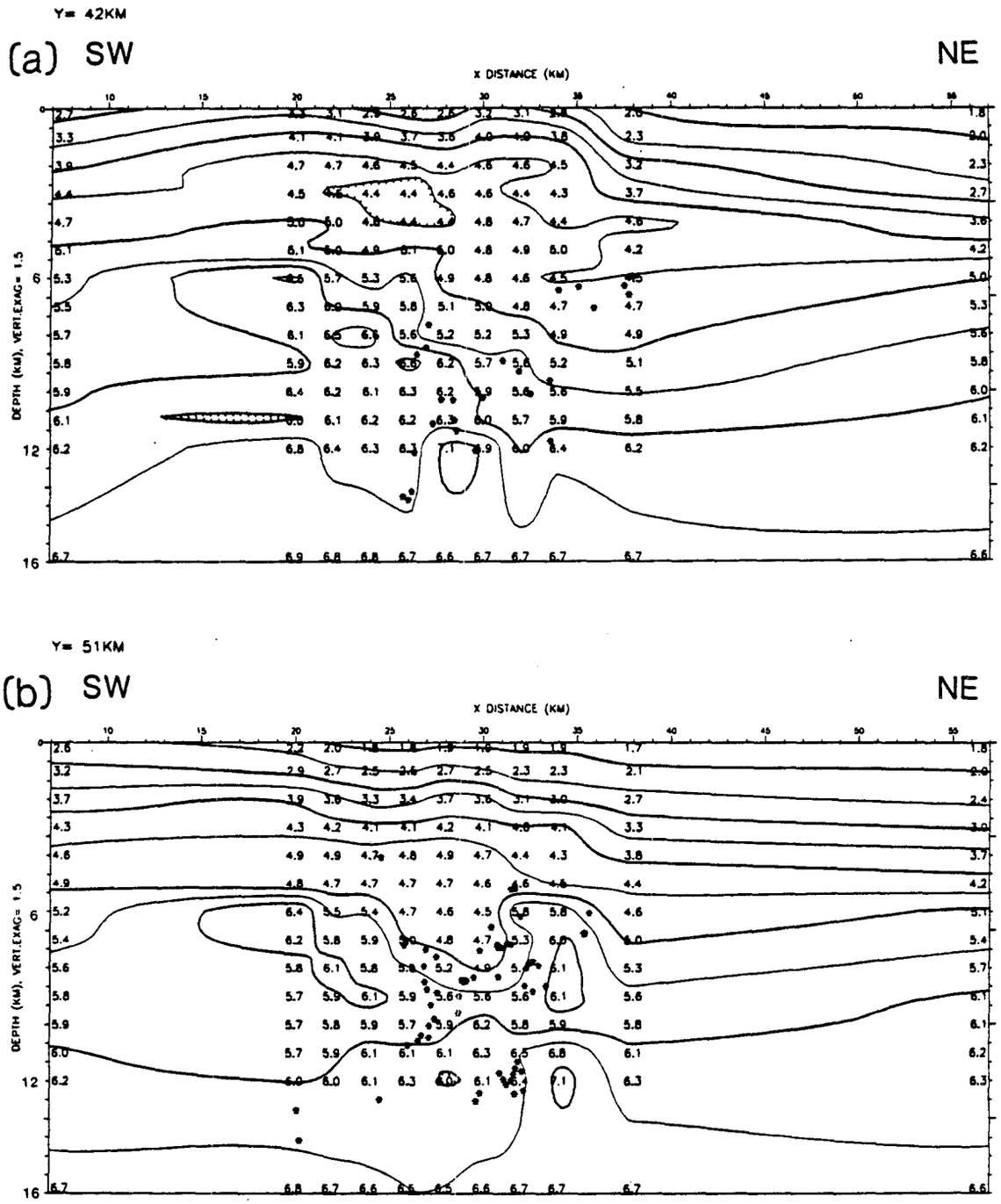

Figure 17. Cross-sections of velocity solution, run G, which uses refraction model velocities for z=0 to 5 km. (a) y=42, (b) y=51.

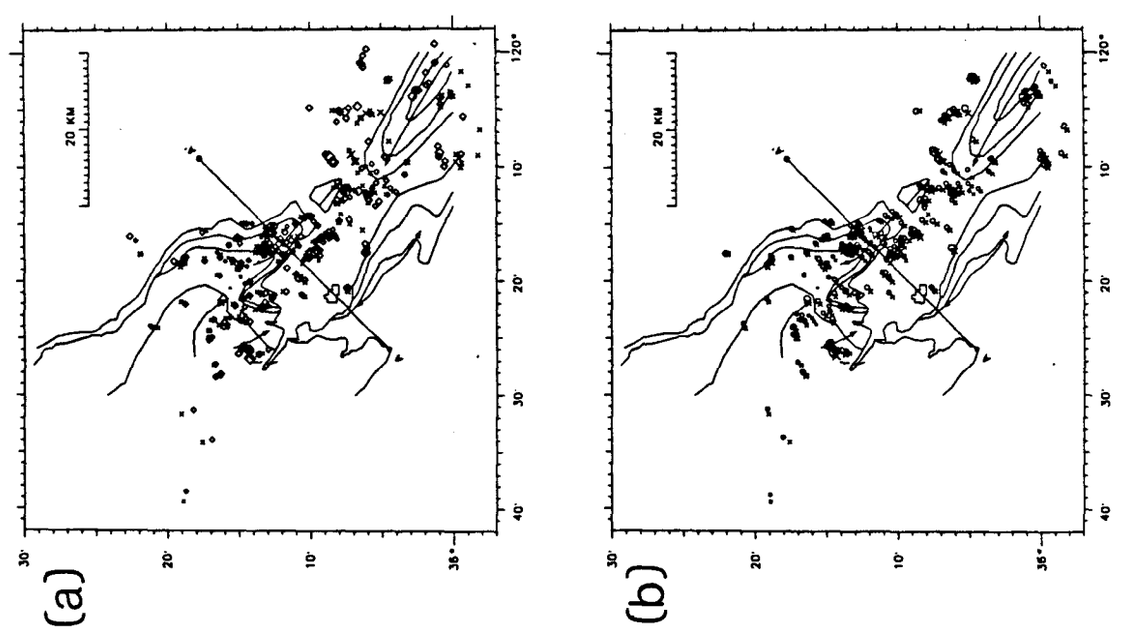

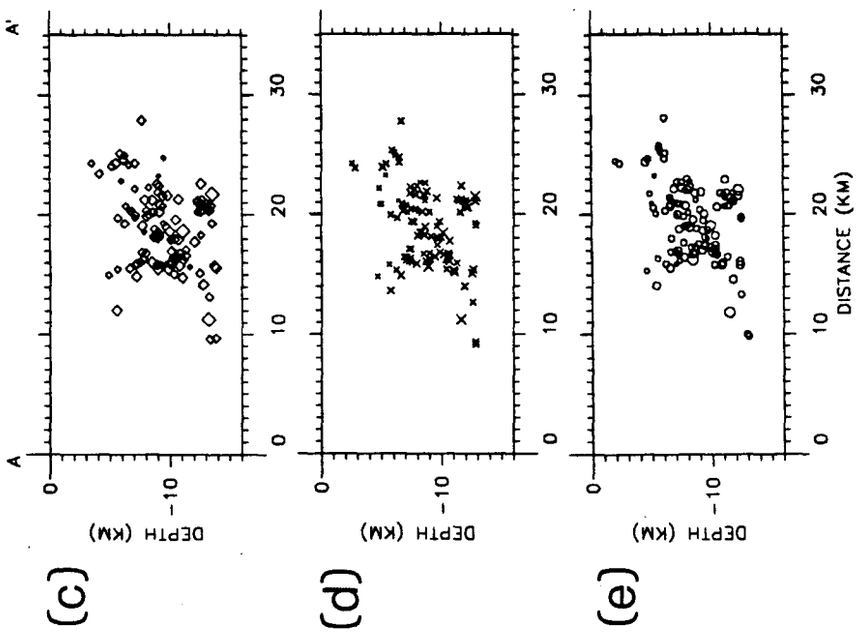

Figure 18. Comparison of hypocenters from 1D velocity model with station corrections (1D, diamonds), 3D velocity model E (X's) and 3D velocity model H with station corrections (circles). Map views with geologic basemap of (a) 1D and E and (b) E and H. Cross-sections across anticline, with hypocenters within 10 km of AA' plotted, (c) 1D, (d) E, (e) H.

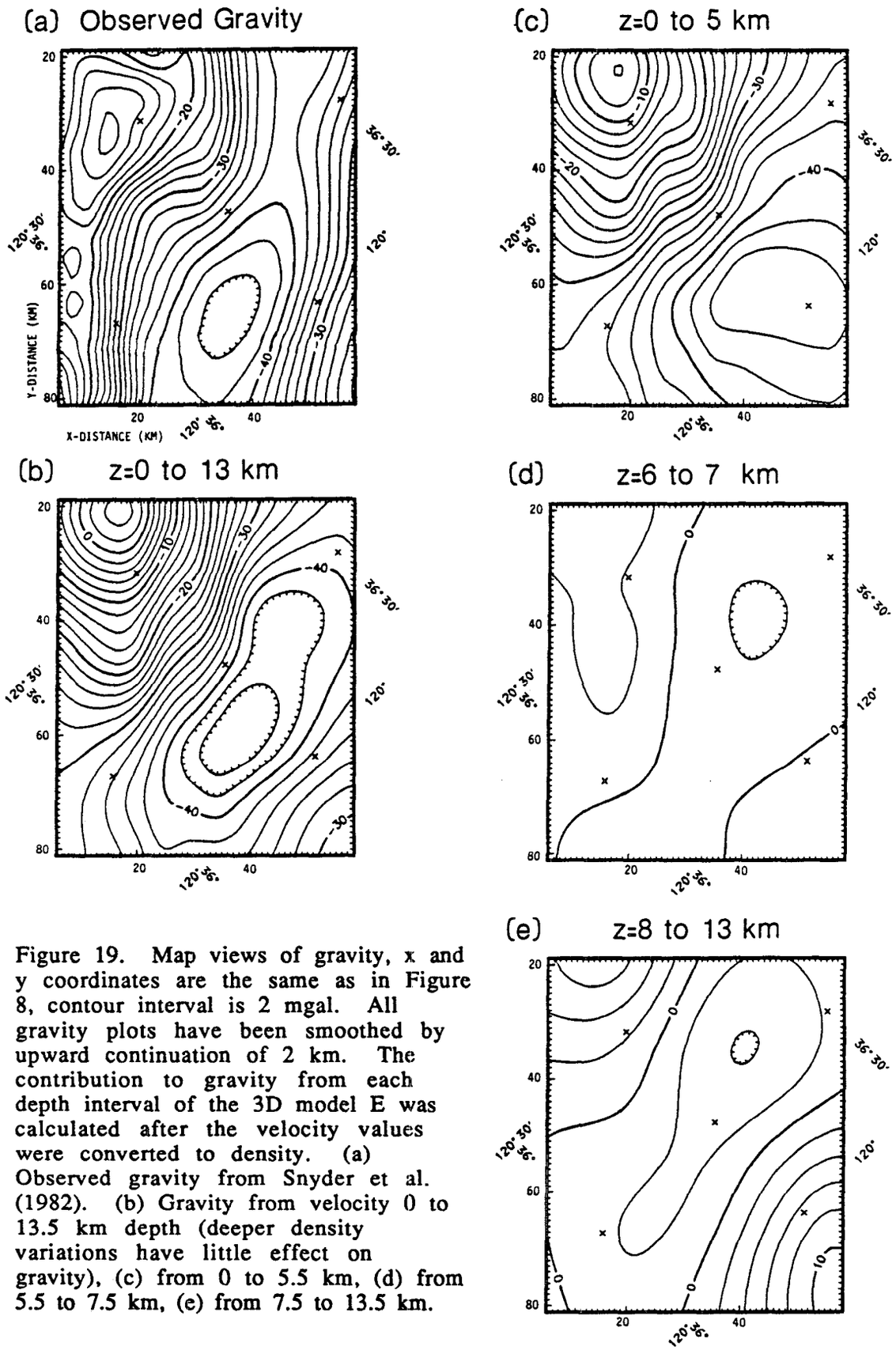

Figure 19. Map views of gravity, x and y coordinates are the same as in Figure 8, contour interval is 2 mgal. All gravity plots have been smoothed by upward continuation of 2 km. The contribution to gravity from each depth interval of the 3D model E was calculated after the velocity values were converted to density. (a) Observed gravity from Snyder et al. (1982). (b) Gravity from velocity 0 to 13.5 km depth (deeper density variations have little effect on gravity), (c) from 0 to 5.5 km, (d) from 5.5 to 7.5 km, (e) from 7.5 to 13.5 km.

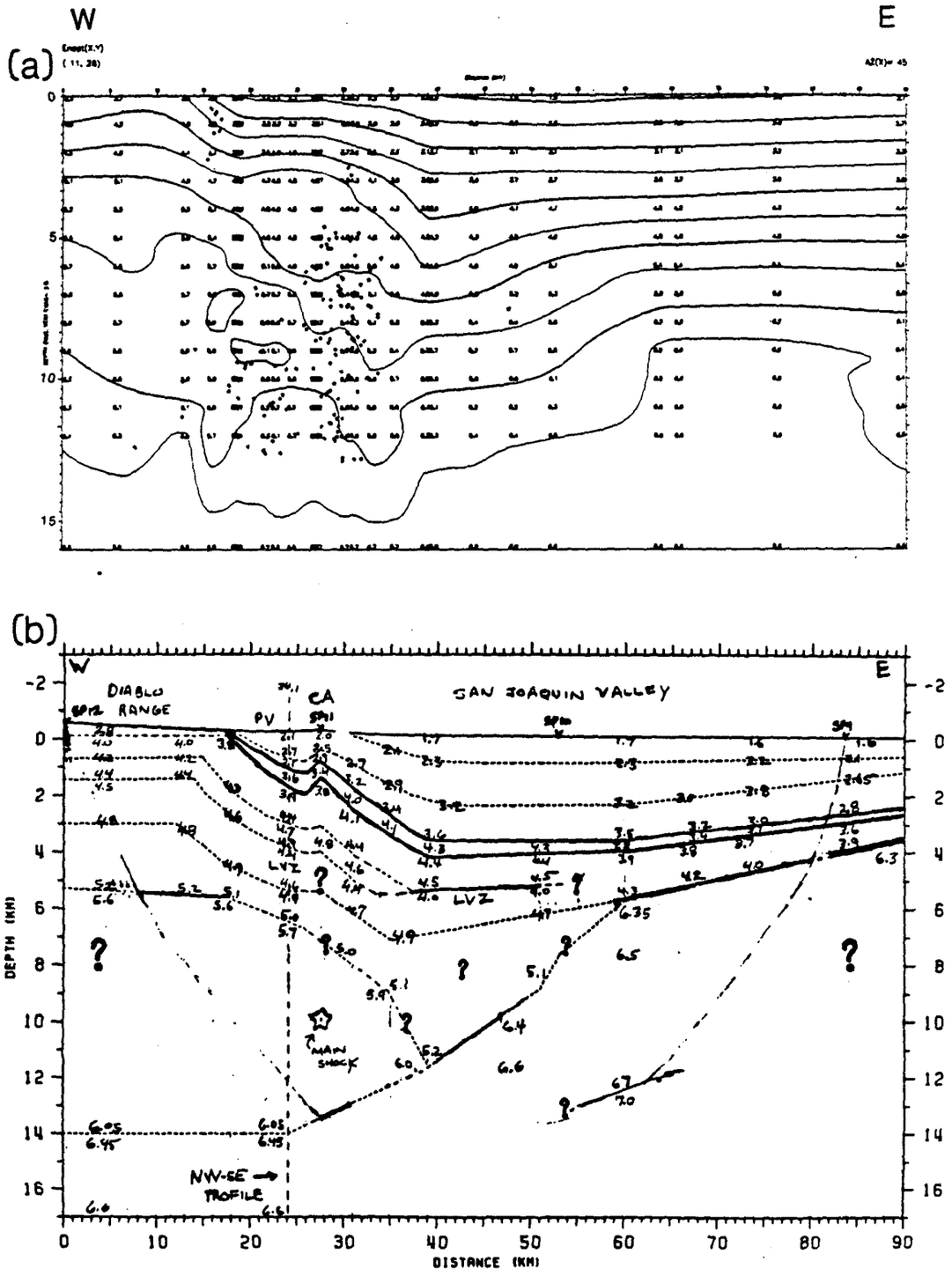

Figure 20. Comparison of 3D velocity solution with refraction model. (a) Model E interpolated along the E-W refraction line (Figure 5), vertical exaggeration is 3 and hypocenters within 10 km are plotted. (b) Refraction model of Walter (1988).

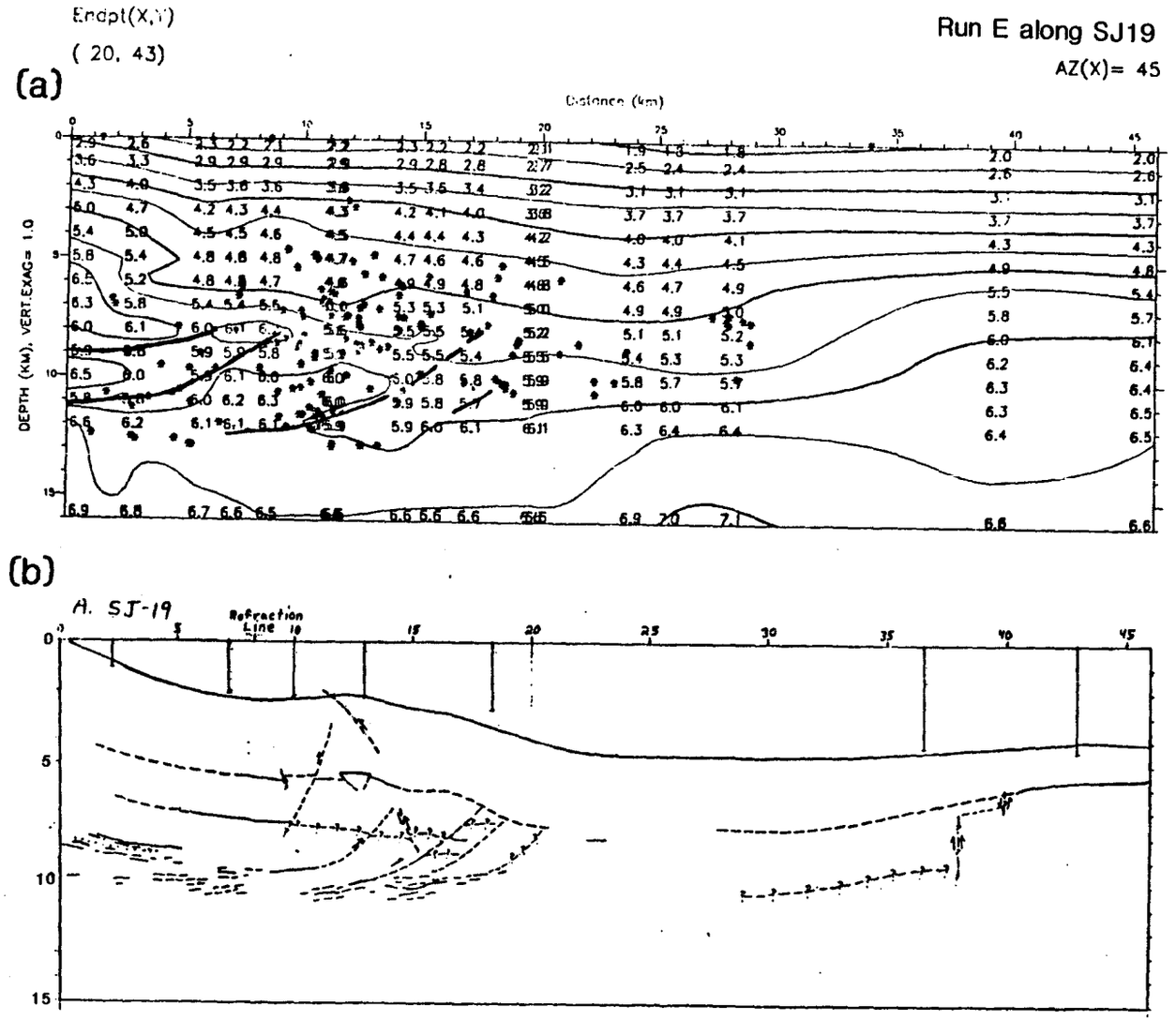

Figure 21. Comparison of 3D velocity solution with reflection record. (a) Model E interpolated along the E-W reflection line, no vertical exaggeration and hypocenters within 10 km are plotted. Heavy lines are drawn through low-velocity zones. (b) Interpretation of reflection record SJ-19 from Wentworth and Zoback (1988).

Chapter 3.

Active Faulting and Deformation of the Coalinga Anticline as Interpreted from 3D Velocity Structure and Seismicity

ABSTRACT

Interpretation of hypocenters and fault-plane solutions, from the 1983 Coalinga, California, earthquake sequence, in combination with the three-dimensional velocity structure shows that the character of the seismicity varies along the anticline with the amount of previous deformation on each section of the anticline. The faulting structure beneath the fold primarily consists of a set of southwest-dipping thrusts uplifting blocks of higher-velocity material. Above the main thrust there is a conjugate fault, steeply northeast-dipping, that provides the western limit of the aftershocks within the Coalinga Anticline and that corresponds in location and spatial extent with the adjacent Pleasant Valley syncline. Where the previous uplift was largest, the shallow seismicity shows distinct zones of secondary faulting on either side of the fold with orientations that correspond to the pre-existing geologic structure. Where there was relatively little previous deformation, only diffuse seismicity occurs and the velocity structure does not show evidence of uplifted blocks of material since well-defined fault zones have not developed. The mainshock rupture terminated where the fold trend was no longer uniform but had competing north and west-trending features. The upward extent of the mainshock rupture ended at the approximate boundary between the Franciscan and Great Valley Sequence rocks. Above that depth the main southwest-dipping thrust appears to splay into a steeper segment and a near-

horizontal segment. Thus the extent of rupture area is determined by the area of uniform structural orientation and by the type of material.

For this analysis, hypocenters and fault-plane solutions were recomputed using the three-dimensional (3D) velocity model. The main advantage of obtaining 3D hypocenters is the ability to jointly analyze the seismicity and the velocity structure. Each individual hypocenter moved slightly (0 to 2 km) in accord with the details of the surrounding velocity structure, so that some secondary features revealed in the seismicity patterns are more detailed. Taken as a whole, the set of hypocenters did not change in a systematic way from the set computed with a local one-dimensional model and station corrections. The overall character of the fault-plane solutions was not altered by the 3D model, but the 3D ray paths did result in distinct changes. The most systematic change is that the southwest-dipping nodal planes have slightly greater dips; there are few nodal planes that have dips shallower than 30° when the 3D velocity model is used. In particular, the mainshock has a fault plane dipping 30° southwest instead of the 23° obtained with the 1D model.

INTRODUCTION

The three-dimensional velocity model determined from inversion of local earthquake and shot data, as described in Chapter 2, can be used to obtain more accurate earthquake hypocenters and fault-plane solutions for the 1983 Coalinga earthquake sequence. The Coalinga region is of interest both because the mainshock was such a large event, magnitude 6.7, without surface rupture, and because it produced a complex and numerous aftershock sequence (Figure 1). Use of the 3D model may provide new insights into the details of faulting processes along the Coast Ranges / Great Valley margin.

The main features of the 3D velocity model are shown in the cross-section in Figure 2. In the center the uplifted Coalinga Anticline is observed and on the northeast the relatively low-velocity thick sediments of the San Joaquin Valley are shown. The basement is shallowest beneath the San Joaquin Valley and apparently dips down beneath the anticline. Wentworth and Zoback (1989a) have proposed that, rather than a continuous dip of the basement, there is actually a step in the basement northeast of the folds. They further suggest that such a basement discontinuity predetermined the location of the current compressional deformation.

The 3D model shows additional features below the folded sedimentary strata. On the western edge of the Coalinga area, there is a high-velocity body, which may be ophiolite or high-grade metamorphic rock. At 6-km depth, within the sedimentary Great Valley Sequence, there is a low-velocity zone which may be caused by high pore pressure. In the hypocentral zone from 8- to 12-km depth, the velocities range from 5.7 to 6.2 km/s, typical of Franciscan assemblage, but do not show a simple pattern of increased velocity with depth. The velocities vary from high to low so that a pattern of three discontinuous low-velocity zones is observed below the Coalinga Anticline.

Earthquake locations and fault-plane solutions should be more accurate with a 3D velocity model than with a 1D model because the ray paths will be more accurate. One-dimensional velocity models attempt to correct for lateral heterogeneity with station corrections, but they essentially assume the heterogeneity is directly below the station and they can only provide an average of the velocity variations sampled by ray paths from all directions to that station. Accurate ray paths are important for fault-plane solutions since the take-off angle of the ray path determines the location of the station on the focal sphere. Hence the Coalinga aftershock sequence gives us an opportunity

to compare 1D and 3D locations and fault-plane solutions and to evaluate the importance of a 3D velocity model as a location tool.

With the relocated aftershocks and fault-plane solutions, we can interpret the seismicity together with the velocity structure. Usually the structure is interpreted from the aftershocks and nodal planes, but it is very helpful to have the velocity structure. Note that, while the 3D velocity inversion solution is not a perfectly accurate representation of the velocity structure, it is most accurate in the areas with concentrated aftershock activity since the resolution is best where there are the most ray paths. We can assess how the pattern of aftershock occurrence relates to variations in velocity. We can consider how the nodal planes compare to the geologic structure inferred from the velocity model. And we can evaluate how variations in the character of the seismicity in different sections of the aftershock area relate to differences in the velocity structure along the length of the anticline.

HYPOCENTERS

The hypocenter part of the velocity-hypocenter inversion program was used to compute the 3D locations. Thus the velocity structure is defined on the same 3D grid, with linear interpolation between gridpoints, and the same method of ray tracing is used as in Chapter 2. The velocity model (Run H in Chapter 2, Table 1) used has 3- to 9-km gridspacing, with 1- to 3-km gridspacing in the hypocentral region. It also includes station corrections to help describe the near-surface velocity since the velocity model is less detailed at depths above the seismically active zone.

About 1600 aftershocks of magnitude $\geq$ 2 were relocated with the 3D velocity model. In Table 1 these locations are compared to those done with a 1D model with station corrections by Eberhart-Phillips and Reasenberg (1989).

While the 3D model is markedly different than a 1D model, the hypocenters changed surprisingly little. Thus the 3D hypocenters changed 0 to 2 km, but each individual hypocenter changed in accord with the details of the surrounding velocity structure and the entire group of hypocenters did not move in a systematic direction. On average, 3D locations have 0.02 s lower rms residual, and are 0.6 km northeast and 0.6 km shallower. The vertical changes are largest for the northern part of the aftershock zone and the horizontal changes are largest for the southern part. However, the 3D hypocenters are not systematically different from the 1D hypocenters in a statistically significant way since the standard deviations of the changes are of roughly the same size as the average changes. This indicates that the 1D model used was an excellent model, that little improvement could be gained by using a different 1D model.

We can therefore expect that the hypocenter patterns will be similar to those with the 1D model, but that some of the secondary features may be more detailed. The main advantage of the 3D inversion is the ability to compare the hypocenters to the velocity structure. If someone only desired earthquake locations and was not interested in interpreting the velocity structure, it would probably be more efficient to simply compute a good local 1D model, with station corrections, than to put in the effort of developing a 3D model.

FAULT-PLANE SOLUTIONS

The fault-plane solutions for events of magnitude $\geq$ 3 were computed using the hand-timed data of Eaton (1985, 1989) and Michael (1987) in the automated focal-mechanism program of Reasenberg and Oppenheimer (1985). This method does a grid search over the range of dip direction, dip and rake, and, for each possible source model, it compares the theoretical P-wave radiation pattern with the observed polarities. In order to compute a misfit

function, F, for each source model, the observed polarities are weighted by their assigned quality and the theoretical polarities are weighted by their amplitudes. The source models are then ranked by their F value. The best-fitting (lowest F) model is considered the fault-plane solution, and it is output together with the range of source models that describe the 90-percent confidence interval of F. This range of reasonable models is considered to represent the estimated uncertainties in dip direction, dip and rake of the fault-plane solution.

The automated fault-plane solution (FPS) method is faster than the hand-drawn FPS method and it thus allows relatively rapid recalculation of FPS when a new velocity model is used. Perhaps more importantly, it also avoids preconceived notions of what the fault-plane should be and gives useful estimates of the uncertainties in the FPS parameters. Histograms of these uncertainties are shown in Figure 3. For this set of FPS, the dip direction and dip are better constrained than the rake. Most of the FPS have uncertainties of 10° or less in the dip direction and dip, and most have uncertainties of 15° or less in rake. This is essentially telling us that one nodal plane, described by the dip and dip direction, is better constrained than the other. The rake describes the position of the other nodal plane and the type of slip represented by the FPS. A variation in the rake can change a FPS from predominantly dip-slip to predominantly strike-slip motion.

Note that for some poorly-constrained FPS, multiple solutions may be possible; adequate F are computed for source models in different unconnected parts of the searched grid of FPS parameters. The uncertainty for a given solution does not take into account any multiple solutions. For the Coalinga solutions computed here, 22 events had multiple solutions. All but two of these are events that occurred either before or after the operational period of the

temporary network of "5Day" recorders (Chapter 2), and so they have few close-in observations. Three of these events were deleted because they had relatively few (< 50) observations or because both possible solutions were reasonable. The other events with multiple solutions had numerous azimuthally-distributed observations and the source model was chosen that was most consistent with the rest of the Coalinga FPS.

The 3D fault-plane solutions are compared to those of Eaton (1989), who used a 1D model, in Figures 4 and 5. The 3D fault-plane solutions are also very similar overall to the 1D solutions, however there are some systematic differences. The difference in dip is plotted versus the dip of the 3D solutions in Figure 4a. The dips of most of the solutions vary by < 20°. The 3D solutions tend to dip more steeply than the 1D solutions. There are only seven 3D FPS with dips less than 30°, while there were twenty-eight 1D FPS with planes dipping less than 30°. An example of this is illustrated in Figure 4b. With the changes in ray paths, many of the dilational arrivals in the NE quadrant have moved to the SW quadrant. This has caused the shallowly-SW-dipping plane to become slightly steeper and the steeply-NE-dipping plane to become slightly shallower. A small component of strike-slip has also been put into the solution.

The difference in the dip direction is plotted versus the difference in rake in Figure 5a. The majority of the FPS differ from the 1D solutions by less than 20° in dip direction and less than 30° in rake. However, the most noticeable feature of the plot is that the solutions plot in a roughly linear trend, indicating that, if the 3D FPS has a greater dip direction, it will also have a greater rake. This basically shows the range of solutions since most are reverse but could have components of left or right-lateral slip. Consider the example drawn in Figure 5b and highlighted in Figure 5a. Changes in the ray

paths have had little effect on the northeast-dipping nodal plane, but have moved several of the dilatational arrivals so that the orientation of the southwest-dipping nodal plane must be changed. Thus, while the 1D solution has a small component of left-lateral slip, the 3D solution has a small component of right-lateral slip.

About 12 percent of the FPS fall outside of the dominant trend in Figure 5a. For most of these solutions with large changes in FPS parameters one of the nodal planes is near vertical. For a near-vertical plane a moderate change in dip can can have dramatic effects on the dip direction and rake. For instance normal slip on a steeply-southwest-dipping plane could be changed to reverse slip on a steeply northeast-dipping plane. Of the other events with large changes, two had 1D FPS that were poorer-fitting multiples of the 3D FPS. Three had 3D solutions that were distinctively different than the 1D solutions and, due to differences in ray paths, were able to better fit the data. And there were three events that had distinctively different solutions, yet neither the 3D nor 1D solution really fit the observations well.

In order to avoid the coordinate system problem described above, the 3D and 1D fault-plane solutions are compared with a different method in Figure 6. The minimum angle of rotation and the corresponding rotation vector describe how one FPS could be transformed into another FPS (A. J. Michael, written communication, 1988). Figure 6a is a histogram of the calculated rotation angles. They tend to be less than 35° and the largest is 90°, so there are none of the very large changes seen in the simple FPS parameter plot of Figure 5a. The rotation vectors are shown in Figure 6b, with stars indicating positive (clockwise) rotation angles and circles indicating negative (counterclockwise) rotation angles. To envision what these rotation vectors represent, consider what the rotation vectors would be for changes in each of

the FPS parameters for a southwest-dipping reverse-slip FPS. "A", in the center of the plot, would indicate a change in the dip direction; "B", 90° from the dip direction, would indicate a change in dip; "C", normal to the nodal plane, would indicate a change in rake; and "D" would indicate changes in both the rake and the dip direction. Since the FPS have varied dip directions, the rotation vectors can be more easily analyzed in Figure 6c, where the rotation vector trend minus the dip direction is plotted. The mean vector with its 95 % confidence region is also shown. While the rotation vectors are varied, the mean shows that the predominant differences, between the 3D and 1D FPS, are changes in rake accompanied by changes in dip direction. The numbers of FPS with increased rakes and decreased rakes are roughly the same. This is the same feature evident in Figure 5a. There is also a tendency for the 3D FPS to have larger dips, as seen in Figure 4a.

Thus the 3D ray paths have produced distinct changes in the fault-plane solutions. The fundamental style of deformation is not altered by ray-path variations; overall the Coalinga sequence shows compressional deformation on southwest- or northeast-dipping planes. Perhaps the most systematic change in the fault-plane solutions is that the southwest-dipping nodal planes have slightly greater dips; there are few nodal planes that have dips shallower than 30° when the 3D velocity model is used.

The ray paths are different both because of heterogeneity in the 3D velocity model and because the 1D model is a layered model. As shown in Figures 4b and 5b, a layered 1D model plots the arrivals in a ring pattern on the focal sphere. The M5 model of Eaton (1989) has a single layer throughout the hypocentral depth zone, from 9- to 14-km depth. This causes the moderately distant stations along the San Andreas fault, at 30- to 40-km hypocentral distance, to have near-horizontal upgoing ray paths, which plot

in the northeast quadrant of the focal sphere (Figures 4b and 5b). In contrast, for these stations, the 3D model gives slightly downgoing ray paths, with take-off angles of 70° to 80°, which plot in the southwest quadrant. Figure 7 shows 3D model take-off angles plotted versus hypocentral distances. Because of the lateral heterogeneity there is a wide range of take-off angles, particularly at distances less than 40 km. Stations to the southwest and west are more likely to have upgoing ray paths and stations on the east and northeast are more likely to have downgoing ray paths. At further distances, there is quite a bit of variability, but stations to the south tend to have smaller take-off angles (more steeply downgoing ray paths) than stations to the west.

REGIONAL ANALYSIS

Pattern of seismicity

The hypocenters are shown in map view in Figure 1. The mainshock is located in the center of the aftershock zone, near the fold axis of the Coalinga Anticline. The seismicity pattern varies along the length of the fold structure. The most dense concentration of aftershocks extends south of the mainshock for the length of the Coalinga Anticline. Further south, as the Coalinga Anticline peters out, the seismicity is more diffuse, and the concentration of aftershocks shifts somewhat to the southwest. North of the mainshock, the seismicity is also diffuse and the width of the aftershock zones broadens as the Coalinga Anticline merges in with the more westerly-trending Joaquin Ridge Anticline and the Diablo Range. Hence in later discussion, the seismicity will be separated into the northern, central and southern zones as indicated in Figure 1. While the trends of seismicity are not as distinct as typically seen for vertical faults, the trends do follow local structure. In the central area the seismicity tends to parallel the Coalinga Anticline. To the south, trends are less distinct. In the north, the seismicity tends to follow the varied orientation

of the shape of the fold, as indicated by the mapped geologic contacts. The mainshock rupture is estimated to be 8 km in length (Stein, 1986), as shown in Figure 1. Thus the area of the mainshock rupture zone seems to be limited by the region of uniform structural orientation. This is further seen in the fault-plane solutions.

There are no aftershocks in the area directly north and west of the mainshock hypocenter. In other earthquake sequences that have detailed models of slip distribution, there is an absence of aftershock activity in the portion of the rupture plane that sustained the maximum coseismic displacement (Mendoza and Hartzell, 1988). Thus the area near the Coalinga mainshock that lacks aftershocks is probably the area of greatest slip and stress release during the mainshock.

Mainshock

The mainshock fault-plane solution is shown in Figure 8. We prefer the thrust plane dipping 30° southwest. Note that this is slightly steeper than the 23° dip calculated earlier (Eaton, 1985, 1989) with a 1D model. As discussed by Wentworth and Zoback (1989a), it is the most appropriate plane to produce the uplift of the anticline since the overall geologic pattern is up on the southwest and down on the northeast. A southwest-dipping plane can fit the geodetic data well if it is considered to be a listric fault (Stein, 1986). It is also the most apparent plane in the aftershocks surrounding the mainshock. While there is a large northeast-dipping zone of aftershocks, it locates on the edge of the aftershock zone, southwest of the mainshock, and does not extend as far north as the modelled mainshock rupture. Aftershocks should locate around the mainshock fault-plane since the region around the mainshock rupture should be the area of greatest stress perturbation and hence subsequent aftershocks. The southwest-dipping listric plane runs through the aftershock region, and

the other areas of aftershocks are adjoining it, except an area of shallow north-striking rupture, the Nuñez events, which had rupture delayed a month after the mainshock occurrence.

Range of Fault-Plane Solutions

Figure 9a shows the dip direction and the rake of all the fault-plane solutions computed. The mainshock solution is the solid symbol. In Figure 9b, to aid in interpretation of Figure 9a, sample fault-plane solutions (FPS) are shown. These FPS do not correspond to particular Coalinga solutions, but are simply presented for illustration purposes. The sample FPS are all shown with planes dipping 45°, since this plot does not specify dip. FPS 6 is pure reverse slip on a southwest-dipping plane, similar to the mainshock; 3 is reverse slip on a southeast-dipping plane; 1 is pure right-lateral slip on a southeast-dipping plane, 2 is left-lateral slip on a north-dipping plane; and the line of FPS 4 through 8 shows a range of similar solutions from pure left-lateral to reverse to pure right-lateral slip.

For comparison, the most southwest-dipping nodal plane (i.e. most similar to the mainshock fault plane) was plotted in Figure 9a. Most of the solutions have reverse dip slip on planes with dip directions ranging from 150° (S30°E) to 290° (N30°W). Predominantly strike-slip motion is evident in 25 % of the solutions. These tend to be right-lateral strike slip on west-northwest or east-southeast dipping planes, or left-lateral strike slip on southwest-dipping planes. There are three solutions that show predominantly normal dip slip. One of these, dip direction 195° and rake -50, seems clearly to have a large normal component of motion. The other two have near-vertical nodal planes, and these planes could dip the other direction resulting in predominantly reverse dip-slip.

Central Zone

For the central zone, stereoviews of the hypocenters and fault-plane solutions are shown in Figures 10a and b, respectively. Note that the viewpoint is from the southeast, the box corresponds to the rectangular area defined in Figure 1, and the geologic basemap is plotted on the surface. In Figure 11a, the hypocenters are plotted on a velocity cross-section through the central zone, as indicated in Figure 1. The rakes and dip directions of the fault-plane solutions are plotted in Figure 11b and the principal stress axes, obtained through inversion of the FPS following Michael (1987), are plotted in Figure 11c.

Figure 11b shows that in the central zone, fault-plane solutions are almost uniformly similar to the mainshock, southwesterly reverse dip-slip, with small components of strike-slip. Part of the variation is due to nonuniqueness of the fault-plane solution. There is always a range of reasonable solutions, and which solution is chosen as the best solution depends on the distribution of the data. However, the largest computed uncertainties in dip direction and rake are 28° and 35°, respectively, and typical uncertainties are only 10°. Thus the variation in fault-plane solutions does indicate slip on a range of orientations of planes. Note that, because the rake varies along with the dip direction, the slip direction, about 230° (S50°W), is actually more uniform than the dip direction.

The stress axes computed for central zone FPS are shown in Figure 11c, along with their 95 % confidence regions, and are listed in Table 2. The most compressional stress axis, σ_1, is very similar to the P axis of the mainshock (Figure 8). It is nearly horizontal and trends 42° (N42°E). The least compressional stress axis, σ_3, plunges 76°, but is vertical within the 95 % confidence region.

The stereoview of hypocenters (Figure 10a) shows that the aftershocks in the central zone primarily occurred on two sets of conjugate faults. The larger set contains the primary mainshock rupture, a southwest-dipping thrust, and a northeast-dipping reverse fault branching off within the hanging wall. The other conjugate fault set is smaller, less than half the size, and occurs below and slightly east of the main thrust. This pattern of conjugate faults is also seen in the fault-plane solutions (Figure 10b), however, since only $M \geq 3$ events are in the fault-plane solution plot, different aspects are emphasized. The southwest-dipping thrust solutions across the middle of the aftershock zone are the most dominant feature. While it is a sharply defined planar feature in the hypocenter plot, the northeast-dipping reverse fault in the hanging wall has only a few FPS, and hence is a fault zone where numerous smaller magnitude earthquakes predominate. The smaller, deeper conjugate fault set in the footwall has a group of FPS near the intersection of its two fault orientations. It is noteworthy that, in the FPS plot, neither the northeast-dipping reverse fault nor the smaller conjugate fault set appear to connect to the main southwest-dipping thrust, although they do connect in the hypocenter plot that includes smaller magnitudes.

Above 8 km, in both the seismicity pattern and the fault-plane solutions (Figure 10), the main southwest-dipping thrust appears to splay into a steeper segment and a near-horizontal segment. This is consistent with bent-fault (Wentworth and Zoback, 1989a) and listric fault (Stein, 1986) models that do not consider the mainshock rupture to have occurred on a simple plane of uniform dip. As seen in the velocity cross-section (Figure 11a), this complexity occurs near the 5.5 km/s velocity contour, which roughly indicates the transition from Franciscan to GVS rock. The character of the seismicity

apparently varies with the rock type since the two rock units have different material properties.

At relatively shallow depths, 4 to 7 km, we also see a group of aftershocks beneath the eastern edge of the fold. These tend to be small magnitude aftershocks and have only one associated FPS. They are particularly interesting when we consider their relationship to the velocity structure (Figure 11a). They are at the position of steepest uplift gradient in the sedimentary section. This would be the region of greatest bending stress as the rock is folded.

At even shallower depths there are virtually no aftershocks. This absence of events suggests that strain is being accommodated aseismically in the upper low velocity material. As discussed by Stein and King (1984), compressional deformation can take the form of discrete faulting events at depth that terminate into aseismic folding which is seen in surface geology. At relatively shallow depths, there are diffuse smaller magnitude aftershocks in the middle of the fold between the conjugate planes (Figures 10,11a). These tend to be small magnitude events located in the area of velocity reduction within the GVS (Figure 2) and may be related to the high pore pressure there since the pore pressure also effects material properties.

There are some interesting relationships observed between the interpreted faulting and the velocity structure when the hypocenters are projected onto a cross-section of the velocity model (Figure 11a). The sets of conjugate faults suggest upward movement of blocks of higher velocity material. If we consider that, prior to deformation in this region, the area had a typical velocity gradient increasing with depth, then the expected result of cumulative deformation on southwest-dipping thrusts would be to pull up higher-velocity toward the northeast and push down lower-velocity material

toward the southwest. A pattern like this is seen in Figure 11a, where the inferred fault zones correspond with low-velocity zones and the overall velocity pattern shows relatively high velocities in the southwest half of the anticline, the hanging wall, and relatively low velocities in the northeast half of the anticline, the footwall. The northeast-dipping faults of the conjugate sets seem to be associated with the upper edges of the upward-moving blocks.

The most distinct northeast-dipping feature appears to line up with the Pleasant Valley Syncline. Both its orientation in cross-section (Figure 11a) and its spatial extent in mapview (Figure 1) indicate that it is causally related to the syncline. While aftershocks occur at greater depths farther southwest, this feature represents the edge of the local fold in the shallower material and in the mapped geology. It is notable that the western high-velocity body has no associated earthquakes, suggesting that it is some older feature, unrelated to the current uplift.

Northern Zone

The rake and dip direction of the fault-plane solutions for the northern zone are plotted in Figure 12b. The solutions are more varied than for the central zone (Figure 11b). There are mostly reverse solutions, but there are also a large proportion of strike-slip solutions. The dip directions for the reverse solutions are more varied than those for central zone but are overall more westerly.

The stress axes computed for northern zone FPS are shown in Figure 12c, along with their 95 % confidence regions, and are listed in Table 2. The least compressional stress axis, σ_3, is nearly vertical. The most compressional stress axis, σ_1, is nearly horizontal and trends 61° (N61°E), 19° more easterly than the central zone. In contrast, in inversions with the 1D FPS, Michael

(1987) did not observe any significant difference in stress axes between the northern and central zones (Table 2).

Figure 13 shows stereoviews of hypocenters and fault plane solutions for the northern zone. The mainshock slip plane is included for reference. The deeper seismicity is similar to that observed in the central zone, while the shallower seismicity shows different patterns. The southwest-dipping main thrust is evident and there is a set of conjugate planes as noted in the central zone. These do not extend to shallow depths and there is correspondingly less diffuse shallow seismicity in the center of the anticline. In the northern cross-section (Figure 12a), the velocity features are similar to the central section, with the primary difference being that there is a much larger amount of uplift here, and correspondingly lower velocities beneath the eastern edge.

The shallow eastern group of aftershocks is more numerous and has larger magnitude events than in the central zone. Note that this group of aftershocks is not as broad as it looks in this view. When looked at from a variety of orientations, these appear to form a pattern bending with the shape of the anticline. The larger magnitude events in this group form a distinct cluster in both the hypocenter and FPS plots beneath the northeastern edge of the mapped fold. In the velocity cross-section (Figure 12a), the folded rocks here show the greatest degree of flexure, and it is again precisely at the point of greatest flexure that the group of shallow aftershocks show up. Since there has been more uplift in the northern zone, the eastern edge of the anticline is more strongly folded and so has more aftershock activity than the central zone.

On the other side of the anticline there are events extending from the surface to approximately 8-km depth (Figure 12a). This group of shallow aftershocks indicates a north-striking reverse fault, corresponding to the

Nuñez surface rupture (Chapter 2, Figure 1). The M 5.2 Nuñez event, with reverse dip slip on a plane dipping 56° to the east, occurred a month after the Coalinga mainshock, and was relatively shallow, 3 km. A month later it was followed by two more magnitude 5 events and a M 6.0 event, which were deeper, 8 km, occurring near the downdip edge of the north-striking fault zone (Figure 13b). Since so many of the northern zone larger events, which have computed FPS, are on north-striking, east-dipping planes, they have a strong influence on the stress axes.

In the mapped geology (Figure 1 and Chapter 2, Figure 1) the Pleasant Valley Syncline adopts a more northerly trend toward the north, and the rocks near the northwest end of Pleasant Valley tend to strike in a northerly orientation. Thus the geologic structure is consistent with rupture on the north-striking Nuñez fault. However, the anticline, the structure that is associated with the mainshock, takes on a more westerly trend toward the north, as the Coalinga Anticline merges with the westerly trending Joaquin Ridge Anticline. It appears that these west-striking features are not as well-oriented for large slip as the north-striking features, and hence secondary rupture has occurred west of the mainshock anticline where north-striking, east-dipping, fault planes are available. This east-dipping secondary faulting is apparently bounded on the south, from the southwest-dipping mainshock faulting, by an area of right-lateral strike-slip faulting in its footwall (Figure 13b; and Eaton, 1985).

Southern Zone

The rake and dip of the fault-plane solutions for the southern zone are plotted in Figure 14b. The solutions are also predominantly reverse but have dip directions about 10° more southerly than the central zone. The stress axes computed for southern zone FPS are shown in Figure 14c, along with their

95 % confidence regions, and are listed in Table 2. The most compressional stress axis, σ_1, is nearly horizontal and trends 23° (N23°E), 19° more northerly than for the central mainshock zone. This is in accord with local structure since the Kettleman Hills Anticline trends a little more westerly than the Coalinga Anticline. The least compressional stress axis, σ_3, is near vertical, but is virtually unconstrained within the 95 % confidence region. Along with the very low ϕ value, 0.04, this would suggest that σ_2 and σ_3 are of roughly equal magnitude.

Figure 15 shows stereoviews of the hypocenters and fault-plane solutions for the southern zone. Compared to the rest of the aftershock zone, the southern zone has diffuse smaller-magnitude seismicity. There is a large proportion of shallow seismicity, from 0- to 7-km depth, but there are no clusters of events on the eastern and western sides of the fold as were found in the central and northern zones.

The fault-plane solutions (Figure 15b) suggest that there may be a shallowly southwest-dipping thrust, that bounds the seismicity from below. There is a hint of two steeply northeast-dipping reverse faults, although they are not distinct enough to affirm. The hypocenters do not form such distinct planar features as were apparent in the central and northern zones. The proposed mainshock rupture plane (Figure 1; Stein, 1986) does not reach the southern zone, and hence one reason for the diffuse nature of seismicity here may be the distance from the mainshock rupture. However the fact that the geologic structure here is neither as large nor as uniform as farther north is also likely to influence the seismicity pattern.

When we consider the velocity structure in the southern zone (Figure 14a), we see a very different pattern than in the mainshock regions. It is simpler, with few well-defined low-velocity-zones. The local folds are

observed as only a broad region of minor uplift, without a distinct fold axis. There is no large uplift of higher velocity material in the core of the anticline, and no corresponding lower-velocity region on the east.

Therefore this section appears to be in an early stage of deformation, with only gentle folding occurring. The seismicity is diffuse because distinct faults have not yet formed within the anticline. Similarly there is negligible flexure on the eastern flank and so there is no associated seismicity there.

DISCUSSION

The extent of the rupture area of the Coalinga earthquake seems to be determined by the area of uniform structural orientation and by variation in material properties. The mainshock rupture terminated to the north where the fold trend was no longer uniform but had competing north and west-trending features. The orientation of the compressional stress axis also varies to the north and to the south of the mainshock area. Geometric complexities have been suggested by King (1983) and King and Nabelek (1985) to be the natural termination of rupture because they distribute the stress concentration of the propagating rupture. They suggest that, upon propagation to a fault bend, movement on the main fault causes movement on numerous small faults of varied orientation near the fault bend. This deformation surrounding the bend absorbs much of the stress from the crack tip of the main fault and creates numerous small offsets that can effectively form an asperity on the main fault. The upward mainshock rupture ended at the approximate boundary between Franciscan and Great Valley Sequence rock. Subsequently, aftershocks and postseismic deformation, observed geodetically (Stein, 1986), extended the main thrust zone through the GVS.

The faulting structure beneath the fold consists primarily of a set of southwest-dipping thrusts uplifting blocks of higher-velocity material. As

shown in Figure 16b, the earthquakes primarily occurred on two sets of conjugate faults. One contains the mainshock fault plane, a southwest-dipping listric fault, and a northeast-dipping reverse fault in the hanging wall. These faults are appropriate for creation of the local folds. Recurrent slip on the southwest-dipping fault has produced the Coalinga Anticline at the surface, and recurrent slip on the northeast-dipping fault has produced the Pleasant Valley syncline. The other conjugate fault set is smaller and occurs below and slightly east of the main thrust. The larger magnitude events, and hence the larger amounts of uplift, tend to occur on the southwest-dipping planes.

The 3D velocity structure (Figure 16b) is appropriate for the uplift of blocks of higher-velocity material. It shows a series of low-velocity zones at hypocentral depths below the Coalinga Anticline. These could easily be created by the uplift of higher-velocity material over lower-velocity material, without requiring (but not disallowing) velocity reduction from overpressure in the hypocentral zone or some other change in the material properties. Along with pushing up higher-velocity material within the anticline, these faults have also pushed down lower-velocity material on the eastern side. Thus particularly low velocities are observed at 9-km depth below the eastern flank of the anticline. The shallow velocity structure is consistent with the aseismic folding of sedimentary strata above the deeper faulting. A simple schematic cross-section, in Figure 17, illustrates the gross deformational style. If such a pattern characterizes other folds, the 3D inversion method may be useful in discerning the location of major thrust faults.

The character of the seismicity varies along the anticline with the amount of previous deformation on each section of the anticline. By comparing the seismicity to the velocity structure we can understand how the pre-existing geologic structure influences seismic activity. In the central

(mainshock) zone, there has been a moderate amount of uplift, evidenced by the Coalinga Anticline and adjoining syncline, Pleasant Valley. There conjugate faulting occurs from 7- to 13-km depth, with most of the deformation on a southwest-dipping thrust across the anticline. At shallower depths there is some diffuse seismicity above these distinct faults. Along other parts of the fold, with different amounts of previous deformation, different aspects of the central seismicity pattern are emphasized.

In the southern zone, there has been relatively little previous deformation and the aftershocks show diffuse seismicity from 0- to 11-km depth. Neither the velocity structure nor the seismicity show evidence of blocks of material (Figure 16c). Thus, in this area of gentle folding, well-defined fault zones have not yet developed. However it is important to note that, since this area does exhibit aftershocks, the lack of structure does not signify a lack of seismic potential.

In the northern zone, there has been the largest amount of previous deformation, including the development of a sharp bend on the eastern flank of the fold (Figure 16a). There the seismicity pattern primarily shows southwest-dipping thrusts from 8- to 13-km, similarly to the central zone. However, since this is north of Pleasant Valley, the associated northeast-dipping reverse fault is absent. There is very little diffuse shallow seismicity and the shallow material is not simply folding aseismically. The shallow seismicity shows distinct zones of secondary faulting on either side of the fold with orientations that correspond to the pre-existing geologic structure. On the eastern side, at the point of greatest flexure of the sedimentary material, small magnitude aftershocks occurred with southwest-dipping reverse slip. On the western side, large magnitude secondary faulting on east-dipping

reverse faults forms a zone from 8-km depth to the surface, including the surface rupture of the Nuñez fault.

We have observed a steady rotation of σ_1, the compressional stress axis, along the length of the folds by 38°. This is statistically significant; there is some overlap of the central zone confidence region with those of the northern and southern zones, but the northern and southern zones' confidence regions are clearly separated. If the inversion solution stress axes truly represent the local stress, then this shows a rotation in the compression axis along the Coast Ranges / Great Valley margin. Wentworth and Zoback (1989b) also observe that the compression axis varies along the margin so that it is everywhere perpendicular to the local fold axes. However when all the FPS are combined in the stress inversion, the fit to the fault-planes is not much worse than for the three separate inversions (compare β in Table 2). Thus an alternative explanation is that the actual stress does not vary, but that different types of focal mechanisms are characteristic of each zone and so the inversion solution shows different σ_1 axes. Hence it is not clear that the variation in σ_1 axes implies any variation in stress direction. It may simply describe the reaction of faults of locally varying orientation to a uniformly-oriented stress.

CONCLUSIONS

This study of the Coalinga aftershock sequence shows that it is valuable to analyze the three-dimensional velocity structure together with the seismicity in order to get the most complete picture of the faulting and deformation that result from a large earthquake. Secondary features of the seismicity can be interpreted with the velocity structure, and even for the mainshock, the relationship between this episode of faulting and the long-term tectonic process can be more readily understood by also considering the velocity structure.

Hypocenters located with the 3D velocity model showed virtually no systematic change from those computed with a local 1D model and station corrections. Each event moved in accord with the details of the surrounding velocity structure, and hence the resulting picture of seismicity is clearer. The primary benefit of the 3D locations is the ability to analyze them in relationship to the geologic structure, inferred from velocity.

The overall style of deformation shown by fault-plane solutions (FPS) computed with the 3D velocity model is not altered by the changes in ray paths, but there are distinct differences from FPS with the 1D model. In particular southwest-dipping nodal planes are slightly steeper; the mainshock fault plane dips 30° southwest instead of the 23° given by the 1D model.

The faulting structure beneath the fold primarily consists of a set of southwest-dipping thrusts uplifting blocks of higher-velocity material. In the velocity structure this appears as a series of low-velocity zones, and in the seismicity the earthquakes primarily occur on two sets of conjugate faults. One contains the mainshock fault plane, a southwest-dipping listric fault, and a northeast-dipping reverse fault in the hanging wall. The larger magnitude events, and hence the larger amounts of uplift, tend to occur on the southwest-dipping planes.

The extent of the rupture area of the Coalinga earthquake seems to be determined by the area of uniform structural orientation and by variation in material properties. The mainshock rupture terminated to the north where the fold trend was no longer uniform but had competing north and west-trending features. The upward extent of the mainshock rupture ended at the approximate boundary between the Franciscan and Great Valley Sequence rocks. Above that depth the main southwest-dipping thrust appears to splay into a steeper segment and a near-horizontal segment.

The character of the seismicity varies along the anticline with the amount of previous deformation on each section of the anticline. Where the previous uplift was largest, the velocity structure shows a relatively sharp fold and the shallow seismicity shows distinct zones of secondary faulting on either side of the fold with orientations that correspond to the pre-existing geologic structure. Where there was relatively little previous deformation, only diffuse seismicity occurs and the velocity structure shows a gentle fold without evidence of uplifted blocks of material since well-defined fault zones have not developed.

REFERENCES

Eaton, J. P., The May 2, 1983 Coalinga earthquake and its aftershocks: A detailed study of the hypocenter distribution and of the focal mechanisms of the larger aftershocks, in Mechanics of the May 2, 1983 Coalinga Earthquake, U. S. Geol. Surv. Open-File Rept. 85-44, edited by M. Rymer and W. Ellsworth, pp. 132-201, 1985.

Eaton, J. P., The May 2, 1983 Coalinga earthquake and its aftershocks from May 2 through September 30, 1983, in The Coalinga, California, Earthquake of May 2, 1983, U. S. Geol. Surv. Prof. Pap., edited by M. Rymer and W. Ellsworth, 1989.

Eberhart-Phillips, D., and P. A. Reasenberg, Complex faulting structure inferred from local seismic observations of M $\geq$ 1.0 aftershocks, May 2 - June 30, 1983, in The Coalinga, California, Earthquake of May 2, 1983, U. S. Geol. Surv. Prof. Pap., edited by M. Rymer and W. Ellsworth, 1989.

King, G., The accommodation of large strains in the upper lithosphere of the earth and other solids by self-similar fault systems: the geometrical origin of b-value, Pure and Appl. Geophys., 121, 761-815, 1983.

King, G., and J. Nabelek, The role of fault bends in the initiation and termination of earthquake rupture, Science, 228, 984-987, 1985.

Mendoza, C. and S. H. Hartzell, Aftershock patterns and main shock faulting, Bull. Seismol. Soc. Am., 78, 1438-1449, 1988.

Michael, A. J., Stress rotation during the Coalinga aftershock sequence, J. Geophys. Res., 92, 7963-7979, 1987.

Reasenberg, P., and D. Oppenheimer, FPFIT, FPPLOT and FPPAGE: Fortran computer programs for calculating and displaying earthquake fault-plane solutions, U. S. Geol. Surv. Open-File Rept. 85-739, 1985.

Stein, R. S., Evidence for surface folding and subsurface fault slip from geodetic elevation changes associated with the 1983 Coalinga earthquake, in Mechanics of the May 2, 1983 Coalinga Earthquake, U. S. Geol. Surv. Open-File Rept. 85-44, edited by M. Rymer and W. Ellsworth, pp. 225-253, 1985.

Stein, R. S., Postseismic growth of the Coalinga Fold (abstract), EOS Trans. AGU, 67, 1223, 1986.

Stein, R. S., and G. C. P. King, Seismic potential revealed by surface folding: 1983 Coalinga, California, earthquake, Science, 224, 869-872, 1984.

Wentworth, C. M., and M. D. Zoback, Structure of the Coalinga area and thrust origin of the May 2, 1983 earthquake, in The Coalinga, California, Earthquake of May 2, 1983, U. S. Geol. Surv. Prof. Pap., edited by M. Rymer and W. Ellsworth, 1989.

Wentworth, C. M., and M. D. Zoback, The style of Late Cenozoic deformation at the eastern front of the California Coast Ranges, Tectonics, in press, 1989.

Table 1

3D Hypocenters Compared to Hypocenters with 1D Model + Station Corrections					
Area	Rms Residual (s)	Origin Time (s)	Change in Location (km)		
	Smaller	Later	East	North	Shallower
All	0.02 ± 0.06	0.17 ± 0.15	0.28 ± 0.65	0.56 ± 0.54	0.61 ± 1.19
Northern	0.01 ± 0.07	0.18 ± 0.14	0.22 ± 0.54	0.52 ± 0.61	1.10 ± 0.89
Central	0.02 ± 0.05	0.19 ± 0.09	0.32 ± 0.61	0.54 ± 0.48	0.57 ± 0.81
Southern	0.03 ± 0.05	0.13 ± 0.20	0.35 ± 0.64	0.64 ± 0.44	0.13 ± 0.16

Table 2

Area	Stress Axes						ϕ	95 % confidence range	$\bar{\beta}$
	σ_1		σ_2		σ_3				
	trend	plunge	trend	plunge	trend	plunge			
From FPS with 3D model:									
Northern	61	5	331	2	217	85	0.31	0.09 to 0.54	27 ± 29
Central	42	1	132	14	307	76	0.39	0.12 to 0.70	32 ± 33
Southern	23	2	114	13	284	76	0.04	0.00 to 0.49	24 ± 24
All	48	2	138	1	249	88	0.36	0.18 to 0.54	34 ± 34
From Michael, 1987:									
Northern	50	1	320	7	141	82	0.39	0.22 to 0.60	17 ± 16
Central	51	1	141	4	337	86	0.49	0.19 to 0.81	25 ± 23
Southern	24	3	124	5	254	85	0.56	0.28 to 0.85	29 ± 23

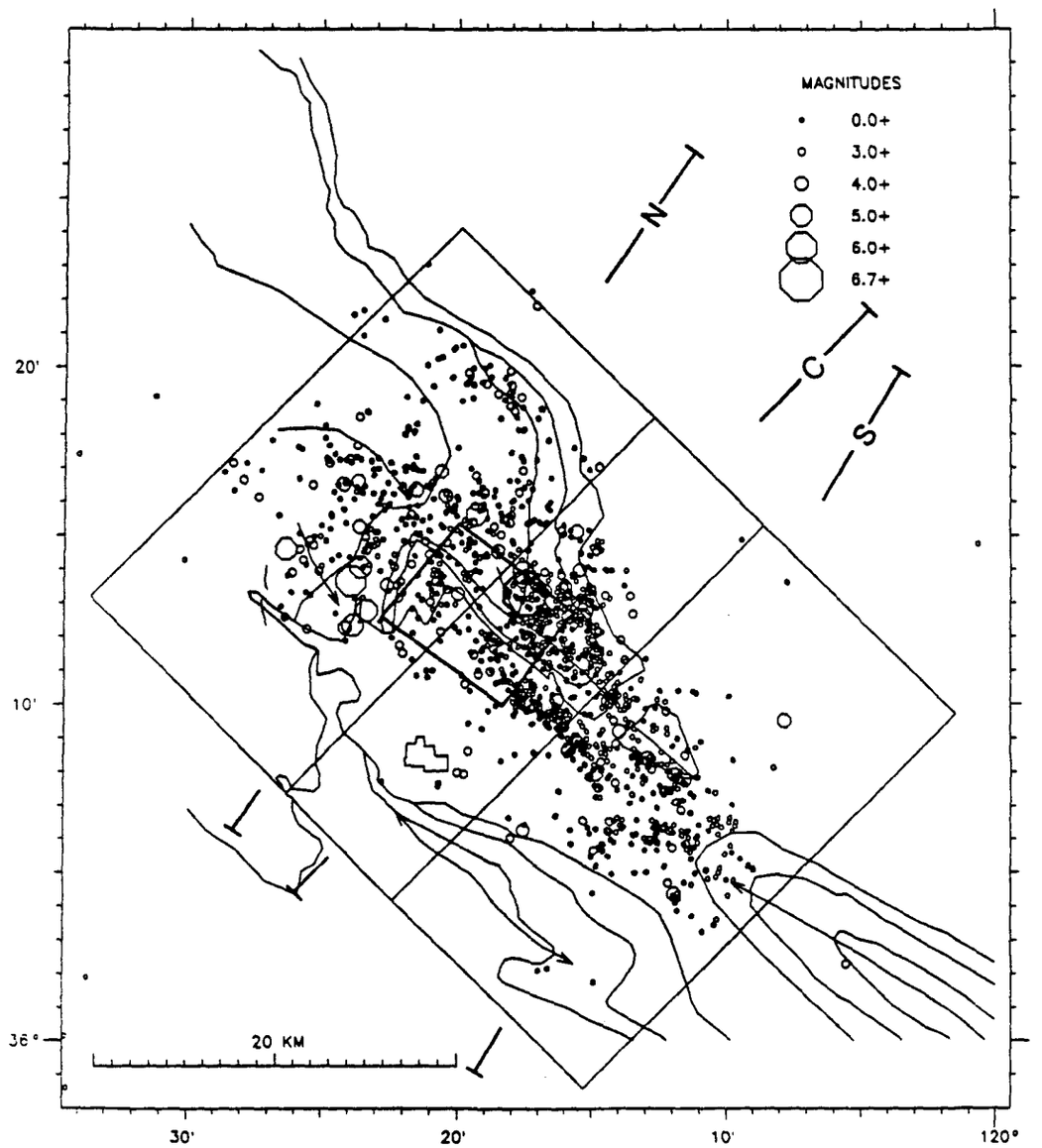

Figure 1. Map view of Coalinga aftershock sequence with geologic basemap described in Chapter 2, Figure 1. Well-located events M $\geq$ 2.0, from the period of near-by temporary recorders, May 4 through June 30, and all events M $\geq$ 3.5. The basemap shows geologic contacts and the town of Coalinga, as described in Chapter 2, Figure 1. The mainshock is indicated by a large bold symbol and the surrounding bold rectangle is the surface projection of Stein's (1986) listric fault model for the mainshock rupture. The larger outlined areas indicate the northern, central and southern zones that are shown in stereoviews in Figures 10,13,15, respectively. Lines N, C and S denote the positions of cross-sections shown in Figures 11, 12 and 14. (The orientation of each stereoview was chosen to best show the seismicity features in that zone and then each cross-section was drawn with a corresponding orientation.)

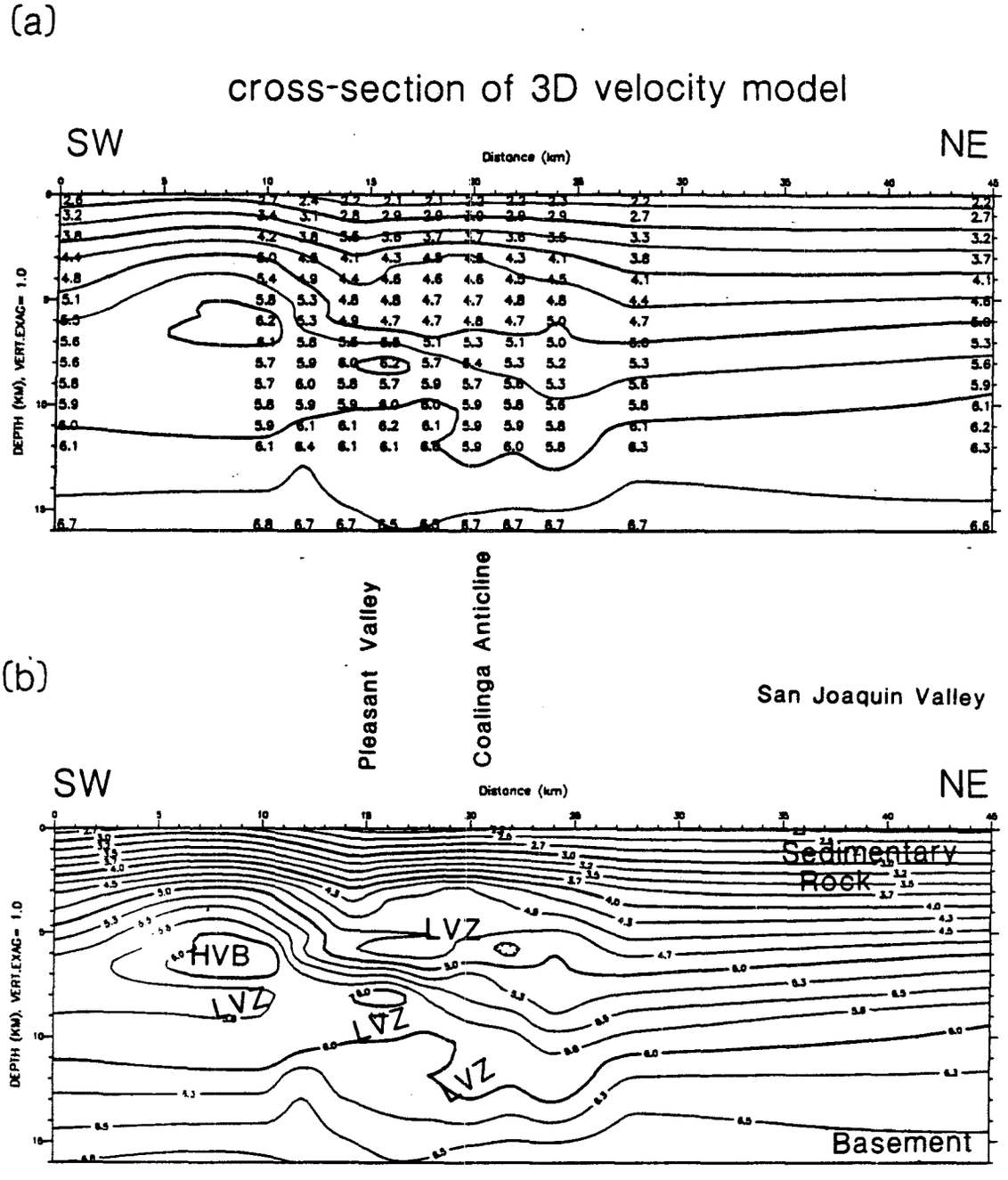

Figure 2. Cross-section of 3D velocity model along line C (Figure 1), normal to the fold axis. Depths range from 0 to 16 km and there is no vertical exaggeration. (a) Numbers indicate the velocity solution at the gridpoints in this cross-section, contour interval is 0.5 km/s. (b) Features of the velocity structure are noted on a section with 0.25 km/s contour interval.

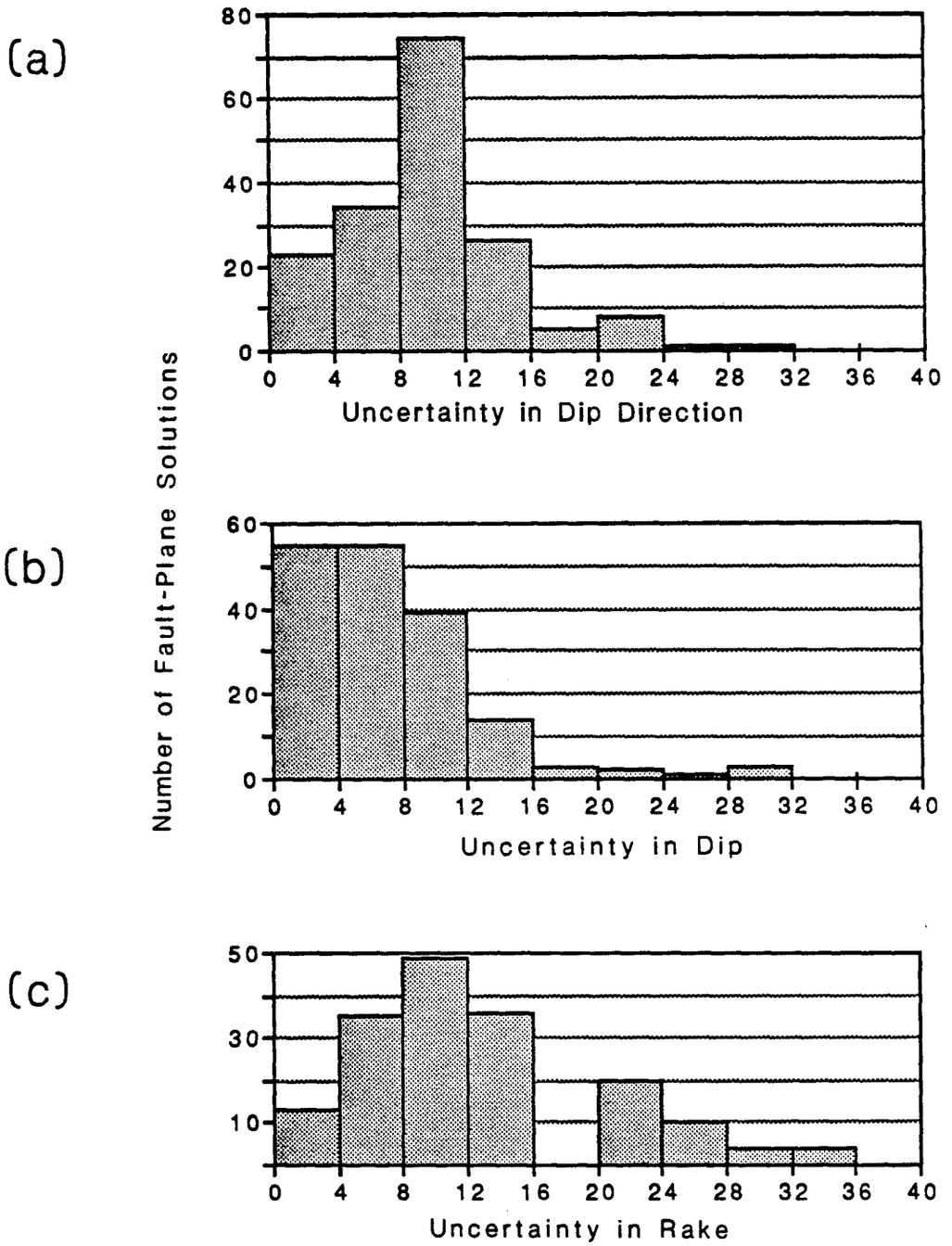

Figure 3. Histograms showing estimated uncertainties (in degrees) in fault-plane-solution parameters, computed with FPFIT (Reasenberg and Oppenheimer, 1985) and 3D velocity model. (a) Dip direction, (b) dip and (c) rake.

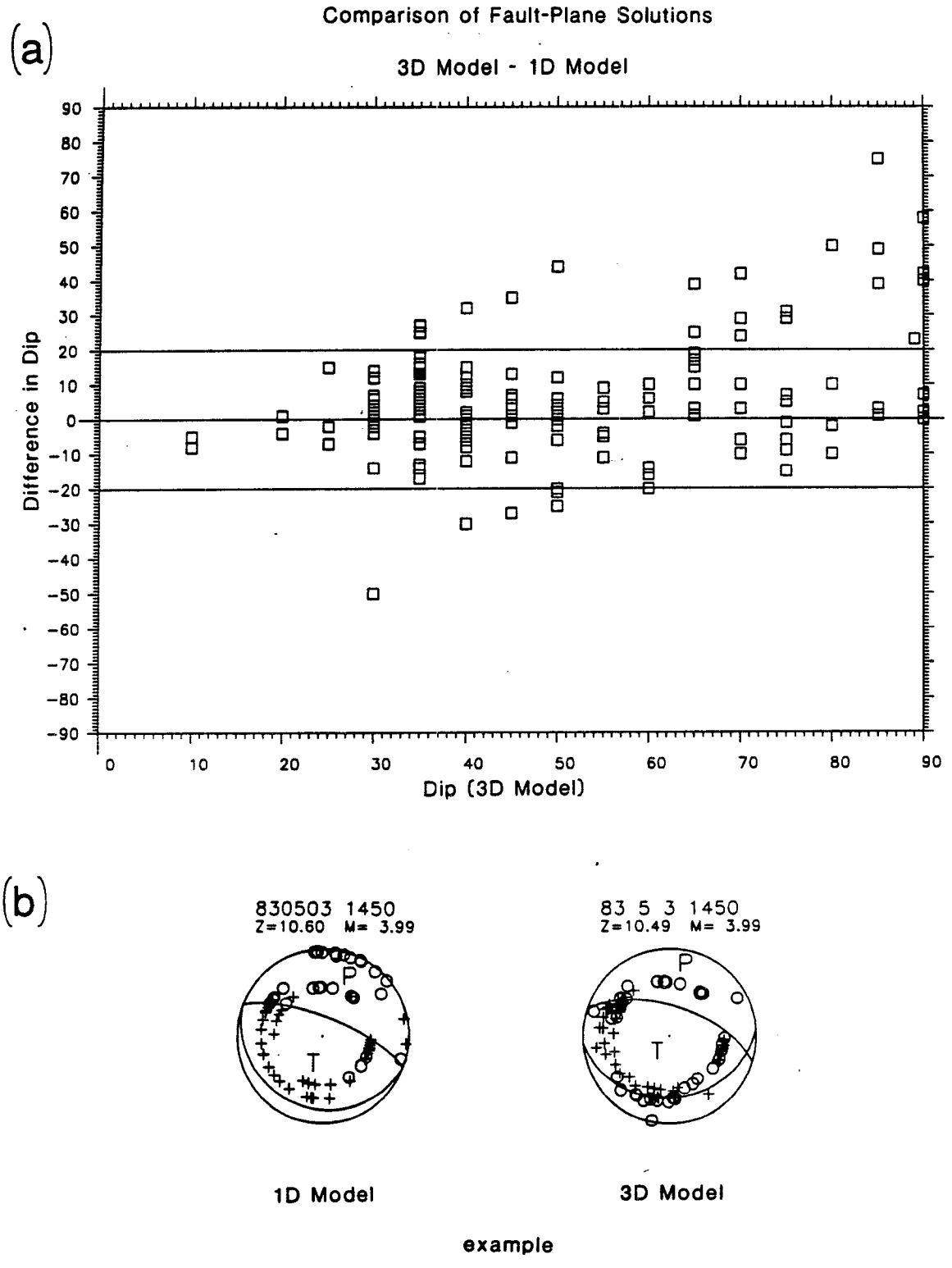

Figure 4. Comparison of fault-plane solutions with 3D velocity model to those of Eaton (1989) with 1D velocity model. (a) Difference in dip (3D - 1D) versus dip with 3D model. Highlighted event is shown below. (b) Example of difference in nodal planes for 1D and 3D model fault-plane solutions. Circles represent dilatations, pluses represent compressions; P and T axes are shown.

(a)

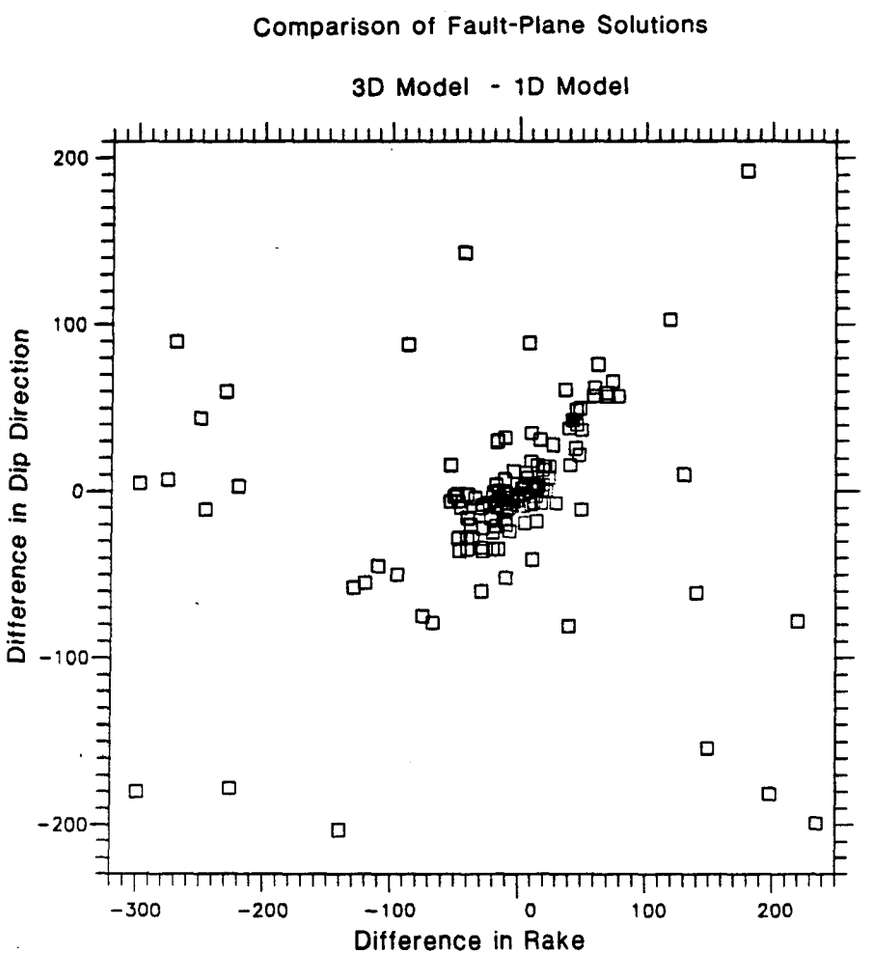

(b)

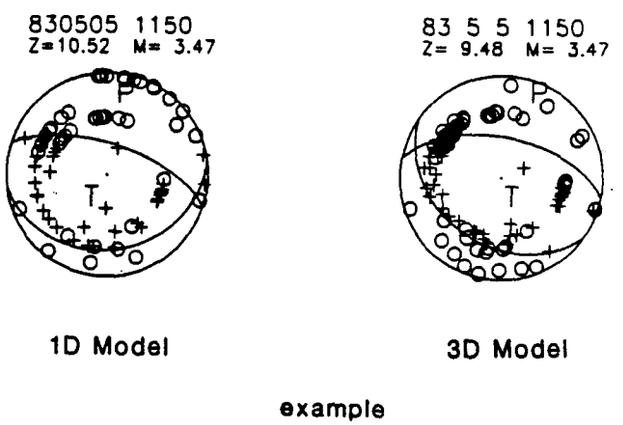

Figure 5. Comparison of fault-plane solutions with 3D velocity model to those of Eaton (1989) with 1D velocity model. (a) Difference in dip direction (3D - 1D) versus difference in rake (3D - 1D). Highlighted event is shown below. (b) Example of differences for 1D and 3D model fault-plane solutions. Circles represent dilatations, pluses represent compressions; P and T axes are shown.

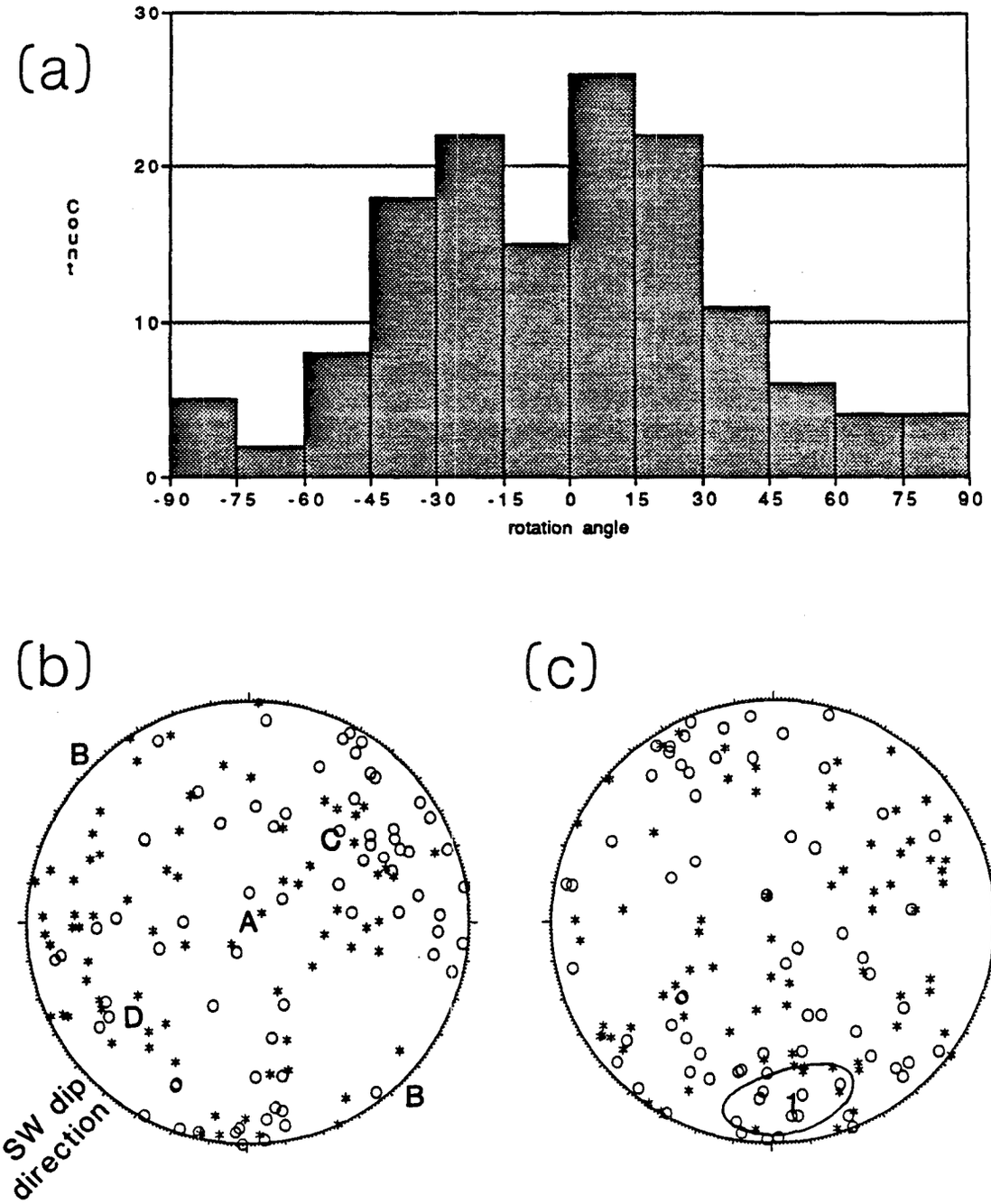

Figure 6. The minimum angles for rotating the 3D FPS to the 1D FPS of Eaton (1989). (a) Histogram of rotation angles. (b) Lower hemisphere plot of rotation vectors, stars correspond to positive (clockwise) rotation angles and circles correspond to negative (counterclockwise) rotation angles. Vectors A, B, C and D are shown for explanation. Considering a southwest-dipping reverse fault, A would indicate a change in dip direction only, B would indicate a change in dip only, C (normal to nodal planes) would indicate a change in rake only, and D would indicate changes in both rake and dip direction. (c) The trend of the rotation vector minus the dip direction is plotted, to evaluate FPS changes for FPS of varied dip direction. In this plot, for positive angles, trend of 90° means the 3D FPS has steeper dip, trend of 180° means larger rake, and trend of 270° means shallower dip. The mean is shown by "1" with an ellipse indicating its 95 % confidence region.

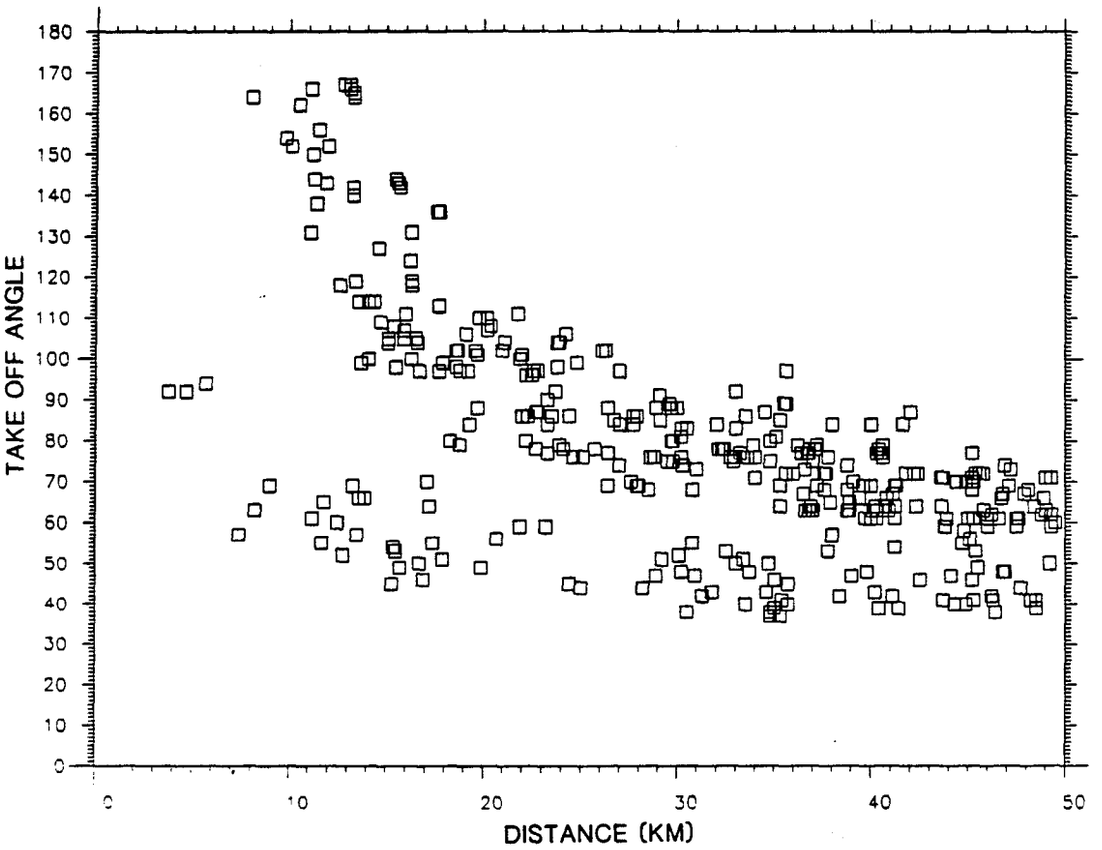

Figure 7. Take-off angles for ray paths in 3D velocity model plotted versus hypocentral distance.

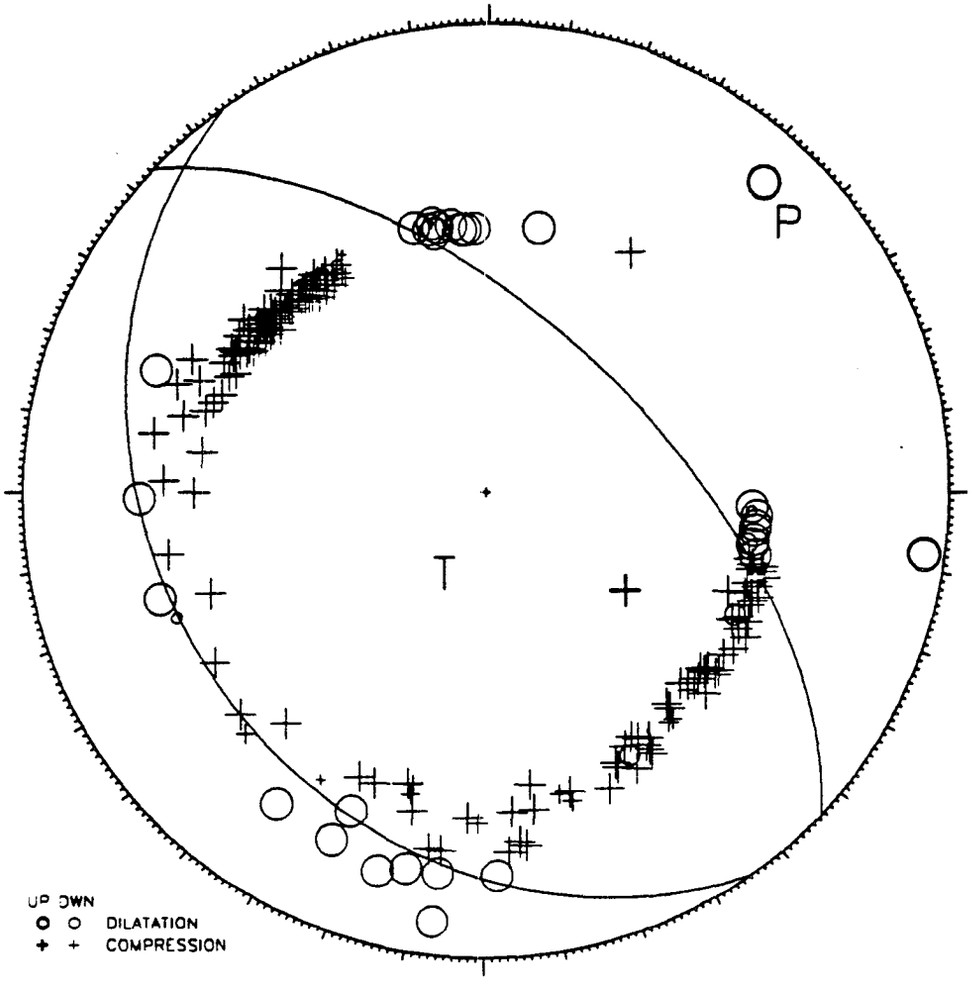

Figure 8. Mainshock fault-plane solution. Circles represent dilatations, pluses represent compressions; P and T axes are shown. Dip direction is 235° (S55°W), dip is 30°, and rake is 100.

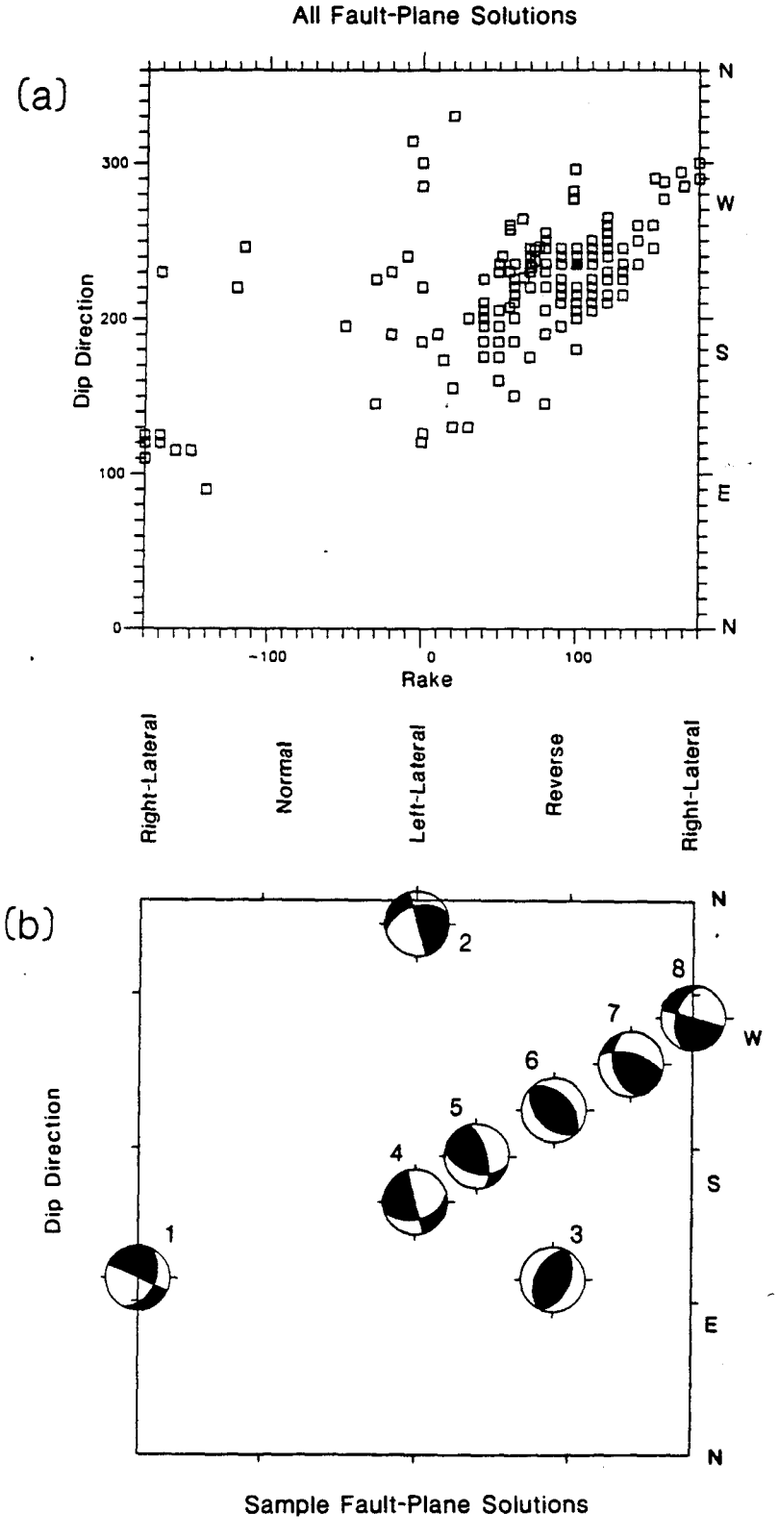

Figure 9. (a) Dip direction plotted versus rake for all 3D model fault-plane solutions. The highlighted solution is the mainshock. (b) To aid in understanding the plot above, sample types fault-plane solutions are shown on a similar plot. Since the dip value is not included, the sample solutions were all drawn with 45°. (These solutions are only for illustration and do not represent specific Coalinga solutions.)

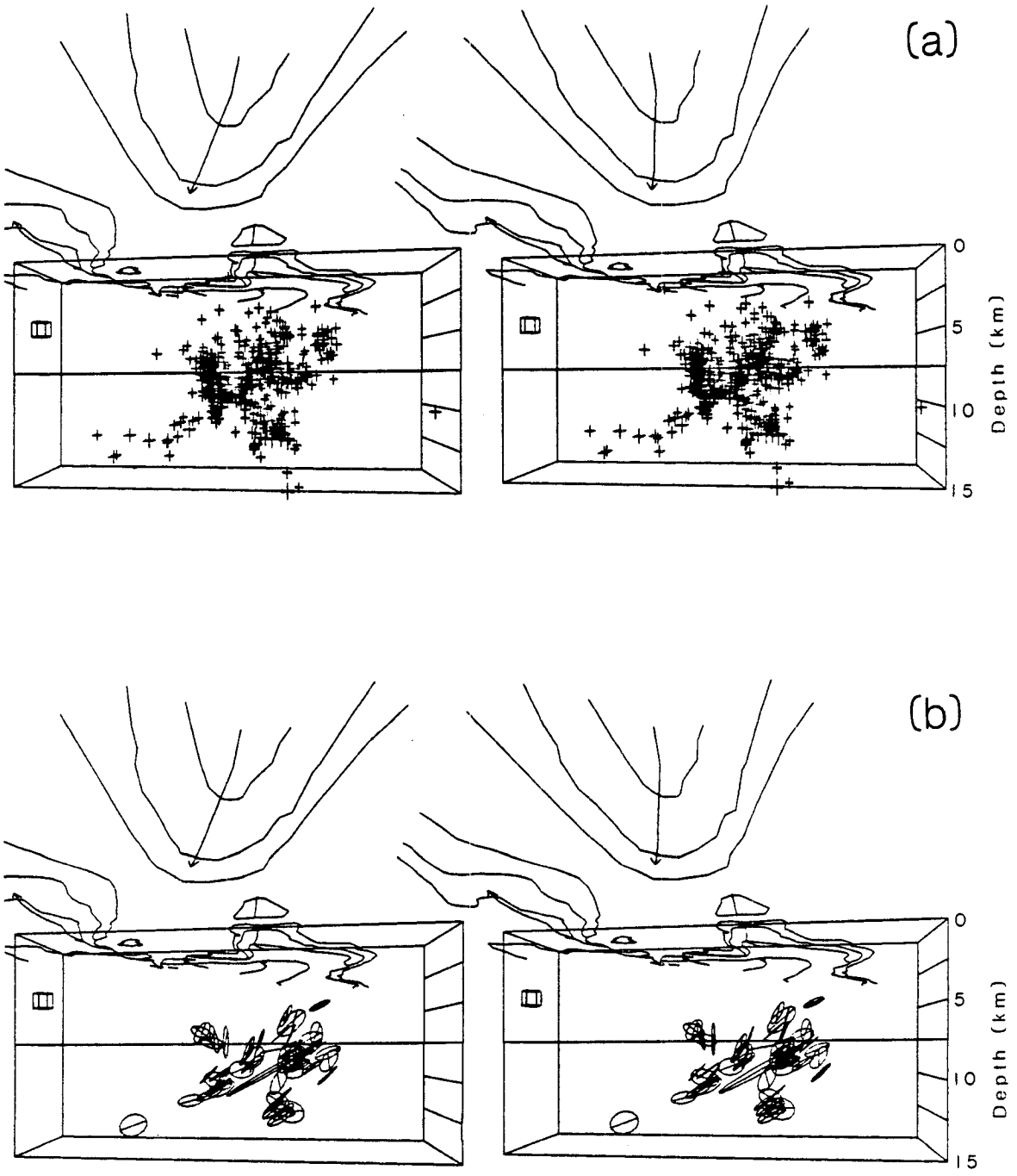

Figure 10. Stereoviews of aftershocks in central zone. Box (outlined in Figure 1) extends from surface to 15-km depth, simplified geology (Chapter 2, Figure 1) is drawn on the surface, and a 1-km cube with horizontal edges aligned north-south and east-west is show for scale. View is from the southeast toward azimuth 315°. (a) Well-located hypocenters, $M \geq 2$. (b) Circles representing slip planes of fault-plane solutions for events $M \geq 3.5$. Nodal planes most consistent with hypocenter patterns and with other nearby solutions were selected for plotting. The diameter lines indicate the slip directions. The large slip plane is the mainshock, plotted with dimension approximately equal to the size of the inferred rupture plane (Stein, 1986).

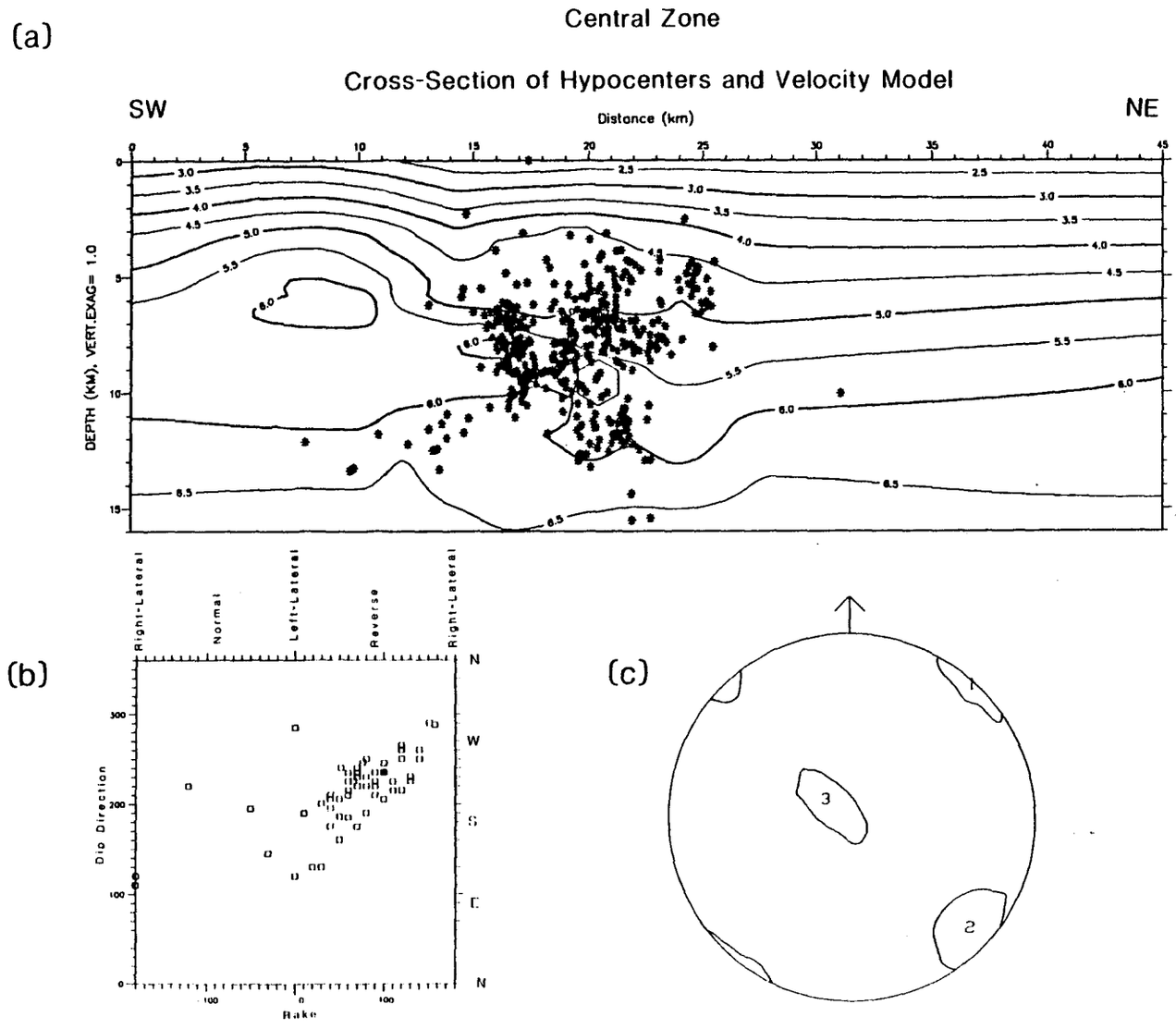

Figure 11. (a) Hypocenters in central zone projected onto a cross-section of the 3D velocity structure along line C, Figure 1. There is no vertical exaggeration and the contour interval is 0.5 km/s. Large hexagon is mainshock. (b) Dip direction versus rake for central zone fault-plane solutions, mainshock is highlighted. See Figure 9b for explanation. (c) Stress axes from inversion of central zone fault-plane solutions with their 95 % confidence regions.

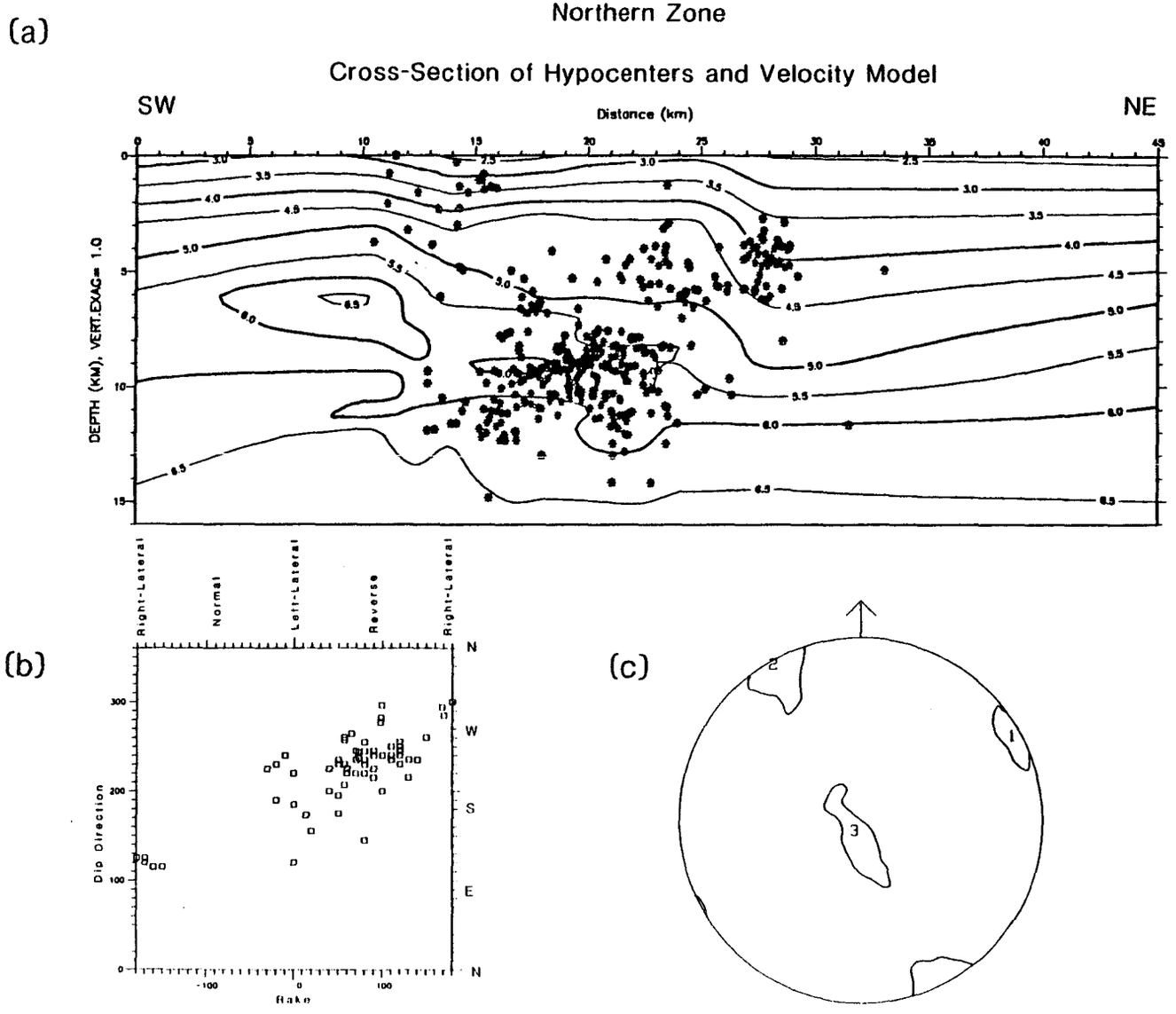

Figure 12. (a) Hypocenters in the northern zone projected onto a cross-section of the 3D velocity structure along line N, Figure 1. There is no vertical exaggeration and the contour interval is 0.5 km/s. (b) Dip direction versus rake for northern zone fault-plane solutions. See Figure 9b for further explanation. (c) Stress axes from inversion of northern zone fault-plane solutions with their 95 % confidence regions.

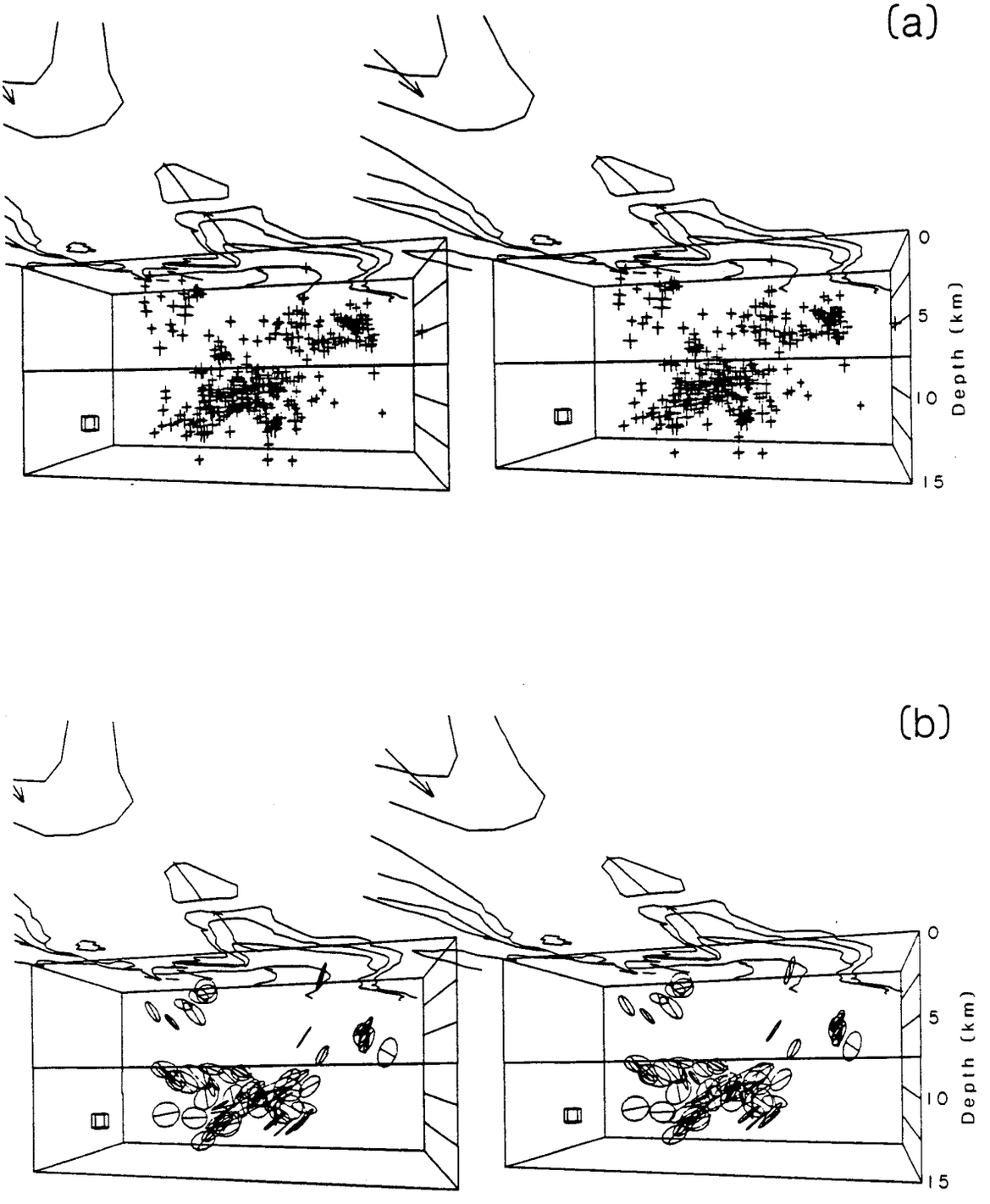

Figure 13. Stereoviews of aftershocks in northern zone. Box (outlined in Figure 1) extends from surface to 15-km depth, simplified geology (Chapter 2, Figure 1) is drawn on the surface, and a 1-km cube with horizontal edges aligned north-south and east-west is show for scale. View is from the southeast. (a) Well-located hypocenters, $M \geq 2$. (b) Circles representing slip planes of fault-plane solutions for events $M \geq 3.5$. Nodal planes most consistent with hypocenter patterns and with other nearby solutions were selected for plotting. The diameter lines indicate the slip directions. The mainshock is also included since the rupture plane extends into the northern zone.

(a)

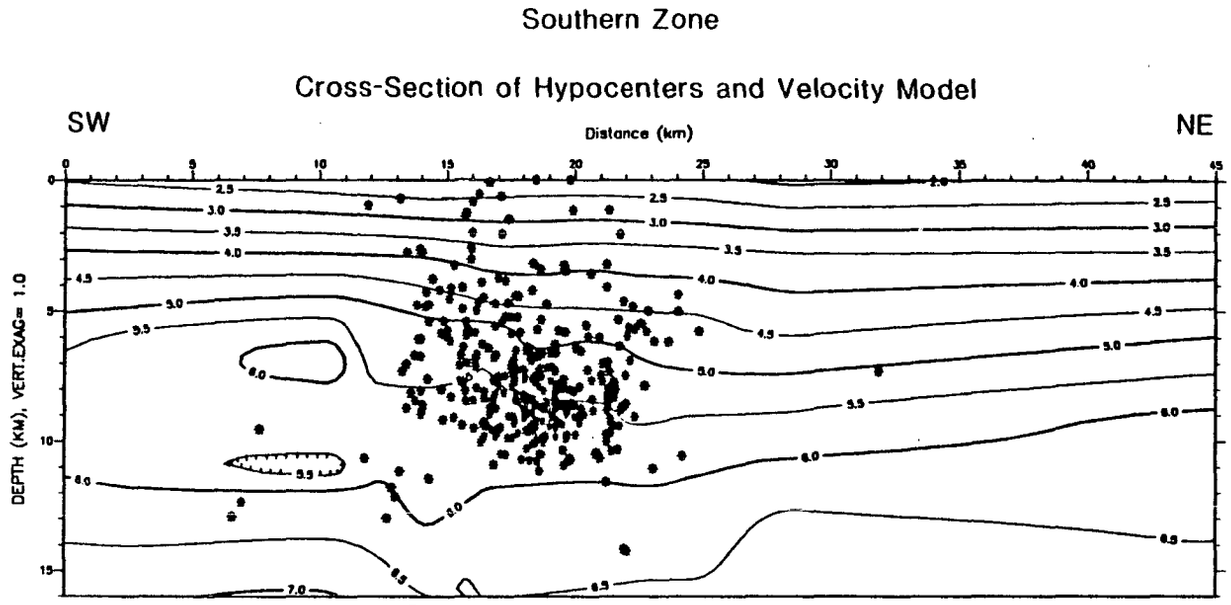

(b)

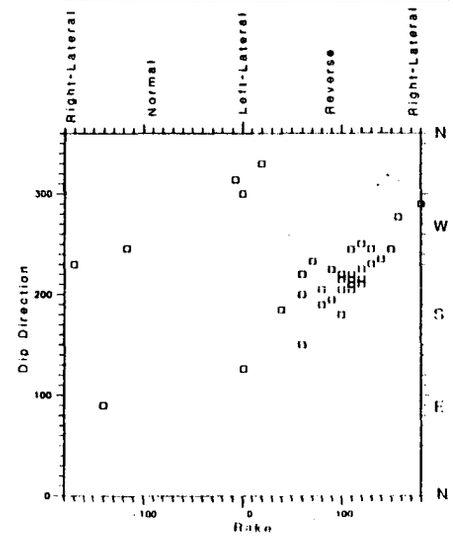

(c)

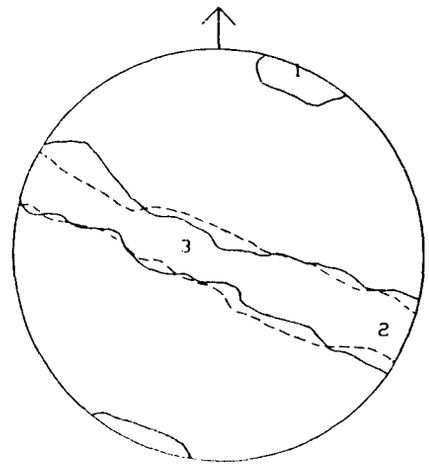

Figure 14. (a) Hypocenters in the southern zone projected onto a cross-section of the 3D velocity structure along line S, Figure 1. There is no vertical exaggeration and the contour interval is 0.5 km/s. (b) Dip direction versus rake for southern zone fault-plane solutions. See Figure 9b for further explanation. (c) Stress axes from inversion of southern zone fault-plane solutions with their 95 % confidence regions. For σ_2 and σ_3 the confidence regions are indicated by solid and dashed lines, respectively.

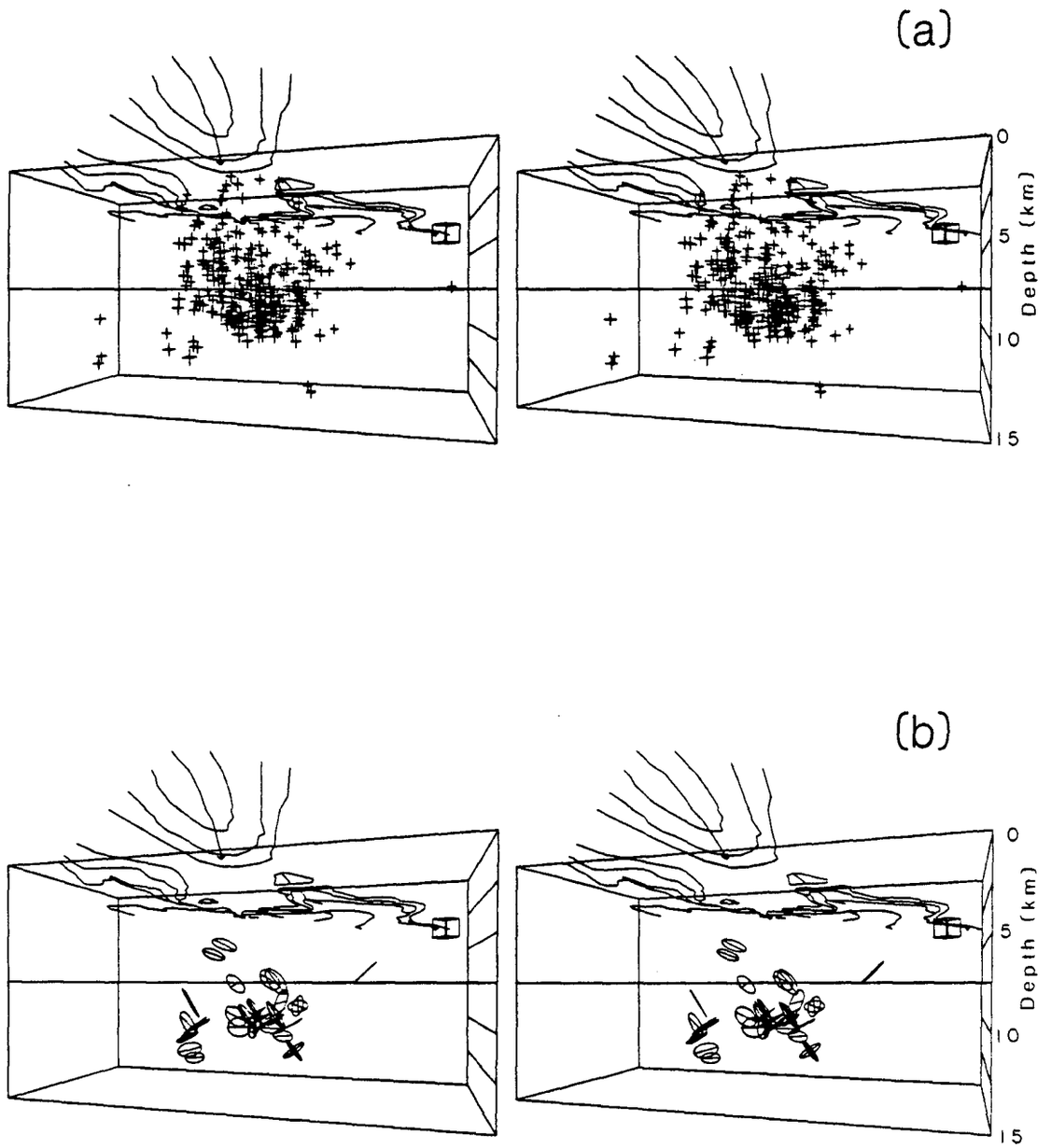

Figure 15. Stereoviews of aftershocks in southern zone. Box (outlined in Figure 1) extends from surface to 15-km depth, simplified geology (Chapter 2, Figure 1) is drawn on the surface, and a 1-km cube with horizontal edges aligned north-south and east-west is show for scale. View is from the southeast. (a) Well-located hypocenters, $M \geq 2$. (b) Circles representing slip planes of fault-plane solutions for events $M \geq 3.5$. Nodal planes most consistent with hypocenter patterns and with other nearby solutions were selected for plotting. The diameter lines indicate the slip directions.

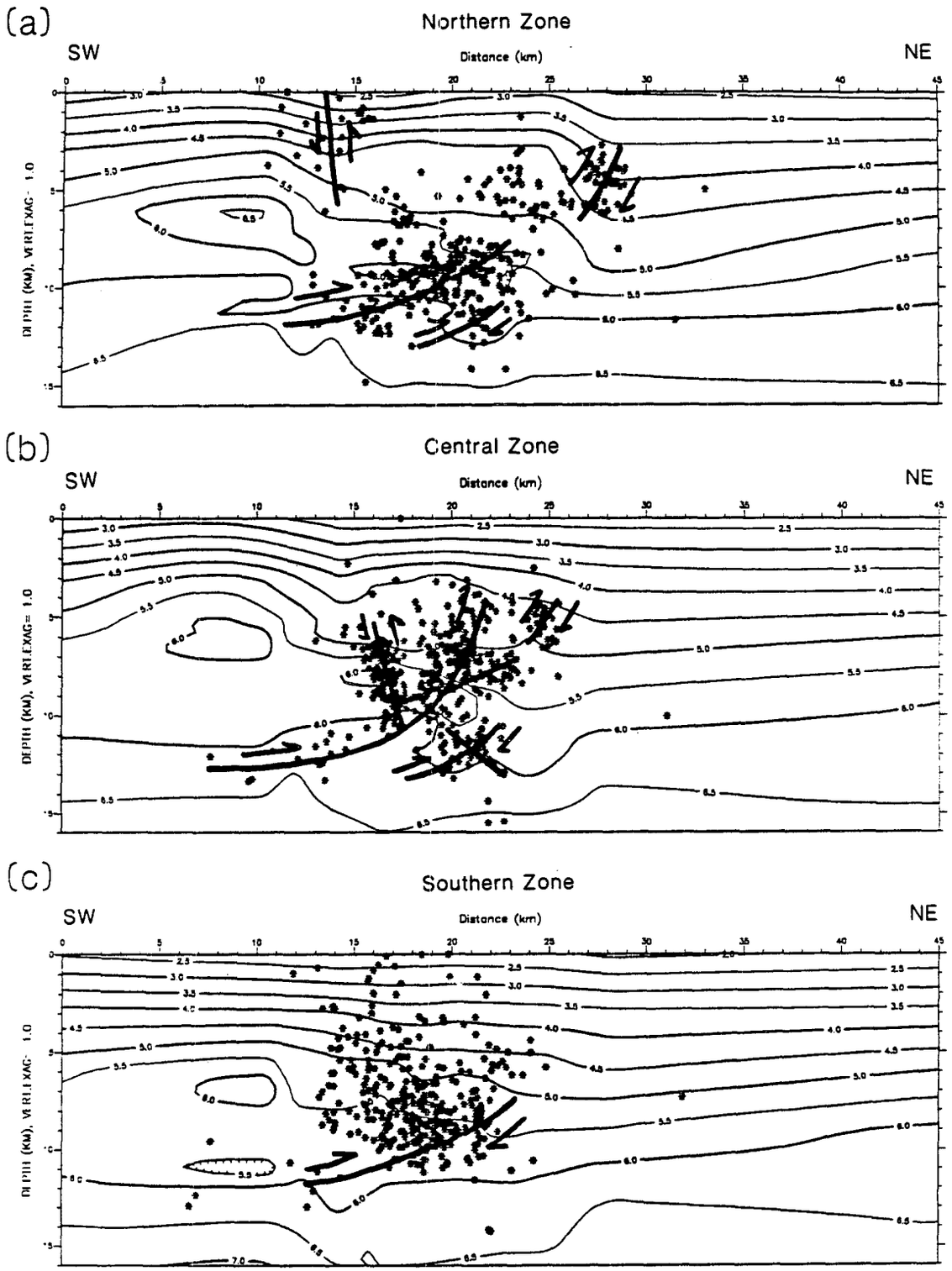

Figure 16. Variation in seismicity and velocity structure along the anticline, shown in cross-sections for the (a) northern, (b) central (large octagon indicates mainshock) and (c) southern parts of the aftershock zone (as indicated in Figure 1). Inferred faults are sketched in to illustrate the character of deformation in each zone.

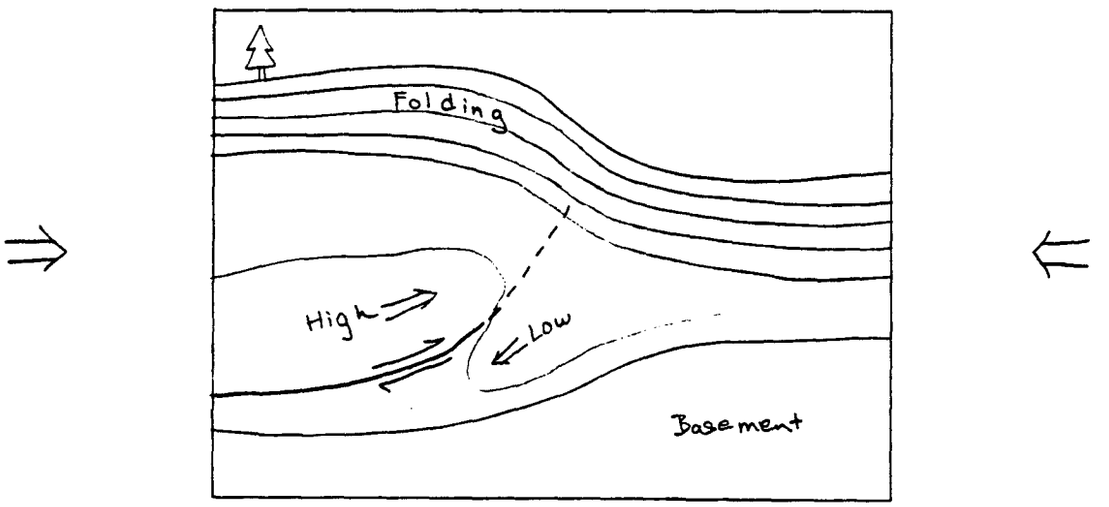

Figure 17. Cartoon of a schematic cross-sectional view of the gross deformation indicated by the velocity structure and earthquake mechanisms. Responding to regional compression, thrust faulting pushes high-velocity material upward and low-velocity material downward. The shallower material deforms by folding so that both the surface geology and the shallow velocity structure show a simple anticline.

Chapter 4.

Crustal Strain near the Big Bend of the San Andreas Fault: Analysis of the Los Padres - Tehachapi Trilateration Networks, California

ABSTRACT

In the region of the Los Padres-Tehachapi geodetic network, the San Andreas fault changes its orientation by over 30° from N40°W, close to that predicted by plate motion for a transform boundary, to N73°W. The strain orientation near the SAF is consistent with right-lateral shear along the fault, with maximum shear of 0.38 ± 0.01 μrad/yr at N63°W. In contrast, away from the SAF the strain orientations on both sides of the fault are consistent with fault-normal compression, with maximum shear of 0.19 ± 0.01 μrad/yr at N44°W. The strain rate does not drop off rapidly away from the fault, and thus, the area is fit by either a broad shear zone below the SAF or a single fault with a relatively deep locking depth. The fit to the line-length data is poor for locking depth, d, less than 25 km. For d of 25 km, the computed slip rate is 30 ± 6 mm/yr. We also computed multiple fault slip models that included the Garlock and Big Pine faults, in addition to the SAF. Other faults were unconstrained by the Los Padres-Tehachapi network. The best fitting Garlock fault model had computed slip of 11 ± 2 mm/yr below 10 km and had an rms residual of 2.6 mm/yr. Left-lateral shear deformation is indicated within the Western Transverse Ranges. The Big Pine fault provides significant reduction in line-length residuals, however deformation there is probably more complicated than a single vertical Big Pine fault. A sub-horizontal detachment

on the southern side of the SAF cannot be well-constrained by this data. We investigated the location of the SAF and found that a vertical fault below the surface trace fits the data much better than either a dipping fault or a fault located to the south.

INTRODUCTION

In the western Transverse Ranges, the San Andreas fault (SAF), the presumed plate boundary between the North American and Pacific plates, changes its orientation from N40°W to N73°W (Figure 1). The N40°W SAF segment is roughly parallel to the global plate motion (DeMets, et al., 1987), implying essentially pure right-lateral strike-slip deformation. Although the N73°W SAF segment is poorly oriented for a purely dextral transform boundary, implying oblique motion, studies of crustal strain (Savage et al., 1986) show that the observed strain accumulation along this portion of the SAF is nearly pure right-lateral strike-slip regardless of the strike of the fault with respect to plate motion. Also Sieh (1978) found that the magnitude $8\frac{1}{4}$ 1857 SAF earthquake had pure right-lateral movement along a 400-long segment of the fault through the western Transverse Ranges. Therefore there must be some other features to account for the additional compressive component of plate motion in the Big Bend region of the SAF.

Several models of deformation for this complicated region have been proposed. Hill (1982) and Bird and Rosenstock (1984) model southern California by including numerous additional smaller plates and then considering which faults could assume the motion along these other "plate boundaries". For instance, Hill (1982) and Davis and Burchfiel (1973) consider that the Garlock fault is a transform structure accommodating motion between a Great Valley/ Sierra Nevada block and a Mojave block. Sheffels and McNutt (1986) and Humphreys (1987) suggest that there is either subduction of the

Pacific plate or else thickening of the Pacific plate from a convective mantle downwelling "drip". Weldon and Humphreys (1986) consider that the upper brittle crust behaves as blocks but is detached from the (subducting) lower crust/mantle by a horizontal decollement. Davis and Yerkes (1988) consider that the upper crust in the western Transverse Ranges behaves as a broad fold and thrust belt above the proposed decollement, and consider that the SAF dips to the south so that it is located 12-km south of its surface trace at 10-km depth.

Since the USGS geodetic network in the western Transverse Ranges extends, on both sides of the SAF, relatively far from the fault trace, detailed analysis of the geodetic data can address some of the tectonic complexities of the Big Bend. Variations in strain orientation for subnets along the fault and away from the fault can be evaluated in order to consider the interplay between the local fault and the regional strain. After computing the displacement field from the line lengths, models of fault slip at depth can be compared to find the location of deep slip relative to the surface trace and to estimate the locking depth and slip rate of the SAF in this region. Through inversion of the geodetic data more complicated slip models can be studied and, thus, some of the additional faults, that have been proposed to be actively slipping, can be included to see whether they are required by the geodetic data.

The USGS Los Padres trilateration network extends from the SAF bend to the coast near Ventura, 60 km away from the fault (Figure 1). A uniform strain solution for the Los Padres network was computed by Savage et al. (1986) for the 1973-1984 data. They obtained principal strain rates oriented north-south with 0.14 ± 0.01 compressive μstrain/yr and east-west with 0.12 ± 0.01 extensional μstrain/yr. Thus, instead of indicating strain appropriate for the local SAF, the Los Padres uniform strain solution is oriented appropriately for

the overall San Andreas system - plate motion direction. Since this is a complicated area, calculation of strain for separate subnets may be necessary to determine strain at the SAF. Another interesting feature of the Los Padres uniform strain solution is that the strain rate is lower than typically observed on well-oriented segments of the SAF. For example, the Pt. Reyes network observes a uniform strain rate more than double that of the Los Padres network (Prescott and Yu, 1986). Again, calculations for subnets and consideration of the displacement field can provide more detailed information about the SAF strain rate.

Better constrained strain rates could be obtained if we had measurements extending on both sides of the fault. Therefore we decided to include the Tehachapi network which adjoins the northeastern edge of the Los Padres network and extends 80 km away from the SAF, across the Antelope Valley and the Garlock Fault. The Tehachapi network data from 1973-1983 was analyzed by King and Savage (1984). Their uniform strain solution gave principal strain rates of 0.12 ± 0.01 compressive μstrain/yr oriented N76°E and 0.08 ± 0.01 extensional μstrain/yr oriented N14°W. Compared to Los Padres, the strain rates are of similar size but differ in their orientation. However, through consideration of separate subnets, King and Savage (1984) showed that the strain near the SAF is oriented northwest-southeast and northeast-southwest, while the strain away from the SAF is oriented north-south and east-west.

DATA

The geodetic data used in this study are observations of line lengths of USGS Los Padres and Tehachapi trilateration networks. The data cover 130 km along the San Andreas fault and 140 km across the fault. The Tehachapi network is located east of the Los Padres network, but joins the Los Padres

network at two stations, Wheeler2 and Tecuya (Figure 1). Thus the networks balance each other well across the fault from northeast to southwest. However stations on the east and west peripheries of the combined network will be only weakly constrained in displacement solutions.

Distances between monuments were measured with a Geodolite, and corrected for refractivity as described by Savage and Prescott (1973). The data cover the period 1973-1987, although the temporal distribution of measurements varies somewhat from line to line. Some stations were added to the networks during the time period. Some stations have had to be replaced because of vandalism or environmental problems and measurements to replacement stations have been reduced to correspond to the original stations.

In surveying lines, some observations may actually be erroneous measurements, called blunders. We would like not to include any blunders, however we do not want to discard observations simply because they do not fit our models of strain accumulation. Thus we applied the simple conservative criterion suggested by Savage et al. (1986): a linear fit in time is done separately for each survey line and any measurement that deviates from the linear fit by greater than three observed standard errors, as calculated for that survey line, is considered to be a surveying blunder. Only one measurement in the original data set was considered a blunder. A total of 881 observations of 73 lines remained for this study.

UNIFORM STRAIN SOLUTIONS

The strain rate for a network of repeated line-length measurements is found using the method of Prescott et. al (1979). This is a least squares solution assuming the strain rate is uniform in space and time. We did solutions for the two networks as well as subnets along the San Andreas fault (SAF) and off the fault. Table 1 lists the strain rates, and Figure 2 shows the orientations of

maximum shear strain. Note that the x_1 axis is east and the x_2 axis is north, and positive strain is extension.

Both networks show principal strains of approximately north-south compression and east-west extension, and negligible dilatation, indicating maximum right-lateral shear along northwest striking planes. Although the strain rates are similar, the Tehachapi maximum shear strain solution is rotated 13° from the Los Padres: as shown in Figure 2a, the Los Padres orientation of maximum shear (L) is N47°W while the Tehachapi (T) is N60°W. The Tehachapi network is fully within the Big Bend, however the Los Padres includes the western end of the Big Bend and may be indicating a transitional strain field from the N40°W section of the SAF, adjacent to the northwest.

In order to consider the relationship between the strain and the local orientation of the San Andreas, we have divided the networks into "along-fault" and "off-fault" subnets, with lines indicated in Figure 1 by "A" and "O", respectively. The along-fault group includes lines that cross the fault or are within 10 km of the fault. The off-fault group includes lines that are more than 10 km from the fault. These subnets show two significant results, a difference in orientation of strain and a relatively small reduction in strain rate away from the fault.

The strain rates for the off-fault nets, covering areas 15 to 70 km from the fault, are only 50% lower that the strain rates along the San Andreas (Table 1). As discussed in more detail below, this implies that the trilateration lines are sensing either relatively deep slip or a broad shear zone. Surprisingly, the off-fault data of the two networks, on different sides of the SAF and on different plates, give nearly identical strain rates and orientations. The off-fault orientations of maximum right-lateral shear (Figure 2b) are N44°W, significantly more northerly than for either of the whole networks.

This is closer to the plate motion direction than to the local fault orientation, and thus suggests that geodetic data farther from the fault are more likely to sense the overall plate motion direction.

Conversely the along-fault data give strain rates which are higher than for the whole networks, and give orientations of maximum shear which are more westerly than the whole networks and are closer to the local fault orientation. As shown in Figure 2c, the results are not as similar between the two networks as for the off-fault data. The Los Padres data gives a shear strain orientation (L) at N47°W, however this is dominated by lines at the northwest end of the network where the SAF is N40°W. When these lines, to Temblor, Caliente and Salisbury, are removed the maximum shear strain orientation (Le) is N59°W. The Tehachapi shear strain (T) is oriented slightly more westerly at N65°W. The combined along-fault data in Figure 2c indicate maximum shear strain (LT) oriented N63°W, twenty degrees from that of the off-fault data in Figure 2b. Compared to the along-fault data from the Los Padres network, the Tehachapi network gives a 10 to 20 % higher shear strain rate, which is marginally significant. In terms of the commonly-used model of shear strain resulting from slip on a buried screw dislocation (Prescott and Nur, 1981) where, with x the distance normal to the fault, d the locking depth, and $\dot{b}$ the slip rate,

$$\dot{\varepsilon}_{xy} = \frac{\dot{b}}{2\pi}\left(\frac{d}{d^2 + x^2}\right) \qquad (1)$$

this observation could indicate a slightly smaller d and thus slightly shallower slip on the fault at depth. Perhaps more likely, this could be simply the result of data distribution with Tehachapi along-fault data including a relatively larger proportion of lines that do not extend more that 5 km from the fault.

Note that the shear direction of the off-fault data is correct for left-lateral movement on the Garlock fault, which strikes N57°E. This might imply that the Garlock fault is controlling the Tehachapi off-fault strain. However the remarkable similarity in off-fault strain, irrespective of which side of the SAF we are observing, would argue that overall plate motion is the greater influence away from the SAF. Thus crustal strain due to deep slip on the Garlock fault does not appear to be the controlling feature in the orientation of crustal strain in the off-fault Tehachapi network.

The key result that comes out of these uniform strain rate solutions is that strain along the fault is controlled by the local fault (plate boundary) orientation, while farther away from the fault, the strain orientation is closer to the overall plate motion direction. The spatial pattern of the principal strain rates is shown in Figure 3. Away from the fault the strain rates and orientations are virtually the same on either side of the fault. The plate motion implies a component of compression normal to the fault, but the strain results show that compression is not a factor directly at the plate boundary. This pattern of strain is consistent with the observation of fault-normal compressive stress reported by Zoback et al. (1987). They propose that the SAF is a weak fault and therefore is able to reorient the stresses to fault-normal compression. In contrast to the SAF in central and northern California, here in the western Transverse Ranges fault-normal compression is the proper orientation for plate motion. But these geodetic results concur with the idea of a weak SAF since the strain along the fault does not indicate compressive strain, but rather shows nearly pure shear.

DISPLACEMENT SOLUTIONS

In order to consider the individual stations in the network and to observe spatial variations not apparent in the uniform strain solutions,

displacement fields can be determined from the line-length data. As described by Prescott (1981), this is a non-unique problem so that a constraint must be included to select the most appropriate solution. Two standard ways are the inner-coordinate solution, that minimizes the rotation of all stations, and the outer coordinate solution, that minimizes displacement normal to a preferred direction for fault-slip. Segall and Matthews (1988) have recently proposed using a more general constraint where the preferred direction at each station is taken from the displacement field of any given fault-slip model.

The outer-coordinate solution is the most common since it only requires the simple, yet reasonable, assumption of a preferred slip direction, and it yields displacement vectors that can readily be compared to plate motion velocities and to fault locations and orientations. The displacement parallel to the fault can be modelled with analytic solutions (Prescott et al., 1981) for slip on a single fault locked above a given depth as discussed above

$$\dot{u} = \frac{-\dot{b}}{\pi} \tan^{-1}\left(\frac{x}{d}\right) \qquad (2)$$

or for distributed shear over a zone from -w to +w,

$$\dot{u} = \frac{\dot{b}}{2\pi w}\left[(x-w)\tan^{-1}\left(\frac{x-w}{d}\right) - (x+w)\tan^{-1}\left(\frac{x+w}{d}\right) - \frac{d}{2}\ln\left(\frac{d^2+(x-w)^2}{d^2+(x+w)^2}\right)\right] \qquad (3)$$

We begin our analysis by using the outer coordinate solution and consider constraining directions, perpendicular to which the displacement is minimized, that range from N39°W, the plate velocity direction, to N73°W, the local orientation of the SAF across our networks. Figures 4 and 5 show mapviews and cross-sections of solutions with N39°W and N73°W constraints, respectively. The normal components of station displacement are much smaller for the N73°W constraint than for the N39°W constraint (compare Figure 5c to Figure 4c). Also the component parallel to N39°W varies linearly

with distance and does not show the type of arctangent decay expected for movement due to fault slip (Equation 2). The N73°W parallel component does decay with distance although, as discussed below, the points are more scattered than expected for characteristic deformation due to a single fault. Thus the N73°W constraint seems most appropriate.

In comparing the Figures 4a and 5a, we see that the displacement solutions are similar in the center of the network but differ by as much as 45° on the periphery where the station distribution does not constrain the solution very much. Both show displacement vectors that roughly parallel the fault strike as one moves around the bend in the SAF. This is most apparent in the Pacific plate, southwest of the SAF, but it is also evident in the North American plate, northeast of the SAF. Along the SAF, the displacements are quite small (as the fault is locked) and are aligned with the fault, except at station Tecuya, which shows a small displacement predominantly normal to the fault in both solutions.

Because there is a trade-off between $\dot{b}$, d and w (Equations 2,3), there is no unique model to describe the Los Padres and Tehachapi displacement field. Deepening the locking depth, d, and extending the width of the shear zone both make the displacement profile flatten out. Increasing the strain rate, $\dot{b}$, will increase the amplitude of the profile, however decreasing d will also effectively increase the amplitude. As shown in the next section, for a single fault inversion of the line-length data can find the statistically best locking depth. In Figure 5b two possible models are shown, one for a single fault slipping below 25 km at 30 mm/yr, and another for a shear zone with 30 mm/yr slip below 20 km distributed over a region extending 25 km on each side of the fault. It is not possible to distinguish between these markedly different models.

Note that the stations that poorly fit the single fault model tend to be those stations that are away from the N73°W segment of the SAF. Those stations are indicated by triangles in Figure 5b. More realistic fault models with multiple segments will improve the fit at these stations.

Despite their simplicity and nonuniqueness, the single fault models point out two important features of the Los Padres-Tehachapi displacement field. The displacements are primarily due either to a single fault or shear zone centered below the surface trace of the San Andreas, and the locking depth is relatively deep. For a single fault, the open circles in Figure 7c and 7d show the rms fit of the data plotted versus the slip, $\dot{b}$, and the locking depth, d. The trade-off between $\dot{b}$ and d is evident. The locking depth is at least 20 km and for a single fault 25 or 30 km is preferred. This contrasts with the 16 km locking depth computed for the Parkfield segment of the SAF, located to the northwest (King, et. al, 1987).

These locking depths are relatively deep compared to the base of the brittle zone, usually estimated at 10 to 15 km. Li and Rice (1987), by coupling the freely slipping lower fault to the mantle through a viscoelastic intracrustal asthenospheric layer, explain why apparently deep locking depths may be observed late in the earthquake cycle. They compute a broad zone of deformation without having a wide shear zone or deep locking depth. Continuous deep-seated mantle motion, at the plate velocity rate, loads the crust and the elastic upper crust ruptures only during earthquakes, but on the lower fault slip varies with time, slipping rapidly following an earthquake and slowly before the next earthquake. Their rheological model, interpreted in terms of our simple dislocation model, also gives somewhat higher slip rates. For the Tehachapi area they have 32 mm/yr of slip in the upper mantle coupled through a viscoelastic asthenosphere to a freely slipping lower fault

from 9 to 25 km. At a time 77% of the way through the earthquake cycle, a broad region of asthenosphere accommodates the deep slip so that the lower fault zone is slipping at only about 5 mm/yr. If such a low level of slip is occurring above 25-km depth, it would have little effect on the estimate of locking depth in our simpler models. Li and Rice's results should be kept in mind, since all of our locking depths could be shallower if we considered a more complicated rheological model. However in order to study more complicated fault geometries, we have modeled faults as having only locked and freely slipping zones.

MULTIPLE FAULT SLIP SOLUTIONS

While modeling with a single fault can provide some useful insights, clearly this region is characterized by numerous fault segments of varied orientation. The San Andreas changes its orientation markedly across these networks, and other adjoining Quarternary faults, such as the Garlock and Big Pine, strike through the area at angles completely different from the SAF.

In order to include many fault segments of any given orientation and sense of slip, we used the program of Savage et al. (1979) to invert for multiple fault slip. The segments tested are shown in Figure 6. The SAF is divided into three segments: a semi-infinite N40°W segment, the local N73°W segment, and a semi-infinite N63°W segment. Since we are modeling deep slip, small segments contribute little to the total slip and greater detail of the fault bend is not necessary. Secondary faults were also considered. For the SAF, Garlock, and Big Pine faults, the results of this analysis were fairly stable regardless of changes in fault parameters and so these are the only faults discussed in the solutions for this set of geodetic data. With this data we were unable to resolve slip on other faults tested.

1. San Andreas Fault

For comparison, we initially did a series of solutions for slip on a single fault, striking N73°W with d of 15 to 30 km. As mentioned above, the residuals for these were all similar, although the d=25 solution is slightly better. This solution is similar to the forward model estimated in Figure 5b (solid line). The locking depth primarily effects the slip rate: d=25 km gives a calculated slip of 26 mm/yr while d=15 km gives 18 mm/yr.

Next we approximated the SAF with the three segments described in Figure 6. However our network does not constrain the slip on the two semi-infinite segments very well as along these segments there are only a few stations near the ends. The simplest assumption is to have a uniform rate of slip on the whole length of the SAF. Thus we decided to fix the slip on the two end segments to be the same as the slip that is computed for the middle segment.

Figure 7 shows, for a wide range of multiple fault models, the slip rates and locking depths plotted versus the rms residual of each model. Each type of model is shown with a different symbol and the rms error is shown for the calculated slip rates. There is clearly a dramatic decrease in rms residual when the SAF is modelled with three segments instead of one. For the 3-segment SAF, models are shown for locking depths of 15 to 40 km. The deepest d, 40 km, is statistically the best since it has the lowest rms residual. There is little difference with d from 25 to 40 km, but the fits for models with d less than 25 km are noticeably worse. For d=25 km, the computed slip rate is 30 $\pm$ 6 mm/yr. Figure 8 shows the calculated velocities for the fit to d=25 km, as well as the residual velocity vectors computed from the set of individual line-length residuals. (The residual velocities are plotted at a scale roughly 3-times larger than the model velocities.) Since the model serves to remove the fault-

related displacements, there should not necessarily be any remaining systematic displacement, and hence the inner-coordinate solution is used to compute the residual velocity vectors (J. Savage, oral communication, 1988). Note that in order to compute a displacement solution we can only use a closed network. Hence stations that have only one line are not used in Figure 8b, although they are used in the inversions for fault slip. Particularly large residual velocities remain at station Caliente, on the northwest edge of the network, and at many stations in the area between the SAF and Garlock faults.

2. Including Garlock fault

The displacement field of a secondary fault segment will be distinct from that of the SAF. It may have different directions of displacement due to its different fault orientation, may be quite varied spatially if the segment ends in the middle of the network, and may have much lower magnitude of displacement if the segment is not an infinite fault. These factors are all shown by the Garlock Fault, when we look at displacement due to slip only on that fault, in Figure 9a. Hence by superimposing displacement due to the SAF and Garlock, the inversion may better fit the line-length data.

On the northeast side of the SAF the Garlock fault is the primary fault through our network. As discussed above, it has an ideal orientation for slip in the off-fault strain solution. To assess possible slip on the Garlock, we ran a series of models with the SAF locking depth (d_{SAF}) from 20 to 30 km and the Garlock locking depth (d_{Gar}) from 0 to d_{SAF} . Models with the Garlock Fault and the 3-segment SAF were significantly better than those with the 3-segment SAF alone. The addition of the Garlock fault resulted in a 14% reduction (0.4 mm/yr) in rms residual. For all d_{SAF} there is little difference in rms residual for d_{Gar} from 5 km to 25 km, although d_{Gar} less than 5 km have much poorer fits (open squares in Figure 7e). The best combination is d_{SAF} of 25 km and d_{Gar}

of 10 km, with computed slip rates for the SAF of 32 ± 6 mm/yr and for the Garlock of 11 ± 2 mm/yr. For d from 5 to 25 km, the computed slip on the Garlock ranged from 8 to 20 mm/yr. The slip on the Garlock has fairly low rms error (open squares in Figure 7b) and does not have much effect on the SAF slip rate (open squares in Figure 7c). Thus the Garlock fault is fitting a different component of the observed strain field than the SAF.

For the combined Garlock and SAF, the calculated velocities and residual velocities are shown in Figure 10. The most noticeable difference (compared to Figure 8) is in the Mojave area, where the velocity vectors point away from the two faults instead of simply parallel to the SAF. There is also some improvement in residual velocities north of the Garlock fault and at Caliente.

3. Including Big Pine

The Big Pine fault is a left-lateral fault across the Los Padres network. It is considered by Wesnousky (1986) to be an active fault with a modest slip rate, on the order of 1 mm/yr. As shown in Figure 6, we model it as two segments since it changes orientation across our network. We use a fault length equivalent to the mapped surface trace, although a longer or semi-infinite fault would fit the data as well and would give a much lower slip rate. Figure 9b shows the displacement for slip on the Big Pine fault alone. Due to its short length, it contributes much less displacement than the SAF or Garlock. But the spatial pattern is quite distinct from that of the SAF (Figure 8a) or the Garlock (Figure 9a), and hence it may improve the fit in the inversion solution.

Inversions were done for slip on the Big Pine varying its locking depth, d_{BP}, from 10 km to d_{SAF}, with d_{Gar} of 10 km and d_{SAF} of 20 km and 25 km. The inclusion of the Big Pine significantly improved the fit to the data. The addition of the Big Pine fault reduced the rms residual by 15 % (0.4 mm/yr). This is the same amount of improvement contributed by the Garlock fault. Its

inclusion also slightly reduced the computed slip on the Garlock (solid squares in Figure 7b) and slightly increased the slip on the SAF (solid squares in Figure 7c). As shown in Figure 7f, the best fit is for the deepest d_{BP}, 25 km. Because the modeled fault segment is relatively short, varying the locking depth caused large variations in the slip rate (Figure 7a). In all cases slip on the eastern segment was about 13 mm/yr less than on the western segment. For d_{BP} of 25 km, the computed slip rates are 43 ±16 and 31 ±12 mm/yr for the west and east segments respectively, or 39 ± 15 mm/yr for slip constrained to be equal on both segments. The calculated displacements and residual displacements for this model are shown in Figure 11. Caliente remains the station with the largest residual.

While the statistical reduction in residuals for this solution is significant, the high slip rate on the Big Pine and the relatively deep locking depth compared to the Garlock make this specific solution appear improbable. However we can clearly say that the geodetic data favor a non-trivial amount of left-lateral slip on the Big Pine fault at depth. The large amount of slip could be reduced if more faults similar to the Big Pine were added to the model or if the Big Pine fault was considered to be longer than its mapped surface trace. For example if it were modeled to be semi-infinite like the Garlock, its computed slip rate would be reduced to a few mm/yr. Also its locking depth could be reduced if it was considered to be a shear zone at depth rather than a single planar fault. Thus, the Big Pine fault is important, but probably something more than slip along the simple fault trace is going on.

4. Are Garlock and Big Pine major faults that break the lithosphere?

All of the multiple fault segment models discussed above assume that the additional faults behave similarly to the SAF. That is, they extend throughout the thickness of the lithospheric plate and slip continuously below the brittle-

ductile transition. Alternatively the surface faults could end abruptly within the crust and the lower crust/mantle could deform independently, thus creating some sort of regional horizontal detachment at the brittle-ductile transition. In their interpretation of a CoCorp seismic reflection line across the eastern portion of the Garlock fault, Cheadle et al. (1986) suggest that the Garlock fault does not extend below 9 km. Contradicting this, Astiz and Allen (1983) find that the Garlock is a seismically active fault, with earthquakes occurring down to 15 km (typical depths for earthquakes along the SAF) but clustering at about 7.5 km depth. They infer that the western portion, through the Tehachapi geodetic network, is creeping, but that there is potential for large earthquakes on the eastern portion. They estimate the Garlock slip rate to be approximately 7 mm/yr, similar to the 6 to 11 mm/yr that we compute for a 10-km locking depth.

To investigate this issue, we ran a series of models with the Garlock fault having finite depth extent. The upper locking depth varied from 5 to 10 km, and the vertical width of the slipping fault segment varied from 10 to 25 km. These all had slightly higher rms (by about 0.1 mm/yr) residuals than the models discussed earlier with unlimited depth extent (Figure 7b,e; Table 2). For models with the upper locking depth at 5 km, the slip rate is about 10 mm/yr, similar to our earlier models, but with the upper locking depth at 10 km, the computed slip rate nearly doubles. The best fit is obtained with slip confined to a depth interval of 5 to 30 or 5 to 25 km. A few models were tried with even shallower upper locking depth, but the fit was sharply degraded. Thus, while the best fitting Garlock fault extends throughout the lithosphere, the geodetic data can be reasonably fit by a fault extending only through the crust to 25 km. The geodetic data cannot be fit by a Garlock fault that only extends to 9 km depth, as suggested by Cheadle et al. (1986).

The Big Pine fault could be extended to join with the Rinconada fault zone, which trends roughly parallel to the SAF and is considered to have a few mm/yr of right-lateral slip (Wesnousky, 1986). Thus the Big Pine fault could be considered to form the southern boundary of Salinia, an accreted terrane which paleomagnetic data suggests may have been transported 2500 km (Champion, et al., 1984). Page (1982, 1987) considers that Salinia probably encompassed the whole lithosphere when it travelled long distances, although it may now be a crustal "flake".

In block tectonic models, the Big Pine fault has been used as the active boundary of the Salinian block by several authors. In Hill's (1982) construction, the Big Pine is the boundary between the Salinian and western Transverse Ranges blocks. Bird and Rosenstock (1984), in their detailed kinematic block model of southern California, include a fault similar to the Big Pine with 6 to 9 mm/yr of right-lateral slip. Interestingly, they consider the eastern corner of the Salinian block to be a separate block, the Carrizo Plain block. This small additional block would contain the station Caliente, which was poorly fit by our multiple fault models. Cheng et al. (1987) used a different approach than ours to invert geodetic data, by including every possible fault or boundary, even those that are poorly constrained by geodetic networks. They invert for block motion and fault slip in a detailed model similar to that proposed by Bird and Rosenstock (1984), and used Bird and Rosenstock's slip rates and a locking depth of 10 $\pm$ 5 km as prior estimates. In Cheng et al.'s final model, the Big Pine fault has an eastern segment with negligible slip and a western semi-infinite segment with 4.7 $\pm$ 3.1 mm/yr of left-lateral slip. However they note that it could be left out of the solution without degrading the fit very much.

Based on our analysis, we can only say that our solution is consistent with the idea that the Big Pine fault is an active left-lateral boundary of the Salinian block; particularly if the modelled fault was made longer so that the large computed slip rate could be reduced. Since the best locking depth for this fault was relatively deep, 25 km, it could not be fit with a fault of limited depth extent, such as was done above for the Garlock. So a throughgoing lithospheric fault may be favored. On the other hand either a broad shear zone or a detachment surface may better explain the elastic weakness of the southern plate. We investigate the effect of a detachment surface in the next section.

DETACHMENT SURFACE

Hearn and Clayton (1986) find that the lateral velocity variations in the lower crust do not correlate with surface features and hence they conclude that the lower crust and mantle must be decoupled from the upper crust. Weldon and Humphreys (1986) propose a detachment under the entire region southwest of the SAF allowing an upper southern California block to freely rotate counterclockwise over the lower part of the Pacific plate. They suggest 23 mm/yr of convergence, oriented N5°W, across the western Transverse Ranges. Davis and Yerkes (1988) take the step of putting together a specific detailed geologic cross-section across the western Transverse Ranges. They have a regional horizontal detachment surface at about 15 km with the upper plate moving south relative to the lower plate, which proceeds to subduct under North America.

We included a fairly simple sub-horizontal fault that could be put in as an additional fault segment to the SAF and Garlock model. It is a rectangular surface approximating Weldon and Humphreys' detachment. It strikes N73°W, so that it encompasses the region south of the SAF in this area, and it extends

200 km along the SAF and 120 km toward the ocean. Faults dipping 7° to the north and 7° to the south were tried, and the north-dipping fault fit the data somewhat better. Both dip-slip and strike-slip displacement were allowed, so that the direction of slip would not be tightly constrained by the strike direction.

How such a detachment fault influences displacement is illustrated in Figure 12 by the displacement fields for 30 mm/yr of thrust and right-lateral slip. The direction of displacement is uniform, but the magnitude of displacement decreases at stations located, north of the SAF, away from the detachment surface. Before we even do the computations, it is apparent that this horizontal feature is not a major tectonic component since the displacement residuals, Figure 10b, do not have a uniform direction.

Of the models we tried, the best fitting solution, included in Table 2, had 1 ± 2 mm/yr of normal dip-slip and 5 ± 4 mm/yr of right-lateral strike-slip on a north-dipping fault, dipping 7°N from the surface to a depth of 15 km at the SAF. While these values are poorly constrained, they are not similar to Weldon and Humphreys' in either direction or magnitude. When we tried a fixed amount of convergence of 23 mm/yr the fit was very much degraded and left-lateral slip was computed for the SAF. However we found that we could adjust the location, strike and dip of the detachment surface to get solutions with almost any slip, reverse or normal, right or left lateral. For example, with an overall deeper south-dipping surface, dipping 7°S from 10-km depth on the SAF, we computed 21 ± 11 mm/yr thrust and 103 ± 52 mm/yr right-lateral strike-slip. Therefore we cannot really use this geodetic data to confirm or deny a detachment.

LOCATION OF SAN ANDREAS FAULT AT DEPTH

Sheffels and McNutt (1986) use a flexural plate model of two plates with a load attached to the end of the southern plate to approximate a subducted slab. In order to match the gravity profile, they put the plate boundary south of the surface trace of the SAF by several tens of km. In their constructed western Transverse Range cross-section, Davis and Yerkes(1988) also place the SAF at depth 20 km south of its surface trace.

Since we are using geodetic networks that extend over 40 km either side of the SAF, we can use the geodetic data to help resolve the issue of the fault location at depth. We tested models with the SAF located 10, 20 and 30 km south of its surface, as well as one model with the fault dipping 60° to the south. Because it is difficult to imagine how such segments would connect with the adjoining N40°W trending SAF segment and the Garlock fault, we ran simple models with only a single infinite SAF segment. The results are shown as solid circles in Figure 7c, d. All of the off-trace SAF solutions are significantly worse than any of the other one-segment SAF solutions. Therefore we can conclude that the plate boundary at depth is not located away from the mapped SAF, but rather is directly below the surface trace.

However it is intriguing that both Sheffels and McNutt's "subduction" feature and Humphreys' "drip" feature both are east-west striking sub-surface features located south of the SAF in the western Transverse Ranges. They explain that this feature is due to the component of compression resulting from the mismatch between the local SAF orientation and the plate-motion direction. We decided to look at this residual plate motion in detail.

We will consider that at some depth below the fractured brittle crust, the Pacific and North American plates are large continuous plates moving N40°W and S40°E, respectively, at 48 mm/yr (DeMets et al., 1987), and that along the

plate boundary away from the Big Bend, the SAF takes up this motion perfectly. Near the Big Bend, there will be a residual displacement field resulting from the plate motion that cannot be accounted for by movement on the SAF. A map of this is shown in Figure 13. Note that, in the western Transverse Ranges, the area with the largest amount of residual displacement is not centered along the SAF, but is centered far south of the SAF. In particular, if we look for the area with the largest gradient in residual displacement, it is very similar to the location of Humphreys' high-velocity feature.

Therefore we propose that the location of the east-west striking sub-surface feature is not at all surprising, but rather is very similar to what we would expect to be caused by deep slip on a SAF plate boundary extending below the surface trace. Since Sheffels and McNutt have shown that a subducting slab model does not fit the mapped SAF location, our conclusion favors some other sort of mechanism for mantle downwelling, such as Humphreys' (1987) thermal instability/drip ideas. Perhaps the gravity could also be fit by a plate, broken at the mapped SAF, but with the subsurface load distributed away from the end of the southern plate.

SUMMARY

In the region of the Los Padres-Tehachapi geodetic network, the San Andreas fault changes its orientation by over 30° from N40°W, close to that predicted by plate motion for a transform boundary, to N73°W. The geodetic data can be used to tell us where the fault is located at depth and what type of motion occurs on the SAF and secondary faults, as well as provide insight into the relationship between the SAF plate boundary and plate motion.

The strain orientation near the SAF is consistent with right-lateral shear along the fault. In contrast, away from the SAF the strain orientations

on both sides of the fault are consistent with fault-normal compression. We divided the network into along-fault and off-fault subnets and then calculated the strain, uniform in space and time, for each subnet. The strain rates along-fault showed maximum shear of 0.38 ± 0.01 μrad/yr at N63°W. The off-fault shear strain is smaller and is oriented more northerly than along-fault. Virtually identical strain rates are found for the two off-fault subnets, on either side of the SAF, with maximum shear of 0.19 ± 0.01 μrad/yr at N44°W. The local fault orientation apparently controls the strain along the SAF, while the overall plate motion direction dominates the strain away from the fault. Thus the compressional component of plate motion is not a factor directly at the plate boundary.

The geodetic data indicates a relatively deep locking depth on the SAF and a slip rate of approximately 30 mm/yr. A solution for station displacement vectors has been obtained from the geodetic data and the local SAF orientation. The dominant features of the displacement field are the change in direction across the SAF and the increase in magnitude away from the fault, both characteristic of SAF slip at depth. Since the strain rate does not drop off rapidly away from the fault, but is still 50% of the along-fault value, the area is fit by either a broad shear zone below the SAF or a single fault with a relatively deep locking depth. For instance, a 50-km-wide zone below 20 km depth with 30 mm/yr of distributed shear or a single fault with 30 mm/yr of slip below 25 km are reasonable. Through an inversion of the line-length data, we modelled the SAF with a more realistic varied orientation that fits the data significantly better than a fault of uniform orientation. We divided the SAF into three segments: the local N73°W segment and two adjoining semi-infinite segments. The fit is poor for locking depth, d, less than 25 km. For d

of 25 km, the computed slip rate is 30 ± 6 mm/yr and the rms residual is 3.1 mm/yr.

We also computed multiple fault slip models that included the Garlock and Big Pine faults, in addition to the SAF. Other faults were unconstrained by the Los Padres-Tehachapi network.

The best fitting Garlock fault model had computed slip of 11 ± 2 mm/yr below 10 km and had an rms residual of 2.6 mm/yr. The data also could be reasonably fit with a Garlock fault extending only through the crust from 5 to 25 km. Thus the Garlock fault may be a significant feature breaking the lithosphere, but even if limited to the crust, it is still an important fault accumulating about 10 mm/yr of slip and may have potential for a large earthquake.

Left-lateral shear deformation is indicated within the western Transverse Ranges. On the southern side of the SAF, the Big Pine fault is probably an active fault. The addition of this fault resulted in an rms residual of 2.2 mm/y for 39 ± 15 mm/yr of slip below 25 km, or 15 ± 6 mm/yr of slip if the Big Pine was a semi-infinite fault. The Big Pine fault runs through the Los Padres network and is the fault that provides the most significant reduction in line-length residuals, however the plate on the southern side of the SAF is relatively weak and the deformation there is probably more complicated than a single vertical fault below the mapped Big Pine. Since the locking depth is deep relative to the Garlock, perhaps a broad shear zone would be reasonable.

The remaining rms residual, about 2 mm/yr, is similar to the theoretical standard deviation of the rate of line-length change for each line. Forty-two percent of the residuals are less than the theoretical standard deviations, and 82% of the residuals are less than three times the theoretical standard deviations. The lines most poorly fit by the model are to station Tejon32, near

the White Wolf fault, so there may be some unmodelled slip on that fault. The next most poorly fit line crosses the SAF on the edge of the network from Caliente to Pattiway. Variable slip on the SAF and greater detail for the fault-bend geometry might improve the fit for this line.

A much more complicated deformation model could probably reduce the rms residual further, such as done by Cheng et al. (1987). However such models were too non-unique. We tried adding other faults, such as the Santa Ynez, San Gabriel and White Wolf, but their calculated slip was unconstrained and they did not provide any significant reduction in rms residual. Therefore, with this particular data set, the only secondary faults that we can determine to be actively slipping are the Garlock and Big Pine. We cannot say anything conclusive about other faults.

A sub-horizontal detachment on the southern side of the SAF also cannot be well-constrained by this data. For a calculated slip of a few mm/yr we obtained a slight improvement in rms residual. The data could not be fit when we included a large amount of slip, 23 mm/yr, on a regional detachment. However, we found that by adjusting the size, location and depth of the detachment surface, almost any amount of slip could be calculated.

We investigated the location of the SAF since several authors have suggested that the fault at depth is located 20 to 30 km south of the mapped trace. We found that a simple vertical fault below the surface trace fits the line-length data much better than either a dipping fault or a fault located to the south. However there is actually no contradiction between the surface-trace location of the SAF and the Humphreys et al.'s (1984) more southern east-west trending high-velocity feature. The residual displacement, obtained by subtracting the displacement field of SAF motion from uniform plate motion, would predict the observed location of a subsurface compressional feature.

Since a subducting slab does not fit the mapped SAF location (Sheffels and McNutt, 1986), some other sort of mechanism to produce the mantle downwelling is favored.

REFERENCES

Astiz, L., and C. R. Allen, Seismicity of the Garlock fault, California, Bull. Seismol. Soc. Am., 73, 1721-1734, 1983.

Bird, P., and R. W. Rosenstock, Kinematics of present crust and mantle flow in southern California, Geol. Soc. Am. Bull., 95, 946-957, 1984.

Champion, D. E., D. G. Howell, and C. S. Gromme, Paleomagnetic and geologic data indicating 2500 km of northward displacement for the Salinian and related terranes, California, J. Geophys. Res., 89, 7736-7752, 1984.

Cheadle, M. J., B. L. Czuchra, C. J. Ando, T. Byrne, L. D. Brown, J. E. Oliver, and S. Kaufman, in Reflection Seismology: The Continental Crust, edited by M. Barazangi and L. Brown, pp. 305-312, American Geophysical Union, Washington, D. C., 1986.

Cheng, A., D. D. Jackson, and M. Matsu'ura, Aseismic crustal deformation in the Transverse Ranges of southern California, Tectonophysics, 144, 159-180, 1987.

Davis, G. A., and B. C. Burchfiel, Garlock fault: An intracontinental transform structure, southern California, Geol. Soc. Am. Bull., 84, 1407-1422, 1973.

Davis, T., and R. F. Yerkes, The Whittier Narrows earthquake (M=5.9) and its relationship to active folding and thrust faulting along the northern margin of the Los Angeles basin, EOS Trans. Am. Geophys. Un., 69, 261, 1988.

DeMets, C., R. G. Gordon, S. Stein, and D. F. Argus, A revised estimate of Pacific-North America motion and implications for western North America plate boundary zone tectonics, Geophys. Res. Lett., 14, 911-914, 1987.

Hearn, T. M., and R. W. Clayton, Lateral velocity variations in southern California. II. Results for the lower crust from P_n waves, Bull. Seismol. Soc. Am., 76, 511-520, 1986.

Hill, D. P., Contemporary block tectonics: California and Nevada, J. Geophys. Res., 87, 5433-5450, 1982.

Humphreys, E., Mantle dynamics of the southern Great Basin - Sierra Nevada region (abstract), EOS Trans. Am. Geophys. Un., 68, 1450, 1987.

Humphreys, E., R. W. Clayton, and B. H. Hager, A tomographic image of mantle structure beneath southern California, Geophys. Res. Lett., 11, 625-627, 1984.

King, N. E., and J. C. Savage, Regional deformation near Palmdale, California, 1973-1983, J. Geophys. Res., 89, 2471-2477, 1984.

King, N. E., P. Segall, and W. Prescott, Geodetic measurements near Parkfield, California, 1959-5984, J. Geophys. Res., 92, 2747-2766,1987.

Li, V. C., and J. R. Rice, Crustal deformation in great California earthquake cycles, J. Geophys. Res., 92, 11533-11551, 1987.

Page, B. M., Migration of Salinian composite block, California, and disappearance of fragments, Am. J. Sci., 282, 1694-1734, 1982.

Page, B. M., Geology and tectonics of the southern Coast Ranges, central California: Current models and major uncertainties, EOS Trans. Am. Geophys. Un., 68, 1365, 1987.

Prescott, W. H., J. C. Savage, and W. T. Kinoshita, Strain accumulation rates in the western United States between 1970 and 1978, J. Geophys. Res., 84, 5423-5435, 1979.

Prescott, W. H., The determination of displacement fields from geodetic data along a strike-slip fault, J. Geophys. Res., 86, 6067-6072, 1981.

Prescott, W. H., and A. Nur, The accommodation of relative motion at depth on the San Andreas Fault system in California, J. Geophys. Res., 86, 999-1004, 1981.

Prescott, W. H., M. Lisowski, and J. C. Savage, Geodetic measurement of crustal deformation on the San Andreas, Hayward, and Calaveras faults near San Francisco, California, J. Geophys. Res., 86, 10853-10869, 1981.

Prescott, W. H., and S-B Yu, Geodetic measurement of horizontal deformation in the Northern San Francisco Bay Region, California, J. Geophys. Res., 91, 7475-7484, 1986.

Savage, J. C., and W. H. Prescott, Precision of geodolite distance measurements for determining fault movements, J. Geophys. Res., 78, 6001-6008, 1973.

Savage, J. C., W. H. Prescott, M. Lisowski, and N. King, Deformation across the Salton Trough, California, 1973-1977, J. Geophys. Res., 84, 3069-3080, 1979.

Savage, J. C., W. H. Prescott, and G. Gu, Strain accumulation in southern California, 1973-1984, J. Geophys. Res., 91, 7455-7473, 1986.

Segall, P., and M. V. Matthews, Displacement calculations from geodetic data and the testing of geophysical deformation models, submitted to J. Geophys. Res., 1988.

Sheffels, B., and M. McNutt, Role of subsurface loads and regional compensation in the isostatic balance of the Transverse Ranges, California: evidence for intracontinental subduction, J. Geophys. Res., 91, 6419-6431, 1986.

Sieh, K. E., Slip along the San Andreas Fault associated with the great 1857 earthquake, Bull. Seismol. Soc. Am., 76, 1421-1448, 1978.

Weldon, R., and E. Humphreys, A kinematic model of southern California, Tectonics, 5, 33-48, 1986.

Wesnousky, S. G., Earthquakes, Quarternary faults, and seismic hazard in California, J. Geophys. Res., 91, 12587-12631, 1986.

Zoback, M. D., M. L. Zoback, V. S. Mount, J. P. Eaton, J. H. Healy, D. Oppenheimer, P. Reasenberg, L. Jones, C. B. Raleigh, I. G. Wong, O. Scotti, and C. Wentworth, New evidence on the state of stress of the San Andreas fault system, Science, 238, 1105-1111, 1987.

Table 1
Uniform Strain Solutions

Area	Strain Rate Components			Max Shear Strain	Max Shear Orientation	Description
	$\dot{\varepsilon}_{11}$ (μstrain/yr)	$\dot{\varepsilon}_{12}$ (μstrain/yr)	$\dot{\varepsilon}_{22}$ (μstrain/yr)	(μrad/yr)	(degrees)	
L	0.15 ± 0.01	0.01 ± 0.004	-0.13 0.01	0.27 ± 0.01	-46.7 ± 0.9	All Los Padres net
T	0.13 ± 0.01	0.07 ± 0.004	-0.12 0.01	0.29 ± 0.01	-59.6 ± 0.8	All Tehachapi net
L,T	0.15 ± 0.01	0.04 ± 0.003	-0.13 0.01	0.28 ± 0.01	-53.4 ± 0.6	All data
L	0.10 ± 0.01	-0.003 ± 0.01	-0.08 0.01	0.18 ± 0.02	-43.9 ± 2.2	Off-Fault
T	0.09 ± 0.01	-0.005 ± 0.01	-0.10 0.01	0.19 ± 0.01	-43.5 ± 2.1	Off-Fault
L	0.17 ± 0.01	0.01 ± 0.01	-0.17 0.01	0.34 ± 0.01	-47.0 ± 1.1	Along Fault
Le	0.08 ± 0.01	0.07 ± 0.01	-0.18 0.01	0.30 ± 0.02	-58.6 ± 1.8	Excluding Temblor, Caliente, Salisbury
T	0.16 ± 0.01	0.12 ± 0.01	-0.14 0.01	0.38 ± 0.02	-64.6 ± 0.9	Along Fault
Le,T	0.17 ± 0.01	0.07 ± 0.004	-0.16 0.01	0.37 ± 0.01	-62.8 ± 0.7	Along Fault

Table 2
Dislocation Models

Model	rms resid. (mm/yr)	San Andreas d (km)	San Andreas slip rate (mm/yr)	Garlock d (km)	Garlock slip rate (mm/yr)	other fault d (km)	other fault slip rate (mm/yr)	Remarks
A	4.158	25	26 ± 4					1 segment SAF
B	3.185	20	25 ± 5					3 segment SAF
C	3.064	25	30 ± 6					3 segment SAF
D	3.019	30	36 ± 8					3 segment SAF
E	2.648	20	26 ± 4	10	12 ± 2			
F	2.636	25	32 ± 6	10	11 ± 2			
G	2.647	30	37 ± 7	10	10 ± 2			
H	2.766	25	31 ± 6	5 to 15	13 ± 3			limited depth Gar.
I	2.733	25	31 ± 6	5 to 30	10 ± 2			limited depth Gar.
J	2.746	25	31 ± 6	10 to 25	19 ± 4			limited depth Gar.
K	2.234	25	37 ± 5	10	6 ± 2	25	39 ± 15	Big Pine, map trace
L	2.297	25	38 ± 6	10	7 ± 2	25	15 ± 6	Big Pine, semi-infinite
M	2.453	25	41 ±15	10	10 ± 2			Detachment surface, dip 7N, z=15km at SAF
							1 ± 2	Normal dip-slip
							5 ± 4	Right-lateral strike-slip

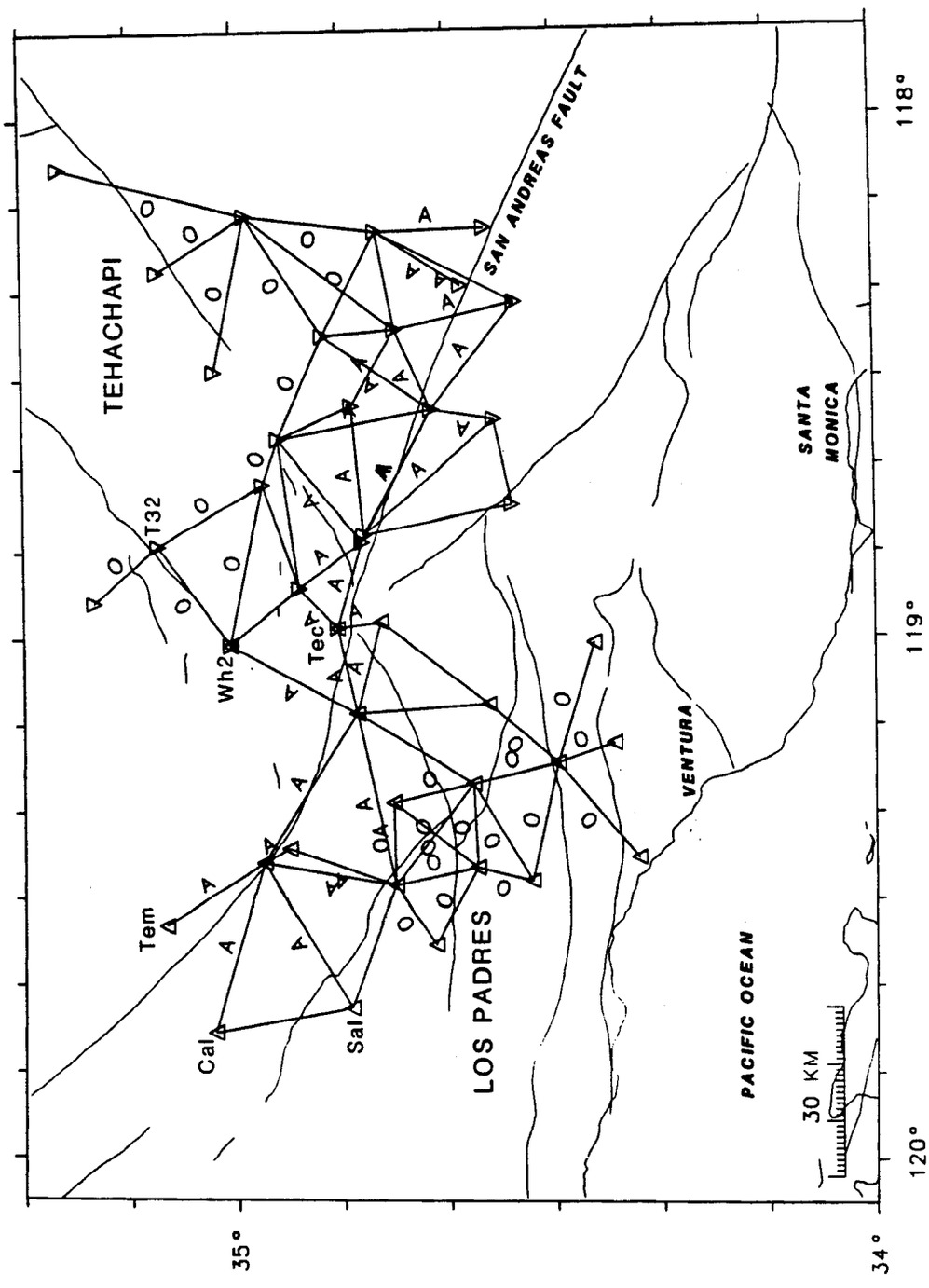

Figure 1. Map of U.S.G.S. trilateration lines used. Upward triangles indicate stations in the Los Padres network, downward triangles indicate stations in the Tehachapi network. Lines marked with 'A' and 'O' were used in 'along-fault' and 'off-fault' subnets, respectively. Stations marked are Cal=Caliente, T32=Tejon32, Tem=Temblor, Sal=Salisbury, Wh2=Wheeler2.

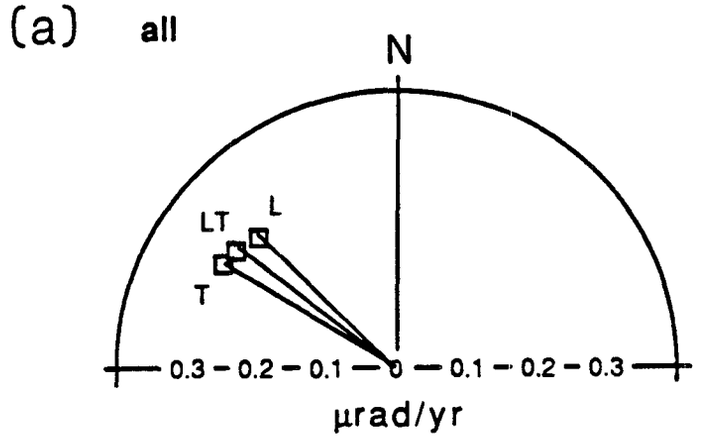

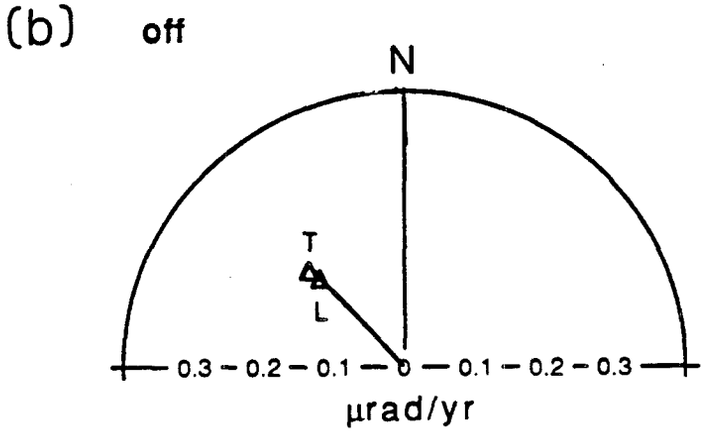

Figure 2. Plots of amount and orientation of maximum shear strain in uniform strain solutions for various subnets. L = Los Padres, T = Tehachapi, LT = combined, Le = excluding stations northwest of bend. a) all data for each network, b) off-fault subnets, c) along-fault subnets.

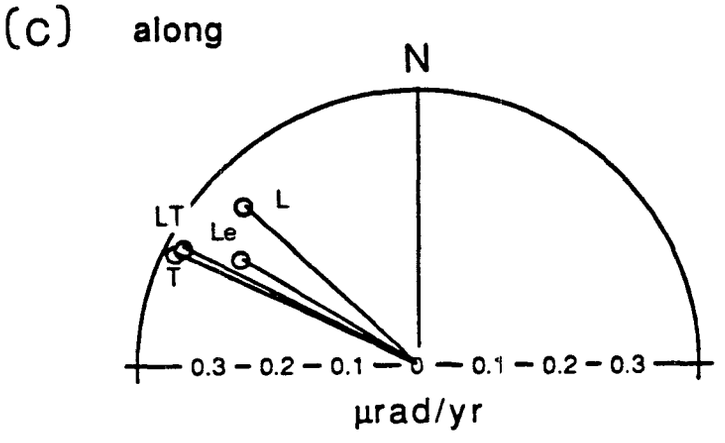

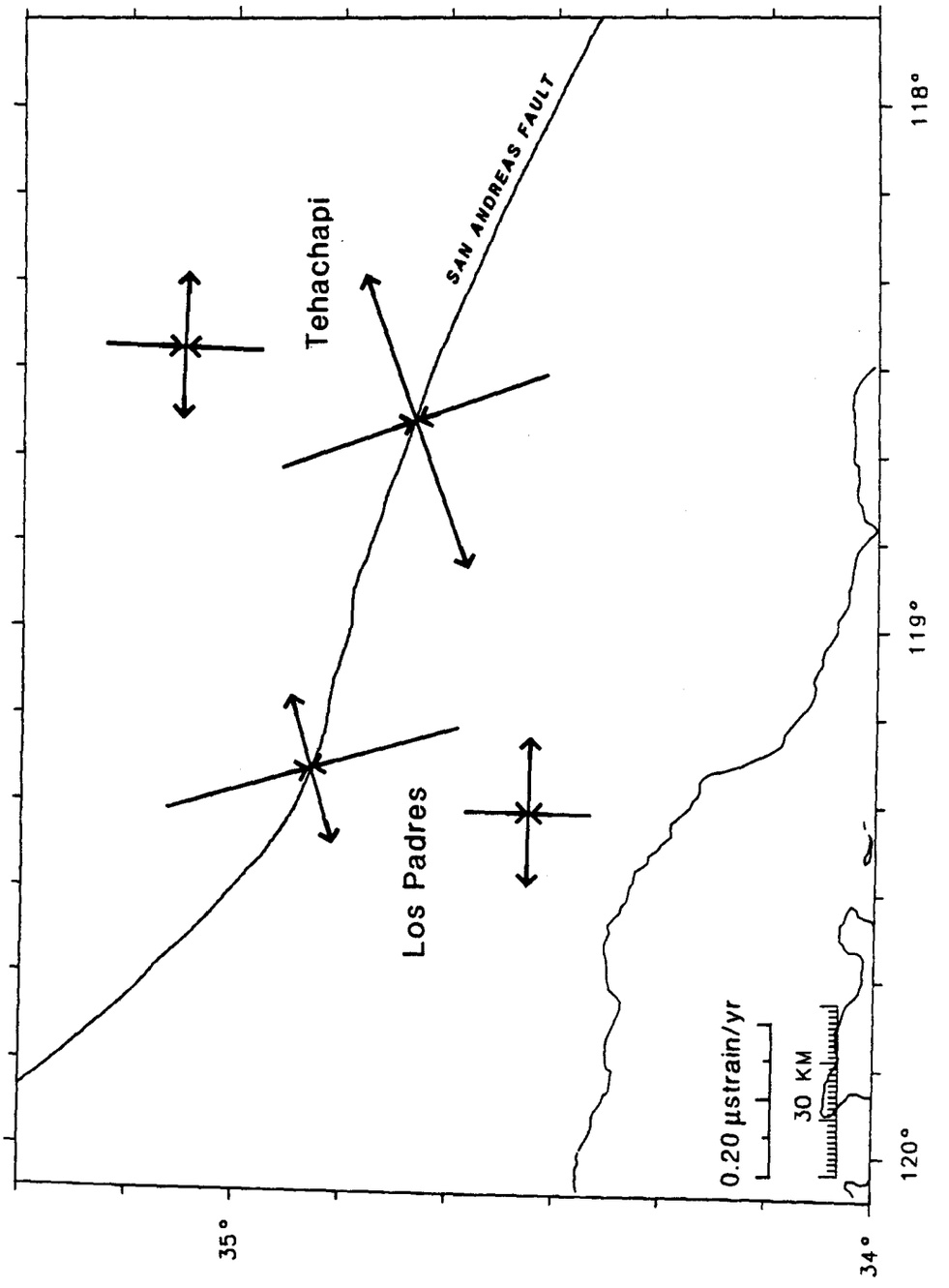

Figure 3.
Principal strain rates for along-fault and off-fault subnets of the Los Padres and Tehachapi geodetic networks, as defined in Figure 1.

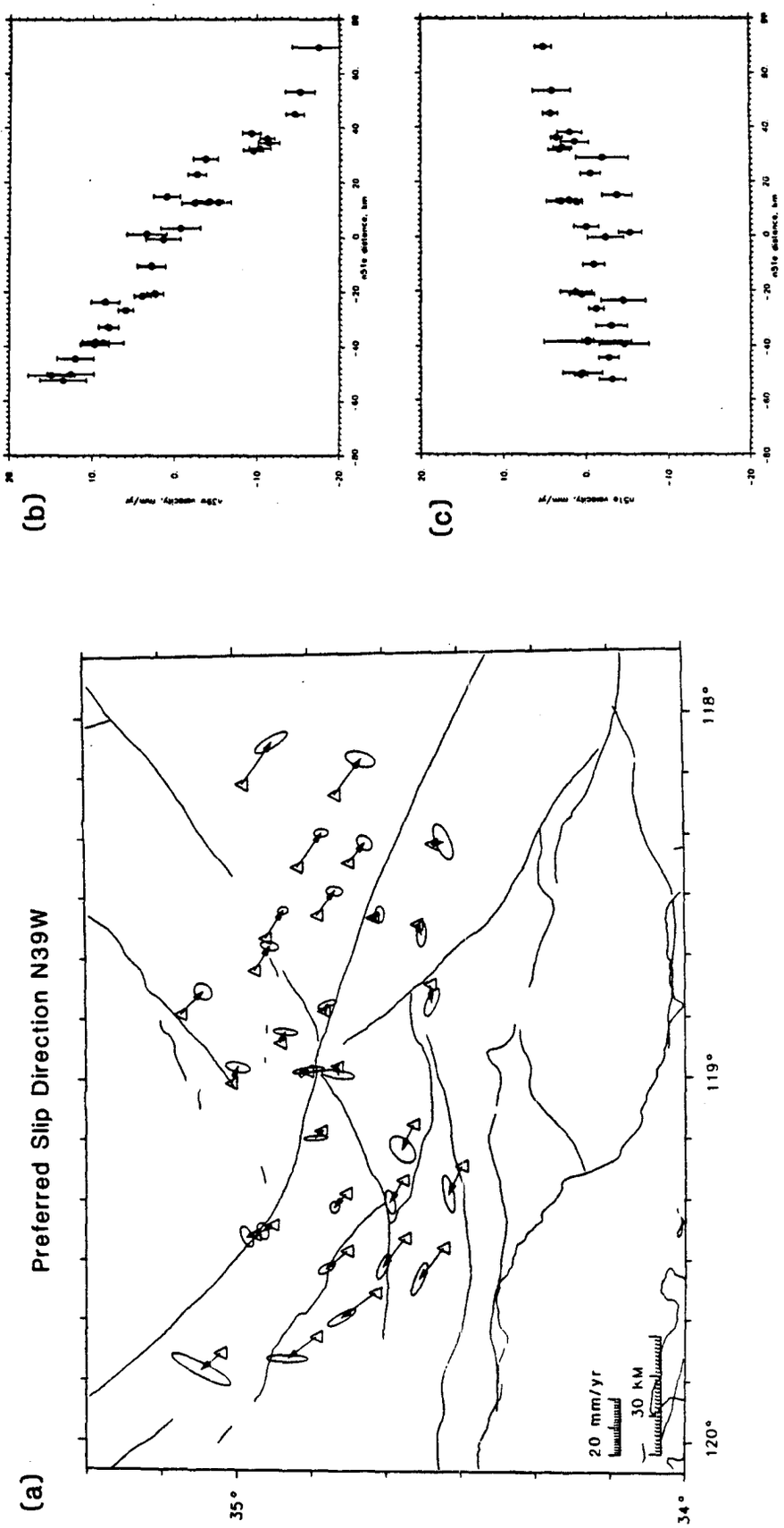

Figure 4. Outer coordinate solution for station velocity vectors, minimizing velocity normal to plate motion. a) Mapview with error ellipses, b) and c) show velocity parallel and normal, respectively, to plate motion for a profile across the plate boundary.

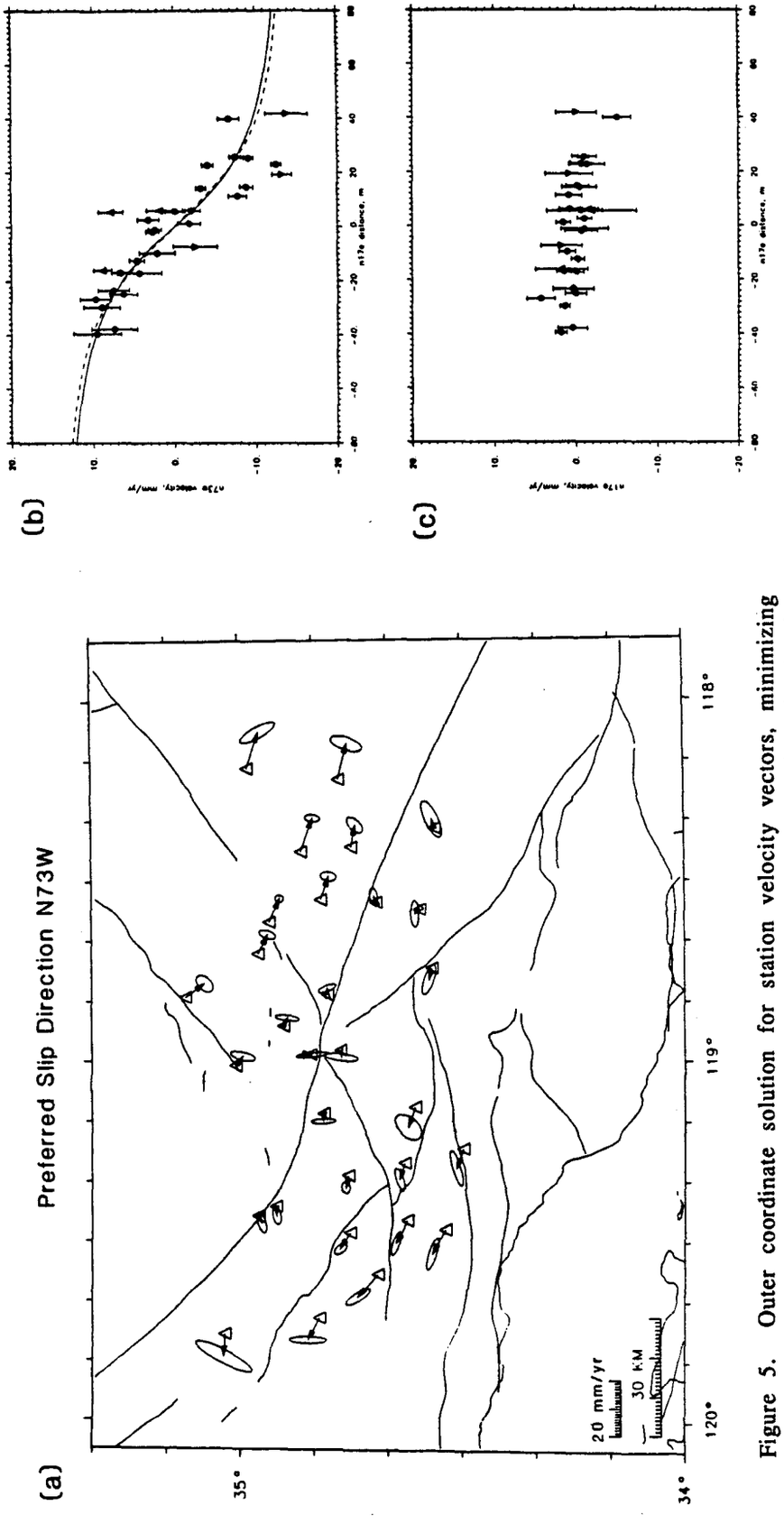

Figure 5. Outer coordinate solution for station velocity vectors, minimizing velocity normal to the local orientation of the San Andreas fault. a) Mapview with error ellipses, b) and (c) show velocity parallel and normal, respectively, to N73°W for a profile across the fault. In (b), the solid line shows the profile for a single fault slipping below 25 km at 30 mm/yr, and the dashed line shows the profile for 30 mm/yr of slip distributed over a 50-km-wide zone below 20 km; upward and downward triangles indicate stations west and east, respectively, of the N73°W segment of the San Andreas fault.

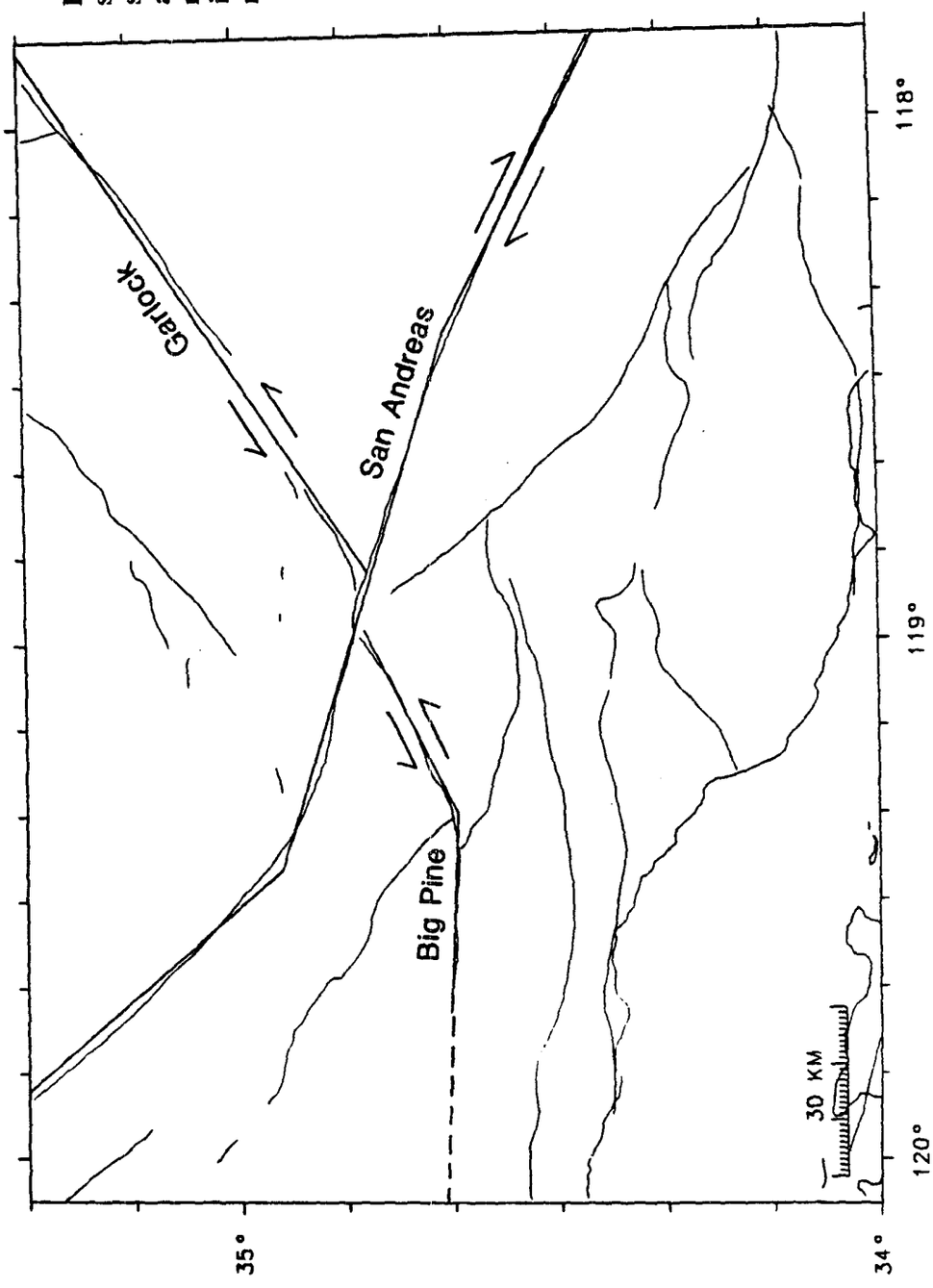

Figure 6. Map showing fault segments, approximated from mapped traces, used in inversions for multiple fault slip.

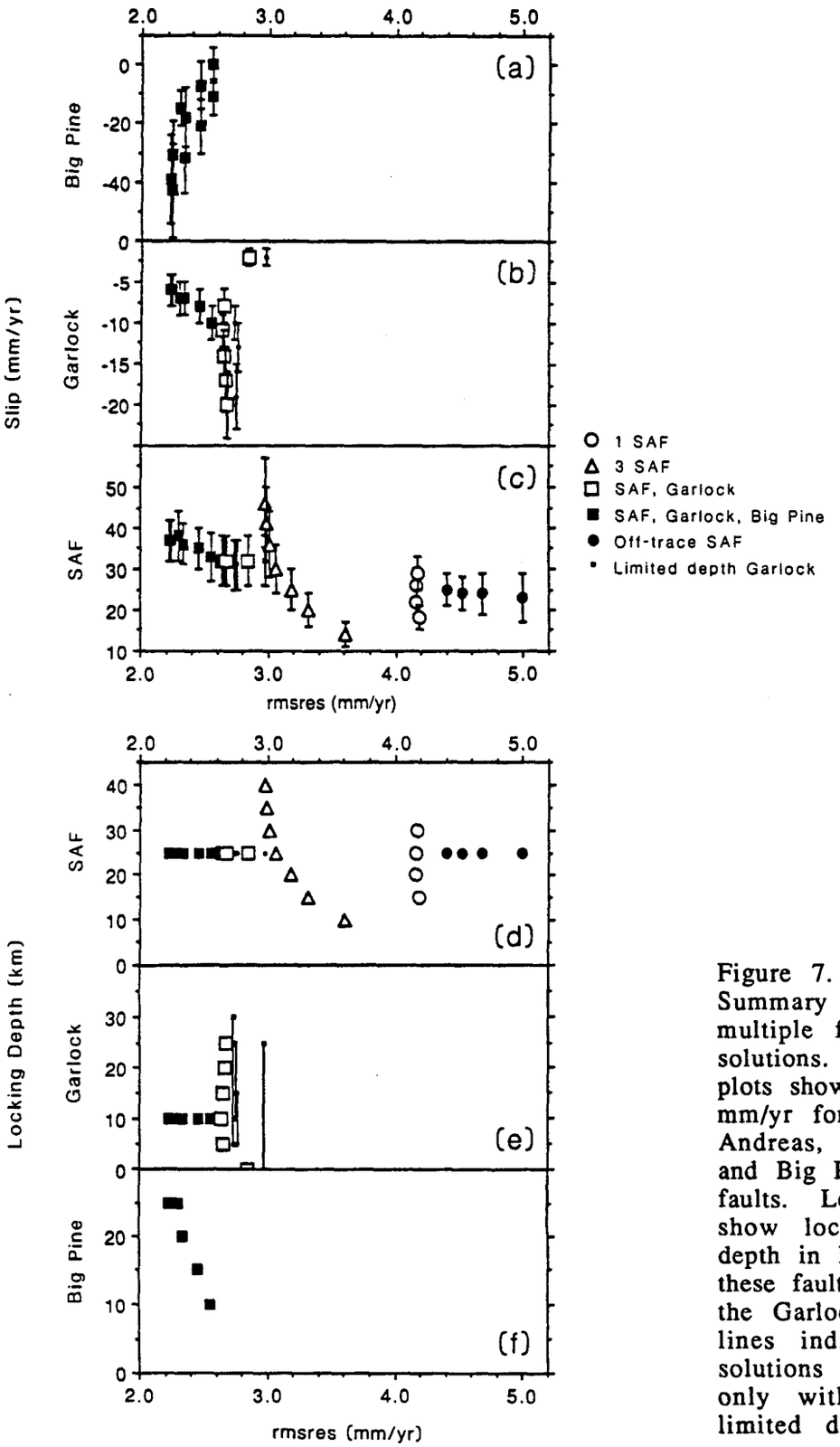

Figure 7. Summary of multiple fault slip solutions. Upper plots show slip in mm/yr for the San Andreas, Garlock and Big Pine faults. Lower plots show locking depth in km for these faults. For the Garlock fault, lines indicate solutions with slip only within limited depths.

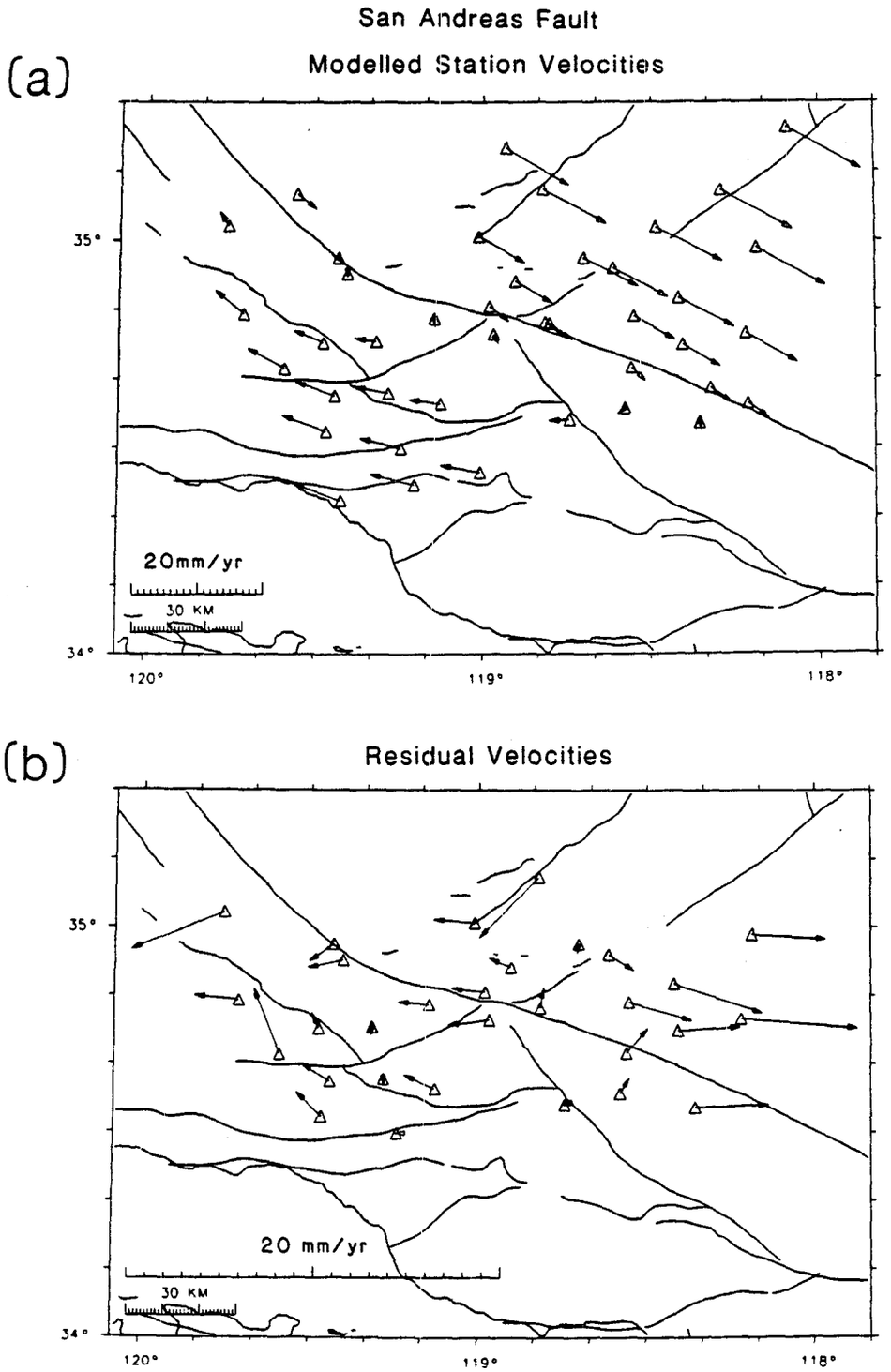

Figure 8. a) Calculated station velocities from 3-segment San Andreas dislocation model, Model C in Table 2. b) Residual velocities computed by using the line-length residuals in an inner coordinate solution; note that only closed lines could be used for this plot. In all these plots, the scale of the vectors is indicated by the 20 mm/yr bar in the lower-left corner.

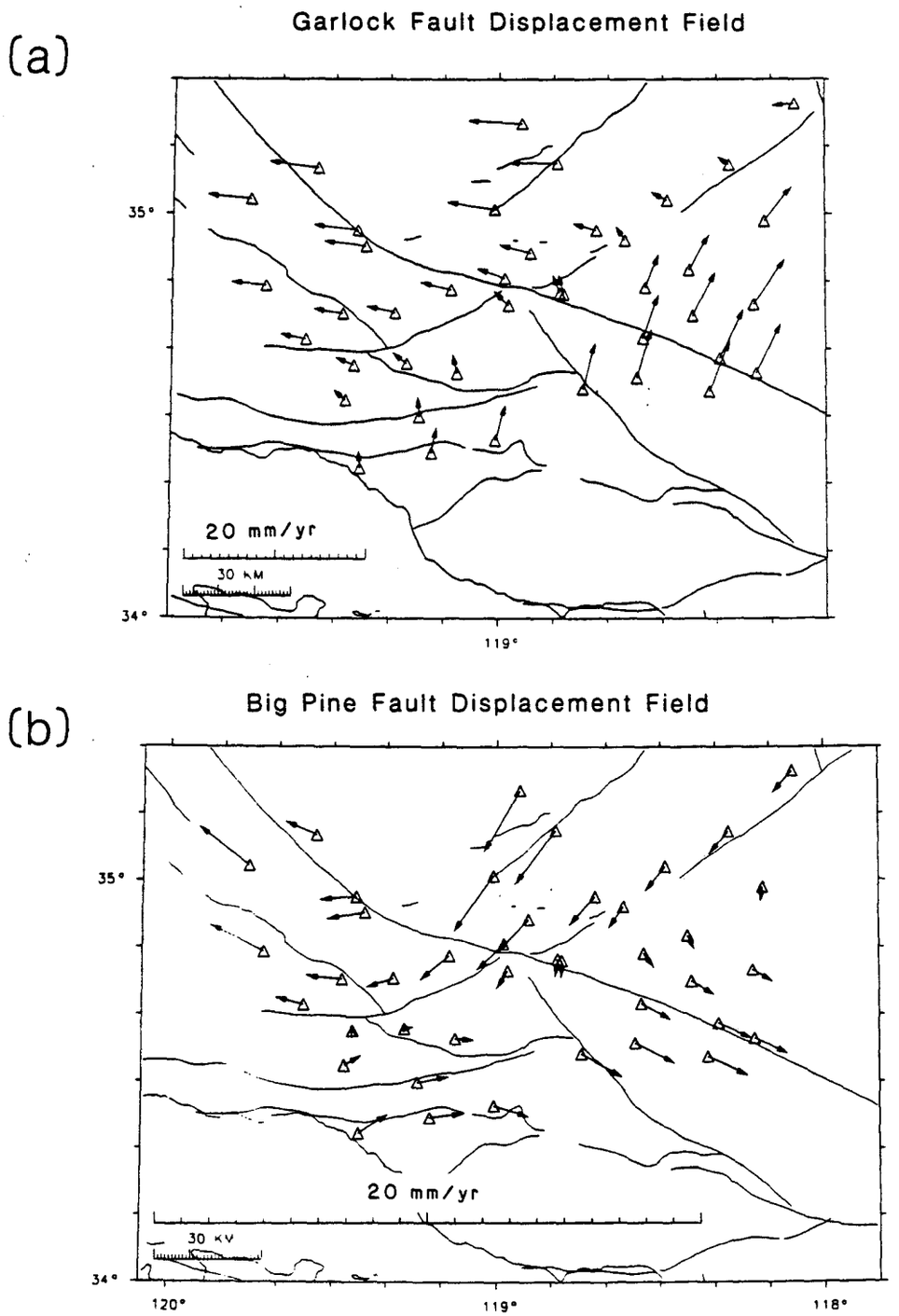

Figure 9. Displacements that would be produced by slip, 30 mm/yr, a) on the Garlock fault only, and b) on the Big Pine fault only.

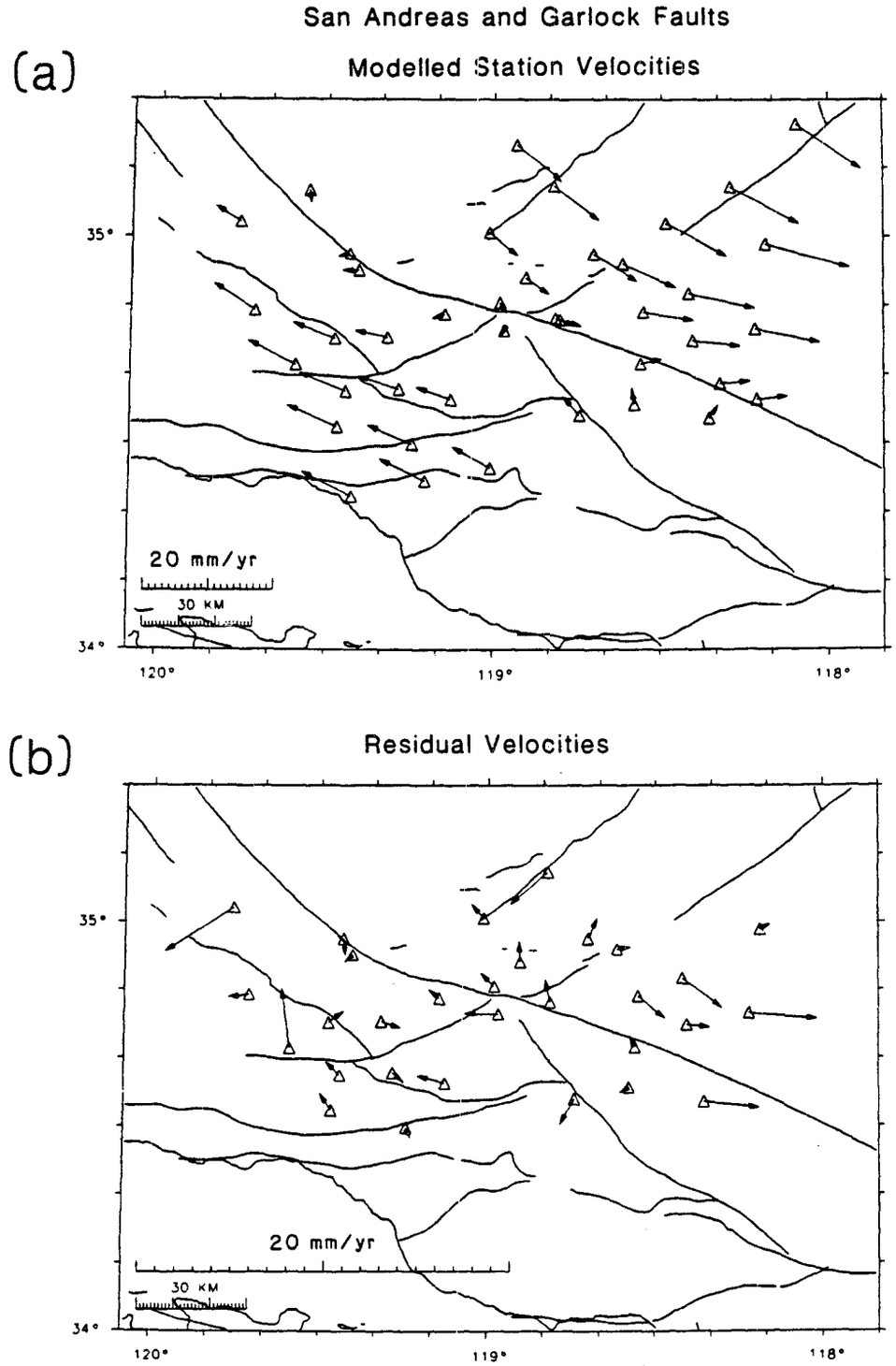

Figure 10. a) Calculated station velocities from Garlock and San Andreas dislocation model, Model F in Table 2. b) Residual velocities computed by using the line-length residuals in an inner coordinate solution.

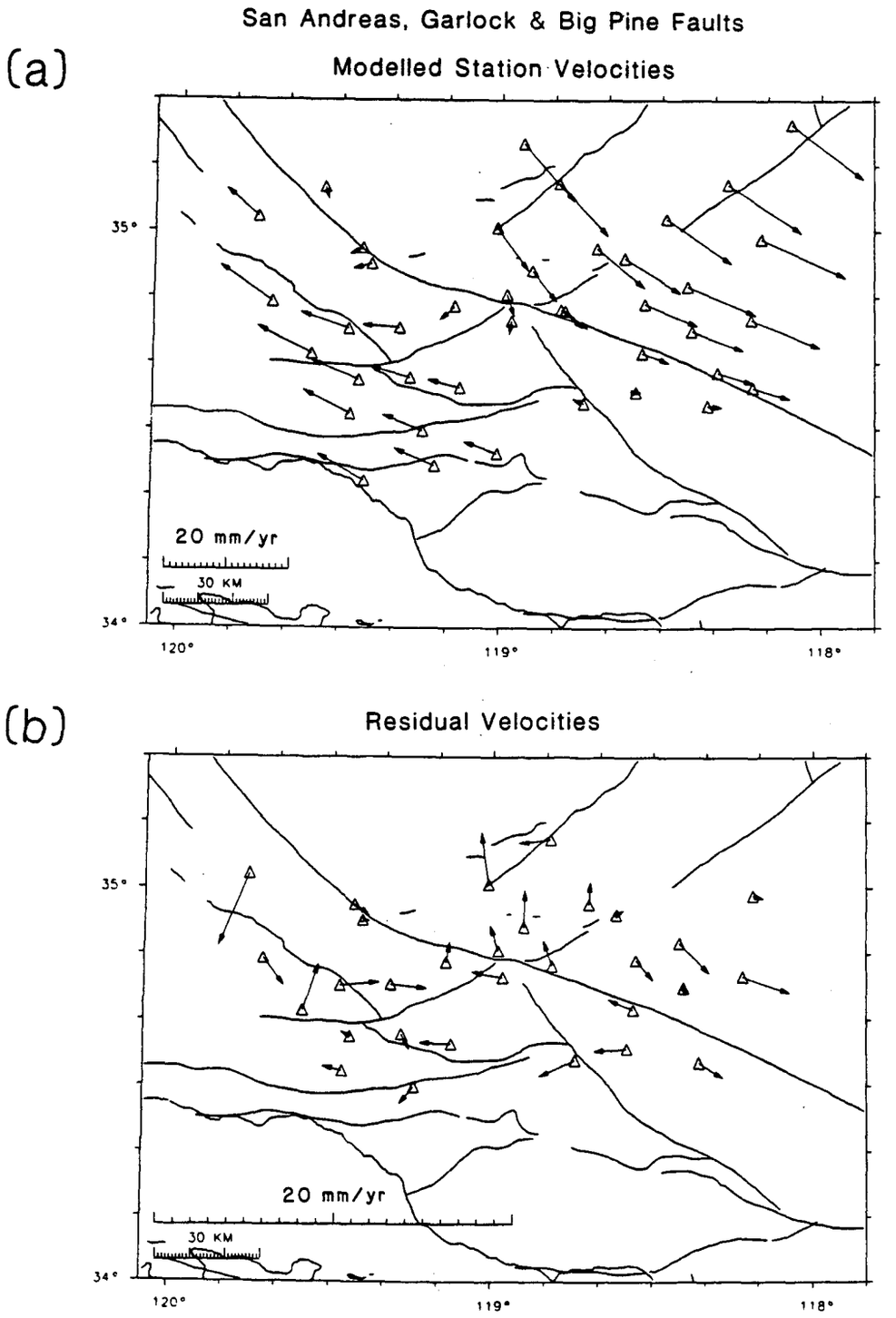

Figure 11. a) Calculated station velocities from Big Pine, Garlock and San Andreas dislocation model, Model K in Table 2. b) Residual velocities computed by using the line-length residuals in an inner coordinate solution.

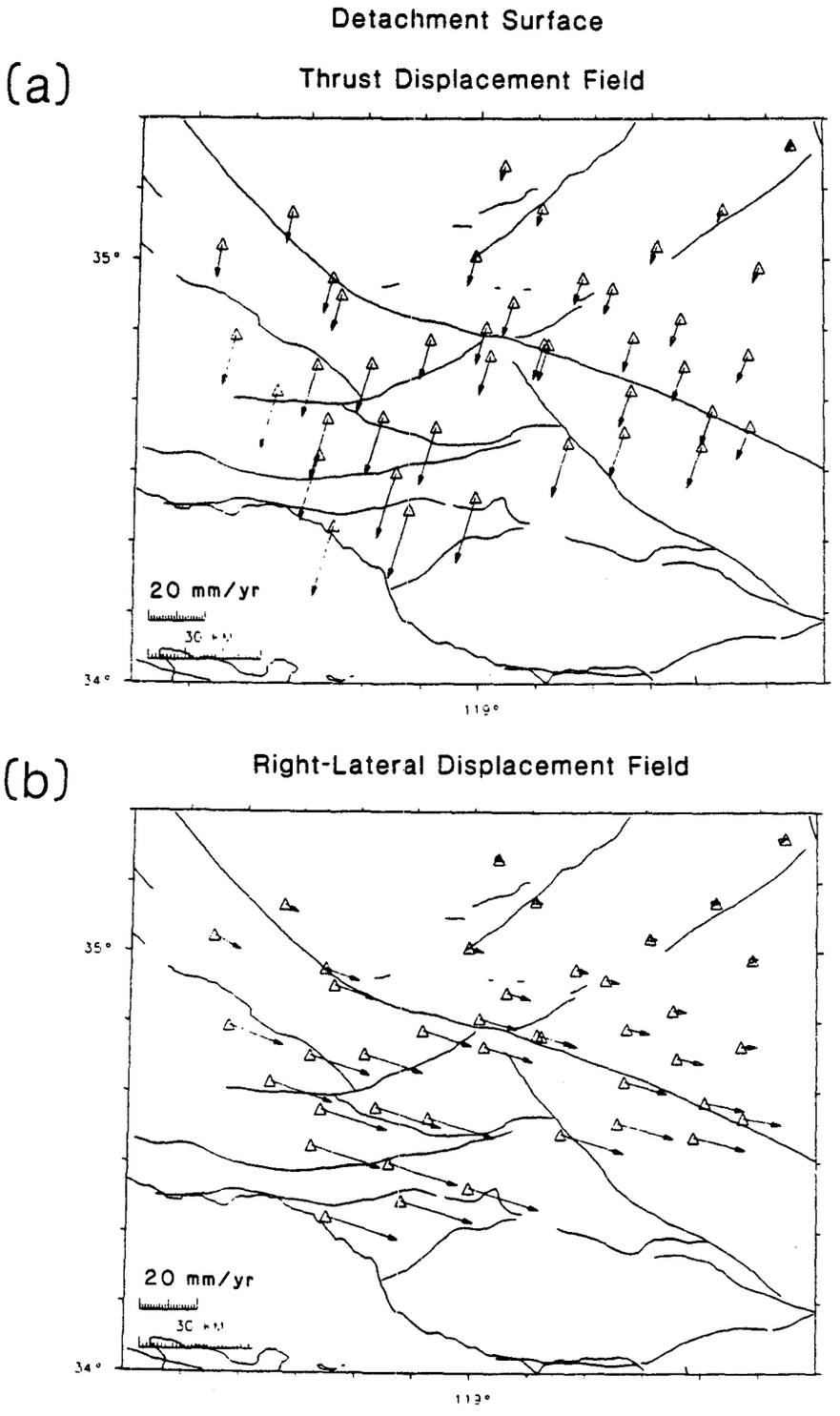

Figure 12. Displacements for a near-horizontal surface on the south side of the SAF, dipping 7°N, with 30 mm/yr: (a) thrust and (b) right-lateral strike-slip.

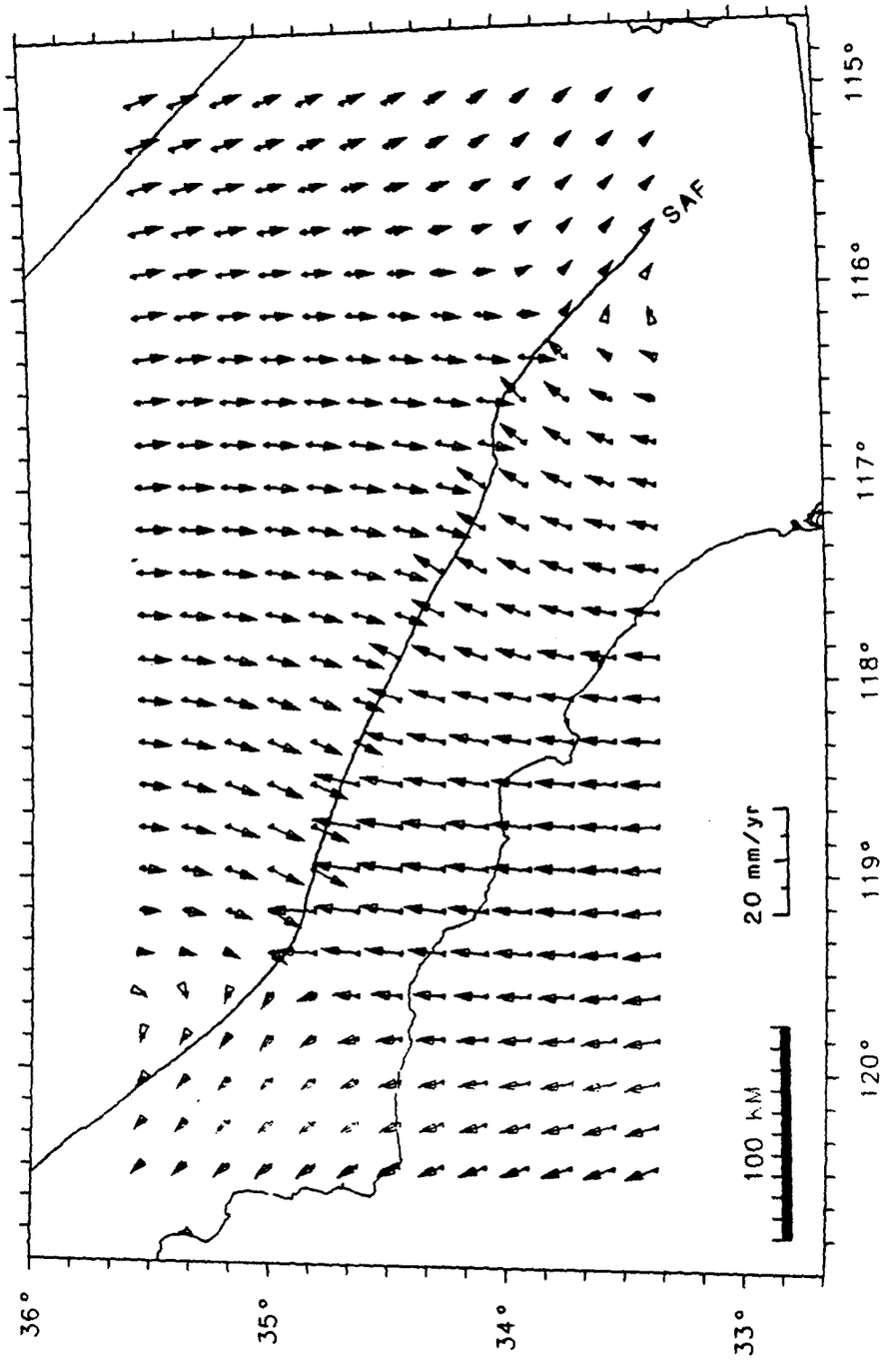

Figure 13. Residual displacement field, the component of plate motion not accounted for by ideal San Andreas Fault displacement field in the Big Bend region.

Chapter 5.

Empirical Relationships Between Seismic Velocity, Effective Pressure, Porosity and Clay Content in Sandstone

ABSTRACT

We use a multivariate analysis to investigate the influence of effective pressure (P_e), porosity (ϕ) and clay content (C) on the compressional and shear velocity of sandstones. Laboratory measurements on water-saturated samples of 64 different sandstones provide a large data set that were analyzed statistically. For each sample, relationships between effective pressure and V_p and V_s have been determined. All samples were well fit by relationships that have an exponential increase in velocity at low P_e, tapering to a linear increase with P_e for P_e greater than 0.2 kbar. There are differences in the pressure dependence of velocity of different rocks, particularly at very low pressures, however they cannot be attributed to ϕ or C. For the combined set of measurements from all samples, the best fitting formulation of parameters is as follows:

$$V_p = 5.77 - 6.94\phi - 1.73\sqrt{C} + 0.446\,(P_e - 1.0\,e^{-16.7P_e})$$

$$V_s = 3.70 - 4.94\phi - 1.57\sqrt{C} + 0.361\,(P_e - 1.0\,e^{-16.7P_e})$$

where P_e is the effective pressure (kbar), the confining pressure reduced by the pore pressure (P_p). While this is admittedly a very simplified parameterization of rocks, it is remarkable how well velocity of the rocks considered here can be predicted based on only the three parameters, ϕ, C and P_e. The model accounts for 95 % of the variance and has rms error of 0.1 km/s. Increasing V_p/V_s indicates decreasing P_e and/or decreasing porosity or increasing clay content.

While the P_e relationship is too inexact to estimate small P_p changes in unsampled rocks, we may be able to use velocity to discern a change from hydrostatic to near-lithostatic P_p, as shown in an example from Coalinga, California. At a depth of 5 km, a typical sandstone exhibits $\Delta V_p = 0.4$ km/s when going from hydrostatic to near-lithostatic P_p.

INTRODUCTION

In a laboratory environment geophysical measurements can accurately be made for a rock sample of known characteristics. As geophysicists commonly try to characterize rocks using measurements made in the field, it is valuable to investigate the possibility of combining laboratory measurements to form empirical relationships that can be applied to estimating characteristics of in-situ rocks. For a given rock, seismic velocity has been shown to be a strong function of effective pressure (P_e), that is the confining pressure reduced by the pore pressure (Todd and Simmons, 1972). As velocity also varies with the porosity and composition of the rock, with an appropriate empirical relationship, we may be able to estimate the effective pressure, and hence the pore pressure, from measurement of in-situ velocity. While the influence of porosity on velocity has been analyzed for many years with such formulas as the Wyllie time-average equation (Wyllie et al., 1956), Han et. al (1986) sought to systematically investigate the additional effect of clay content in sandstones. They showed that even a small amount of clay significantly effects velocity so that clay content must be considered when formulating an empirical velocity relationship.

Han (1986) reported compressional (V_p) and shear (V_s) velocity for a broad suite of sandstones over an effective pressure (P_e) range of 0.02 to 0.49 kbar. All samples were fully water-saturated; thus the influence of gas and oil mixtures on velocity will not be included in this study. He measured velocity for 64 different samples, including clean quarry sandstones, other well-consolidated sandstones from quarries and boreholes, tight-gas sandstones, and samples, some poorly-consolidated, from offshore wells in the Gulf of Mexico. The porosity (ϕ) ranged from 0.02 to 0.30 and was measured by helium porosimeter. The clay content (C) ranged from 0.00 to 0.50 and was measured by point-counting on two thin-sections per sample, 300 counts per section. The velocities were measured with the pulse transmission technique with central frequencies of 1.0 MHz and 0.6 MHz for P and S waves respectively. Absolute errors are estimated to be less than 1% in V_p and less than 2% in V_s. If we assume that this data provides a representative sample of sandstones in general, we can use it to find an empirical relationship describing velocity as a function of porosity, clay content and effective pressure.

Han (1986) varied the confining pressure from 0.01 to 0.80 kbar, while the pore pressure was varied from 0.00 to 0.40 kbar. Samples were prepressurized to 0.50 kbar to reduce hysteresis effects. For a specific sample at a given effective pressure, he found very slight velocity differences for different values of confining pressure and pore pressure, suggesting that both V_p and V_s are essentially functions of effective pressure. We can therefore combine the data from all confining pressures and pore pressures for each rock, and consider velocity to be a function of only the effective pressure.

In this study, we first find a general relationship between velocity and P_e for each individual rock, ignoring the clay and porosity parameters. We show that the pressure dependence for the individual rocks is similar enough that we can estimate the pressure effect for the entire suite of rocks together. Our next step is to combine the entire set of velocity measurements for all rocks and find an empirical relationship based on the three parameters, clay, porosity and effective pressure. Such a relationship is a step in the long-term process of understanding rock behavior: while various, sometimes competing, models of physical processes are being developed, an empirical relationship can provide a useful description, for a very large set of data, of the influence of effective pressure, porosity and clay content on seismic velocity. Finally, we show how this relationship can be applied to estimate a rock sample's velocity, or its porosity and clay content, or the in-situ effective pressure and pore pressure.

VELOCITY-PRESSURE RELATIONSHIPS FOR INDIVIDUAL ROCKS

For each rock sample with a given value of porosity and clay content, we use a relationship between V_p and V_s and P_e of the form

$$V = A + K\,P_e - B\,e^{-DP_e} \tag{1}$$

This type of empirical curve can well describe the laboratory observations of velocity variation with effective pressure for pressures equivalent to those in the upper crust (0 to 1.5 kbar). Although used by others for crystalline rocks (Moos, 1983; Stierman et. al, 1979), it also works well for sedimentary rocks, since it describes well the velocity increase with effective pressure as microcracks and pores close and the rock becomes more incompressible. As illustrated by the derivative of (1),

$$\frac{dV}{dP_e} = K + B\ D\ e^{-DP_e} \tag{2}$$

the velocity increases most rapidly as P_e is initially increased and a relatively large number of microcracks close. Greater B indicates increased relative importance of crack closure, while a larger D indicates that the cracks close more rapidly as P_e is increased. Further increases in P_e are associated with more linear increases in velocity.

To fit (1) to the data in this study, we applied a grid search over a range, 1 $kbar^{-1}$ to 40 $kbar^{-1}$, for the exponential coefficient, D, and for each D calculate the least squares solution for the other (linear) coefficients, A, K and B. For each solution a fit parameter is calculated based on the rms residual in V_p, V_s, shear modulus (μ) and poisson's ratio (ν). The best fitting set of coefficients is chosen to represent each rock sample. Most rocks had seventeen measurements of both V_p and V_s; no solution was calculated for samples that had less than six measurements of both V_p and V_s. Table 1 lists the results for all the rocks studied. Since we were able to fit the observed velocities extremely well (Figure 1), this table substantially provides a summary of the nearly two thousand laboratory measurements.

Figure 1 shows the curves fit to V_p, V_s and V_p/V_s data for 6 samples, representing a broad range of porosity, 0.059 to 0.261, and clay content, 0.00 to 0.45. For a given P_e, there is large variation in the velocity of these samples that is a result of the dependence on ϕ and C (as well as other unmodeled factors and experimental error). Comparing Figures 1e and 1f, we note that these samples have similar ϕ and C and have similar V_p values of 3.3 to 3.5 km/s at 0.2 kbar, whereas Utah Buff (Figure 1a), a low ϕ and low C sample, has much higher V_p of 4.9 km/s at 0.2 kbar. As illustrated, we are able to obtain, for each sample, over the measured range of P_e, an excellent fit to the observed velocities using an equation of the form of (1). The velocity increases linearly with P_e above approximately 0.2 kbar. At lower pressures, the rate of increase in velocity with pressure is greatly enhanced. The V_p/V_s ratio is largest at very low P_e, and decreases as P_e increases. However, while the general pattern of behavior is common to all rocks measured, there are major variations among the individual samples. Compare Gulf124155 (Figure 1e) which shows the largest pressure effects with Utah-Buff (Figure 1a) which shows the least. The shape of the curves is not simply dependent on ϕ

or C. For example, the rocks in Figures 1e and 1f have similar ϕ and C parameters, yet show distinctly different behavior at low P_e.

To investigate further whether the pressure effects on velocity might be dependent on ϕ or C, we applied regression analysis to the coefficients in (1) and the parameters ϕ and C. None of the coefficients show any statistically significant relationship to the parameters, and thus the pressure dependence can be separated from the porosity and clay dependence, and the most valid function for the exponential coefficient, D, is simply a constant, the average value. There is no significant difference between the values obtained using V_p and V_s coefficients. Thus, for both V_p and V_s, the same exponential coefficient can be used, D=16.7±5.3 (for P_e in kbar).

REGRESSION ON ALL DATA

Our next step is to apply forward stepwise multiple regression on all the measured velocity data in order to obtain the best fitting relationship of the form

$$V = f\ [\phi, C, P_e, e^{-DP_e}]$$

thus combining the observed dependence on effective pressure with Han et. al's (1986) observation of clay content and porosity dependence. All the velocity data are used together instead of being separated by rock sample, as done in the preceding section, or by pressure, as done by Han et. al (1986). After searching over possible relationships that included various functions of each parameter, as well as combinations of parameters, the best fit is found for

$$V = B_0 + B_1\phi + B_2\sqrt{C} + B_3P_t \tag{3}$$

where the effective pressure is transformed to

$$P_t = P_e - e^{-DP_e} \tag{4}$$

with the exponential coefficient, D, determined in the preceding section. We initially used a transformation $P_t = P_e - \beta e^{-DP_e}$, similar to (1), but when using all the data together β turned out to be equivalent to 1 kbar within the rms error of the coefficient. Additional terms in (3) do not provide any significant improvement in the fit to the data. The square root helps account for the effect on velocity of the initial clay addition, thus adding 4% clay to clean sandstone has the same effect as

adding 20% clay to a rock that originally had 10% clay. Han et. al(1986), in regression for ϕ and C on a smaller number of data points at one pressure, have tried to adjust for this effect by separating out the 0% clay samples. In our study, using all the data from all pressures together, the $\sqrt{C}$ parameter is still significantly better than C even when the clean sandstones are removed. Note that we also tried other clay exponents from $C^{0.25}$ to $C^{0.90}$, and the $\sqrt{C}$ turned out to be the best parameter for V_p and V_s.

We find that V_p and V_s can be described by

$$V_p = 5.77 - 6.94\phi - 1.73\sqrt{C} + 0.446\,(P_e - 1.0\,e^{-16.7P_e}) \quad (5)$$

$$V_s = 3.70 - 4.94\phi - 1.57\sqrt{C} + 0.361\,(P_e - 1.0\,e^{-16.7P_e}) \quad (6)$$

with P_e in kbar. The Appendix explains the reasoning involved in selecting the form of these equations and presents partial residual plots that justify the individual coefficients. The coefficients, along with their rms errors and F-test values, are listed in Table 2. The size of the coefficient shows how strongly a given parameter influences velocity, since ϕ, C and P_t have roughly the same numerical range, whereas the F-value shows how statistically significant that parameter is in the regression. The porosity and clay terms have the largest effects, but the effective pressure term is also highly significant, as shown by the F-values. The total reduction in data variance is 95 % for V_p and 93 % for V_s (Table 3). The predicted velocities and residuals are shown for V_p in Figures 2a,b and for V_s in Figures 2c,d. It is remarkable, considering that rocks are complex systems, how well velocity of the rocks considered here can be predicted based on only the three parameters, ϕ, C and P_e. In Figures 2a,c, the points cluster tightly around a 45° line. There are no extreme outliers and the largest residual is only 0.35km/s, about 12 % of the range of measured variation. The rms error for both V_p and V_s is about 0.1 km/s, and thus (5) and (6) are achieving a reasonably good fit to the measured velocities. Figure 2b,d show the residuals plotted at a scale five times that of Figure 2a,c, so that different types of residual patterns can easily be observed, and lines are drawn that enclose plus and minus two rms errors.

DISCUSSION

Fit of Individual Rocks to Regression Model

There are a few distinct series of points in Figure 2 that systematically do not fit the line and correspond to particular rocks. We can consider how well (5) and (6) predict the velocities for an individual rock sample by looking at the residuals for the data that are fit most poorly. In the residual plot, the average velocity residual for a particular sample is related to how well the empirical coefficients for porosity and clay describe that rock's behavior, since porosity and clay are constant for a given rock sample. Patterns in the residuals for an individual sample reflect discrepancies between the velocity variation with P_e of the empirical model and that of the particular rock sample. In Figure 2b, samples are highlighted that have numerous large size V_p residuals and/or unusual trends in residuals. For Utah Buff, which has very little variation with pressure (Figure 1a), the average predicted velocity is about the same as the average observed velocity, however the predicted velocity is too low at low pressures and too high at high pressures, thus creating a distinct pattern. In contrast, for Gulf12677 all predicted velocities are too high: the residual for one measurement is greater than three rms errors. There is also a strong pattern in the residuals since this sample has larger variation with pressure, in both the linear (K) and exponential (B) terms, than the regression relationship expects. Despite having very similar characteristics to Gulf12677, the sample Gulf12676 has predicted velocities that are all too low. The trend of residuals is also less pronounced with fairly uniform residuals for P_e above 0.06 kbar, since the linear part of the velocity variation with P_e is slightly less than the regression model, while the exponential decay is larger. StPeter1 shows a combination of the residual trends observed for other rocks. It has a smaller linear increase with P_e, yet a larger exponential decrease at low P_e than most of the samples (Figure 1d). P72754 and Berea500 do not exhibit particular trends in their residuals since the empirical V_p-P_e relationship fits these samples well. P727154 has generally uniform large positive residuals, while Berea500 is one of the best fitting rocks with uniformly small residuals. Thus the porosity and clay terms are underestimating velocity for P727154, but are providing fairly accurate estimates for Berea500. Figure 2d shows the V_s residuals with the same rocks highlighted. The average residuals and residual patterns are similar

to those for V_p. A difference is that Berea500 has larger shear velocities than predicted. P727154 shows a much larger exponential decrease in V_s at P_e less than 0.05 kbar, however this may be partly due to greater difficulty in measuring shear velocity at low effective pressures (Han,1986).

All these effects are results of factors, such as grain and pore size and shape, and degree of compaction and cementation, which are not included in our simple empirical relationship. Microstructural variations can particularly effect velocity at low P_e, even for rock samples with exactly the same composition and porosity (Bourbie and Zinszner, 1985). Additionally, the simple measurement of percent clay does not fully describe the rock's composition. However, the very good fit we obtain (Table 3) shows that the empirical relationship accounts for the majority of velocity variation within our sample observations, and thus may be a useful tool to estimate velocity within the uncertainty indicated in Figure 2, for similar rocks that have no available laboratory measurements. It would be difficult to adjust for additional complexity in any simple uniform manner, as is illustrated by Gulf12676 and Gulf12677 which are very similar samples, but have distinctly different patterns of residuals.

Estimating Velocity and Sample Parameters

Given the empirical velocity relationship we can estimate the velocity for given values of porosity, clay content and effective pressure. While this cannot perfectly describe the velocity for all sandstones, it should be reasonable for most samples similar to those studied, and is thus useful for predicting velocity of similar rocks for which laboratory measurements are unavailable. In particular, with field measurements which average over a much larger, and more varied, volume of rock than laboratory measurements, it may be more appropriate to use a general sandstone velocity than a velocity of a particular sample. Most measurements of velocity at increasing pressures show that at some point between 1 and 2 kbar, the linear increase with pressure becomes less pronounced and above 5 kbar the curves are nearly flat (Christensen, 1984a). Thus, effective pressure will only be extrapolated to 1.5 kbar.

In order to visualize a function of three variables, we show level surfaces of the function. Figure 3 shows the surfaces V_p (ϕ,C,P_e) = 3.5 km/s, 4.5 km/s, 5.5 km/s in the ϕ, C, P_e coordinate

system. Thus a rock with a V_p of 4.5 km/s should be characterized by some point on the V_p = 4.5 surface. The surfaces are curved because of the $\sqrt{C}$ term and flatten at low effective pressure because of the exponential pressure term. The surfaces for different velocities are quite distinct. In these plots the gridlines represent values of constant porosity and clay content. For example, the bold lines on the V_p =4.5 surface are lines for ϕ =0.06 and C = 0.30; a rock with ϕ = 0.06, C = 0.30 and V_p = 4.5 would be a point on the surface at the intersection of these lines, with estimated P_e of 0.23 kbar. For a relatively high V_p of 5.5 km/s, fairly large effective pressures are indicated except for extremely pure, low porosity sandstones.

We observe the influence of V_p/V_s ratio by plotting intersection lines of various V_s level surfaces on the V_p level surface (Figure 4). The combinations of (ϕ,C,P_e) that predict a given V_p and V_s using our relationships are described by the intersection of the two surfaces. For pressures above the exponential decay, the V_p/V_s ratio seems to be most correlated with the porosity, since the V_p/V_s lines are generally aligned with lines of constant porosity, except for low clay content where small amounts of clay greatly influence the elastic moduli. A normal to a V_p/V_s line (arrow in Figure 4) shows that an increase in V_p/V_s ratio indicates a decrease in effective pressure, as is commonly observed, and/or an increase in the clay content or decrease in porosity.

One of the most important applications of an empirical velocity relationship is to use velocity to predict porosity, clay content or effective pressure. If we can obtain distinct estimates of the rock parameters and effective pressure when error and uncertainty are taken into account, then our simple empirical model will have useful applications. Figure 5 shows curves for V_p =4.00 bounded by curves for one standard error of the regression analysis (Table 3). Thus for a certain velocity measurement, we can say only that the parameter values are expected to be within these bounds. (This could be visualized as an envelope around a surface of Figure 3.) The crosses, in each figure, indicate, for one (ϕ,C,P_e) point, what the uncertainty in one parameter would be if all the others were known exactly. For the indicated point, these individual uncertainties are 0.017 porosity, 0.047 clay, and 0.23 kbar P_e, which are low enough that our model may give useful estimates of individual parameters. The uncertainties for clay and P_e vary, becoming larger with increasing clay content and smaller for

lower pressures.

In reality there is uncertainty in all of the measured parameters, as well as the one we would like to estimate, making the estimated uncertainty even larger. We can estimate this by taking partial derivatives of equation (3). For example, we can consider that when we are estimating P_e, the uncertainty in the estimated value of P_e is estimated to be

$$\Delta P_e = [(\Delta V + SE) + \Delta\phi\frac{\partial V}{\partial \phi} + \Delta C\frac{\partial V}{\partial C}]/\frac{\partial V}{\partial P_e}$$

for a particular (V,ϕ,C,P_e) given measurement uncertainties in velocity (ΔV), porosity ($\Delta\phi$), and clay content (ΔC), and standard error of the regression model (SE). This is illustrated in Figure 6. Examples are shown of 2 different rocks with low and high clay content, each at low and high P_e, and the uncertainty in P_e is indicated for various uncertainties in ϕ and C. The porosity needs to be known more accurately than the clay content in order to predict the effective pressure. The pressure is also predicted more accurately at lower pressure. However, because $\frac{\partial V}{\partial P_e}$ is approximately constant above 0.3 kbar, the P_e uncertainty, at higher pressures, does not get larger than shown in Figure 6b,d for 0.4 kbar. For small uncertainties in porosity and clay, the predicted P_e may still be useful at the higher effective pressures, however for large uncertainties in porosity and clay, the estimated uncertainty in P_e becomes so large that it may be of little use to try to predict P_e.

Estimating Pore Pressure

Another interesting application is to the case where effective pressure is estimated from velocities measured for a continuous rock unit at a given depth, as has been discussed for oceanic basalts by Christensen (1984b). Thus if we had a case in which the porosity and clay content were approximately constant throughout a stratigraphic unit, then spatial variations in velocity would be related to variations in P_e. As the unit would be at an approximately constant depth (ie: constant confining pressure), changes in P_e would reflect changes in pore pressure. For our regression model, a change in velocity is linearly related to a change in the transformed pressure parameter:

$$V_p = V_{p_0} + 0.446P_t \quad or \quad \Delta V_p = 0.446\Delta P_t.$$

The transformation of P_e to P_t is shown in Figure 7, which can be used to estimate P_e. Consider the case of a given rock unit at 5 km depth. P_e is 0.66 kbar for hydrostatic pore pressure (point A in Figure 7). If a V_p decrease of 0.4 km/s is observed, a decrease of 0.9 is predicted in P_t. This would correspond to reducing P_e to 0.08 kbar, or near-lithostatic pore pressure (point B in Figure 7).

Finally we consider an application of this methodology to field data where we have a continuous stratigraphic unit that varies spatially in depth as well as in velocity. In the seismic reflection profile SJ-19 across the Coalinga Anticline, in central California, interval velocities have been calculated for many of the stratigraphic layers (Wentworth and Zoback, 1987). In the Santa Margarita layer, which is continuous across the profile, the velocity decreases from 3.3 km/s (point I) to 2.7 km/s (point II), above the anticline. ϕ and C are unknown, but are assumed to be approximately constant within the particular rock unit. As described in Table 3, the associated change in P_e will be composed of a change due to the decrease in hydrostatic P_e at the shallower depth and a change due to change in the pore pressure. In this example, the P_e at point II is predicted to be 0.02 kbar, or very nearly lithostatic pore pressure. This prediction of high pore pressure is confirmed by Yerkes, et. al (1987) on the basis of fluid pressures from well data.

CONCLUSIONS

For each of 64 different water-saturated sandstones, relationships between effective pressure and V_p and V_s have been determined. All samples could be well fit by relationships that have an exponential increase in velocity at low P_e, tapering to a linear increase with P_e at higher P_e. Variations in the pressure dependence among the samples do not correlate with porosity or clay content. The most useful form, considering all the samples is $\Delta V \ \alpha \ (P_e - 1.0\, e^{-16.7P_e})$, where P_e is in kbar.

We have applied forward stepwise multiple regression on the entire combined data set to find the best fitting empirical relationships.

$$V_p = 5.77 - 6.94\phi - 1.73\sqrt{C} + 0.446\,(P_e - 1.0\, e^{-16.7P_e})$$

$$V_s = 3.70 - 4.94\phi - 1.57\sqrt{C} + 0.361\,(P_e - 1.0\, e^{-16.7P_e})$$

The reduction in data variance is about 95% and the rms error is about 0.1 km/s. Since such complicating factors as grainsize and poreshape distributions, amount of compaction, and degree of

cementation are not described in the simple characterization by porosity and clay content, some samples are poorly fit by these empirical equations. Residual plots show that poorly-fit rocks have uniformly large-size residuals due to a poor fit in the ϕ and C terms or unusual trends in residuals due to greater or lesser P_e variation than the typical sample.

The empirical relationship is able to provide a useful description, for a very large set of data, of the influence of effective pressure, porosity and clay content on seismic velocity. While it cannot exactly describe the velocity for all sandstones, it is reasonable for these varied samples, and thus may be useful for estimating velocity of rocks for which laboratory measurements are unavailable.

For an in-situ velocity measurement, the effective pressure can be estimated since the confining pressure is equivalent to the weight of the overburden and the pore pressure will range between hydrostatic and lithostatic. Hence velocity variations within a given rock unit at a given depth can be ascribed to variations in pore pressure. While the P_e relationship is too inexact to estimate small P_p changes in unknown rocks, we may be able to use velocity to discern a change from hydrostatic to near-lithostatic P_p, as shown in an example from a seismic reflection profile at Coalinga, California.

APPENDIX

In this appendix we assess the fit of the multiple regression model (equation 5) by making plots of partial residuals. These show the distribution of residuals left over when all parameters but one are accounted for. Thus, if we can fit a straight line through a given plot of partial residuals, then it is a good assumption that the velocity is linearly related to the given parameter. Conversely, if a straight line cannot fit the partial residuals, or the partial residuals are not normally distributed about the straight line, or there is a curve of another form that clearly fits the partial residuals better than a straight line, then we must search for an other than linear relationship for that parameter. The linear trends of the partial residuals (Figure A1) show that equation (5) is a fair empirical model. The slope of the line is tightly constrained for porosity (Figure A1a). For $\sqrt{C}$ (Figure A1b), the points are not as tightly clustered about the line, but the line is still fairly well constrained. For P_t (Figure A1c), the line is not as well constrained as for ϕ or $\sqrt{C}$ and the standard error for the coefficient of P_t is

over 2% (Table 2), however the points are normally distributed about the line and no other form is apparent that could better fit the partial residuals.

Note that our model correlates velocity with the square root of clay instead of clay. The reasoning for this is shown in Figure A2, which displays the results of an initial regression model with a linear term. By comparing the partial residuals for clay (Figure A2a) with those for square root of clay (Figure A1b), we see that the linear clay parameter does not fit the observations as well since the partial residuals are not normally distributed about the regression line. The residuals (Figure A2b) are particularly useful in helping us select an appropriate empirical clay parameter. They are not randomly distributed, but have an obvious functional relationship to clay content. From the pattern of residuals, we can see that a relationship of the negative square root form will be a good selection. The final data variance for the model with the square root of clay term is 26 % less than for the model with clay. Note that we also tried other clay exponents from $C^{0.25}$ to $C^{0.90}$, and the square root turned out to be the best parameter for V_p and V_s.

The square root describes that the initial addition of clay has the largest effect on velocity. Adding 4% clay to clean sandstone has the same effect as adding 20% clay to a rock that originally had 10% clay. Han et. al(1986), in regression for ϕ and C on a smaller number of data points at one pressure, have tried to adjust for this effect by separating out the 0% clay samples. In our study, using all the data from all pressures together, the $\sqrt{C}$ parameter is still significantly better than C even when the clean sandstones are removed.

Similarly we can consider the pressure parameter. Figure A3 shows the residuals and partial residuals for a regression model with a linear P_e term. The fit is poor; it is apparent that an improved fit could be obtained by transforming P_e to a parameter which includes an exponential decrease at low P_e. Thus we selected $P_t = P_e - 1.0\, e^{-DP_e}$ as an appropriate pressure parameter. Note that we also tried a transformation to $P_e^{\frac{1}{6}}$, considered proportional to V_p for sediments (Marion, 1986), which fit nearly as well overall as the selected transformation (4); however, the fit is not as good at very low pressures (< 50 bar) or for pressures above 300 bar.

REFERENCES

Bourbie, T., and B. Zinszner, Hydraulic and acoustic properties as a function of porosity in Fontainebleau sandstone, *J. Geophys. Res.*, *90*, 11524-11532, 1985.

Christensen, N. I., Seismic velocities, in *CRC Handbook of Physical Properties of Rocks*, vol. II, edited by R. S. Carmichael, pp. 1-228, CRC Press, Boca Raton, 1984.

Christensen, N. I., Pore pressure and oceanic crustal seismic structure, *Geophys. J. R. Astr. Soc.*, *79*, 411-423, 1984.

Han, De-hua, Effects of porosity and clay content on acoustic properties of sandstones and unconsolidated sediments, Ph.D. dissertation, Stanford Univ., 1986.

Han, De-hua, A. Nur, and Dale Morgan, Effects of velocity and clay content on wave velocities in sandstones, *Geophysics*, *51*, 2093-2107, 1986.

Marion, D., Determination of the average coordination number of a granular material from acoustical, electrical and mechanical properties, *Stanford Rock Physics Rept.*, *27*, 129-152, 1986.

Moos, Daniel, Velocity, attenuation, and natural fractures in shallow boreholes, Ph.D. dissertation, Stanford Univ., 1983.

Stierman, D. J., J. H. Healy, and R. L. Kovach, Pressure-induced velocity gradient: an alternative to a P_g refractor in the Gabilan Range, central California, *Bull. Seism. Soc. Am.*, *69*, 397-415,

Todd, T., and G. Simmons, Effect of pore pressure on the velocity of compressional waves in low-porosity rocks, *J. Geophys. Res.*, *77*, 3731-3743, 1972.

Wentworth, C. M., and M. D. Zoback, Structure of the Coalinga area and thrust origin of the May 2, 1983 earthquake, *U. S. Geological Survey Prof. Paper*, 1987.

Wyllie, M. R. J., A. R. Gregory, and L. W. Gardner, Elastic wave velocities in heterogeneous and porous media, *Geophysics*, *21*, 41-70, 1956.

Yerkes, R. F., P. Levine, and C. M. Wentworth, Abnormally high fluid pressures in the region of the Coalinga earthquakes and their significance, *U. S. Geological Survey Prof. Paper*, 1987.

Table 1
Velocity-Pressure Relationships for Individual Rocks

$$V = A + K(P_e) - B\,e^{-DP_e}$$

Sample	ϕ	C	V_p A	V_p K	V_p B	V_p D	V_s A	V_s K	V_s B	V_s D
BEAVER	0.064	0.00	5.47	0.199	0.503	9	3.44	0.381	0.399	11
BEREA350	0.227	0.06	3.91	0.307	0.622	22	2.31	0.197	0.537	19
BEREA400	0.222	0.03	3.82	0.346	0.441	18	2.32	0.208	0.353	12
BEREA500	0.195	0.09	4.01	0.216	0.451	10	2.44	0.256	0.443	13
BOISE	0.259	0.06	3.65	0.221	0.337	23	2.04	0.109	0.139	15
COCONINO	0.111	0.06	4.68	0.146	0.187	9	2.90	0.243	0.141	13
CONOTTON	0.236	0.04	3.80	0.346	0.716	24	2.28	0.206	0.616	17
DELAWAREBR	0.111	0.05	4.53	0.500	0.397	16	2.69	0.474	0.407	18
DELLIGHTGR	0.046	0.07	5.17	0.138	0.419	8	3.06	0.266	0.270	15
DELTANBUFF	0.160	0.03	4.45	0.403	0.257	28	2.73	0.238	0.278	18
FONTAINBL	0.156	0.00	4.70	0.294	0.532	35	3.00	0.232	0.518	30
FONTAINBLB	0.200	0.00	4.36	0.256	0.664	22	2.78	0.175	0.571	19
GULF10379	0.144	0.44	3.58	0.372	0.492	26	1.85	0.291	0.365	27
GULF10381	0.143	0.46	3.50	0.326	0.301	14	1.92	0.177	0.224	14
GULF10392	0.132	0.51	3.46	0.511	0.425	19	1.93	0.194	0.399	16
GULF10431	0.312	0.11	3.12	0.235	0.558	17	1.65	0.271	0.389	18
GULF10432	0.305	0.12	3.11	0.197	0.435	14	1.73	0.107	0.333	13
GULF10452V	0.111	0.41	3.86	0.313	0.429	16	2.14	0.127	0.390	13
GULF12409B	0.158	0.29	3.72	0.720	0.608	22	1.96	0.488	0.625	21
GULF12409	0.162	0.27	3.74	0.595	0.631	13	1.99	0.339	0.556	13
GULF124155	0.256	0.22	3.20	0.396	0.732	19	1.80	0.252	0.643	13
GULF12416	0.264	0.12	3.38	0.448	0.641	14	1.87	0.202	0.515	11
GULF12418	0.155	0.37	3.64	0.326	0.502	15	2.00	0.295	0.418	12
GULF124255	0.123	0.44	3.69	0.373	0.359	24	2.05	0.230	0.374	19
GULF126605	0.159	0.27	3.69	0.367	0.466	19	2.00	0.353	0.437	20
GULF12670	0.272	0.08	3.55	0.324	0.610	16	2.09	0.273	0.398	14
GULF12674	0.276	0.06	3.45	0.414	0.713	18	1.98	0.291	0.774	17
GULF12676	0.294	0.11	3.41	0.393	0.807	19	1.94	0.294	0.674	17
GULF12677B	0.283	0.08	3.41	0.429	0.795	15	1.96	0.322	0.632	13
GULF12677	0.275	0.07	3.32	0.475	0.716	13	1.81	0.440	0.804	21
GULF14807	0.213	0.11	3.60	0.694	0.747	18	2.07	0.421	0.605	12
GULF15845	0.127	0.21	4.00	0.637	0.682	17	2.38	0.317	0.409	6
GULF15879	0.162	0.06	4.37	0.608	0.776	12	2.41	0.757	0.681	18
GULF158XX	0.117	0.23	4.17	0.625	0.568	14	2.37	0.588	0.485	12
GULF15930	0.069	0.24	4.42	0.446	0.675	14	2.57	0.424	1.270	28
GULF15949	0.161	0.18	3.89	0.464	0.452	14	2.22	0.372	0.451	16
INDIANADA1	0.266	0.16	3.20	0.353	0.308	12	1.92	0.159	0.305	10
INDIANADA2	0.261	0.16	3.37	0.460	0.323	20	1.91	0.367	0.301	25
INDIANALI1	0.240	0.10	3.70	0.049	0.366	7	2.12	0.258	0.294	16
INDIANALI2	0.245	0.10	3.48	0.550	0.380	21	2.04	0.319	0.390	20
MASSBURGUN	0.243	0.03	3.71	0.501	0.507	24	2.26	0.277	0.320	19
MASSILDAR1	0.184	0.06	4.21	0.325	0.378	15	2.54	0.216	0.369	13
MASSILDAR2	0.184	0.06	4.16	0.357	0.343	16	2.47	0.244	0.345	17
MASSILLON	0.212	0.04	3.94	0.241	0.646	12	2.25	0.365	0.522	17
NUGGETH	0.097	0.08	4.76	0.315	0.239	13	2.93	0.261	0.308	15
NUGGETV	0.096	0.08	4.59	0.277	0.364	13	2.77	0.418	0.322	20
P615561	0.073	0.38	4.30	0.207	0.375	15	2.55	0.192	0.386	21
P636249	0.080	0.40	4.17	0.239	0.271	19	2.38	0.272	0.377	31
P636254	0.121	0.37	3.95	0.382	0.464	24	2.23	0.294	0.424	27
P646256	0.098	0.40	4.21	0.141	0.323	8	2.44	0.204	0.296	13
P646258	0.103	0.35	4.06	0.331	0.299	14	2.31	0.313	0.330	21
P646260	0.077	0.45	4.22	0.304	0.387	13	2.45	0.275	0.376	15
P646264	0.147	0.13	4.44	0.241	0.742	7	2.55	0.259	0.575	11
P727154	0.170	0.14	4.13	0.499	0.380	21	2.37	0.436	0.548	30
P748797	0.162	0.10	4.03	0.586	0.472	15	2.36	0.377	0.464	12
P827377	0.180	0.11	4.07	0.409	0.572	13	2.31	0.317	0.509	11
P827379	0.177	0.16	4.00	0.486	0.478	13	2.26	0.416	0.515	17
REDSTONE	0.167	0.28	3.66	0.426	0.338	19	2.01	0.173	0.357	19
STABARBARA	0.131	0.27	3.92	0.364	0.539	14	2.11	0.327	0.484	17
STPETER2	0.205	0.00	4.21	0.187	0.746	24	2.58	0.160	0.781	20
STPETER1	0.187	0.00	4.55	0.298	0.800	19	2.83	0.195	0.741	16
TORREY	0.136	0.14	4.17	0.138	0.467	6	2.22	0.439	0.255	13
UNIONH	0.194	0.05	4.03	0.411	0.669	19	2.39	0.280	0.535	15
UTAHBUFF	0.059	0.06	4.86	0.201	0.109	14	3.05	0.193	0.123	17

Table 2
Linear Regression Solution (P_e in kbar)
$V = B_0 + B_1\phi + B_2\sqrt{C} + B_3 (P_e - e^{-16.7P_e})$

	parameter	coefficient	rms error of coeff.	*F-value**
P-Velocity				
B_0		5.771		
B_1	porosity	-6.938	0.052	17937
B_2	claysqrt	-1.725	0.020	7238
B_3	$P_e - e^{-DP_e}$	0.446	0.010	2034
S-Velocity				
B_0		3.704		
B_1	porosity	-4.937	0.050	9649
B_2	claysqrt	-1.568	0.019	6635
B_3	$P_e - e^{-DP_e}$	0.361	0.010	1324

* Note: critical F-value is 4.00

Table 3
Fit of Regression Model

	rms error (km/s)	reduction in data variance
V_p	0.105	96 %
V_s	0.099	94 %

Table 4
Estimating P_e from V_p Variation
Coalinga Anticline

	depth (km)	V_p (km/s)	ΔP_t from ΔV_p	P_e hyd. (kbar)	ΔP_t hyd.	ΔP_t from ΔP_p	P_t est.	P_e est. (kbar)
I	4.8	3.3		0.63				
II	2.6	2.7	1.35	0.34	0.29	1.06	-0.72	0.02

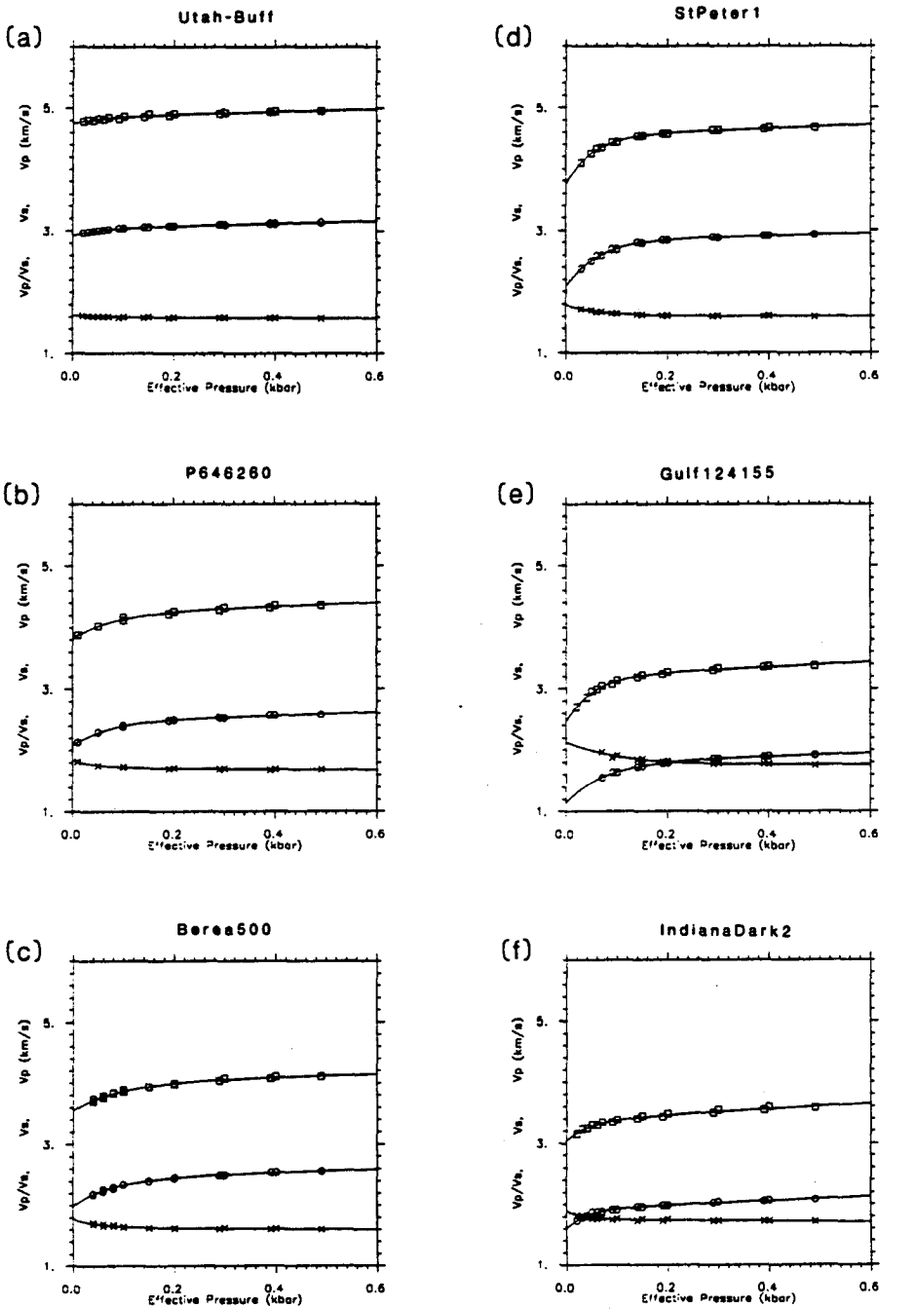

Figure 1. Plots of calculated velocity-pressure relationships for six representative samples. Circles are measured velocities and stars are measured V_p/V_s ratios. a) Utah-Buff, ϕ=0.059, C=0.06; b) P646260, ϕ=0.077, C=0.45; c) Berea500, ϕ=0.195, C=0.09; d) StPeter1, ϕ=0.205, C=0.00; e) Gulf124155, ϕ=0.256, C=0.22; f) IndianaDark2, ϕ=0.261, C=0.16.

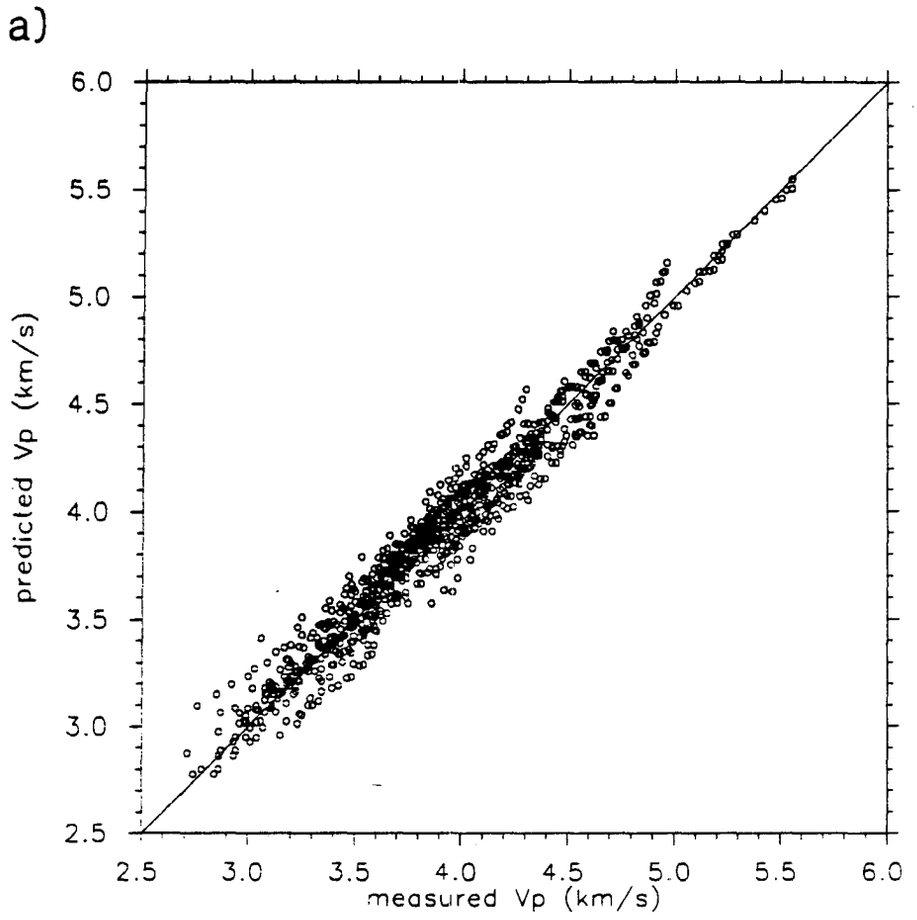

Figure 2. Plots of velocities calculated using equations (5) and (6). a) predicted versus measured V_p,

b)

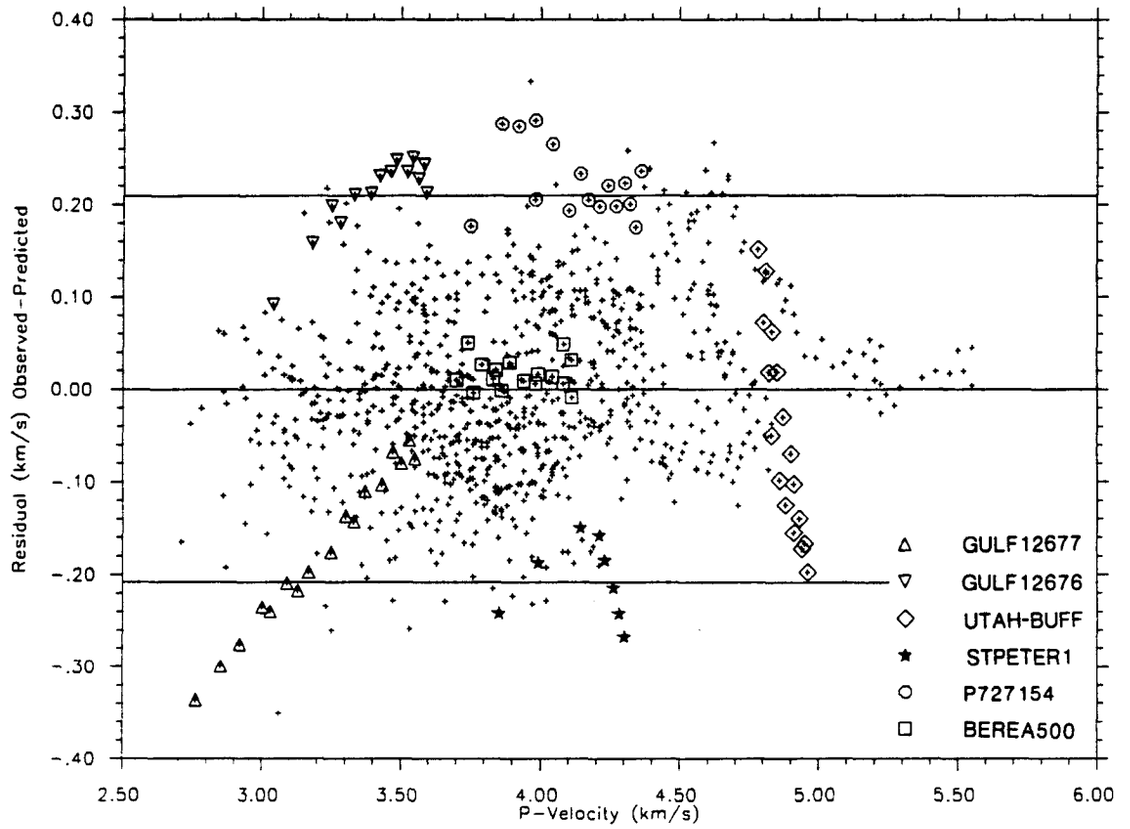

Figure 2 continued. b) V_p residuals (observed - predicted) versus measured V_p, with samples marked that have numerous large residuals or unusual trends in residuals. Lines indicate ±2 rms error.

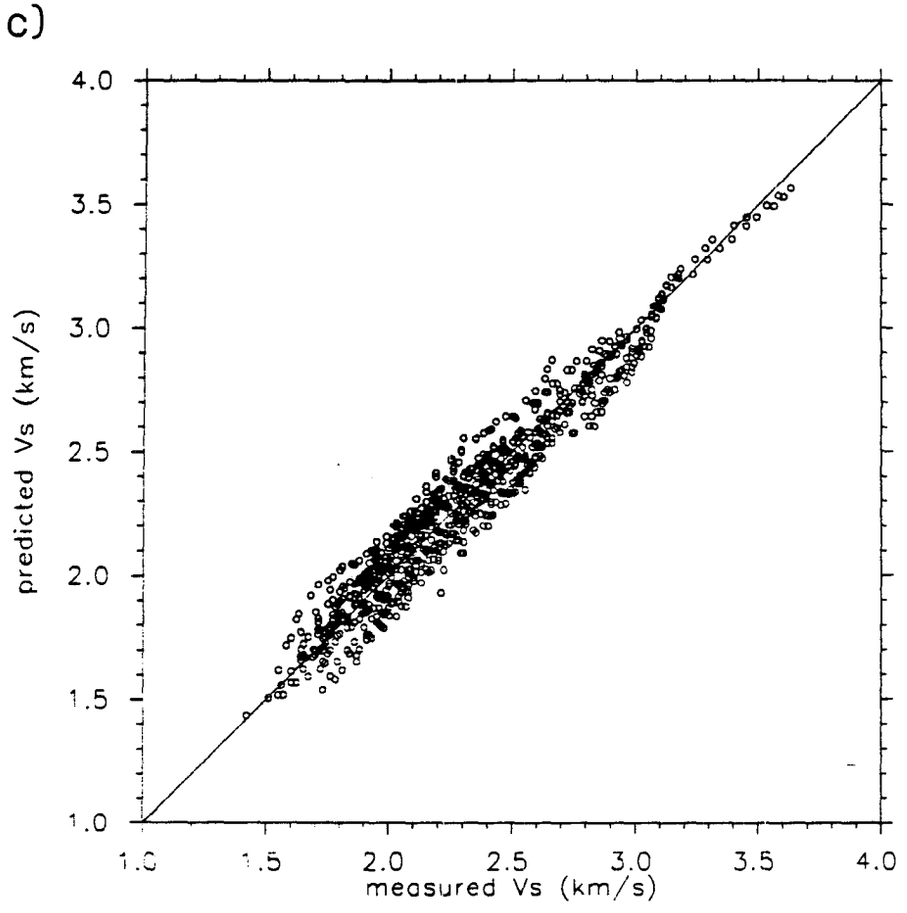

Figure 2 continued. c) predicted versus measured V_s.

d)

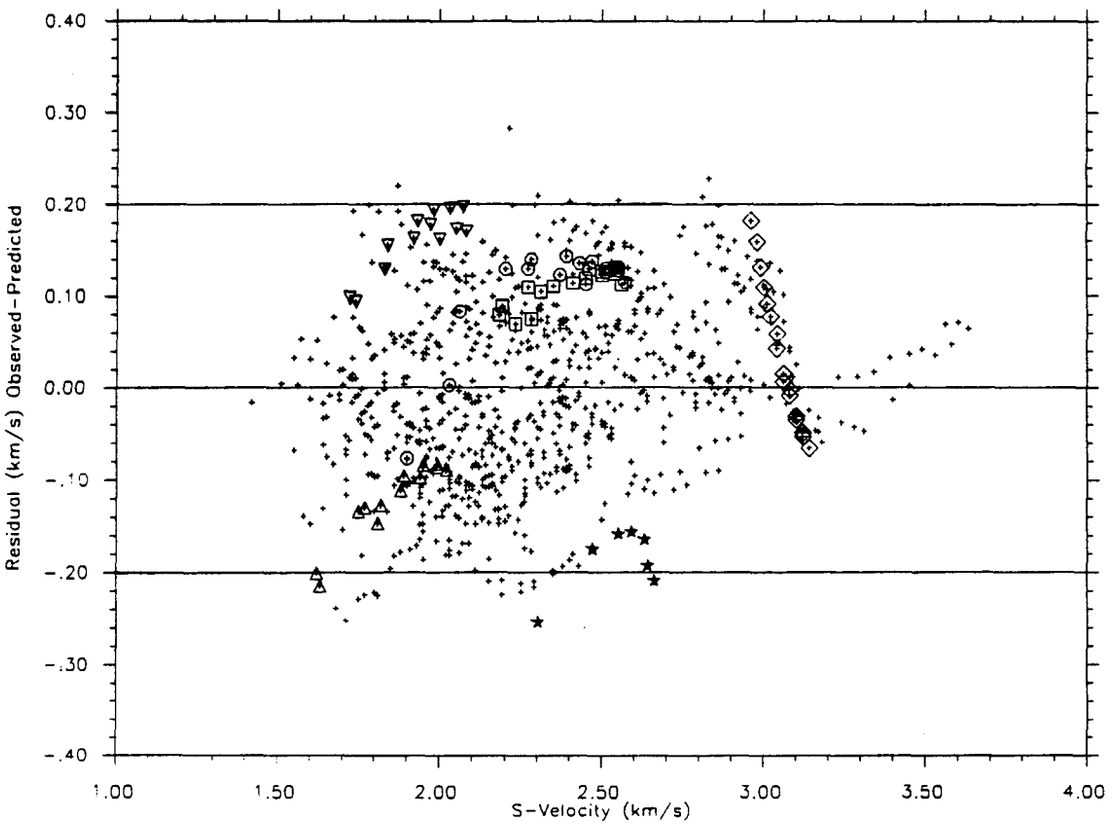

Figure 2 continued. d) V_s residuals versus measured V_s, with the same samples marked as in (b).

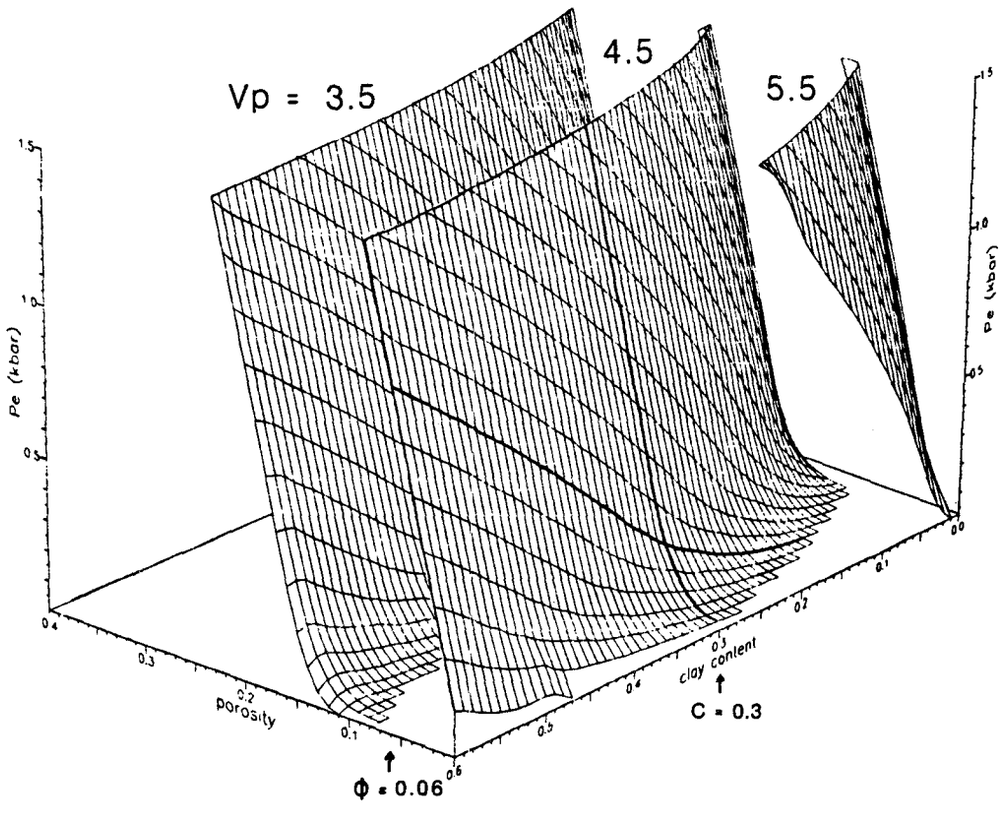

Figure 3. Level surfaces, in the ϕ, C, P_e coordinate system, for increasing V_p. V_p = 3.50, V_p = 4.50, V_p = 5.50. Most measurements of velocity at increasing pressures show that at some point between 1 and 2 kbar, the linear increase with pressure becomes less pronounced and above 5 kbar the curves are nearly flat (Christensen, 1984). Thus, effective pressure is extrapolated to 1.5 kbar.

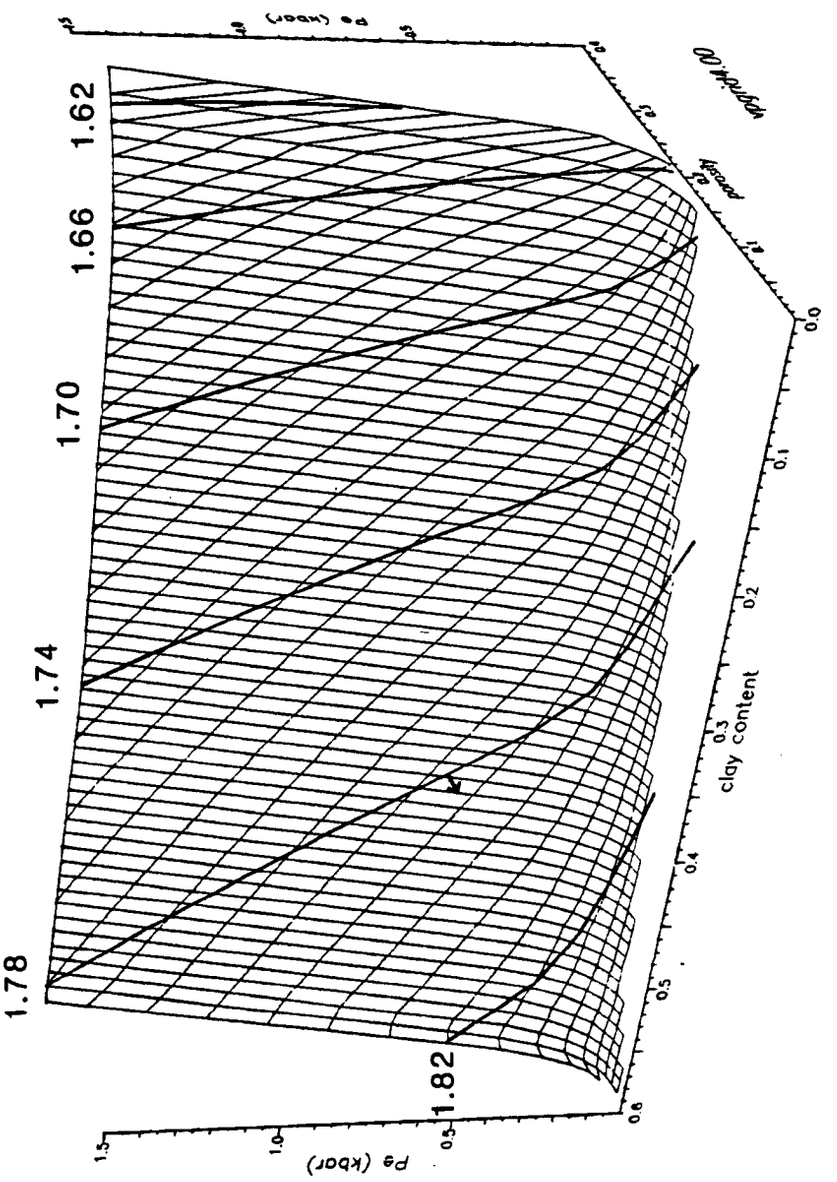

Figure 4. Plot showing effect of varying V_p/V_s ratio for V_p = 4.00. Lines represent intersections with various V_s surfaces. Number next to line indicates the corresponding V_p/V_s ratio.

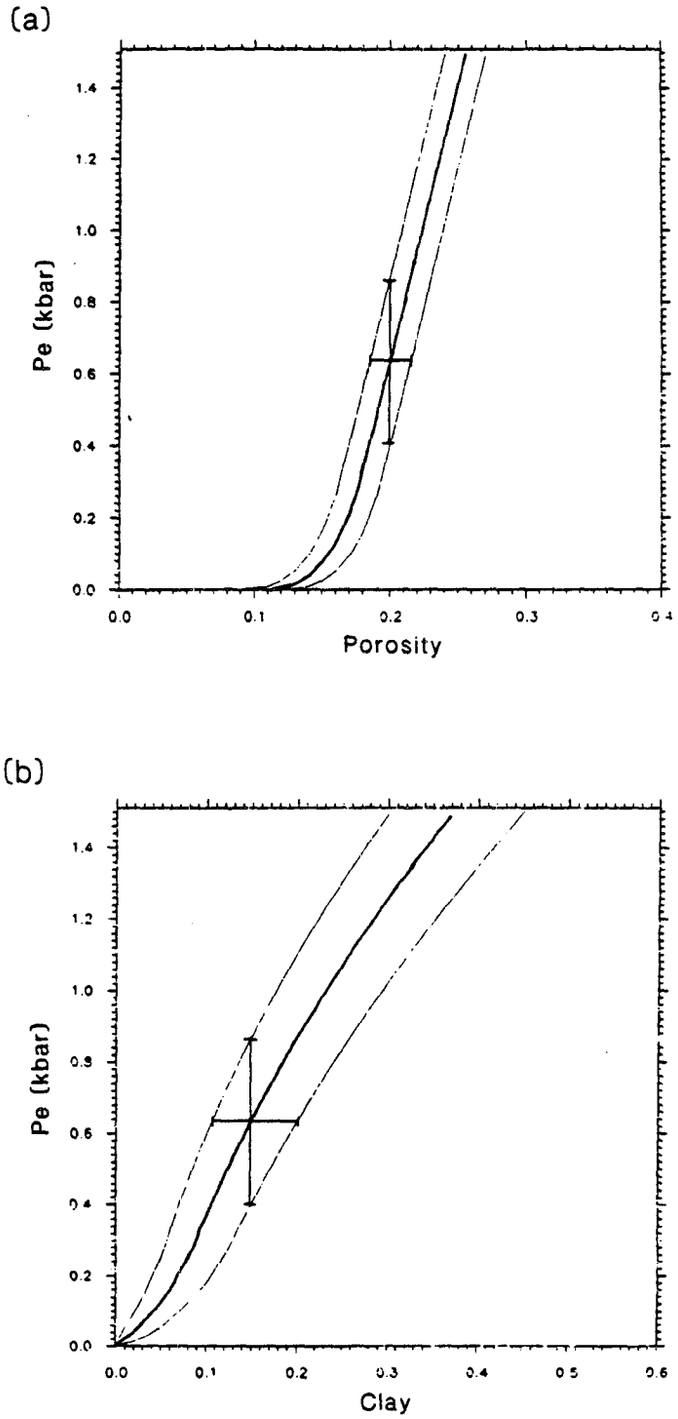

Figure 5. a) Curves showing V_p = 4.00 bounded by curves for 1 SE. a) Shown in ϕ–P_e plane for C=0.15. b) Shown in C-P_e plane for ϕ=0.20. Uncertainties in individual parameters for 1 SE are indicated for the point (ϕ=0.20,C=0.15,P_e=0.62).

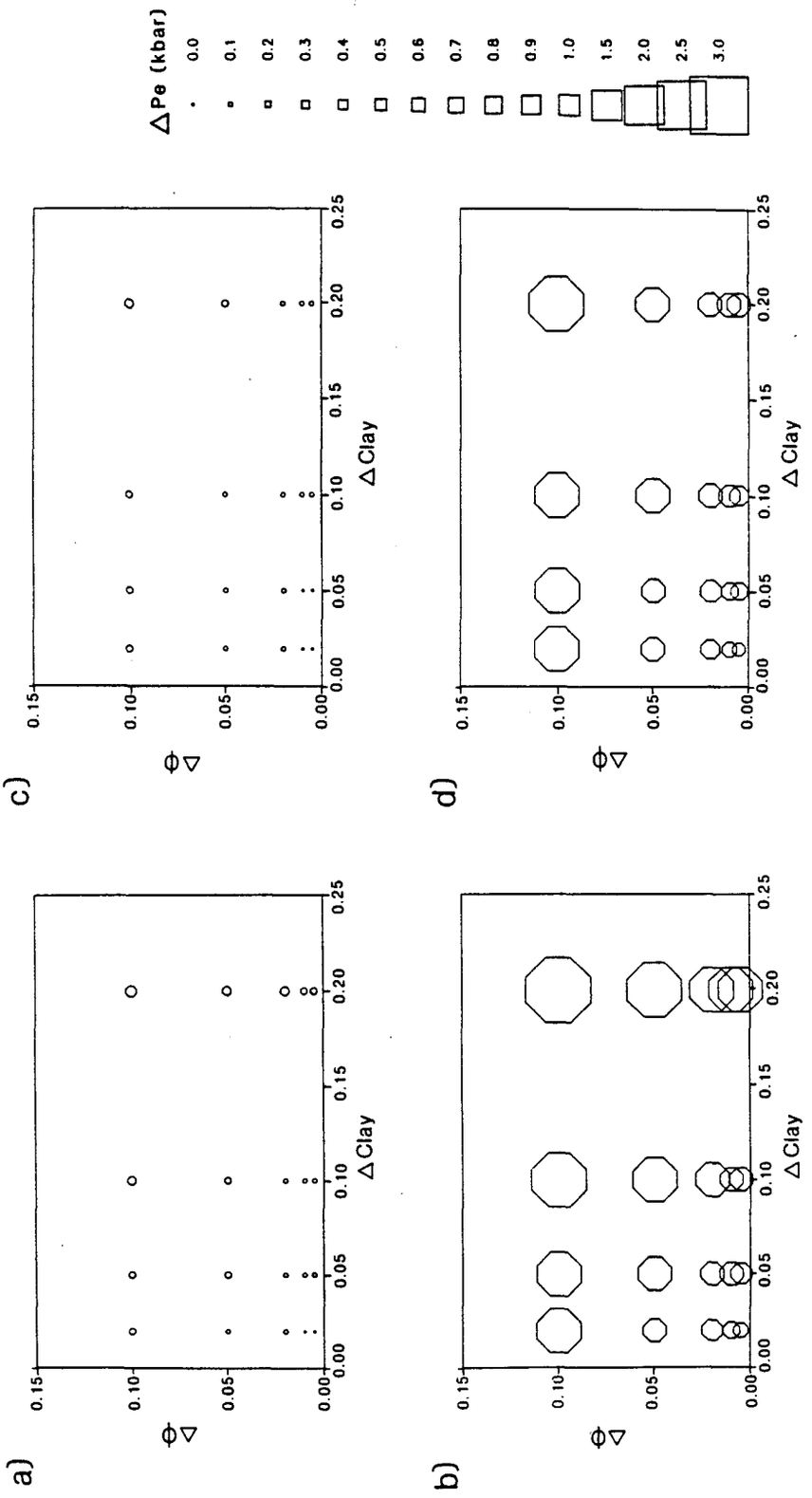

Figure 6. Estimated uncertainty in P_e, indicated by symbol size, for various measurement uncertainties in porosity ($\Delta\phi$) and clay content (ΔC). All plots assume an uncertainty in velocity of 0.1 km/s. a) For ϕ=0.10, C=0.05 at P_e=0.05 kbar (V_p=4.52 km/s), and b) at P_e=0.40 kbar (V_p=4.87 km/s). c) For ϕ=0.10, C=0.30 at P_e=0.05 kbar (V_p=3.96 km/s), and d) at P_e=0.40 kbar (V_p=4.31 km/s).

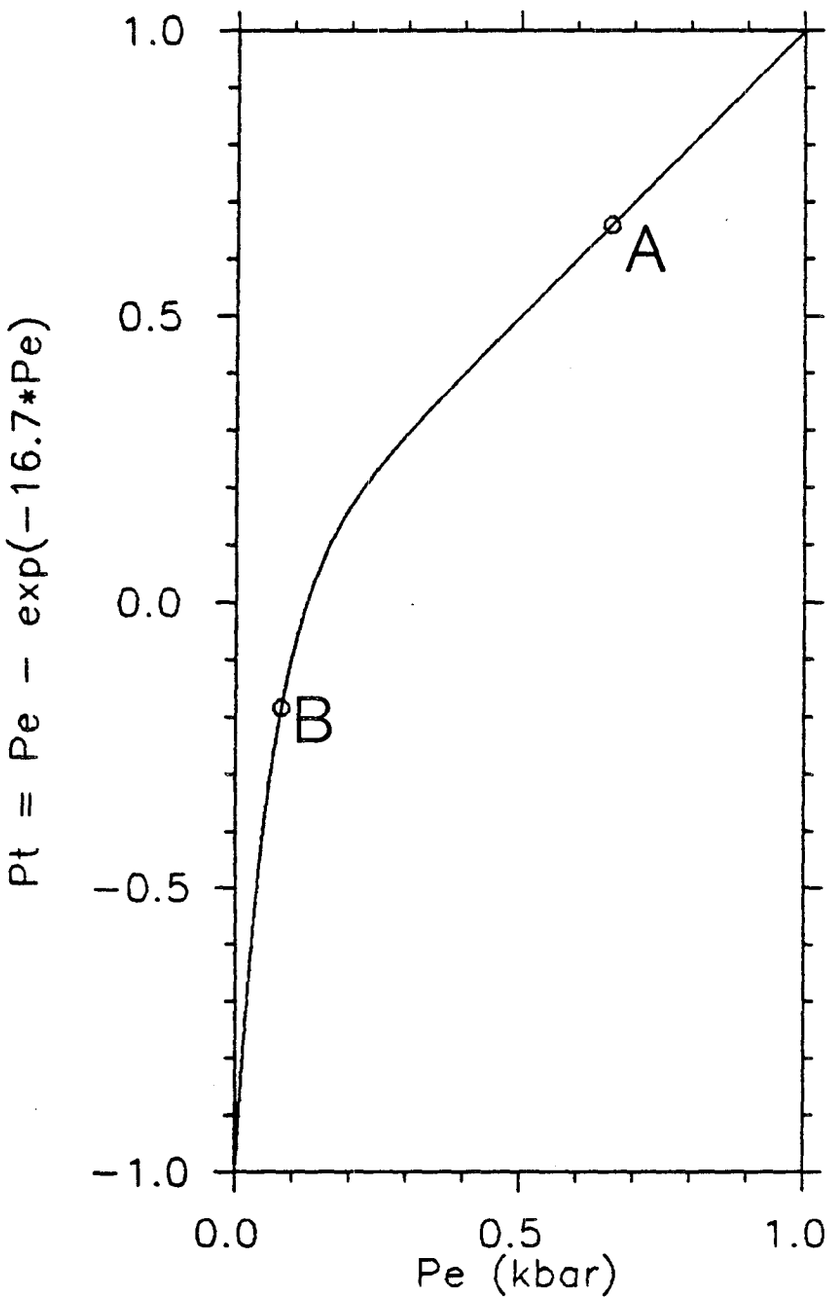

Figure 7. Transformation of P_e to P_t. A = case of hydrostatic P_p at 5 km depth. B = pressure change corresponding to V_p change of 0.4 km/s.

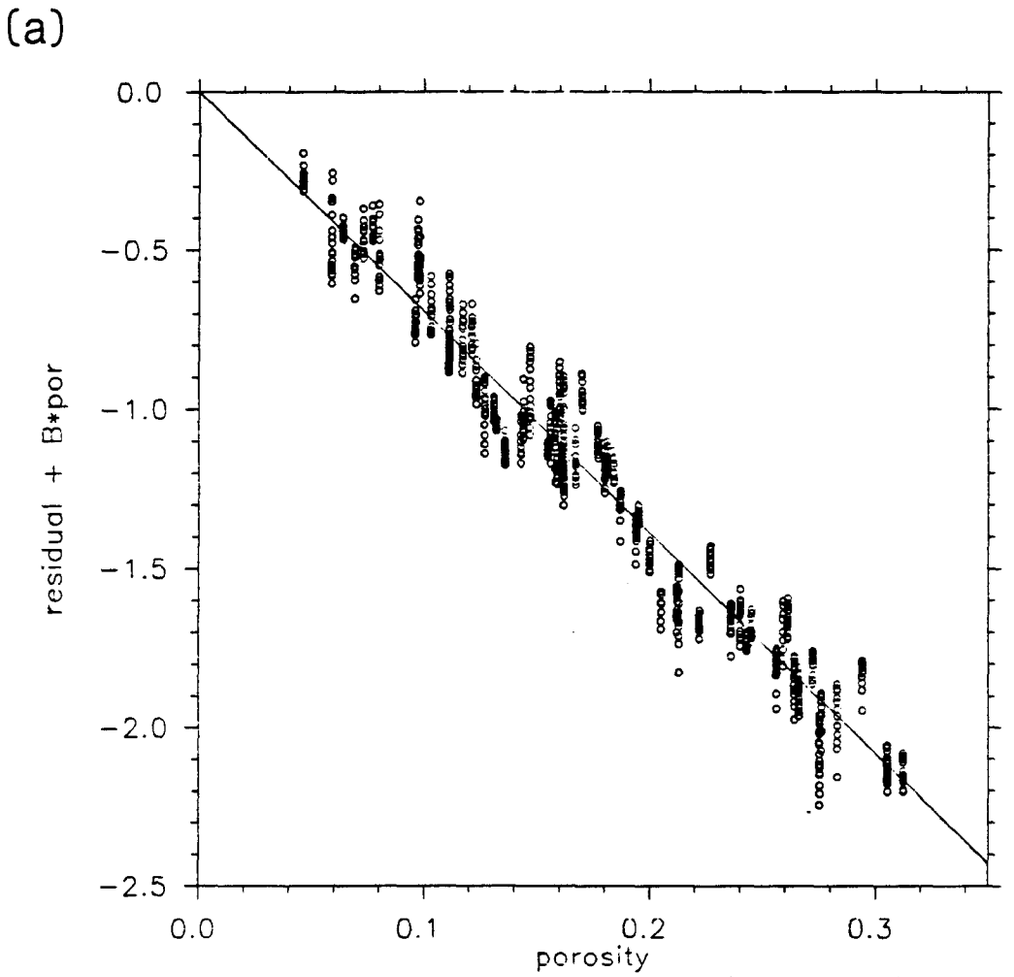

Figure A1. Partial residual plots for each parameter of equation (2), (final residual $+ B_n X_n$). a) Porosity,

(b)

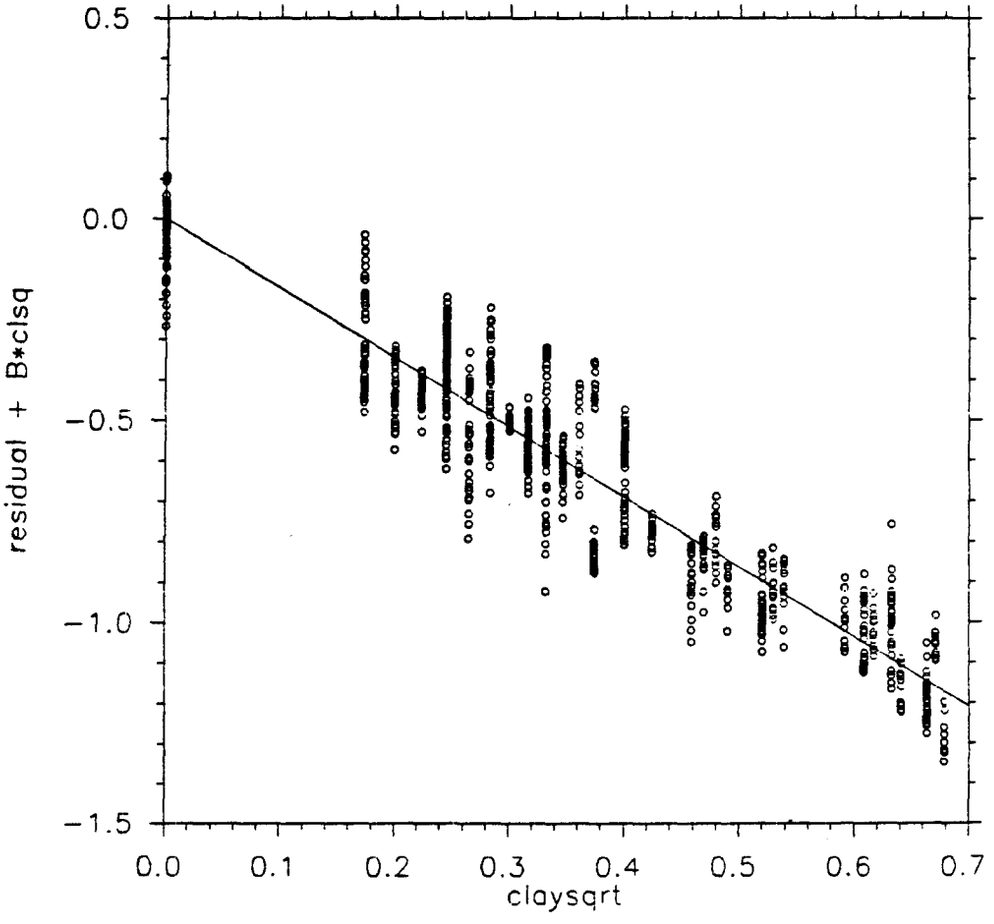

Figure A1 continued. b) $\sqrt{clay}$,

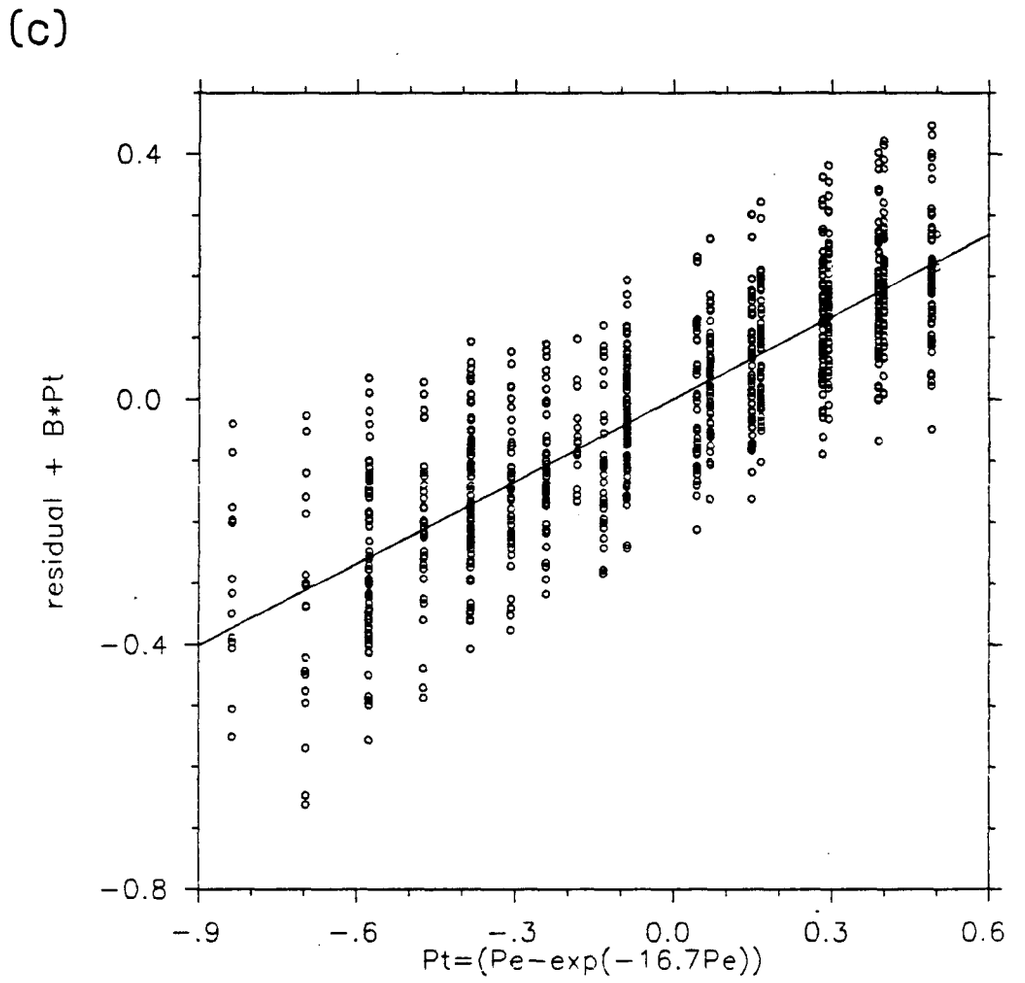

Figure A1 continued. c) $P_e - exp(-16.7P_e)$.

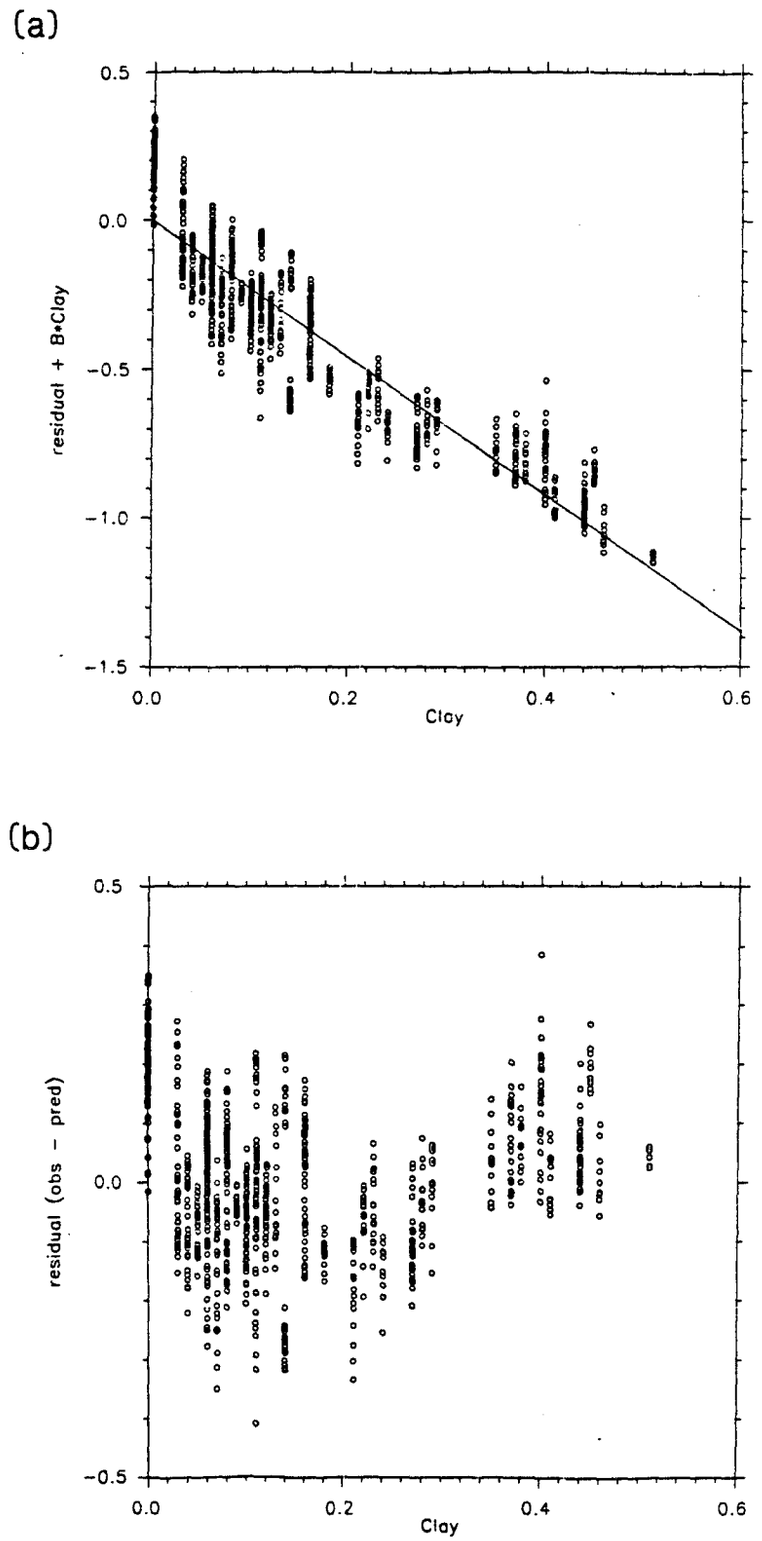

Figure A2. a) partial residual and b) residual plots for the model where $X_2 = C$ instead of $\sqrt{C}$.

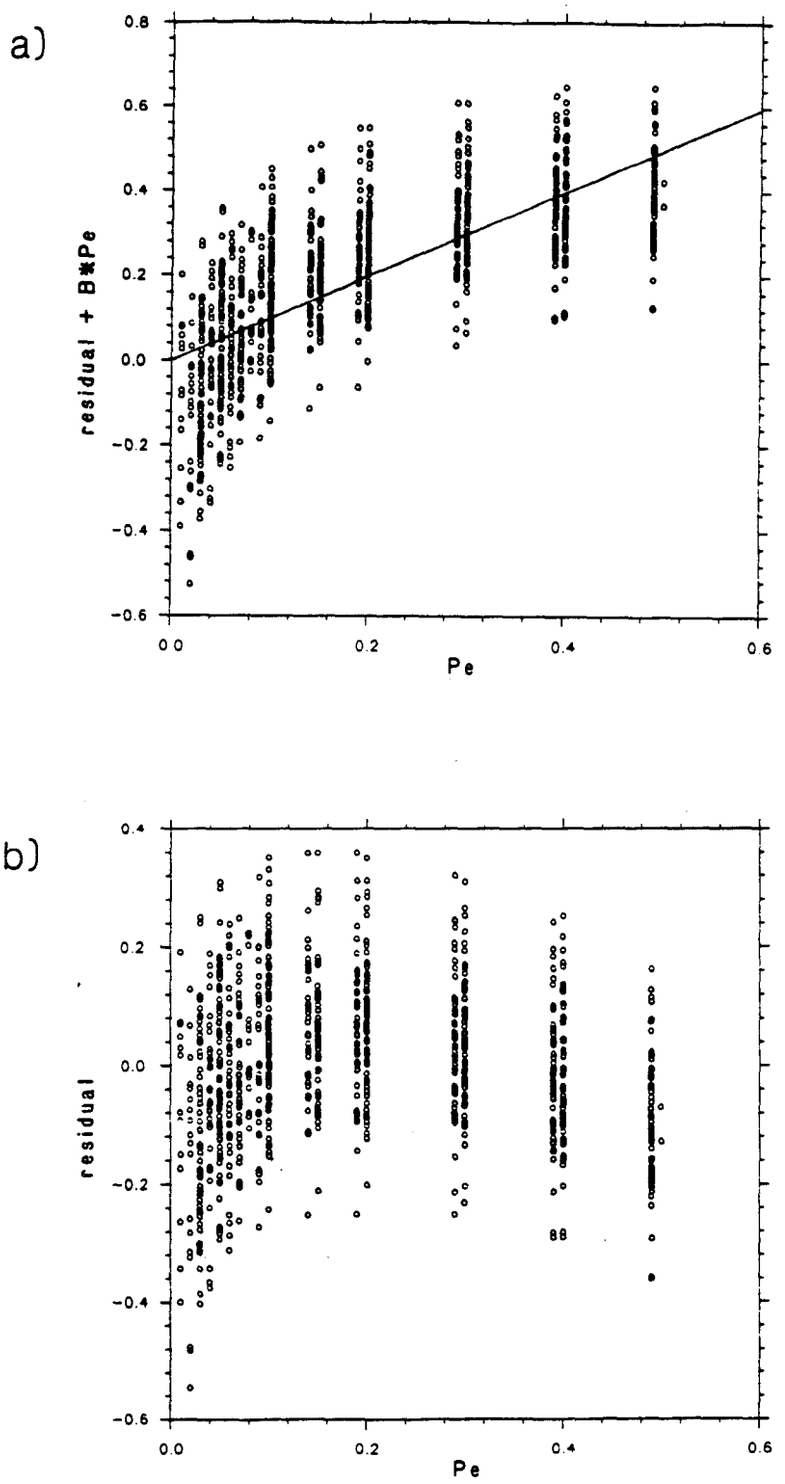

Figure A3. a) partial residual and b) residual plots for the model where $X_3 = P_e$ instead of P_t.